Electronic and magnetic properties of hybrid interfaces. From single molecules to ultra-thin molecular films on metallic substrates.

THÈSE de Doctorat

pour obtenir le grade de

Docteur de l'université Strasbourg
Discipline/Specialité: Physique

Université Strasbourg, École Doctorale de Physique et Chimie-Physique

en cotutelle internationale avec le:

Karlsruhe Institute of Technology

presentée par

Manuel Gruber
né le 19 Mai 1987 à Strasbourg, France

Jury:

Thèse dirigée par:
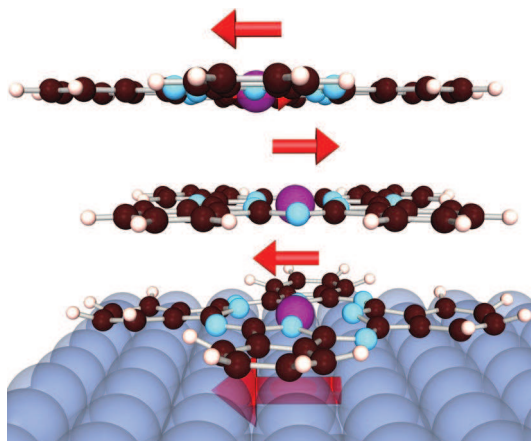Dr. Eric Beaurepaire
Prof. Dr. Wulf Wulfhekel

Rapporteurs:
Prof. Dr. Pietro Gambardella
Prof. Dr. Richard Berndt

Examinateurs:
Prof. Dr. Mébarek Alouani
Prof. Dr. Kirill Melnikov
Dr. Philippe Ohresser

Soutenue le 28 Novembre 2014

Acknowledgment

Up to now, performing my PhD studies was most likely the biggest challenge of my life. Now that I can turn a new page, I realize that the three last years were scientifically and socially very rich; and the satisfaction that I can feel today comes from the combination of both aspects. I had the chance to be surrounded by extraordinary persons, who gave me almost infinite support, motivation, inspiration and joy. I therefore want to express my gratitude to these persons.

I had also the chance to benefit from top-level infrastructures and equipment. I think that it's worth to mention that I have carried out my PhD studies in cotutelle between the Institute of Physics and Chemistry of Materials in Strasbourg (University of Strasbourg and Centre National de la Recherche Scientifique in France) and the Institute of Physics (Karlsruhe Institute of Technology in Germany). I have also spent many weeks at the synchrotron SOLEIL to carry out experiments. I am grateful to these structures and their representatives for hosting me. I am also grateful for the different funding, such as the funding from the French-German University, which allowed such top-level international projects.

First of all, I would like to thank Dr. Eric Beaurepaire: my French PhD supervisor. I should first thank you for giving me the opportunity to perform my doctoral study research. I also appreciated to benefit from your experience and deep knowledge in physics. Furthermore, you always took time for very interesting discussions about physics and academic career. I am also deeply grateful for the trust you had/have in me; and the opportunities for numerous international conferences you provided to me.

I also want to express my gratitude to Prof. Dr. Wulf Wulfhekel: my German PhD supervisor. I thank you for the access to the low temperature STMs. I also appreciated the constant sharing of your knowledge about technical aspects (notably

STM) even if I am still very far from being an expert. I also enjoyed the discussion we had about physics and your general optimistic view. Finally, I was positively surprised by the constant care you manifest to all of your students and the resulting nice atmosphere of the group with numerous parties and memorable ski seminars.

I similarly would like to thank the jury members: Prof. Dr. Pietro Gambardella, Prof. Dr. Richard Berndt, Prof. Dr. Mébarek Alouani, Dr. Philippe Ohresser and Prof. Dr. Kirill Melnikov. I am honored to have such a high-level group of reviewers. I thank you very much for the evaluation of my PhD work.

Now it's the turn of magic miyamac 🍎, also known as Dr. Toshio Miyamachi. I had the chance to benefit from your STM-measurement teaching. There are also other aspects for which I am grateful for: I certainly learned a lot from your"nice looking"/elegant rule for scientific documents. It's for sure not scientific but certainly helps to "sell" the physics we carried out. I was also already a hard worker but I was happy to see that there is still much crazier than me. Finally I really enjoyed the interesting conversations during the numerous diners we had together when we were measuring late.

There are still plenty of people that I should thank, and I hope to not forget too many of them. From the coworkers in IPCMS, I would like to start to thank Dr. Victor Da Costa. I think we made a very good team. Both of us wanted to take extra care of the equipment, proceed step by step and constantly improved the setup. These aspects greatly helped for the design of the "multiprobe" that is quite advanced at the moment. I also would like to thank you for the AFM teaching at the beginning of my PhD work. I also want to express my gratitude to Dr. Fabrice Scheurer. Your door was always open for fruitful discussions, and I appreciated the time we spent together during synchrotron runs. From these synchrotron runs, I remember that you were always motivated and optimistic for trying new things even when we were super tired. These aspects certainly boosted the experiments that led to nice results. Additionally, you shared with me your knowledge about UHV and more generally about technical aspects; these aspects were very useful for me and will still be useful for my future career. The next one in the list is Dr. Loïc Joly. You always answered my questions about synchrotron radiations and X-ray absorption. More specially, you greatly helped me for the data analysis. My software for analysis would certainly not be that advanced without your inspiration and help. I believe that a large part of the results obtained in this thesis are due to the quick qualitative data analysis we performed while measuring. You were also always motivated to implement new acquisition scripts when we had crazy ideas for new measurements. I deeply appreciated all these aspects. Thank you. I also would like to acknowledge Prof. Dr. Wolfgang Weber for the interesting discussions about magnetism and your investment for the experimental runs. It surely boosted all the experiments. I also would like to thank you for inviting me in side experiments (mainly spin-polarized photoemission). Even if these experiments are not part of this thesis, I really enjoyed the associated physics and of course learned a lot of things. My gratitude also goes to Jacek Arabski. I enjoyed our physical and non-physical subjects of conversation. You were always present and motivated to help for any problem. If I needed something,

you always knew whom I could ask for it. Thank you for everything, especially the permanent supports. Dr. Martin Bowen, I also own you a lot. I remember you saying "Work hard, play hard", and I believe that you're totally right. I appreciated both aspects. I remember during the synchrotron runs the intensive reflections and "debate" we had and the constant consideration for improving efficiency. During the same synchrotron runs, I also remember our memorable Frisbee games in the night while acquiring data. Finally, I must admit that I considerably improved my writing skills with you. At present, I would like to thank Dr. Samy Boukari. You were always ready helping me to solve a given problem, especially when it involved small mathematical models. I also greatly appreciated your general pessimistic view, since it always helped to reinforce our data/explanation/comprehension.

I also would like to acknowledge my "PhD coworkers": MichałStudniarek, Ufuk Halisdemir, Dr. Vincent Davesne, Hashim Jabbar, Dr. Saber Gueddida and Dr. Fatima Ibrahim. I should also thank Virginie Speisser, Jacques Faerber and Dr. Michelangelo Romeo. You were always present to help me and to answer my questions about technical aspects (mainly UHV). Concerning technical assistance, I am very grateful to Bernard Muller, Arnaud Boulard, Christophe Kieber, Daniel Spor, Manuel Acosta and Guy Schmerber. I should not forget to thank Dr. Guillaume Schull and Dr. Laurent Limot for the interesting discussions about STM physics and my future career. I have spent many weeks at synchrotron SOLEIL, and more precisely at DEIMOS beamline. I would like to thank again Dr. Philippe Ohresser. I really appreciated the pedagogical answers you provided to my questions (mainly about X-ray absorption and the beamline). You always took time to explain me the things well and also time for considering crazy ideas for new experimental procedure that I proposed. I also would like to thank Dr. Edwige Otero, Dr. Fadi Choueikani and Dr. Kai Chen for"hosting" me and the permanent support for our experiments.

From KIT, I am deeply grateful to the group of Prof. Dr. Wulfhekel. A special thank to Lukas Gerhard who took special care to teach me all the basis of UHV and the STM setups. It was at the beginning of my masterwork but this knowledge was very useful during my PhD studies. I should also thank Dr. Hironari Isshiki, Dr. Michael Schackert, Moritz Peter, Dr. Marie Hervé, Dr. Timofey Balashov, Tobias Märkl, Dr. Tobias Schuh, Dr. Stefan Schmaus, Jasmin Jandke, Dr. Lei Zhang, Dr. Noelia Bajales Luna, Lorentz Schmidt. In fact I am grateful to all the present and past members of Wulfhekel's group. I enjoyed very much the numerous parties and the ski seminars.

From IPCMS, there are also a lot of people/colleagues/friends with whom I didn't necessarily work with, but I spent very nice moment with you. With some of you, we almost always had lunch together, coffee breaks, parties, trips (Barcelona, Berlin, . . .). I owe you so much but it's impossible for me to write it down. So thanks to Dr. Christian Andreas, Silvia Zanettini, Dr. Céline Etrillard, Dr. Gaël Reecht, Dr. Ondřej Vlašín, Dr. Vina Faramarzi, Dimitra Xenioti, Florian Godel, Tindara Verduci, Michael Chong, Guillaume Froehlicher, François Federspiel, Dominik Metten, Déborah Persuy, Mathilde Menard, Kerstin Bücker, Tsiky Hasiniaina, Nicolas Bachellier, Ufuk Halisdemir, Dr. Filip Schleicher, MichałStudniarek, Dr. Wojciech

Contents

III Investigation of organic functional molecules on surfaces: spin-crossover molecules

Résumé

Introduction

La miniaturisation des composants électroniques a permis de considérablement augmenter la puissance et la capacité de stockage de nos appareils électroniques. Dans le but de faire face aux besoins croissants dans le domaine des télécommunications, l'industrie du silicium souhaite maintenir cette constante miniaturisation en suivant une loi, dite de Moore, qui vise à doubler le nombre de composants sur une puce tous les deux ans. Cependant, la miniaturisation des composants à base de silicium va très bientôt se confronter à des limites physiques infranchissables d'origine quantique telle que l'effet tunnel.

Pour aller au delà de ces limitations, il faudrait changer de matériaux ou bien radicalement changer de concepts. Une des branches émergente et active allant dans cette direction est l'électronique moléculaire dont le but est de réaliser des composants électroniques à partir d'une molécule unique. De plus, les molécules représentent des candidats prometteurs pour des concepts nouveaux tels que l'électronique de spin,[1] aussi appelée la spintronique, ainsi que l'informatique quantique.[2]

L'utilisation de molécules organiques pour la fabrication de dispositifs basés sur la spintronique présente de nombreux avantages tels que le potentiel faible coup de production et la longue durée de vie du spin attendu pour ce type de matériaux. Au cours de cette dernière décennie, la communauté de la spintronique organique a considérablement œuvré pour la réalisation de dispositifs opérationnels et robustes opérant à température ambiante.[1,3] Cependant, malgré tous ces efforts au niveau de la recherche fondamentale, le transport polarisé en spin dans ce type de systèmes soulève encore de nombreuses questions très intéressantes d'un point de vue fondamental. Par exemple, des mesures sur des échantillons hybrides com-

posés d'électrodes ferromagnétiques à partir de matériaux inorganiques ainsi qu'un espaceur organique, montrent une magneto-résistance tunnel bien supérieure aux prédictions des modèles actuels.[4,5] Un consensus a émergé mettant en avant l'importance de l'interface molécules/ferromagnétique pour l'injection de courants polarisés en spin de l'électrode ferromagnétique à l'espaceur inorganique. L'interface hybride molécules/ferromagnétique est désormais vu comme un levier pour moduler la réponse d'un dispositif spintronique.[3,4] Par conséquent, une meilleure compréhension de la physique prenant place au niveau de ces interfaces semble indispensable pour un meilleur contrôle des propriétés des futurs dispositifs et fait l'objet de cette thèse.

La première partie de cette thèse est consacrée à l'étude des propriétés électroniques et magnétiques des interfaces molécules/métal. Pour cette étude, nous avons utilisé des molécules de phtalocyanine de manganèse (MnPc) déposées sur un substrat de cobalt ferromagnétique. Des études antérieures ont montré que la première monocouche de MnPc est ferromagnétiquement couplée au substrat de cobalt, et ceci même à température ambiante indiquant un couplage fort.[6] Par ailleurs, des mesures de photoemission polarisée en spin réalisées à température ambiante mettent en avant la création d'une "spinterface" fortement polarisée en spin proche du niveau de Fermi suite à l'adsorption des molécules de MnPc.[7] Ces observations expérimentales ont été confirmées par des calculs *ab initio* réalisés par nos collaborateurs. A noter que les outils de calculs que nos collaborateurs utilisent semblent avoir atteint une certaine maturité depuis l'inclusion des forces de Van-der-Waals.[8] Dans cette thèse, à l'aide de la spectroscopie d'absorption des rayons X, nous étudions l'influence du substrat magnétique et de la spinterface sur les couches moléculaires de MnPc, au delà de la première monocouche. Contre toute attente, l'adsorption de molécules de MnPc sur le substrat de cobalt peut modifier les propriétés magnétiques de ce dernier. De manière alternative, nous avons également étudié le couplage magnétique entre la première monocouche de MnPc et le substrat de cobalt à travers un espaceur non magnétique.

La deuxième partie de cette thèse porte sur l'étude de molécules fonctionnelles sur des substrats métalliques. Comme cela a été précédemment relevé, nous pouvons imaginer des futurs composants électroniques réalisés à partir de molécules uniques qui incorporent des fonctions particulières. Ces fonctions peuvent être ajustées à souhaits en modifiant adéquatement les molécules à l'aide de la chimie. Cependant, pour utiliser ces molécules à des fins applicatives, les molécules doivent être déposées sur des surfaces bien que leur adsorption puisse considérablement altérer leurs propriétés ou fonctions. Dans cette thèse, l'accent est porté sur une classe particulière de molécules fonctionnelles : les molécules à transition de spin.[9] Ces complexes sont des commutateurs moléculaires qui peuvent être commutés entre un état bas spin et un état haut spin en utilisant différents stimuli. La question qui se pose naturellement est de savoir si ce type de molécule peut garder ses propriétés de commutateurs dès lors qu'elles sont déposées sur des surfaces. En combinant des mesures à l'aide d'un microscope à effet tunnel à basse température et de la spectroscopie d'absorption des rayons X, nous avons mis en évidence que des molécules de $Fe(phen)_2(NCS)_2$ peuvent être déposées sur des surfaces métalliques et que des molécules dans les deux états

de spin coexistent à basse température. Nous avons étudié cette coexistence plus en détails puisque pour ce type de molécules nous nous attendrions à des molécules uniquement dans un état bas spin. Nous avons également montré que ces molécules peuvent être commutés d'un état de spin à l'autre de manière sélective et déterministe via l'application d'impulsions de tension à l'aide de la pointe du microscope, pourvu que les molécules soient suffisamment découplées du substrat métallique.

Etude de l'interface hybride MnPc/métal

La molécule utilisée pour ces travaux est la phtalocyanine de manganèse (voir Fig. Ia) déposée sur un substrat magnétique de cobalt. Le choix se justifie par les précédentes observations d'un fort couplage magnétique entre l'ion de manganèse et le substrat, ainsi que la formation d'une spinterface très fortement polarisée en spin. Par ailleurs, les molécules de MnPc, et ceci semble général pour les dérivés de phtalocyanine, s'organisent en colonnes dans leur forme cristalline. Ceci mène à des corrélations magnétiques à très basse température entre des molécules voisines au sein d'une même colonne.[10–12] Les corrélations magnétiques peuvent être antiferromagnétiques ou ferromagnétiques suivant la phase cristalline des molécules (forme α ou β). Dans cette thèse, nous donnons des éléments de réponse à la question qui se pose naturellement : peut-on, de manière avantageuse, tirer profit des corrélations magnétiques entre les molécules pour fabriquer des spinterfaces opérationnelles et robustes ? Et quel serait l'impact de ces corrélations magnétiques sur les propriétés magnétiques du substrat ?
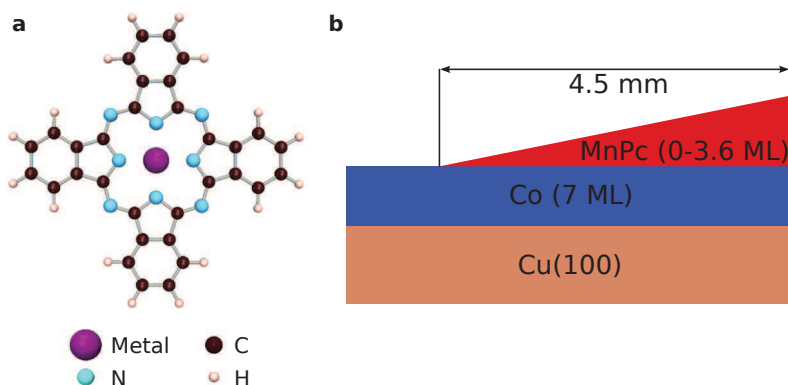
Figure I. – **Molécule de phtalocyanine de manganèse et schéma de l'échantillon étudié**.

Puisque l'organisation structurale des molécules a une forte incidence sur leurs propriétés magnétiques, la première grande étape de l'étude a consisté à déterminer l'orientation des molécules de MnPc par rapport à la surface de cobalt, et ceci pour des épaisseurs croissantes de MnPc. Pour ce faire, nous avons réalisé des échantillons
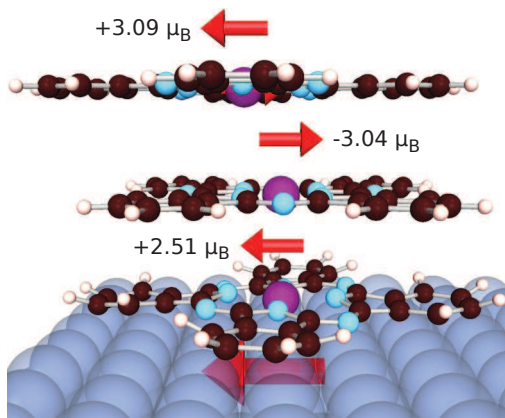
Figure II. – **Molécules de MnPc empilés montrant un ordre antiferro-
magnétique**. La valeur des moments magnétiques des ions de manganèse
issue des calculs *ab initio* est indiquée.

avec une épaisseur de MnPc variable allant de 0 à 3.6 ML (voir Fig. Ib) que nous avons
étudié à l'aide du dichroïsme linéaire des rayons X sur le seuil de l'azote. Ces mesures
ont révélé que les deux premières monocouches de MnPc s'adsorbent à plat sur la
surface tandis que les molécules formant la troisième et la quatrième monocouche
sont bien plus désordonnées.

Concernant les propriétés magnétiques de la première monocouche de molécules,
les mesures de dichroïsme circulaire magnétique de rayons X (XMCD) ont montré
que les ions de manganèse sont ferromagnétiquement couplés au substrat de cobalt, en
accord avec les expériences précédentes. Les ions de manganèse des molécules formant
la seconde monocouche sont couplés de manière antiferromagnétique au substrat, et
ceci même à température ambiante (voir Fig. II). Quant aux mesures XMCD sur les
ions manganèse des molécules composant la troisième et quatrième monocouche, les
résultats mettent en avant une dominance de molécules non-magnétiquement couplées
au substrat. Nous supposons que les molécules non-magnétiquement couplées sont
celles qui sont structuralement désordonnées. L'ordre antiferromagnétique dans les
colonnes de MnPc sur un substrat de cobalt est également prédit par des calculs *ab
initio*.

Ces résultats sont très encourageants et permettent d'entrevoir des perspectives
pour le transport polarisé en spin au travers d'espaceurs moléculaires. L'ordre magné-
tique observé pour les premières monocouches moléculaires laisse supposer un impact
sur le transport polarisé en spin que l'on peut espérer moduler via une ingénierie
des interactions magnétiques entre les molécules.[13] Par ailleurs, le système étudié
présente des similitudes avec des échantillons purement inorganiques composés d'une
couche antiferromagnétique en contact avec une couche ferromagnétique. Pour ces
derniers échantillons, en dessous d'une certaine température, la couche antiferromag-
nétique peut induire une anisotropie d'échange (exchange bias) et se manifester par
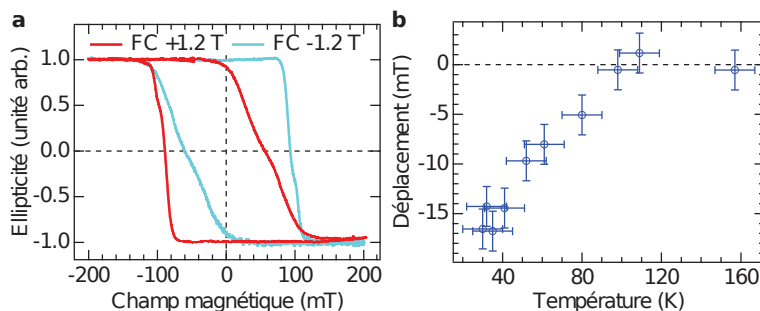
Figure III. – **Anisotropie d'échange induite par la couche molécu-
laire de MnPc**. **a**, Cycles d'hystérèse sur un échantillon de
Au(15 ML)/MnPc(50 ML)/Co(20 ML)//Cu(100) obtenus à 32 K après
refroidissement sous des champs magnétiques de 1.2 T et de −1.2 T.
L'hystérèse se retrouve déplacée dans la direction opposée au champ ap-
pliqué durant le refroidissement, ce qui est caractéristique de l'anisotropie
d'échange. **b**, Dépendence en température du déplacement de l'hystérèse
indiquant une température de blocage d'environ 100 K.

un déplacement du cycle d'hystérésis. L'anisotropie d'échange[14] est un effet qui a un
grand nombre d'applications, notamment pour les têtes de lecture magnétorésistives.
De plus, l'anisotropie d'échange suscite également un grand intérêt d'un point de vue
fondamental pour comprendre les mécanismes physiques complexes mis en jeu et qui
à l'heure actuelle ne sont toujours pas complètement élucidés.

Dans le but de tester l'éventuelle présence de l'anisotropie d'échange qui n'a pas
encore été reportée pour des systèmes moléculaires, nous avons fabriqué des échantil-
lons avec la composition suivante : Au(15 ML)/MnPc(50 ML)/Co(20 ML)//Cu(100),
puis nous avons mesuré leurs propriétés magnétiques à l'aide de l'effet Kerr magnéto-
optique. Les cycles d'hystérèses mesurés à basse température après refroidissement
sous champ montrent un déplacement dans le sens opposé au champ utilisé durant le
refroidissement (voir Fig. IIIa). Ceci est caractéristique de l'anisotropie d'échange.
En outre, ces mesures ont été répétées pour différentes températures montrant une
décroissance linéaire du déplacement avec la température, et l'effet disparaît pour une
température de blocage d'environ 100 K (voir Fig. IIIb).

Ci-dessus, nous avons reporté l'anisotropie d'échange, un des piliers de la spin-
tronique inorganique, induit par des systèmes moléculaires. Le domaine de la spintron-
ique organique en ressort renforcé mais il y a encore un certain nombre de limitations
identifiées avant de pouvoir être compétitif avec les dispositifs purement inorganiques.
En premier lieu, nous pouvons citer la température de blocage de l'ordre de 100 K
qui est bien en dessous de la température ambiante. Nous pouvons potentiellement
remédier à ce problème par une ingénierie des interactions moléculaires. D'autre part,
le choix des systèmes moléculaires est relativement restreint. En effet, les propriétés
de la couche magnétique sont généralement très sensibles à l'adsorption d'impuretés
inhérente à l'exposition de la couche à l'air ou à un solvant. Le choix du système
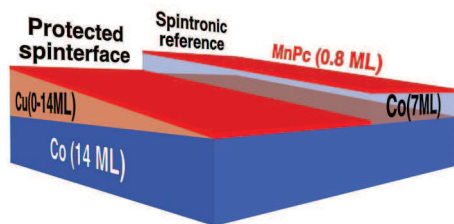
Figure IV. – **Schéma de l'échantillon fabriqué pour l'étude du couplage d'échange au travers d'une couche de cuivre**.

moléculaire se repose donc sur la possibilité de déposer les molécules dans une atmosphère inerte (ou sous vide) en l'absence de solvant. Pour contourner cette limitation nous avons étudié la possibilité de former une spinterface hybride au travers d'un espaceur inorganique non-magnétique qui sert également de couche de protection à l'électrode magnétique. Pour les systèmes inorganiques, un couplage d'échange (interlayer exchange coupling ; IEC) peut coupler deux couches ferromagnétiques séparées par un espaceur non-magnétique.[15, 16]

Un des systèmes de référence en spintronique pour l'IEC est Co/Cu/Co//Cu(100). L'intensité et le signe du couplage magnétique oscillent avec l'épaisseur de cuivre. Pour notre tentative de réalisation d'un système IEC hybride, nous avons opté pour le système suivant : MnPc/Cu/Co//Cu(100), qui est relativement proche du système de référence. Par ailleurs, pour un meilleur contrôle des épaisseurs de cuivre et une meilleure comparaison du système de référence avec le système hybride, les deux systèmes sont fabriquées sur un même échantillon avec une épaisseur de Cu variant de 0 à 14 ML (voir Fig. IV).

Pour le système hybride, à température ambiante, les mesures XMCD ont révélé un couplage magnétique entre l'ion de manganèse des MnPc et la couche de cobalt séparés jusqu'à 4 ML de cuivre (voir Fig. V). Le couplage est ferromagnétique pour 0, 2 et 3 ML de cuivre tandis que pour 1.5 ML de cuivre, le couplage est antiferromagnétique. Ces observations sont en accord complet avec des calculs *ab initio* réalisés par nos collaborateurs.

Nous avons observé l'évolution du couplage magnétique en fonction de l'épaisseur de cuivre de manière plus systématique sur le système hybride et sur le système de référence (voir Fig. VI). Pour le système de référence, les oscillations de couplage sont très marquées et peuvent être reproduites par une expression analytique du IEC. Concernant le système hybride, à température ambiante, les oscillations sont plus faibles et disparaissent pour des épaisseurs importantes de cuivre. Cependant, si la température est abaissée à 4.8 K, les oscillations perdurent pour des épaisseurs de cuivre allant jusqu'à 14 ML. Comme attendu, les oscillations observées ont même période et phase que les oscillations du système de référence. En appliquant un fort champ magnétique externe de 6.5 T, les oscillations sont toujours présentes mais l'XMCD a révélé une plus large proportion de moments des molécules alignées suivant
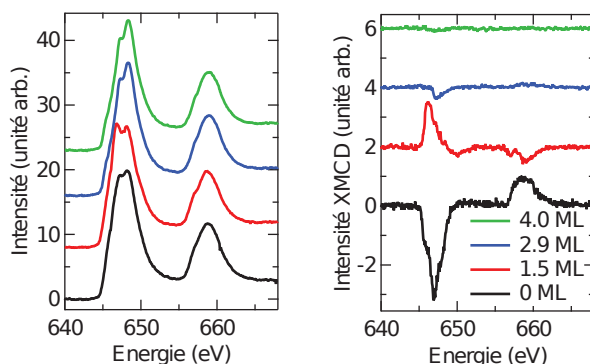
Figure V. – **Spectres d'absorption et de dichroïsme circulaire magné-
tique sur le seuil du manganèse pour différentes épaisseurs de
cuivre**. Le système étudié est le système hybride (MnPc/Cu/Co). Les
mesures ont été effectuées à température ambiante et montrent un cou-
plage entre le manganèse et le substrat de cobalt d'intensités et de signes
variables.

le champ externe. Ceci suggère que les molécules restent paramagnétiques et sont
stabilisées avec un champ effectif venant de l'IEC. A l'aide de différentes mesures
XMCD effectuées sous différents champs magnétiques et à différentes températures,
nous avons pu estimer un champ effectif provenant du couplage d'échange de 80 T
pour 1.5 ML de cuivre, et de l'ordre de 1 T pour 7 ML de Cu.

Concernant les propriétés de transport, ou du moins de la polarisation en spin
proche du niveau de Fermi, les calculs *ab initio* suggèrent de très fortes polarisations
en spin pouvant être bien supérieures au système sans espaceur. Pour une épaisseur
de cuivre de 1 ML, les calculs montrent une polarisation en spin de −98 %. Pour
2 ML la polarisation en spin baisse et change de signe (30 %) tandis que pour 3 ML de
cuivre, la polarisation en spin raugmente fortement pour atteindre 75 %. Ces fortes
polarisations en spin proche du niveau de Fermi devraient promouvoir un excellent
transport polarisé en spin au travers de l'interface.

En outre des perspectives de spinterface protégée de l'adsorption d'impuretés,
nous avons montré qu'utiliser une couche de molécules paramagnétiques permet de
mieux sonder l'intensité et le signe du couplage d'échange (IEC). Par ailleurs, l'absence
d'interactions magnétiques entre les centres paramagnétiques localisés au sein des
molécules permet de sonder le champ d'échange localement et ainsi d'être insensible
aux rugosités des interfaces. Ceci permettrait, a priori, d'explorer plus en profondeur
la physique de l'IEC et des puits quantiques dans des systèmes dont la compréhension
a été limitée, jusqu'à présent, par leur croissance imparfaite.
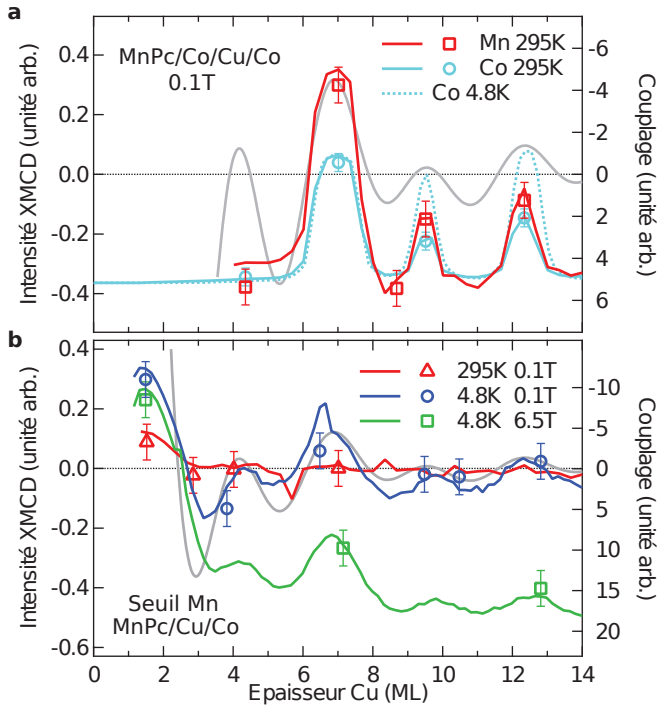
Figure VI. – **Oscillation du couplage d'échange en fonction de l'épaisseur de l'espaceur pour le système de référence et pour le système hybride**. Evolution du couplage d'échange pour **a**, le système de référence et **b**, pour le système hybride.

Molécules à transition de spin sur des surfaces métalliques

Les spinterfaces formées notamment à partir de molécules de phtalocyanine montrent des perspectives relativement intéressantes pour des applications futures. Nous pouvons par exemple entrevoir la fabrication de jonctions à deux états composées de deux électrodes magnétiques et d'un espaceur moléculaire. L'état de la jonction peut représenter la conductance de cette dernière, et dépendre de l'orientation magnétique des électrodes. Si les molécules de Pc composants l'espaceur sont remplacées par des molécules fonctionnelles, nous pourrions éventuellement obtenir des dispositifs spintroniques avec des jonctions de plus de deux états.

Les molécules à transition de spin sont une classe de molécules fonctionnelles qui présentent un grand intérêt. Ces molécules sont des commutateurs pouvant commuter entre deux états : un état haut spin et un état bas spin.[9] Puisque la commutation est accompagnée par un changement de conformation des molécules, nous pouvons nous
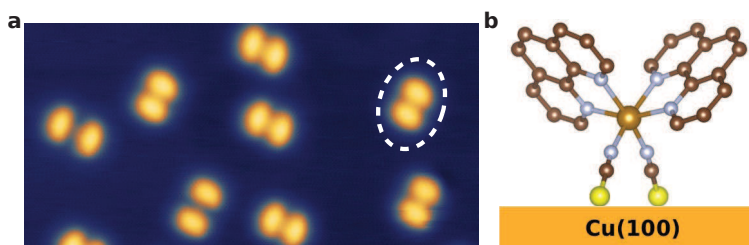
Figure VII. – **Molécules de Fe-phen sur une surface de Cu(100). a**,
Topographie d'une sous monocouhe de Fe-phen sur Cu(100) obtenue à
4 K. L'image a une taille de 17 nm × 8.5 nm. **b**, Schéma de la géométrie
d'adsorption de la molécule de Fe-phen sur Cu(100).

attendre à une conductance des molécules qui dépend de leur état de spin. Dans le
but d'utiliser ces molécules à des fins applicatives, il est nécessaire de les déposer sur
des surfaces. La question que nous tentons d'adresser dans ces travaux est de savoir
si l'interaction des molécules avec le substrat a une influence sur la fonction de ces
dernières.

La molécule à transition de spin utilisée dans ce travail est la $Fe(phen)_2(NCS)_2$
(Fe-phen) qui, dans sa forme massive, est dans l'état bas spin S=0 à basse température
et peut transiter dans l'état haut spin S=2 en augmentant la température au dessus
de 175 K.[17] Nous avons déposé une sous monocouche de molécules de Fe-phen sur
une surface de Cu(100) dans un environnement ultra vide et étudié la surface à l'aide
d'un microscope à effet tunnel (STM) à basse température (4 K). Les topographies
obtenues ressemblent à celle représentée dans la Fig. VII où l'on voit des pairs de
lobes isolés. L'orientation des molécules est telle que les groupements NCS sont dirigés
vers le substrat tandis que les groupes phenanthrolines pointent dans la direction
opposée.

Lorsque le taux de couverture de Fe-phen est augmenté, nous pouvons observer
une belle croissance couche par couche (voir Fig. VIII). Par ailleurs, les molécules
restent "isolées" pour la première monocouche tandis qu'elles forment des îlots et
des structures organisées pour la seconde monocouche. Cette différence de crois-
sance reflète très certainement différentes énergies d'activation pour la diffusion, et
par conséquent différentes amplitudes d'interactions avec le substrat. Par ailleurs,
les topographies présentées dans la Fig. VIII, montrent une déposition de Fe-phen
relativement pure (sans impuretés). Une étude plus détaillée de la croissance des
molécules de Fe-phen suggère que les molécules composant la seconde monocouche
sont renversées par rapport aux molecules de la première monocouche, *i.e.* les groupes
phenanthrolines font faces à la surface. Nous avons également étudié la croissance de
molécules de Fe-phen sur une surface de Cu(111).

Après avoir étudié la croissance de la Fe-phen sur du Cu(100), nous nous sommes
intéressés à l'état de spin des molécules déposées sur la surface. Les topographies en
haute résolution montrent deux différentes conformations pour les molécules, se visu-
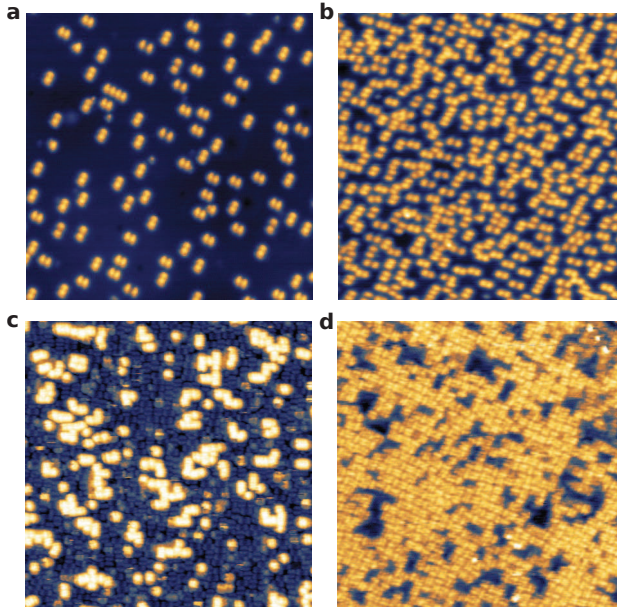
Figure VIII. – **Croissance couche par couche de molécules de Fe-phen sur une surface de Cu(100)**. Topographies obtenues pour des taux de recouvrement de **a** $0.1\,\mathrm{ML}$, **b** $0.4\,\mathrm{ML}$, **c** $1.4\,\mathrm{ML}$ and **d** $1.8\,\mathrm{ML}$. Les images ont une taille de $40\,\mathrm{nm} \times 40\,\mathrm{nm}$.

alisant au niveau de la distance entre les deux lobes d'une même molécule (voir Fig. IX). Pour obtenir davantage d'informations sur les deux différentes conformations nous avons effectué des mesures de spectroscopie tunnel (voir Fig. X). Les spectres de conductance sont relativement différents d'une conformation à l'autre. Les molécules dans la conformation avec la distance entre les lobes la plus grande montrent une résonance localisée au niveau de Fermi tandis que les molécules dans l'autre conformation ne montrent aucune caractéristique spectroscopique dans l'intervalle d'énergie considéré. Par ailleurs, la résonance au niveau de Fermi est spatialement localisée au niveau de l'ion de Fe (voir Fig. Xc). Nous avons attribué cette résonance à une résonance Kondo, qui ne peut se manifester que pour des ions avec des spins non appariés, *i.e.* que pour l'état haut spin.

Pour confirmer ces propos, nous avons réalisé des mesures d'adsorption des rayons X sur le seuil du fer. Le spectre d'absorption X dépend grandement de l'état de spin des molécules (voir Fig. XI). Pour un échantillon de $2\,\mathrm{ML}$ de Fe-phen sur un substrat de Cu(100), le spectre d'absorption peut être reproduit par une combinaison linéaire des spectres de référence pour les états haut et bas spin. Ceci implique une coexistence des états de spin pour l'échantillon de $2\,\mathrm{ML}$ de Fe-phen, en total accord avec les données STM.

Puisque nous avons observé les deux états de spin de la Fe-phen sur Cu(100), nous
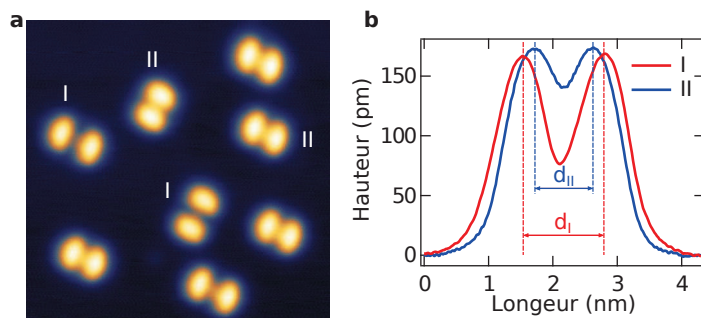
Figure IX. – **Les deux différentes conformations observées pour les molécules de Fe-phen sur une surface de Cu(100)**. **a**, Topographie de molécules de Fe-phen montrant deux différentes conformations notées I et II. L'image a une taille de $13\,\mathrm{nm} \times 13\,\mathrm{nm}$. **b**, Profils de hauteur pour des molécules dans les conformations I et II suivant l'axe long des molécules.
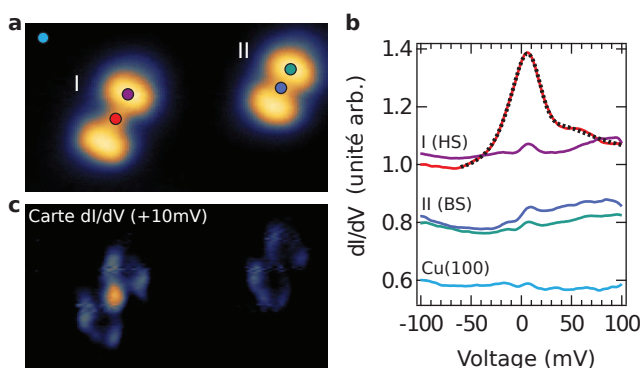
Figure X. – **Spectroscopie sur des molécules de Fe-phen**. **a**, Topographie montrant deux différentes conformations de Fe-phen sur Cu(100). **b**, Spectres dI/dV mesurés au centre et sur les lobes des molécules présentées en **a**. **c**, Carte dI/dV qui montre que la résonance est spatialement localisée au niveau de l'ion de fer de la molécules dans la conformation I. Les images ont une taille de $6.7\,\mathrm{nm} \times 2.7\,\mathrm{nm}$.

avons tenté de commuté une molécule donnée d'un état à l'autre. Malgré l'application de fortes tensions et de forts courants, nous n'avons pas eu d'évidence de commutation. Une des raisons pour cette absence de commutation peut être la trop forte interaction de la molécule avec le substrat de cuivre. Pour vérifier cette hypothèse, nous avons déposé une monocouche de nitrure de cuivre sur la surface de Cu(100) avant de déposer les molécules de Fe-phen. La monocouche de nitrure de cuivre a pour effet de partiellement passiver la surface et donc a priori de découpler les molécules de Fe-phen du substrat. Dans la Fig. XII, nous montrons une topographie de molécule de Fe-phen sur une surface de CuN/Cu(100). L'apparence des molécules est très différente de
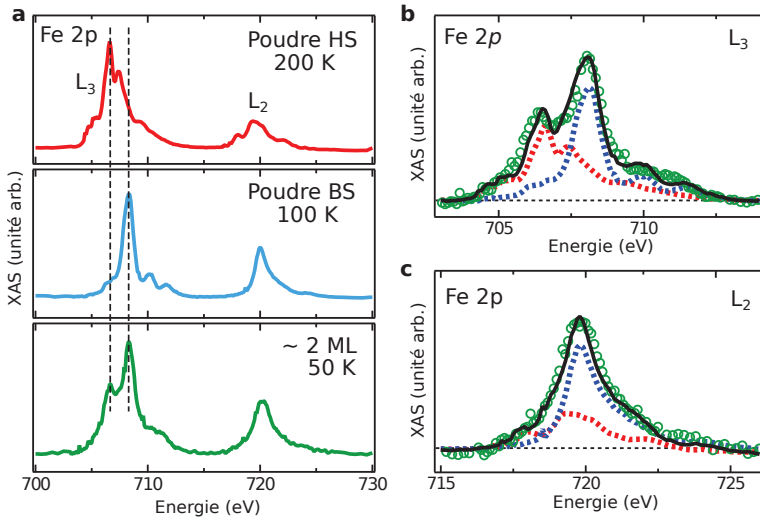
Figure XI. – **Coexistence des états haut et bas spin des molécules de Fe-phen révélée par des mesures d'absorption des rayons X sur le seuil du fer**. **a**, Spectres XAS mesurés sur de la Fe-phen massive dans l'état haut spin (panneau du haut), dans l'état bas spin (panneau du milieu) et sur un échantillon de 2 ML de Fe-phen déposées sur un substrat de Cu(100). Reproduction du seuil **b**, L_3 et **c**, L_2 du fer du spectre obtenu pour l'échantillon de 2 ML de Fe-phen à partir des spectres de référence obtenus sur la Fe-phen massive.

celles des molécules sur Cu(100), probablement dû au découplage de la molécule. En regardant de plus près la topographie (voir Fig. XIIa), nous pouvons constater que les deux molécules présentées diffèrent légèrement en leur centre. L'une des molécules a une hauteur apparente plus élevée en son centre. A nouveau, pour obtenir davantage d'informations sur les molécules, nous avons effectué des mesures de spectroscopie tunnel. L'une des deux molécules montre une résonance proche du niveau de Fermi tandis que la molécule dans l'autre conformation ne montre aucune caractéristique spectroscopique dans l'intervalle d'énergie sondé. Par analogie à l'étude de Fe-phen sur Cu(100), nous attribuons la molécule avec une résonance dans l'état haut spin, et la molécule sans caractéristique spectroscopique dans l'état bas spin. Par ailleurs, la résonance Kondo localisée proche du niveau de Fermi a une largeur plus faible que celle observée sur Fe-phen/Cu(100). Cette largeur est liée à la température de Kondo, qui est une grandeur caractérisant l'amplitude du couplage entre l'ion magnétique et les électrons de conduction du substrat. Comme attendu, les molécules de Fe-phen sont moins couplées avec le substrat de CuN/Cu(100) qu'avec le substrat de Cu(100), augmentant les chances d'observer une transition de spin.

L'étape logique suivant l'identification de l'état de spin des molécules est la tentative de commutation de ces dernières. Pour ce faire, nous avons placé la pointe STM
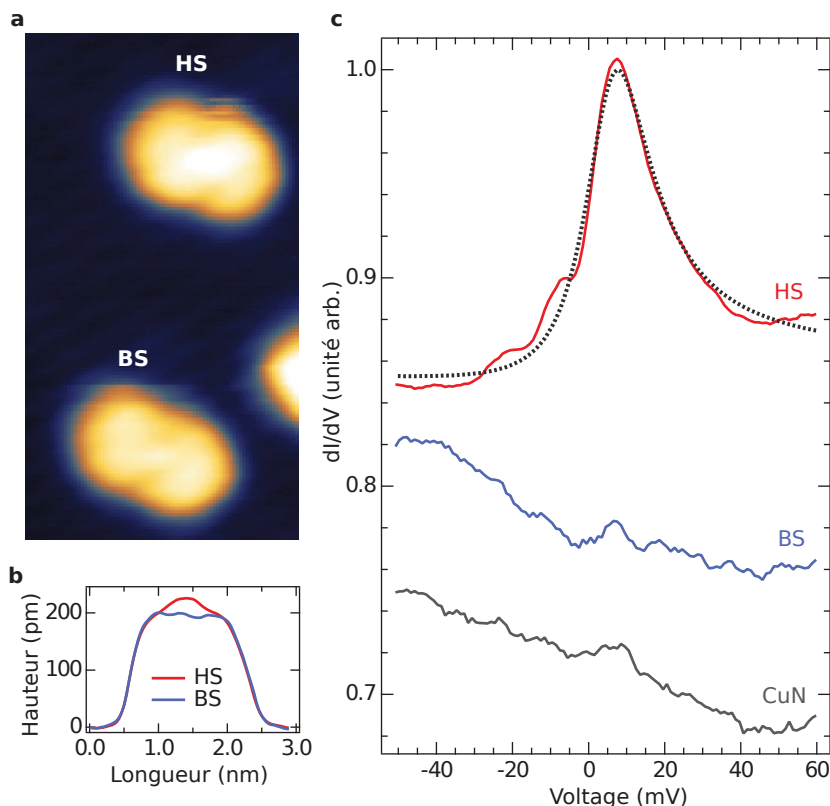
Figure XII. – **Identification des états de spin des molécules de Fe-phen sur une surface de CuN/Cu(100)**. **a**, Topographie montrant deux molécules de Fe-phen dans des conformations différentes. **b**, Profils de hauteur permettant de mieux visualiser les deux différentes conformations. **c**, Spectres dI/dV mesurés sur les deux molécules présentées en **a** et sur le substrat de CuN/Cu(100). L'image a une taille de $3.0\,\mathrm{nm} \times 5.5\,\mathrm{nm}$.

au dessus du centre d'une molécule de Fe-phen, et avons mesuré le courant tunnel en fonction de la tension appliquée sur le substrat (voir Fig. XIIIa). Une telle mesure montre clairement deux états de conductance de la molécule de Fe-phen sondée et les commutations entre les deux états de conductance sont totalement réversibles. Nous avons ensuite identifié les états de haute et basse conductance (voir Fig. XIIIb-e). L'état de haute conductance montre une petite protrusion en son centre (Fig. XIIIb,d) ainsi qu'une résonance dans la courbe dI/dV localisée proche du niveau de Fermi (Fig. XIIIe), tandis que l'état de faible conductance, la molécule ne montre pas de protrusion en son centre (voir Fig. XIIIc,d) et aucune caractéristique spectroscopique dans l'intervalle d'énergie sondé (Fig. XIIIe). Par conséquent, les données de la Fig. XIII montrent qu'une molécule de Fe-phen sur une surface de CuN/Cu(100)
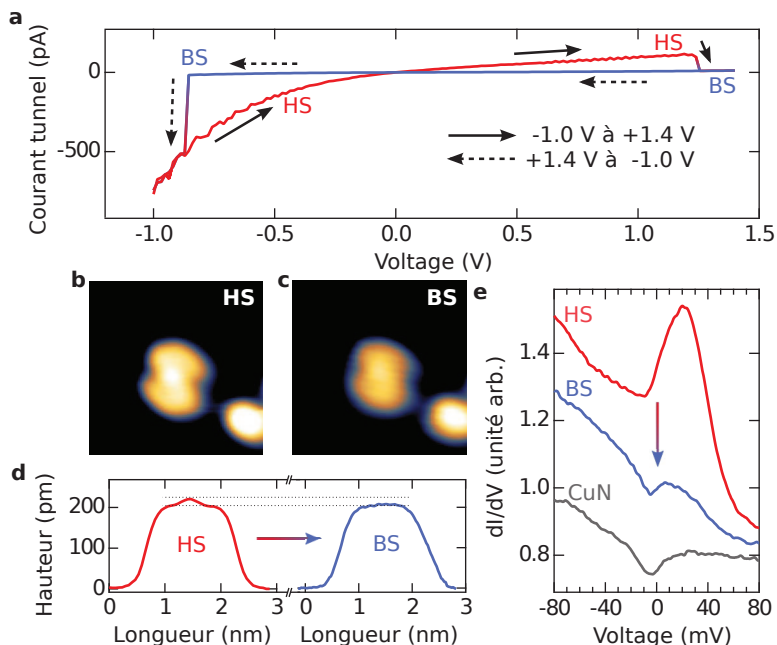
Figure XIII. – **Commutation de l'état de spin et l'état de conductance d'un molécule de Fe-phen sur une surface de CuN/Cu(100)**. **a**, Courbe $I(V)$ mesurée sur une molécule unique. La courbe montre deux états de conductance avec une hystérèse. Topography de la molécule sondée lorsqu'elle est dans l'état de **b**, haute conductance et **c**, basse conductance. Les topographies suggèrent que la molécule est dans **b**, l'état haut spin et **c**, l'état bas spin, respectivement. **d**, Profils de hauteur de la molécule représentée dans les topographies **b** et **c**. **e**, Spectres dI/dV de la molécule lorsqu'elle est dans l'état de haute et basse conductance. Toutes ces données permettent d'attribuer l'état de haute conductance (basse conductance) à l'état haut spin (bas spin). Les images ont une taille de $3.7\,\mathrm{nm} \times 3.7\,\mathrm{nm}$.

peut être commutée d'un état haut spin caractérisé par une haute conductance à un état bas spin de plus faible conductance. Nous avons ainsi montré que l'état de spin d'une molécule de Fe-phen peut être commuté et il est possible de lire l'état de spin en mesurant la conductance de la molécule.

Dans le but d'obtenir davantage de renseignements relatifs aux mécanismes de la commutation et dans le but de rendre le système plus attractif à des fins applicatives, nous avons tenté de commuter des molécules de Fe-phen à l'aide d'impulsions de tension. Dans la Fig. XIV, nous présentons les mesures de courant tunnel obtenues suite à l'application d'une série d'impulsions de tension sur une molécule unique en fonction du temps. Nous pouvons observer que si la molécule de Fe-phen est préparée dans l'état haut spin, une impulsion positive permet de commuter la molécule
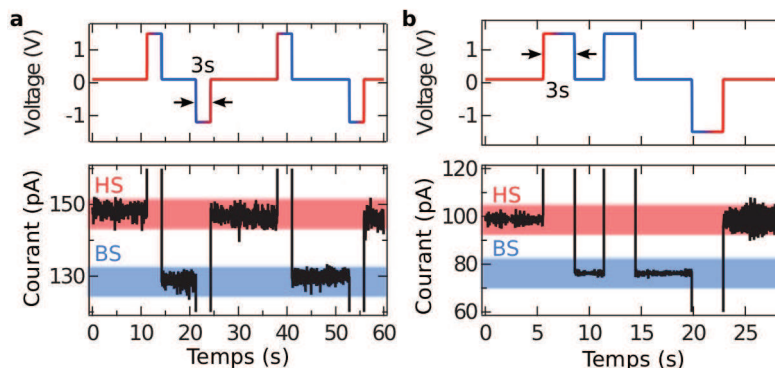
Figure XIV. – **Commutation de l'état de spin d'une molécule de Fe-phen induite par une impulsion de tension**. **a**, Série d'impulsion de tension appliquée sur la molécule en fonction de temps et le courant tunnel correspondant. L'état de spin de la molécule peut être commuté par l'application d'une impulsion de tension et la conductande de la jonction permet de lire l'état de spin. **b**, Experience similaire à celle présentée en **a** qui montre l'importance de la polarité du pulse.

dans l'état bas spin. La commutation inverse est également possible via l'application d'une impulsion de tension de polarité négative. La polarité de l'impulsion joue un rôle primordial puisqu'elle détermine la direction de la commutation. En effet, si la molécule est initialement préparée dans l'état haut spin et commuté dans l'état bas spin via une impulsion de polarité positive, une deuxième impulsion de polarité positive ne permet pas de changer l'état de la molécule de Fe-phen (voir Fig. XIVb). Les commutations ont pu être répétées un très grand nombre de fois sur un certain nombre de molécules, ce qui permet de conclure que les commutations présentées sont reproductibles, robustes et déterministes.

Par ailleurs, en regardant de plus près le courant tunnel pendant l'application d'une impulsion de tension, nous avons pu extraire des taux de transition en fonction du courant tunnel (voir Fig. XVa). La relation liant le taux de transition au courant tunnel dépend de la direction de commutation et suggère des mécanismes physiques différents. A partir de ces relations et des données spectroscopiques, nous avons pu construire un modèle impliquant un état excité de la molécule (voir Fig. XVb) et reproduisant les résultats observés.[18]

Les résultats précédants ont montré qu'il est possible de commuter l'état de spin de la molécule de Fe-phen lorsque cette dernière est suffisamment découplée du substrat à l'aide d'une couche de nitrure de cuivre. De manière alternative, les molécules de Fe-phen composant la deuxième monocouche de molécules sont naturellement découplées du substrat de Cu(100) par la première monocouche de molécules. Par conséquent, nous pouvons a priori supposer que les molécules composant la seconde monocouche peuvent commuter, et nous avons expérimentalement vérifié ce point.
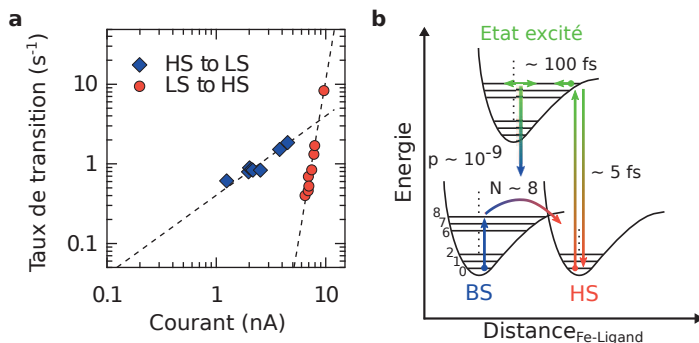
Figure XV. – **Taux de transition en fonction du courant et mécanisme proposé pour la transition de spin d'une molécule de Fe-phen sur un substrat de CuN/Cu(100)**. **a**, Taux de transition mesuré en fonction du courant tunnel pendant l'impulsion de tension. La relation liant les deux quantités dépend de la direction de la commutation suggérant différents mécanismes physiques. **b**, Schéma du mécanisme proposé pour la transition de spin impliquant un état excité.

Une combinaison de données topographiques et spectroscopiques ont permis de déterminer que la seconde monocouche de molécule est principalement dans l'état haut spin. Lorsqu'une topographie de la même région est prise avec une tension plus élevée, les lobes appartenant à une même molécule se rapprochent (voir Fig. XVI). Le rapprochement des lobes en augmentant la tension appliquée sur les molécules peut traduire soit la transition de spin attendue pour ces molécules ou la visualisation d'une orbitale différente.

Pour pouvoir trancher entre les deux scénarios possibles, nous avons effectué toute une série de mesures complémentaires. En premier lieu, pour mieux déterminer la tension à laquelle les changements topographiques se produisent, nous avons configuré le programme d'acquisition de la façon suivante : le programme a continuellement balayé la même ligne orientée suivant l'axe long d'une molécule sélectionnée. Pour chaque nouvelle ligne imagée, la tension a été augmentée d'un incrément. L'image obtenue permet de visualiser les variations topographiques de la molécule en fonction de la tension appliquée (voir Fig. XVIIa). A partir d'une telle image, chaque ligne est extraite et est ajustée avec une double gaussienne pour précisément localiser la position des lobes (Fig. XVIIb). La distance entre les deux lobes est ensuite représentée en fonction de la tension appliquée (Fig. XVIIc) et ajustée avec une fonction sigmoïde, qui permet de déterminer la tension à laquelle la moitié de la transition à lieu, nommée seuil de tension. Toute cette procédure est répétée pour un très grand nombre de courants tunnel et la Fig. XVIId montre la dépendance du seuil de tension avec le courant tunnel. Cette dépendance nous permet d'exclure un possible changement d'orbital sondée puisque l'on ne s'attendrait pas à une variation du seuil de tension avec le courant tunnel. Par ailleurs, nous avons proposé un mécanisme de transition prenant un compte un état excité et une barrière énergétique séparant les états haut
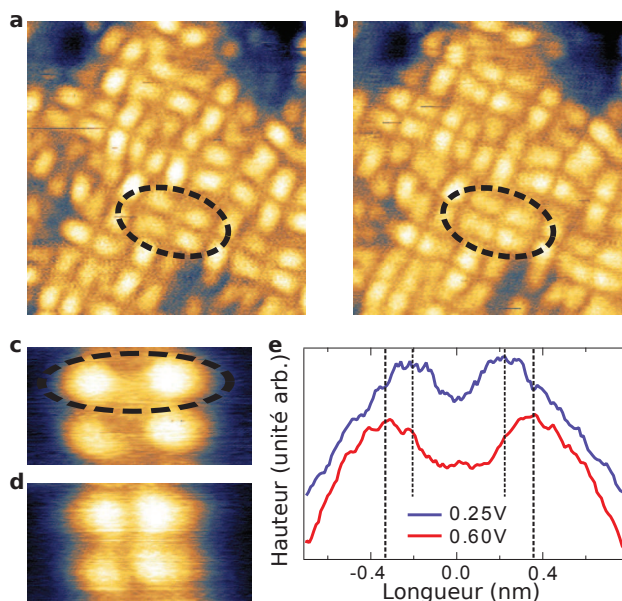
Figure XVI. – **Changements topographiques de la seconde monocouche de molécules de Fe-phen sur un substrat de Cu(100)**. Topographies de molécules de Fe-phen composant la second monocouche obtenus pour une tension de **a**, 0.4 V et **b**, 0.7 V. Topographies faisant un agrandissement sur deux molécules de Fe-phen de la seconde monocouche obtenus pour une tension de **a**, 0.25 V et **b**, 0.60 V. **e**, Profils de hauteurs le long de l'axe long de la molécule du haut représentés dans les topographies **c** et **d**. Les images ont une taille de **a**, **b** 5.50 nm × 5.80 nm et **c**, **d** 2.40 nm × 1.25 nm.

et bas spin. Le modèle proposé est en parfait accord avec les données expérimentales (voir ajustement Fig. XVIId). Nous avons observé des résultats similaires lorsque les molécules de Fe-phen sont déposées sur une surface de Cu(111).

A basse température, les molécules de Fe-phen dans leur forme cristalline sont dans l'état bas spin. Cependent, les résultats suggèrent que les molécules de Fe-phen composant la deuxième monocouche ont un état de base haut spin à basse température (4 K). Par ailleurs, les molécules de la première monocouche sont présentes dans les deux états de spin à basse température. Cette coexistence de l'état de spin est assez surprenante, et nous l'avons davantage étudié. En analysant l'ensemble des données sur des systèmes similaires dans la littérature, il apparaît que la coexistence dépend de la paire molécule/substrat.[19] C'est pourquoi, nous avons étudié la dépendance de la coexistence de l'état de spin en fonction du substrat. Dans la Fig. XVIII, nous pouvons observer des topographies haute résolution de molécules de Fe-phen sur différents substrats : Cu(100), Cu(111) et Au(111). Sur les topographies obtenues sur les trois substrats nous pouvons identifier des molécules dans les états haut spin et
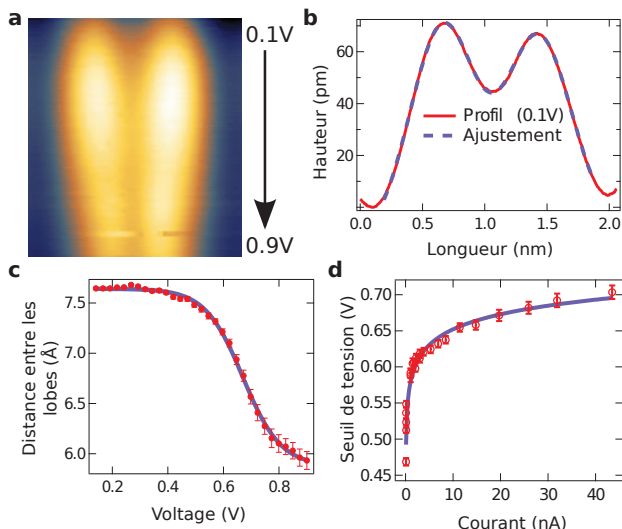
Figure XVII. – **Dépendance en tension et en courant des changements topographiques**. **a**, Evolution du profil de hauteur d'une molecule de Fe-phen de la deuxième monocouche sur un substrat de Cu(100) pour des tension appliquées croissantes. **b**, Profil de hauteur extrait de **a** pour une valeur particulière de tension. **c**, Distance entre les lobes en fonction de la tension appliquée permettant d'extraire le seuil de tension, *i.e.* la tension à laquelle la moitié de la transition a lieu. **d**, Seuil de tension en fonction du courant tunnel. L'image a une largeur de 2.06 nm.

bas spin. Par conséquent, la coexistence de l'état de spin est observable sur les trois substrats. A noter que la coexistence semble disparaître pour la seconde monocouche de molécules et est "contrôlable" pour les molécules déposées sur du CuN/Cu(100). Ceci suggère que la coexistence de l'état de spin provient de l'interaction avec le substrat et/ou d'interactions intermoléculaires.

Les molécules à transition de spin sont sensibles à la pression et notamment à la "pression" élastique venant de leurs plus proches voisins. C'est pourquoi nous avons également étudié la dépendance de la coexistence de l'état de spin en fonction du taux de couverture de la première monocouche de Fe-phen sur Cu(100). Cependant, nous n'avons observé aucune corrélation évidente entre la proportion de molécules dans l'état haut spin et le taux de couverture de Fe-phen. Les interactions intermoléculaires ne sont donc pas responsables de la coexistence de l'état de spin.

Par élimination, la coexistence devrait provenir de l'interaction des molécules avec le substrat. Dans la Fig. XIX, nous montrons des topographies de molécules de Fe-phen dans l'état haut spin et bas spin sur un substrat de Cu(100) que l'on peut observer avec une résolution atomique. Le site d'adsorption du soufre appartenant à la Fe-phen ne peut pas être expérimentalement déterminé, mais nous pouvons voir que l'ion de fer a un site d'adsorption dépendent de l'état de spin de la molécule.
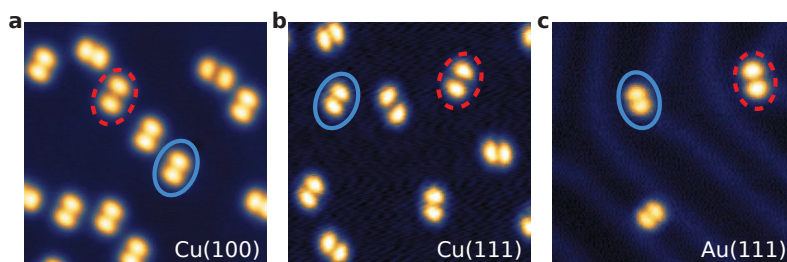
Figure XVIII. – **Coexistence de l'état de spin de la Fe-phen sur trois différents substrats**. Topographies en haute résolution de Fe-phen sur des substrats de **a**, Cu(100) **b**, Cu(111) et **c**, Au(111). Les images ont une taille de 14.1 nm × 14.1 nm.
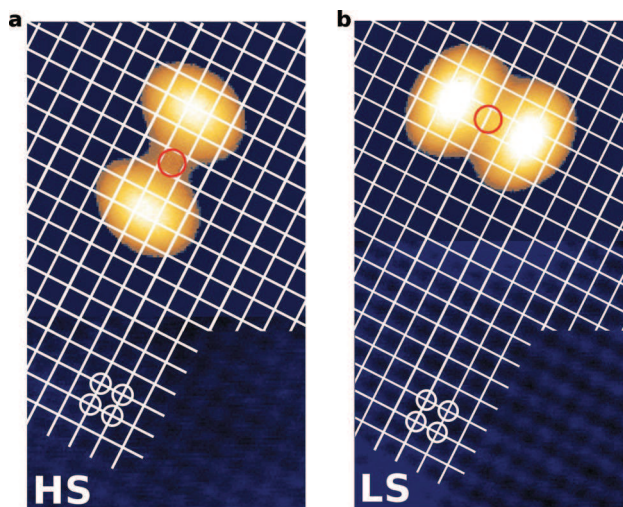
Figure XIX. – **Sites d'adsorption de la Fe-phen sur une surface de Cu(100)**. Topographies de molécules de Fe-phen dans l'état **a** haut spin et **b**, bas spin sur une surface de Cu(100). Le site d'adsorption de l'ion de fer dépend de l'état de spin de la molécule. Les images ont une taille de 2.8 nm × 5.0 nm.

Nous extrapolons que les sites d'adsorption du soufre sont différents. De plus la distance entre les deux soufres d'une molécule de Fe-phen détermine l'état de spin de la molécule. Par conséquent, nous pensons que l'état de spin de la molécule est fixé par le site d'adsorption. Il en suit que, suivant l'importance des interactions avec le substrat, il est plus ou moins facile de changer le site d'absorption de la molécule et ainsi changer son état de spin.

Au travers des résultats présentés, nous montrons l'utilité de combiner des mesures

XAS et STM pour étudier les propriétés électroniques et magnétiques de molécules sur des surfaces métalliques.

Références

[1] V. Alek Dediu, Luis E. Hueso, Ilaria Bergenti, and Carlo Taliani. Spin routes in organic semiconductors. *Nature Materials*, 8(9):707–716, 2009.

[2] Marc Warner, Salahud Din, Igor S. Tupitsyn, Gavin W. Morley, A. Marshall Stoneham, Jules A. Gardener, Zhenlin Wu, Andrew J. Fisher, Sandrine Heutz, Christopher W. M. Kay, and Gabriel Aeppli. Potential for spin-based information processing in a thin-film molecular semiconductor. *Nature*, 503(7477):504–508, 2013.

[3] S. Sanvito. Molecular spintronics. *Chemical Society Reviews*, 40(6):3336–3355, 2011.

[4] Clément Barraud, Pierre Seneor, Richard Mattana, Stéphane Fusil, Karim Bouzehouane, Cyrile Deranlot, Patrizio Graziosi, Luis Hueso, Ilaria Bergenti, Valentin Dediu, Frédéric Petroff, and Albert Fert. Unravelling the role of the interface for spin injection into organic semiconductors. *Nature Physics*, 6(8):615–620, 2010.

[5] Marta Galbiati, Sergio Tatay, Clément Barraud, Alek V. Dediu, Frédéric Petroff, Richard Mattana, and Pierre Seneor. Spinterface: Crafting spintronics at the molecular scale. *MRS Bulletin*, 39(07):602–607, 2014.

[6] S. Javaid, M. Bowen, S. Boukari, L. Joly, J.-B. Beaufrand, Xi Chen, Y. J. Dappe, F. Scheurer, J.-P. Kappler, J. Arabski, W. Wulfhekel, M. Alouani, and E. Beaurepaire. Impact on Interface Spin Polarization of Molecular Bonding to Metallic Surfaces. *Physical Review Letters*, 105(7):077201, 2010.

[7] F. Djeghloul, F. Ibrahim, M. Cantoni, M. Bowen, L. Joly, S. Boukari, P. Ohresser, F. Bertran, P. Le Fèvre, P. Thakur, F. Scheurer, T. Miyamachi, R. Mattana, P. Seneor, A. Jaafar, C. Rinaldi, S. Javaid, J. Arabski, J.-P. Kappler, W. Wulfhekel, N. B. Brookes, R. Bertacco, A. Taleb-Ibrahimi, M. Alouani, E. Beaurepaire, and W. Weber. Direct observation of a highly spin-polarized organic spinterface at room temperature. *Scientific Reports*, 3, 2013.

[8] S. Javaid, S. Lebègue, B. Detlefs, F. Ibrahim, F. Djeghloul, M. Bowen, S. Boukari, T. Miyamachi, J. Arabski, D. Spor, J. Zegenhagen, W. Wulfhekel, W. Weber, E. Beaurepaire, and M. Alouani. Chemisorption of manganese phthalocyanine on Cu(001) surface promoted by van der Waals interactions. *Physical Review B*, 87(15):155418, 2013.

[9] P. Gütlich, Y. Garcia, and H. A. Goodwin. Spin crossover phenomena in Fe (II) complexes. *Chem. Soc. Rev.*, 29(6):419–427, 2000.

[10] S. Heutz, C. Mitra, W. Wu, A. J. Fisher, A. Kerridge, M. Stoneham, A. H. Harker, J. Gardener, H.-H. Tseng, T. S. Jones, C. Renner, and G. Aeppli. Molecular Thin Films: A New Type of Magnetic Switch. *Advanced Materials*, 19(21):3618–3622, 2007.

[11] Xi Chen, Ying-Shuang Fu, Shuai-Hua Ji, Tong Zhang, Peng Cheng, Xu-Cun Ma, Xiao-Long Zou, Wen-Hui Duan, Jin-Feng Jia, and Qi-Kun Xue. Probing Superexchange Interaction in Molecular Magnets by Spin-Flip Spectroscopy and Microscopy. *Physical Review Letters*, 101(19):197208, 2008.

[12] Michele Serri, Wei Wu, Luke R. Fleet, Nicholas M. Harrison, Cyrus F. Hirjibehedin, Christopher W. M. Kay, Andrew J. Fisher, Gabriel Aeppli, and Sandrine Heutz. High-temperature antiferromagnetism in molecular semiconductor thin films and nanostructures. *Nature Communications*, 5, 2014.

[13] Karthik V. Raman, Alexander M. Kamerbeek, Arup Mukherjee, Nicolae Atodiresei, Tamal K. Sen, Predrag Lazić, Vasile Caciuc, Reent Michel, Dietmar Stalke, Swadhin K. Mandal, Stefan Blügel, Markus Münzenberg, and Jagadeesh S. Moodera. Interface-engineered templates for molecular spin memory devices. *Nature*, 493(7433):509–513, 2013.

[14] J Nogués and Ivan K Schuller. Exchange bias. *Journal of Magnetism and Magnetic Materials*, 192(2):203–232, 1999.

[15] Z. Q. Qiu and N. V. Smith. Quantum well states and oscillatory magnetic interlayer coupling. *Journal of Physics: Condensed Matter*, 14(8):R169, 2002.

[16] P. Bruno. Theory of interlayer magnetic coupling. *Physical Review B*, 52(1):411–439, 1995.

[17] S. Shi, G. Schmerber, J. Arabski, J.-B. Beaufrand, D. J. Kim, S. Boukari, M. Bowen, N. T. Kemp, N. Viart, G. Rogez, E. Beaurepaire, H. Aubriet, J. Petersen, C. Becker, and D. Ruch. Study of molecular spin-crossover complex $Fe(phen)_2(NCS)_2$ thin films. *Applied Physics Letters*, 95(4):043303, 2009.

[18] Toshio Miyamachi, Manuel Gruber, Vincent Davesne, Martin Bowen, Samy Boukari, Loïc Joly, Fabrice Scheurer, Guillaume Rogez, Toyo Kazu Yamada, Philippe Ohresser, Eric Beaurepaire, and Wulf Wulfhekel. Robust spin crossover and memristance across a single molecule. *Nature Communications*, 3:938, 2012.

[19] Manuel Gruber, Vincent Davesne, Martin Bowen, Samy Boukari, Eric Beaurepaire, Wulf Wulfhekel, and Toshio Miyamachi. Spin state of spin-crossover complexes: From single molecules to ultrathin films. *Physical Review B*, 89(19):195415, 2014.

1

Introduction

Over the history of computing hardware, the number of transistors in an integrated circuit approximately doubles every two years. Since this "trend" was already predicted in 1965 and then revised in 1975 by Gordon E. Moore, it is usually referred to as Moore's law. Over the time, Moore's law turned from an observation or prediction into a target for the entire industry. Moore's law conjointly stimulated the capabilities of many digital electronic devices such as the memory capacity, the size of the sensors and even the pixel density in the cameras.

Since 2012, we can find commercially available chips fabricated using the 22 nm process. In these chips, half of the distance between identical features is about 22 nm. In the beginning of 2015, chips manufactured using the 14 nm process should be commercialized and the semiconductor companies plan to go down to 5 nm in the horizon 2020. Downsizing the electronic components to these scales not only represents a technological challenge for the large scale production but also approaches the physical limits of semiconductors technology. Indeed, for feature size about 5 nm, the traditional complementary metal-oxide-semiconductor (CMOS) technology will face problems of the quantum word such as tunneling leading to impracticable devices.

In order to go beyond these limitations, we need to use different materials or even different concepts. One of the emerging and active field towards this direction is molecular electronics where the electronic components could be ultimately fabricated out of a single molecule. In addition, (organic) molecules seem to be ideal candidates in novel concepts such as spintronics[1] and quantum computing.[2]

Building spintronic devices using organic molecules present a certain number of advantages, such as their potential low cost and the expected long spin lifetime in organic materials. In the last decade, the organic spintronic community put considerable efforts in order to fabricate efficient and robust organic-spintronic devices working at room temperature.[1,3] While pursuing this objective, the community realized that the adsorption of organic molecules on metallic surfaces can considerably change their

properties, and the transport properties of the device may be completely driven by the physics occurring at the interfaces.[3,4] One therefore needs a better understanding of the physics that takes place at molecule-metal interfaces and particularly concerning the magnetic properties.

The first part of this thesis is devoted to the study of the electronic and magnetic properties of the molecule-metal interfaces. We used manganese phthalocyanine molecules deposited on a ferromagnetic Co substrate. From previous studies, we know that the magnetic moment of the manganese ion within first-monolayer (ML) phthalocyanine is strongly ferromagnetically coupled to the substrate even at room temperature.[5] Furthermore, the hybridization of the first-ML molecules on the ferromagnetic substrate leads to the creation of a strongly spin-polarized spinterface close to the Fermi energy and observed at room temperature.[6] Additionally, the theoretical framework used by our collaborators seems to have reached a certain maturity, notably by the inclusion of the van-der-Waals forces.[7] In this thesis, we investigated the influence of the magnetic substrate on the subsequent phthalocyanine layers using X-ray absorption techniques. We surprisingly observed that the adsorption of molecules on the ferromagnet's surface can alter its magnetic properties. Alternatively, we studied the magnetic coupling of first-ML manganese phthalocyanine with the ferromagnetic substrate through a non-magnetic spacer.

The second part of this thesis is focused on functional molecules on metallic surfaces. As stated before, one can imagine electronic components built out of a single molecule that incorporate a given function. In turn, one can consider tuning the properties or functions of the molecules by adequate chemistry. However, for application perspectives, the functional molecules should be deposited on surfaces and their properties may be altered upon adsorption. In this thesis, we concentrate on a particular class of functional molecules: spin-crossover molecules. These molecules are molecular switches that can be switched between a low- and a high-spin state using various stimuli. The striking question to address was whether the spin-crossover property of the molecules survives upon adsorption on metallic surfaces. Using a combination of scanning tunneling microscopy (STM) at low temperature and X-ray absorption spectroscopy, we observed that both spin states of the molecule coexist on the different investigated substrates. We investigated the spin-state coexistence in more detail since it is unusual for these molecules at low temperatures. We finally show that we can selectively and deterministically switch the spin state of the spin-crossover molecules with the probe tip, provided that the molecules are sufficiently decoupled from the metallic substrate.

This thesis is organized in three parts. In a first part we give the experimental and theoretical background necessary for the understanding of the results. The second part is devoted to the investigation of the hybrid spinterface formed by the manganese phthalocyanine molecules on a Co substrate, while in the third part we focus on the investigation of organic functional molecules on surfaces.

The first part of the thesis starts with a brief overview of **ligand field theory**. The molecules used in this thesis contain a transition-metal ion surrounded by organic

ligands. We will see that the presence of the ligands lift the energy degeneracy of the d orbitals in a way that depends on the symmetry of the ligand arrangement and on the ligand-field strength. This chapter is particularly useful to understand spin crossover. It is followed by chapter 3 **fundamentals of magnetism** focused on three effects experimentally observed in this thesis: exchange bias, interlayer exchange coupling and Kondo physics. In the chapter 4 **X-ray absorption spectroscopy**, we describe the principle of the technique and fundamentals of light-matter interaction. We will then see that from photon-polarization-dependent absorption measurements it is possible to retrieve element-specific magnetic information. Chapter 5 is devoted to the underlying principles of **Scanning tunneling microscopy and spectroscopy**. We will briefly introduce the history and the concept of this high-precision technique, followed by tunneling models that helps to interpret data acquired with a scanning tunneling microscope. Finally we give a short overview of scanning tunneling spectroscopy and inelastic electron tunneling spectroscopy. The last chapter of this part gives details and characteristics of the **methods and experimental setups** used for this work.

The second part of the thesis focused on the investigation of the hybrid spin-terface formed by manganese phthalocyanine molecules and the Co substrate begins with an **introduction to spintronics** that describes the motivations specific to this part. Chapter 8 aims at giving the state-of-the-art information about **phthalo-cyanine molecules and phthalocyanine-based spinterfaces** important for the understanding of the results. The next chapter reports on the observation of **room temperature magnetic order in molecular layers** that even leads to exchange bias at lower temperatures. The final chapter of this part presents a **metal-molecule spinterface stabilized by interlayer exchange coupling** where the molecule is magnetically coupled to the ferromagnetic substrate through a non-magnetic spacer.

The third and last part is devoted to the investigation of organic functional molecules on surfaces and more particularly to spin-crossover molecules. Chapter 11 is the first chapter of this part and is intended to give a brief **introduction to functional molecules**. It is followed by the chapter focused on **spin-crossover molecules** that describes the investigated molecule and gives a thermodynamical description of spin crossover, followed by the possible spin-transition triggers and applications. Chapter 13 presents the **growth of Fe(phen)$_2$(NCS)$_2$** on Cu(100) and Cu(111) substrates from single molecules up to 2 ML. In the next chapter, we show how we were able to identify the spin state of the Fe(phen)$_2$(NCS)$_2$ molecules on the surfaces, followed by the study of **spin-state switching with a STM tip**. Since the molecules were present in both spin states on the surface, we also investigated in more details the **spin-state coexistence** in chapter 15.

Finally, the last chapter of the thesis entitled **conclusions** summarizes the most striking results and present possible perspectives.

Part I.

Experimental and theoretical background

2

Ligand Field Theory

Coordination complexes are compounds composed of a metallic cation, known as electron pair acceptor, coordinated with electron pair donors, the ligands. The ligand field theory (LFT) can predict, to a certain extend, the modification of the electronic and magnetic properties of the metallic cation by the presence of the ligands. LFT combines the crystal field theory that takes into account the electrostatic interactions between the metal orbitals and the ligands, and the molecular orbital theory. In a first part, I will describe the basis of molecular orbitals theory while in a second part, I will discuss the results of the LFT for an octahedral coordination symmetry.

2.1. Molecular orbitals

The derivation of Schrödinger equation applied on a hydrogen atom leads to the atomic orbitals indexed by three quantum numbers: n the principal, l the angular and m_l the angular momentum vector component quantum numbers. Orbitals with angular quantum numbers $l = 0, 1, 2, 3$ are referred to as s, p, d and f, respectively. When we graphically represent an orbital, we usually specify the sign of the wave function solution of the Schrödinger equation. The five different d orbitals are represented in Fig. 2.1, and each of them exhibit an alternation of the sign of the wave function. Note that the d orbitals are represented in a Cartesian basis obtained by a linear combinations of the d orbitals in the m_l basis. For instance, the d_{xy} orbital is composed of four lobes, the wave function being positive for two of them and negative for the two others. While the density of probability of presence of an electron is the same in the four lobes, the wave function sign alternation will have consequence for inter-atomic bondings.

For molecules, the wave function, and thus the orbitals cannot be analytically derived from Schrödinger equation. However good approximate of these molecular
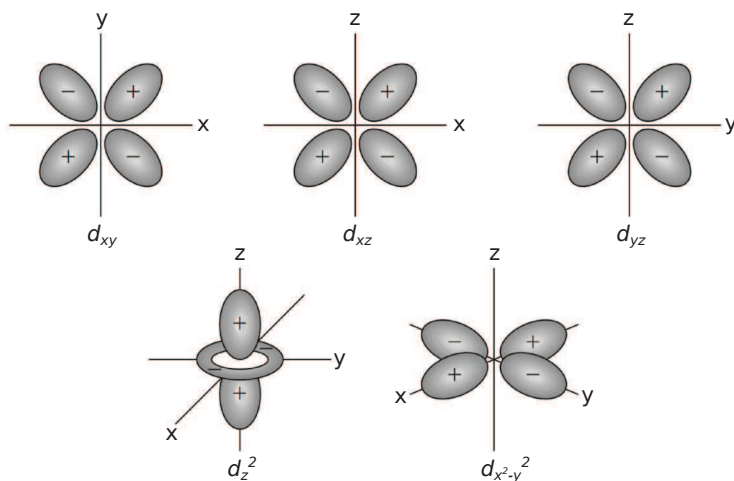
Figure 2.1. – **The five different d atomic orbitals**. The figure is adapted
from Ref. 8.

orbitals can be obtain by linear combinations of the atomic orbitals. For diatomic
molecules, the wave function has the following form[9]:

$$\Psi = c_a \Psi_a + c_b \Psi_b \tag{2.1}$$

where Ψ is the molecular wave function, Ψ_a and Ψ_b are atomic wave functions and
c_a and c_b are the linear-combination coefficients. The coefficients must be chosen
such that Ψ^2 integrated over the whole space is equal to unity (normalized wave
function).

The overlap of the atomic orbitals can lead to bonding, anti-bonding and non-
bonding orbitals. There are three important conditions to fulfill in order to have
bonding from the overlap of orbitals:

- the atomic wave functions must have the same sign in the overlap region

- the atomic orbitals must have similar energies

- the distance between the atoms must be short enough relative to the spacial
  extension of the orbitals.

The first point implies that atomic orbitals from the two atoms have compatible
symmetries. Furthermore, the gain in energy by the formation of the bond decreases
when the difference in energies of the initial atomic orbitals increases (second point).
Finally, a short distance between the atoms insure a good overlap of the atomic
orbitals (third point).

Bonding orbitals are usually denoted σ and π for symmetric (anti-symmetric)
orbitals to rotation about the connection line. Anti-bonding orbitals are referred to
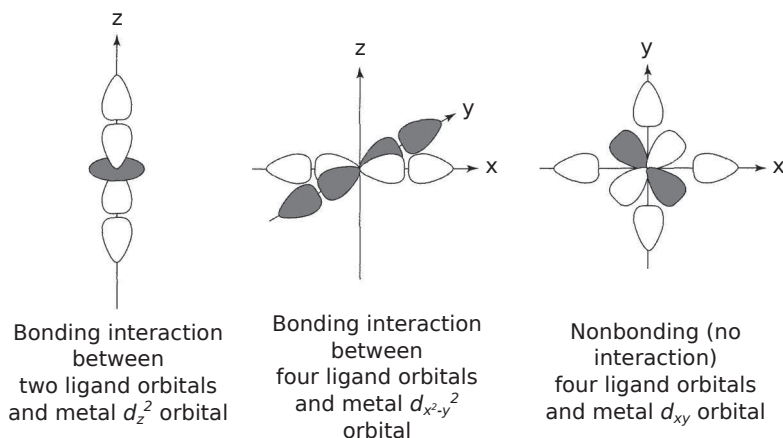
Figure 2.2. – **Orbital interactions in octahedral complexes**. The sign of the wave function is different for shaded and non-shaded areas. The figure is adapted from Ref. 9.

as σ^* and π^*. As a general rule, the number of molecular orbitals must equal the number of initial atomic orbitals.

2.2. Molecular orbitals for octahedral complexes

There is a large variety of coordination complexes and they are usually grouped by set of symmetries operations known as point group. The LFT will be introduced in the case of octahedral-symmetry compounds as it corresponds to the symmetry of most of the coordination compounds and most of the spin-crossover complexes.

For octahedral complexes, if the atomic orbitals are in the center of a Cartesian system of reference, the six ligands are positioned at each extremities of the x, y and z axes. From the d orbitals, only the $d_{x^2-y^2}$ and d_{z^2} orbitals can form bonding orbitals with the ligands while the d_{xy}, d_{xz} and d_{yz} form non-bonding orbitals. These results can be intuitively understood by observing the overlap of the atomic orbitals together with the sign of the wave functions in Fig. 2.2. For the $d_{x^2-y^2}$ and d_{z^2} orbitals, the overlap with ligand orbitals is performed with wave functions of same sign leading to molecular bonding orbitals. In the case of the d_{xy} orbitals (as well as for d_{xz} and d_{yz}, not shown), the overlap with ligand orbitals is alternatively with positive and negative sign of the metal wave function leading to a zero integral of the wave functions in the overlap region, and thus no interaction. The resulting molecular orbitals are non-bonding orbitals.

In order to form an octahedral complex, in addition to the $d_{x^2-y^2}$ and d_{z^2} orbitals, the metallic cation has to provide four other orbitals compatible with the symmetries of the ligand orbitals. The 6 orbitals from the ligands as well as the 6 orbitals from
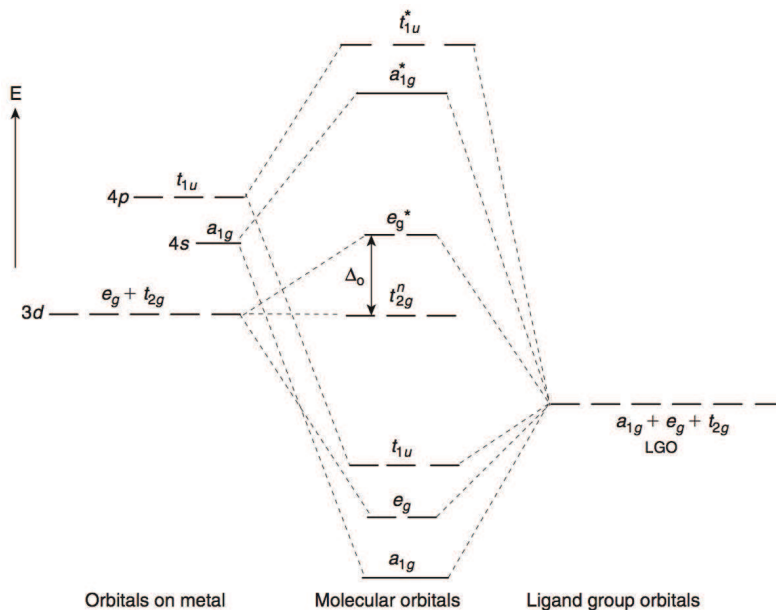
Figure 2.3. – **Molecular orbitals of an octahedral complex obtained by hybridization of metal and ligand orbitals**. The figure is taken from Ref. 8.

the cation hybridize into 6 bonding and 6 anti-bonding orbitals as represented in Fig. 2.3. The molecular orbitals are labeled according to their symmetry (irreducible representation). t_{2g} corresponds to the non-bonding d_{xy}, d_{xz} and d_{yz} orbitals, while e_g^* are the anti-bonding orbitals coming from the hybridization of the $d_{x^2-y^2}$ and d_{z^2} orbitals.

2.3. Energy splitting and spin

As described in the previous section, from the ligand field theory in an octahedral symmetry, we have t_{2g} and e_g^* sets of orbitals. The energy difference between these two sets of orbital is often referred to as $10Dq$ or Δ_o (o for octahedral). In turn, we will see that the electron filling of the t_{2g} and e_g^* orbitals depends on the energy splitting $10Dq$, and thus on the ligand-field strength. The ligand-field strength is directly linked to the interactions and overlap of the central-metal and ligand orbitals. The stronger the orbital interactions the larger the ligand-field strength. We usually distinguish between weak- and strong-field ligands depending on the energy difference $10Dq$ induced by the ligands.[9]

In an octahedral symmetry, for transition-metal ions that have between 4 to 7

electrons in the valence d orbitals, depending on the ligand-field strength induced by the ligands, there are two different possibilities to fill the t_{2g} and the e_g^* orbitals. To explain the two possible electronic configurations, we have to introduce the pairing energy Π, which corresponds to the energy cost for filling two electrons into the same orbital. This energy cost arises from the Coulomb repulsion between the two electrons and the exchange interactions.

Yet, we consider the two possible cases for d^4 through d^7 metal ions. (i) For Π lower than $10Dq$, the t_{2g} orbitals are totally filled (two electrons with opposite spin per orbital) before the filling of the e_g^* orbitals. (ii) For $10Dq$ lower than Π, the t_{2g} and then the e_g^* orbitals are partially filled with one electron before starting to pair electrons in the t_{2g} orbitals. The two different electronic configurations (case (i) and (ii)) lead to different spins and different molecular sizes. Indeed, the spin is smaller in the electronic configuration (i) as the electron pairing is favorable. Concerning the size of the complex, the population of the anti-bonding e_g^* orbitals, favored for configuration (ii) leads to an increased distance between the metal ion and the ligands.

To summarize, transition metal ions in an octahedral symmetry with 4 to 7 electrons in the valence d orbitals can have two different electronic configurations depending on the ligands. When the ligands induce a weak (strong) field on the metal ion, the latter is in its high-spin (low-spin) state. In turn, the high-spin state is characterized by a larger size of metal complex than the low-spin state.

2.4. Influence of the metal-ligand distance

The splitting between the t_{2g} and the e_g^* sets of orbitals, referred to as $10Dq$, strongly depends on the distance between the central metal ion and the ligands. We have seen in the previous section that, depending on the strength of the ligand field, the metallic ion has two possible ground-state electronic configurations: high-spin ($^5T_2$) and low-spin ($^1A_1$) configurations. Other electronic configurations are also possible but are energetically less favorable (see Fig. 2.4).

In Fig. 2.4, we show the calculated energy diagram of different ligand-field states as a function of the energy splitting $10Dq$, for a metal ion with six d valence electrons.[10] The ground state is the HS state ($^5T_2$) for low $10Dq$ and switches to the LS state ($^1A_1$) for larger $10Dq$. The change of the ground state occurs when $10Dq$ equals the pairing energy Π.

For some complexes, $10Dq$ may be close to the pairing energy, such that external stimuli can trigger a ligand-state switch (see Chap. 12). For a given $10Dq$, the Tanabe-Sugano diagram represented in Fig. 2.4 informs us also about the required energy to excite the metal ion from the ground state ($^5T_2$ or $^1A_1$) to an excited state (*e.g.* ^5E), which plays an important role for spin-crossover complexes (see Chap. 12).
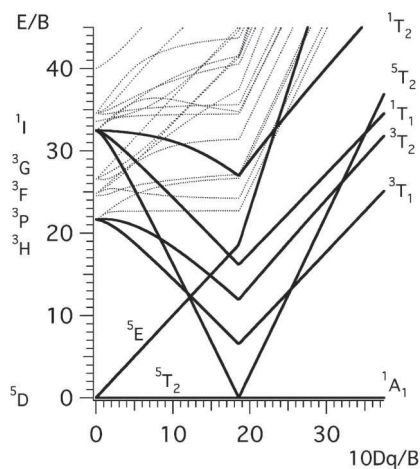
Figure 2.4. – **Tanabe-Sugano diagram for a transition metal ion in an octahedral symmetry**. The diagram shows energy (in units of the Racah parameter B) of the excited ligand-field states as a function of the ligand-field strength $10Dq$ (also in units of the Racah parameter B) for a metal ion with six d valence electrons. The figure is taken from Ref. 10.

3

Fundamentals of magnetism

In this chapter we shortly review the fundamentals of different phenomena that we had to take into account considering molecular layers in interaction with a ferromagnetic substrate. We will start by a description of exchange bias followed by a discussion of interlayer exchange coupling. Finally, we will give insights of the Kondo physics.

3.1. Exchange bias

Exchange bias, also referred to as unidirectional anisotropy, occurs in systems where an antiferromagnetic (AF) material is in contact and interacting with a ferromagnetic (FM) material. The exchange bias effect causes a shift of the hysteresis loop of the system along the magnetic field axis. The phenomenon was discovered by Meiklejohn and Bean in 1956 when studying Co particles surrounded by a CoO shell.[11,12] Since then, exchange bias was observed in many different systems and already found many applications such as magnetic recording media, magnetic sensors, magnetoresistive memories and magnetic read heads (see Refs. 13–15 and references therein). In this section, we will start with a phenomenological intuitive picture of exchange bias. In a second part we consider a simple model of exchange bias that give some insights about the origin of exchange bias.

3.1.1. Phenomenological intuitive picture

The FM (AF) layer has a characteristic Curie (Néel) temperature T_C (T_N) and for temperatures below T_C (T_N) the FM (AF) layer is magnetically ordered. In Fig. 3.1, we illustrate an exchange bias system where the system satisfies the condition $T_C > T_N$. For temperatures ranging from the Néel temperature to the Curie temperature ($T_N < T < T_C$), the FM layer is magnetically ordered while the AF layer remains
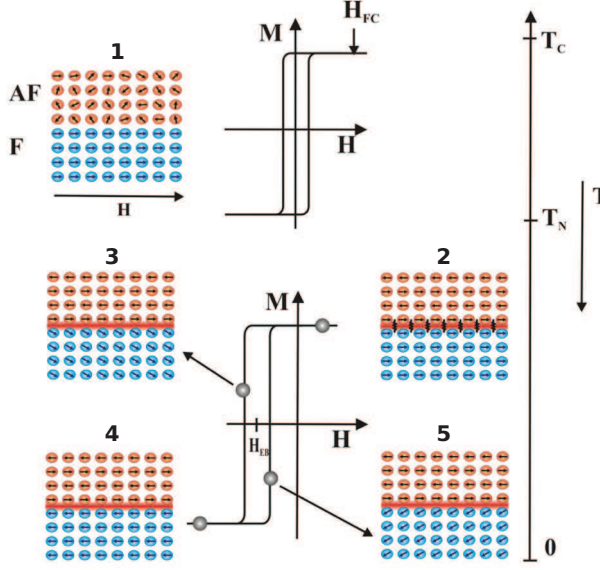
Figure 3.1. – **Phenomenological picture of exchange bias for an AF-FM bilayer**. Step **1** for $T_N < T < T_C$, the FM layer is magnetically ordered while the AF layer is disordered. The corresponding hysteresis loop resembles that of a normal FM layer with the magnetic field H aligned along the easy axis of the FM layer. Step **2** shows the magnetic state of the bilayer after cooling below T_N in a positive external magnetic field. Both AF and FM layers are magnetically ordered and both layers are magnetically coupled between them. The negative magnetic field to apply for rotating the magnetic moments of the FM layer is relatively large due to the interactions with the AF layer, as represented in step **3**. Step **4**, the magnetic moments of the FM layer can be fully reversed while the magnetic moments of the AF layer stay similar to that of step **2** and **3**. In step **5**, the magnetization reversal of the FM layer can occur for a negative external field as the AF-FM interactions favor the magnetic configuration of step **2**. The resulting hysteresis curve for $T < T_N$ is shifted by H_{EB} due to exchange bias. The figure is taken from Ref. 16.

disordered. When the external magnetic field is applied along the easy axis of the FM layer, the magnetic-field dependence of the FM-layer magnetization presents an hysteresis loop typical for FM materials (see Fig. 3.1 step 1). Moreover, the amplitude of the magnetic field required to reverse the FM-layer magnetization, *i.e.* the coercivity, does not depend on the magnetization-reversal direction ($|H_c^1| = |H_c^2|$) leading to a fully symmetric hysteresis loop. From a temperature T that satisfies $T_N < T < T_C$, a strong positive magnetic field H_{FC} is applied to saturate the FM layer and the sample is subsequently cooled below T_N while keeping the strong field H_{FC}. This procedure is usually referred to as *field cooling*.

In exchange-bias systems, after field cooling, the proximity of the AF and FM layers leads to exchange interactions at the interface and the AF layer is magnetically ordered relative to the FM layer. In the case depicted in Fig. 3.1 (step 2), the magnetic moments of the first ML of the AF layer are pointing in the same direction than the moments of the FM layer. Note that here, we will consider a uniform magnetization of the FM layer. When the external magnetic field is reversed, the magnetic moments of the FM layer will try to rotate in the plane to the opposite direction. The strength of the external magnetic field required for the magnetization reversal (H_c^-) is larger than that of the FM layer alone since the magnetic coupling to the rigid AF layers represents an additional force to overcome (see step 3 in Fig. 3.1). For strong negative magnetic fields, the FM layer has a reversed magnetization compared to that of step 2 in Fig. 3.1, while the AF layer is supposed to stay unmodified as illustrated in the step 4 in Fig. 3.1. Note that at the FM-AF interface, the magnetic moments of the FM layer are in an opposite direction to that of the AF layer while the exchange interactions would favor a FM coupling. When decreasing the strength of the external magnetic field, the favored ferromagnetic configuration at the interface between the AF and the FM layers facilitates the rotation of the magnetization to its initial direction (see step 5 in Fig. 3.1). The magnetization reversal to the initial direction can even happen for (small) negative magnetic fields (see Fig. 3.1) depending on the strength of the exchange interactions at the interface. Yet, if we look at the corresponding magnetization hysteresis loop, it is quite different from typical ferromagnets. Notably, we see that the coercive fields depend on the magnetization-reversal direction ($|H_c^1| \neq |H_c^2|$) leading to a shift of the hysteresis loop by $H_{EB} = (H_c^2 + H_c^1)/2$, referred to as the exchange bias field.

In the picture presented in Fig. 3.1, the exchange bias field H_{EB} is negative since the external magnetic field during the cooling process H_{FC} was positive. By applying a negative magnetic field H_{FC} during the cooling through T_N, it is possible to obtain a positive exchange-bias field H_{EB}. Note that for some experimental systems, the exchange shift can be in the same direction as the magnetic field during the cooling process.[17–20]

3.1.2. Rigid antiferromagnet model

Based on the phenomenological observations and on the Stoner-Wohlfarth model,[21] Meiklejohn and Bean[11,12] gave elements to develop a model predicting exchange bias. We will consider this model under the following drastic conditions[14,16,22,23]:

- The magnetization of the FM layer rotates uniformly, as a whole (*i.e.* Stoner-Wohlfarth approach).

- The AF and FM layers are considered to be in a single domain state.

- The interface between the FM and the AF layers is atomically flat.

- The FM and AF layers have in-plane uniaxial anisotropy and both axes are parallel.

- The magnetic moments of the AF layer are rigid.
- The AF and FM layers are magnetically coupled by exchange interaction at the interface.
- The field applied during the cooling process is along the AF and FM easy axes.

Under the above assumptions, we consider a bilayer exchange bias system that has been field cooled in a positive magnetic field. The energy per unit interface area can be expressed as[13, 14, 16, 22]:

$$E = -\mu_0 H M_{FM} t_{FM} \cos(\beta) + K_{FM} t_{FM} \sin(\beta)^2 - J_{INT} \cos(\beta), \qquad (3.1)$$

where H denotes the applied magnetic field in the direction of the AF- and FM-layer easy axes, K_{FM} is the bulk anisotropy of the FM layer and J_{INT} the interfacial exchange energy per unit area. M_{FM} is the magnetization of the FM layer that makes an angle β with its easy axis and t_{FM} is the thickness of the FM layer. The stable positions of the FM magnetization M_{FM} can be obtained by minimizing the energy as a function of the angle β. One finds two possible solution: (i) $\beta = 0$ if $2K_{FM} + \mu_0 H M_{FM} t_{FM} + J_{INT} > 0$ and (ii) $\beta = \pi$ if $2K_{FM} - \mu_0 H M_{FM} t_{FM} - J_{INT} > 0$. Yet, to find the magnetic field at which the magnetization is reversed, one has to look at the limit of the stability of solutions (i) and (ii) and find the corresponding coercive fields:

$$H_c^1 = -\frac{2K_{FM} t_{FM} + J_{INT}}{\mu_0 M_{FM} t_{FM}}, H_c^2 = \frac{2K_{FM} t_{FM} - J_{INT}}{\mu_0 M_{FM} t_{FM}}. \qquad (3.2)$$

Using the definition of the coercive field $H_c = {(H_c^2 - H_c^1)}/{2}$ and the definition of the exchange bias field $H_{EB} = {(H_c^2 + H_c^1)}/{2}$, one reads:

$$H_c = \frac{2K_{FM}}{\mu_0 M_{FM}} \qquad (3.3)$$

$$H_{EB} = -\frac{J_{INT}}{\mu_0 M_{FM} t_{FM}} \qquad (3.4)$$

From Eq. 3.4, we observe that within this simple model, the exchange bias field is inversely proportional to the FM-layer thickness, which is the case of a large number of experimental investigations.[16, 23] Eq. 3.4 also suggests that H_{EB} is proportional to the interfacial exchange energy J_{INT}, parameter that is usually unknown. We generally assume that the strength of the exchange coupling at the interface is equal to or higher than the bulk AF exchange coupling J_{AF} but lower than the bulk FM exchange coupling J_{FM}. However using such values for J_{INT} in Eq. 3.4 leads to H_{EB} orders of magnitude larger than that of the experimentally observed one.[13, 16, 24, 25] Note that if the anisotropy of the AF layer is low in comparison to the interface exchange energy ($K_{AF} t_{AF} < J_{INT}$), it is energetically more favorable that the AF

layer rotates together with the FM layer. In this case, there would be no shift of the hysteresis loop but only an increase of the coercive field.

There is a variety of models that include additional degrees of freedom, and most of them overestimate the exchange bias field H_{EB}.[14–16, 23] Additionally it seems that most of the exchange bias physics takes place at the interface between the FM and the AF layer. The novel models try to have a microscopic understanding of the magnetic properties at the FM-AF interface.[15, 16, 22] There are additional effects ascribed to interfaces effects such as: (i) The shift in the hysteresis loop vanishes above a system-dependent temperature referred to as the blocking temperature T_B, which can be much lower than the bulk Néel temperature of the AF layer.[13] (ii) The exchange field H_{EB} can depend on the number of measurements that has been carried out. This property is often referred to as training effect.[13]

3.2. Interlayer exchange coupling

3.2.1. Introduction

Interlayer exchange coupling (IEC) allows to magnetically couple two ferromagnetic layers separated by a non-magnetic spacer. In 1986, the effect was identified in rare-earth multilayers by Salamon $et\ al.$[26] and by Majkrzak $et\ al.$[27] and in Fe/Cr/Fe samples by Grünberg $et\ al.$[28] Later, in 1990, Parkin $et\ al.$[29] experimentally evidenced that the strength and sign of the IEC evolves in an oscillatory manner with increasing spacer thickness. Additionally, Parkin performed a systematic study and showed that the oscillatory exchange coupling occurs with almost all transition or noble metals.[30]

To the first order, one can express the exchange coupling energy per unit area between two FM layers F_A and F_B separated by a non-magnetic spacer as[31]:

$$E_{A,B} = J \cos \theta \tag{3.5}$$

with θ the angle between the magnetizations of the two FM layers. J describes the strength and the sign of the magnetic interaction. Note that here we use the following convention: a positive (negative) J favors an AF (FM) coupling. In Fig. 3.2, we present the evolution of the IEC of two $Ni_{80}Co_{20}$ magnetic layers separated by a variable thickness of Ru. The oscillatory nature of the coupling is clearly visible.

From a theoretical point of view, various models have been developed to describe IEC[31, 33]:

- the Ruderman-Kittel-Kasuya-Yosida (RKKY) model
- the free-electron model
- the hole confinement model
- the Anderson (sd-mixing) model
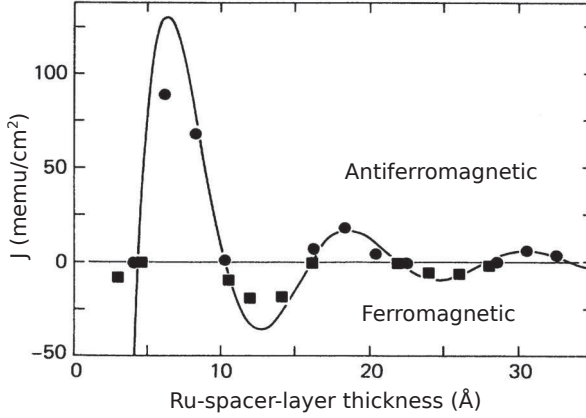
Figure 3.2. – **Illustration of the evolution of interlayer exchange coupling with increasing spacer thickness**. By increasing the thickness of the Ru spacer, the exchange coupling between the $Ni_{80}Co_{20}$ magnetic layers evolves in an oscillatory manner. The figure is taken from Ref. 32.

All of these models can predict the period of the oscillatory exchange coupling based on the Fermi surface of the bulk spacer material. However, experimental studies revealed that the exchange coupling strength also depends on the thickness of the FM layers.[34] Furthermore, the exchange coupling can be influenced by a capping layer deposited on top of a FM layer.[34] These latter results suggest a quantum well nature of the IEC[34] and IEC can indeed be interpreted as quantum size effects.[31, 33, 35] Additionally, it has been shown that all the listed models can be unified into the quantum-size-effect approach.[35] In this approach that we briefly describe in the next section, we consider electrons in quantum wells formed by the interfaces between the non-magnetic and ferromagnetic layers.[31, 33–35]

3.2.2. Quantum-well states to explain interlayer exchange coupling

In this section, we briefly describe the confinement of electrons in a metallic layer in terms of reflection at the interfaces. We will see that the confinement of electrons alters the density of states (DOS) and apply it to IEC systems. Finally, we will give more information about the archetypal Co/Cu/Co(100) system.

3.2.2.1. Electron confinement in a metallic overlayer

We consider the case of a thin metallic overlayer on top of a substrate. The electrons of the overlayer are (partially) confined by the vacuum barrier on one side and by the substrate on the other side. The electrons have a wave vector $\vec{k} = \vec{k}_\parallel + \vec{k}_\perp$, $\vec{k}_\perp$ being

along the surface normal. As we assume an in-plane translational invariance, the projected wave vector $\vec{k}_\parallel$ is unmodified upon reflection at an interface. Thus for a given $\vec{k}_\parallel$, the problem can be reduced to a one-dimensional problem. For the perpendicular wave vector, we distinguish between $\vec{k}_\perp^+$ and $\vec{k}_\perp^-$ for states with positive and negative perpendicular wave vectors, respectively. We define r_v and r_s the reflection coefficients of the electrons on the vacuum barrier and on the overlayer-substrate interface, respectively. They can be expressed as[31]:

$$r_v = |r_v| \exp\left(i\Phi_v\right), r_s = |r_s| \exp\left(i\Phi_s\right), \tag{3.6}$$

where Φ_v and Φ_r are the phase shifts upon reflection of the electrons at the overlayer-vacuum and overlayer-substrate interfaces, respectively. Note that $|r_v| = 1$ for electrons having an energy below the vacuum level and in general $|r_s| < 1$ (partial confinement). Usually, r_v and r_s depend on the electron energy ϵ and on the electron projected wave function $\vec{k}_\parallel$.

In the case of a total confinement of the electron in the overlayer ($r_s = 1$), the phase shift of an electron after a complete round trip can be expressed as[31]:

$$\Phi = \Phi_v + \Phi_s + \left(k_\perp^+ - k_\perp^-\right) D, \tag{3.7}$$

where D represents the thickness of the metallic overlayer. The stationary condition imposes $\Phi = 2\pi n$, with n an integer. In turn, this confinement of the electrons along the surface normal leads to a modification of the $\vec{k}_\parallel$-projected DOS $n(\vec{k}_\parallel, \epsilon)$. For a given set of ϵ and $\vec{k}_\parallel$, $n(\vec{k}_\parallel, \epsilon)$ exhibits sharp peaks at given spacer thicknesses. The periodicity of the peaks is given by[31]:

$$\Lambda = \frac{2\pi}{\left|\vec{k}_\perp^+ - \vec{k}_\perp^-\right|}. \tag{3.8}$$

Note that $\vec{k}_\perp^+$ and $\vec{k}_\perp^-$ are folded into the first Brillouin zone since periods shorter than 2 atomic layers are physically meaningless. Bruno[31] carried out calculations for partial electron confinement in the overlayer. He evidenced that the $\vec{k}_\parallel$-projected DOS stays periodic with the periodicity also given by Eq. 3.8.

The oscillations in the DOS can be revealed by direct and inverse photoemission experiments (see Refs. 31, 34 and references therein). In Fig. 3.3, we show a direct-photoemission measurement performed on a Cu overlayer of varying thickness on top of a Co(100) substrate. At a given binding energy, we clearly observe oscillations in the photoemission signal, *i.e.* the density of states, for increasing Cu thickness.

When considering electron confinement involving a ferromagnetic overlayer or substrate, one has to consider that the reflection coefficients can be spin dependent.[31] In these cases, one generally define the spin asymmetry reflection coefficient:
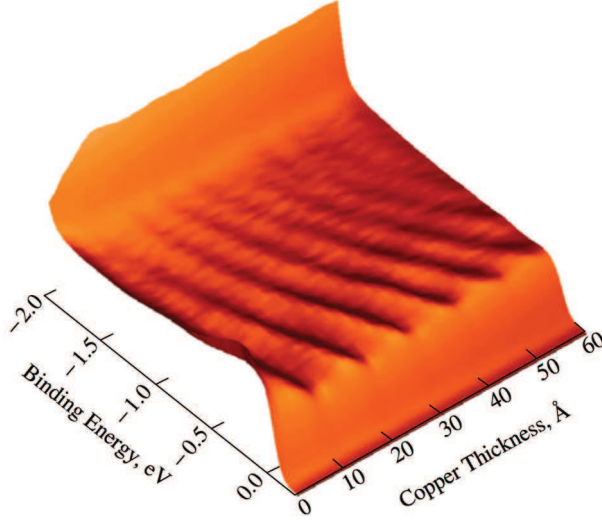
Figure 3.3. – **Evidence of quantum-well states in the Cu overlayer on Co(100)**. Photoemission spectra of Cu/Co(100) taken for $\vec{k}_\parallel = \vec{0}$. The spectra evidence an oscillatory behavior as a function of the Cu thickness and electron binding energy. The figure is taken from Ref. 34.

$$\Delta r_s \equiv \frac{r_s^\uparrow - r_s^\downarrow}{2}, \tag{3.9}$$

where $r_s^\uparrow$ and $r_s^\downarrow$ are the reflection coefficient for spin up and down, respectively.

3.2.2.2. Interpretation of interlayer exchange coupling

Above, we have seen that electron confinement in a metallic layer leads to a variation of the DOS $n(\epsilon)$. We now define $\Delta n(\epsilon)$, the total change in DOS of the system (per unit area), and ΔE the change in total energy that has the following form[31]:

$$\Delta E = \int\limits_{-\infty}^{\epsilon_F} (\epsilon - \epsilon_F) \, \Delta n(\epsilon) d\epsilon, \tag{3.10}$$

where ϵ_F is the Fermi energy.

Typical IEC systems are composed of a non-magnetic layer of thickness D sandwiched between two FM layers. It results that the reflection coefficients at the interfaces, and subsequently the total change in DOS $\Delta n(\epsilon)$ are spin dependent. In turn, the total energy variation ΔE as expressed in Eq. 3.10 depends on the relative mag-

netic orientations of the two FM layers. Bruno derived the energy difference between a FM and an AF configurations of the FM layers[31]:

$$E_{FM} - E_{AF} \approx -\frac{1}{\pi^3} Im \left\{ \int d^2 \vec{k}_\parallel \int_{-\infty}^{\epsilon_F} \Delta r_A \Delta r_B \exp\left[i\left(k_\perp^+ - k_\perp^-\right) D\right] d\epsilon \right\}. \qquad (3.11)$$

The integration on $\vec{k}_\parallel$ is performed over the first two-dimensional Brillouin zone. A and B label the spin-asymmetry reflection coefficient on the FM layers F_A and F_B, respectively. It results that the FM layers are FM or AF coupled depending on the sign of the above integral. We can also observe that the spacer-thickness dependence of IEC is determined by $k_\perp^+ - k_\perp^-$, which is a property of the spacer material.

In the limit of large spacer thickness D, the exponential factor in Eq. 3.11 oscillates rapidly with ϵ and with $\vec{k}_\parallel$. It results that the effects of quantum well state (QWS) are canceled out. However, since the energy integral is abruptly stopped at the Fermi energy ϵ_F, the QWS at ϵ_F give a predominant contribution to IEC. Note that Eq. 3.11 takes implicitly into account the thicknesses of the FM layers and possible capping layers in the Δr_A and Δr_B coefficients.

3.2.2.3. The archetypal Co/Cu/Co(100) system

In the following, we focus on the Co/Cu/Co(100) system. There are several reasons for this choice of system: (i) it is a representative system for IEC[31] (ii) we experimentally investigated this system (see Chap. 10), (iii) Cu has a rather simple Fermi surface and (iv) sample of very good quality can be achieved (low roughness of the interfaces).

As stated above, the dominant contributions come from the QWS at the Fermi energy. In fact, one can even predict the oscillation period(s) by looking at the Fermi surface. In Fig. 3.4, we show a cross section of the copper Fermi surface. The pairs of wave vectors $\vec{k}^+$ and $\vec{k}^-$ that give rise to oscillation are located on the Fermi surface and their difference is along the [100] direction ($\vec{k}_\parallel$ must stay constant). Additionally, the associated phase velocities must have equal amplitudes and opposite signs.[37] By looking at the Cu Fermi surface (see Fig. 3.4), one can see three different solutions, two of them being equivalent. The predicted periods are $\Lambda_1 = 2.6\,\text{ML}$ and $\lambda_2 = 5.9\,\text{ML}$.[36] In Fig. 3.5, we show magnetic-coupling measurements of the Co/Cu/Co(100) system for increasing Cu thicknesses. As predicted, we can observe long- and short-period oscillations of the interlayer exchange coupling.

Additionally, Qiu and Smith[34] derived an analytic formula for the thickness dependence of the IEC strength:

$$J = -\frac{A_1}{D^2} \sin\left(\frac{2\pi D}{\Lambda_1} + \Phi_1\right) - \frac{A_2}{D^2} \sin\left(\frac{2\pi D}{\Lambda_2} + \Phi_2\right), \qquad (3.12)$$
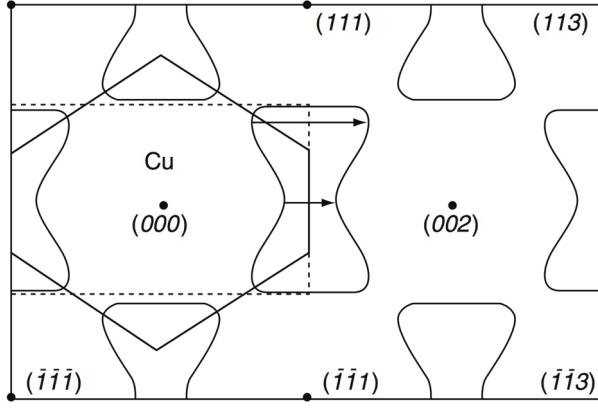
Figure 3.4. – **Cross section of the copper Fermi surface**. The solid points give the vectors of the reciprocal lattice. The arrows indicate the stationary spanning vector along the [100] direction. The figure is taken from Ref. 36.
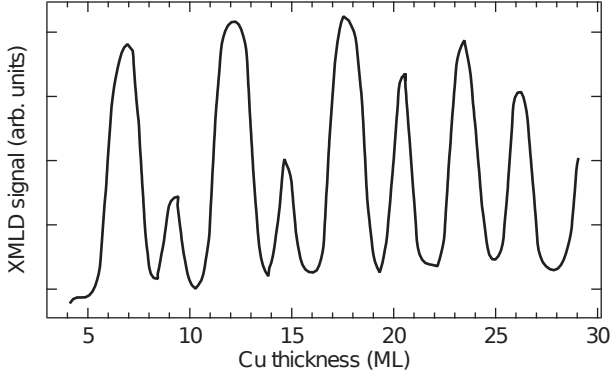
Figure 3.5. – **Oscillation of the magnetic coupling of Co/Cu/Co(100) for increasing Cu thicknesses**. Magnetic coupling measurements on Co/Cu/Co(100) using X-ray magnetic linear dichroism. High dichroic values indicate an AF ordering of the Co layers. The data are taken from Ref. 34.

where Φ_1 (Λ_1) and Φ_2 (Λ_2) are the phases associated to the long- and short-period oscillations (periods), respectively. A_1 and A_2 are the amplitudes of the oscillations and their ratio depends on interfacial roughness.[34] From Eq. 3.12, we observe that the IEC strength decreases with the inverse squared Cu thickness.

3.3. Kondo physics

Generally, the electrical resistance of a metal decreases with temperature as the number of scattering events decreases. However, already in the 1930s, Messner *et al.*[38] and then de Haas *et al.*[39] have observed that the resistance of a metal incorporating magnetic impurities can increase again at very low temperatures. It is only 34 years after these observations that Kondo[40] could attribute the increase of the resistance at low temperature to scattering events on the magnetic impurities.

Kondo used perturbation theory to describe the scattering of the metal conduction electrons by a magnetic impurity. The conduction electrons of the metal are perturbed by an exchange interaction J with the spin in the impurity. For a single impurity, the perturbation Hamiltonian is given by[40]:

$$H = \underbrace{\sum_{k,s} \epsilon_k a_{ks}^* a_{ks}}_{\text{conduction electrons}} \underbrace{- J \sum_{k,k'} \left(a_{k'\uparrow}^* a_{k\uparrow} - a_{k'\downarrow}^* a_{k\downarrow} \right) S_z}_{\text{spin-conserving scattering}} \underbrace{- J \sum_{k,k'} \left(a_{k'\uparrow}^* a_{k\downarrow} S^- - a_{k'\downarrow}^* a_{k\uparrow} S^+ \right)}_{\text{spin-flip scattering}},$$

(3.13)

where ϵ_k is the one-electron energy of the conduction electron with wave number k and spin component s along the z-direction, a_{ks} and a_{ks}^* are the annihilation and creation operators. S is the spin operator of the impurity and its projection along the z-axis is S_z while $S^\pm = S_x \pm i S_y$. The Hamiltonian can be separated into three different parts: the first part accounts for the conduction electrons that are not interacting with the impurity, the second and third terms describe the interaction (scattering) of the conduction electrons with the magnetic impurity without and with spin-flip processes, respectively. Adapting the Hamiltonian expressed in Eq. 3.13 for a given concentration of impurities , Kondo derived the following resistivity[41]:

$$\rho(T) = \rho_0 + aT^5 + bJ \ln\left(\frac{T}{c}\right),$$

(3.14)

where a, b and c are constants. Note that for high temperatures the phonon scattering processes dominate with T^5 and for low temperatures the logarithmic dependence prevail. Yet, the resistivity increase at low temperatures can be explained by an antiferromagnetic coupling between the impurity spin and the conduction electrons ($J < 0$). However, the perturbation series breaks down below a critical temperature referred to as the Kondo temperature T_K.[42] Strictly speaking, the Kondo approach is only valid in the weak coupling regime for $T \gg T_K$. Later in 1975, Wilson[43] treated the Kondo problem for a single spin impurity ($S = \frac{1}{2}$) for temperature close or below T_K using the renormalization group transformation. Wilson's approach revealed that for an antiferromagnetic coupling between the conduction electrons and the impurity spin, the latter is completely screened by the conduction electrons at $T = 0\,\text{K}$, forming a many-body non-magnetic singlet state.

In the last two decades, the access to atomic scale sparked a revival of the Kondo effect. In quantum-dot systems, the confinement of electrons between metallic electrodes can mimic the system of a cobalt impurity in bulk copper, and lead to the observation of the Kondo effect by transport measurements. The quantum-dot system allows an easy control of the parameters of the virtual magnetic impurity, and thus permits a better investigation of the Kondo physics.[44–46] Alternatively, STM allowed to image and manipulate single magnetic impurities on metallic surfaces, and consequently to observe Kondo resonance at the Fermi level. In turn those STM-based studies help to better understand the Kondo physics.[47–52] The Kondo effect has also been observed for single-metal atoms embedded in a molecule deposited on a metallic surface.[53–58] This gives, to a certain extend, the possibility to tune the coupling between the metallic center to the substrate through an adequate choice of the ligands. The Kondo effect could also be detected in fully organic molecules, where the impurity spin arises from charge transfer processes.[59–61]

The Kondo physics is a rather complicated topic, nicely discussed in Ref. 41, 42, 62–65. In the following we will only qualitatively consider the simpler Anderson model that illustrates the many-body phenomenon.

3.3.1. The Anderson model

The Anderson model[66] describes the conditions under which a magnetic impurity with spin $S = 1/2$ embedded in a metal retains its magnetic moment. It is only 5 years later that Schrieffer and Wolff discovered the link between the Anderson model and the Kondo effect.[67] In the simplified Anderson model, the electronic structure of the magnetic impurity is limited to a single d or f orbital. The considered orbital can contain up to two electrons and is interacting with the conduction electrons of the host metal. In order to be magnetic, the orbital has to be singly occupied and the corresponding d^1 state must lie below the Fermi energy with a binding energy ϵ. Due to the Coulomb repulsion, adding a second electron into the orbital costs an extra energy U. The associated d^2 state is located above the Fermi energy to ensure a single occupation of the orbital (see Fig. 3.6a). The hybridization of the d states with the continuum of electronic states of the metal leads to a broadening of the d states by $\Delta = \rho_0|V|^2$ where ρ_0 is the DOS of the metal at the Fermi energy and V the matrix element that describes the coupling between the d state and the metal conduction electrons.

Note that Schrieffer and Wolff have demonstrated the correspondence between the Kondo approach and the Anderson model in the limit of small $s-d$ hybridization.[67] The exchange interaction J of the Kondo Hamiltonian can be expressed as a function of the Anderson variables[67]:

$$J = 2|V|^2 \frac{U}{\epsilon(\epsilon + U)}. \tag{3.15}$$
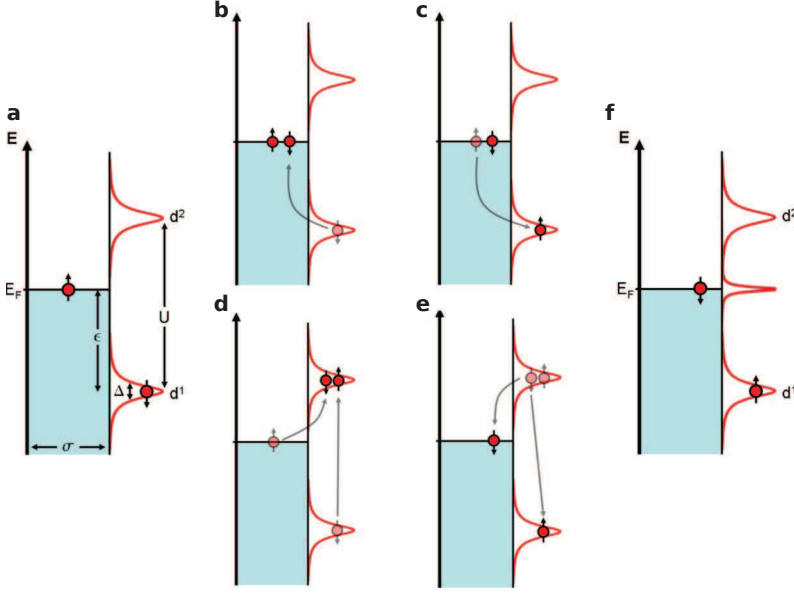
Figure 3.6. – **Spin-flip processes in a single magnetic orbital within the Anderson model**. Schematic drawing of the energy-dependent DOS of a single d orbital in interaction with the metallic substrate. The singly occupied state is located at an energy ϵ below the Fermi level, and at an energy U below the doubly occupied state. Due to the interactions with the metallic host, the orbital levels have a half-width at half maximum of Δ. **a**, The d orbital is initially occupied by a single electron with spin $\downarrow$. Virtual processes can flip the spin of the singly-occupied orbital, either by **b** and **c**, emptying the d orbital or by **d** and **e**, double occupation of the d orbital. **f**, The conduction electron at the Fermi energy involved in the spin-flip virtual processes form a resonance at the Fermi level. The figure is taken from Ref. 42.

There are two possible paths to flip the spin of the singly-occupied orbital with the help of the conduction electrons (see Fig. 3.6). The d orbital can first be emptied and then re-filled by a conduction electron of opposite spin (see Figs. 3.6b,c). Alternatively, the d orbital can at first be doubly occupied, and the initial electron is then transferred to the metal (see Figs. 3.6d,e). In a classical description, these processes can only occur when the system receive an energy of at least $-\epsilon$ for the first process and at least $U + \epsilon$ for the second process. Although no external energy is exchanged with the system, the processes are still possible in a quantum mechanical picture by virtue of the Heisenberg uncertainty principle. Indeed, if the uncertainty in energy is of the order of the excited state energies, the excitation is permitted during a short time interval, and the spin-flip process referred to as a virtual process. The corresponding excitation times must thus be shorter than $h/|\epsilon|$ or $h/|U+\epsilon|$. Taking into account a multitude of these virtual processes, they modify the energy spectrum by

25

generating a new many-body state, the so-called Kondo resonance, close to the Fermi level.[63] In turn, the Kondo resonance is at the origin of abnormal physical properties, such as the conductivity variation, of metals embedding magnetic impurities

3.3.2. Fano resonance

The above Anderson model has been initially treated for magnetic impurities embedded in a non-magnetic metal but remains valid for magnetic adatoms on non-magnetic metallic surfaces. When such a system, *e.g.* Co/Ag(111), is measured using scanning tunneling spectroscopy, the Kondo resonance can appear as a dip in the conductance spectrum (see Fig. 3.7). Since the dI/dV spectrum measured by scanning tunneling spectroscopy should be closely related to the density of states (see Chap. 5), one would rather expect a peak feature.
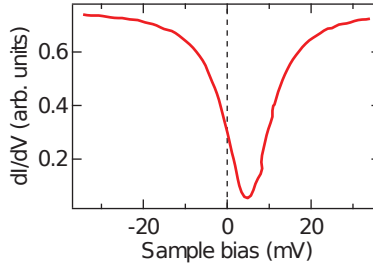
Figure 3.7. – **Lineshape of the Kondo resonance using scanning tunneling spectroscopy**. Kondo resonance of a Co adatom on a Ag(111) surface observed by scanning tunneling spectroscopy. The Kondo resonance increases the density of states close the Fermi level but the resonance has a dip-like shape. The experimental data are taken from Ref. 68.

In fact, when a STM tip is brought close to the system composed of a magnetic impurity lying on a metallic substrate, electrons from the tip can elastically tunnel to the sample using different paths. They can tunnel directly into an empty bulk state above E_F with a probability t_1, or into the Kondo resonance close to E_F with a probability t_2. Since tunneling is a coherent quantum effect, the tunneling current is determined by quantum interference between the two paths.[62] Note that here we assume a weak tip-sample coupling. By taking the interference effects into account, Fano showed that the measured energy spectrum has the following form[69]:

$$\rho(E) \propto \rho_0 + \frac{(q + \epsilon)^2}{1 + \epsilon^2},\tag{3.16}$$

that we call the Fano equation, where the normalized energy reads:
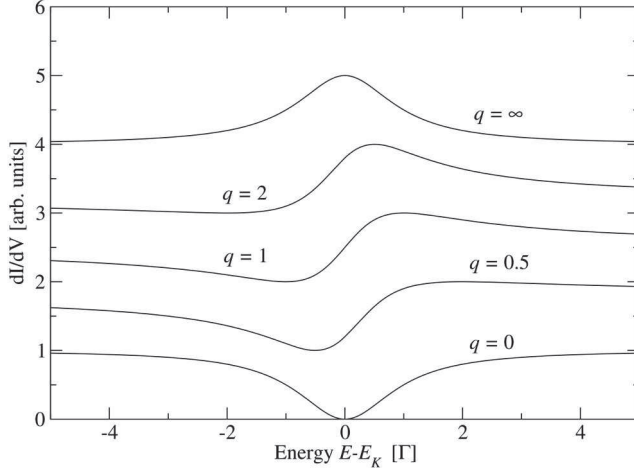
Figure 3.8. – **Influence of the q parameter on the Fano shape**. Set of Fano resonances (Eq. 3.16) for different values of q. The curves are shifted for clarity. The figure is taken from Ref. 62.

$$\epsilon = \frac{E - E_K}{\Gamma}. \tag{3.17}$$

$\Gamma = k_B T_K$ corresponds to the half-width at half maximum of the Kondo resonance, T_K is the so-called Kondo temperature and E_K corresponds to the position of the Kondo resonance relative to the Fermi energy E_F.

The factor q in Eq. 3.16 is linked to the ratio of the tunneling probabilities t_1 and t_2, and can drastically change the shape of the resonance. The expression for q is[70]:

$$q = \frac{t_2}{\pi \rho_0 V t_1} + \Lambda(\epsilon), \tag{3.18}$$

with $\Lambda(\epsilon)$ a slowly varying parameter in energy and V the hybridization matrix element between the localized states and the continuum of the metal.[62] For electrons dominantly tunneling into the Kondo resonance ($t_2 \gg t_1$), the q factor is large and the Fano function has the shape of a Lorentzian peak, while for $t_2 \ll t_1$, the q factor is close to zero and the Fano function has a dip shape (see Fig. 3.8). For intermediate values of q, the Fano function has an asymmetric shape as illustrated in Fig. 3.8.

In general, it is difficult to predict the value of q, but experimental results suggest that q depends both on the investigated magnetic impurity and on the substrate. For example, Wahl *et al.*[51] studied a Co adatom on different substrates, which led to

27

different values of q. Alternatively, Jamneala *et al.*[71] studied different transition-metal impurities onto the same substrate, also observing different q factor.

Note that in some recent work on the Kondo effect,[72–75] the Fano function (Eq. 3.16) was exchanged by a Frota function that better fits the solution of the numerical renormalization group theory and has the following form[42, 74, 76, 77]:

$$\rho(E) \propto \Im\left[i e^{i\phi} \sqrt{\frac{i\Gamma}{eV - e_k + i\Gamma}} \right], \tag{3.19}$$

where Γ is the width parameter ($\Gamma = 1.43 k_B T_K$).[74] e_k accounts for the position of the resonance and ϕ is the line shape parameter.[74]

3.3.3. Dependence of the Kondo resonance on external parameters

Influence of the temperature

At $0\,\mathrm{K}$ the half-width at half-maximum Γ of the Kondo resonance, or the characteristic Kondo temperature $T_K = \Gamma/k_B$, within the framework of the Anderson model, is given by[41, 62]:

$$\Gamma(T = 0\,\mathrm{K}) = k_B T_K \simeq \sqrt{2\Delta \frac{U}{\pi}} \exp\left[-\frac{\pi}{2\Delta} \left(\left|\frac{1}{\epsilon}\right| + \left|\frac{1}{\epsilon + U}\right| \right)^{-1} \right]. \tag{3.20}$$

For increasing temperatures, the width of the resonance Γ broadens and follows:[50, 52, 62]

$$2\Gamma = \sqrt{(\alpha k_B T)^2 + (2 k_B T_K)^2}. \tag{3.21}$$

Strictly speaking Eq. 3.21 is only valid for $T \ll T_K$ (Fermi-liquid model), but is also often used for higher temperatures. Eq. 3.21 nicely fits experimental data, such as represented in Fig. 3.9 and α is experimentally found to be equal to 5.4 by Otte *et al.*[52] Additionally the peak height of the Kondo resonance also evolves with increasing temperatures. For $T \ll T_K$, the peak height decays as $1 - c(T/T_K)^2$, while for $T \geq T_K$ the peak height decays logarithmically.[62]

Influence of the magnetic field

For $T \ll T_K$, the Kondo screening form a singlet state resulting in a non-magnetic ground state. The singlet state is unaffected by small magnetic field. However, Costi[78] predicted that above a critical magnetic field $B = k_B T_K/2g\mu_B$, *i.e.* when the Zeeman energy is comparable to the Kondo interactions, the Kondo resonance is split. The shift of the split peaks scales with the Zeeman energy in agreement with
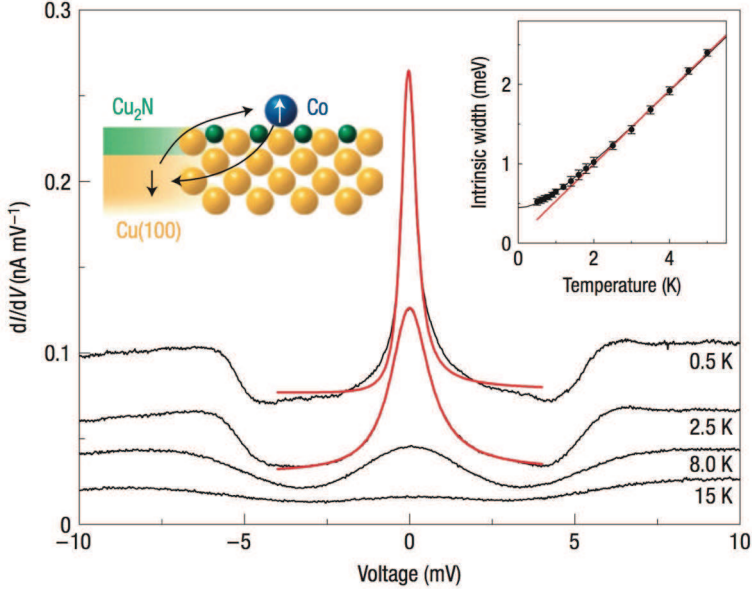
Figure 3.9. – **Temperature depedence of the Kondo resonance**. STS measurements of a Co adatom on CuN as represented in the left inset. The current derivatives show the dependence of the Kondo resonance on temperature. The resonance broadens and the peak intensity decreases with increasing temperature. The right inset presents the resonance width as a function of the temperature. The solid black line represents a fit of the experimental data with Eq. 3.21. The figure is taken from Ref. 52.

experiments.[52, 72, 79, 80] To illustrate the Kondo-resonance splitting, we show in Fig. 3.10 the magnetic-field dependence on the Kondo resonance for a Co adatom on CuN/Cu(100).

Note that the presence of one or more additional magnetic impurity near the impurity of interest can similarly modify the Kondo resonance, through (indirect) magnetic interactions.[80–82]

Finally, the temperature and magnetic-field dependence of the Kondo resonance is often used as a signature of the Kondo effect in experimental studies.
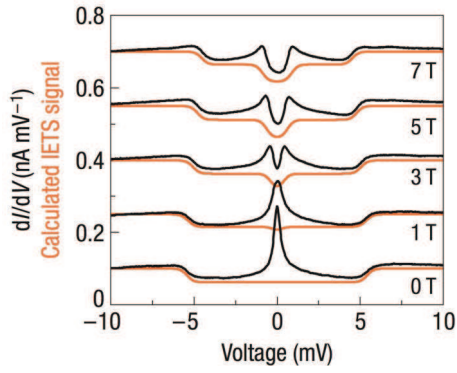
Figure 3.10. – **Magnetic field depedence of the Kondo resonance**.
dI/dV spectra acquired at $0.5\,\mathrm{K}$ on Co/CuN for different magnetic fields.
With increasing magnetic fields, we observe a splitting of the Kondo res-
onance. The figure is taken from Ref. 52.

X-ray absorption spectroscopy

In this chapter, we will start by briefly explaining X-ray absorption spectroscopy (XAS) using a classical description. In a second section, we shortly discuss the electric-dipole selection rules using a quantum mechanical picture. The selections rules help us in the third section to explain the origin of the X-ray magnetic circular dichroism (XMCD) effect. We also present the sum rules that allow to extract the spin and orbital magnetic moments of a given element by using polarized X-rays.

4.1. X-ray absorption spectroscopy

4.1.1. Absorption and cross sections

In this thesis we use X-ray absorption spectroscopy (XAS) to gain information about the electronic and magnetic properties of molecules on surfaces. The X-rays used for this investigation may interact with matter in different ways with different probabilities. In Fig. 4.1, we present the cross sections as a function of the photon energy for a Cu sample. For low photon energy ($E_p < 10\,\text{keV}$), X-ray photons may be elastically scattered by free charged particles (electrons). The upper limit of this Thomson scattering process is the Compton scattering process where the X-ray photon transfers part of its energy to the free charged particle. Compton scattering has its highest cross section for photon energy between $10\,\text{keV}$ to $1000\,\text{keV}$. For even higher photon energies, X-ray photons may generate electron-positron pairs. The photon could also be absorbed by the nucleus that would result in the ejection of a proton or neutron. In this thesis, we experimentally used X-rays with energies ranging from $350\,\text{eV}$ to $1000\,\text{eV}$ and from Fig. 4.1 we can see that, in this photon-energy range, photoelectric absorption is the dominating interaction by orders of magnitude. In the following, we will only consider photoelectric absorption.
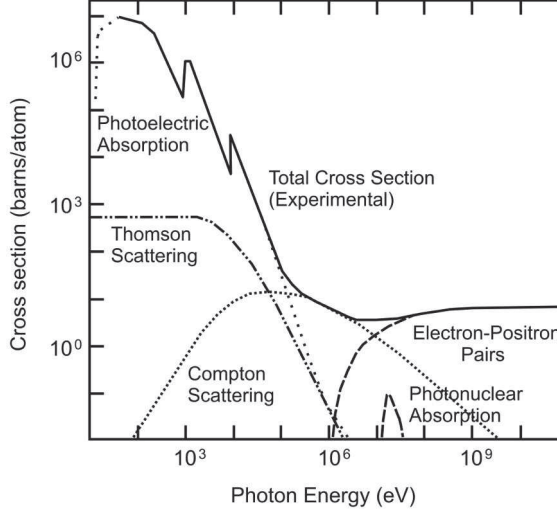
Figure 4.1. – **Photon-energy dependent cross sections**. Cross sections of the photoelectric absorption, Thomson scattering, Compton scattering, electron-positron pairs and photonuclear absorption for Cu as a function of energy. In the soft X-ray range, the photoelectric-absorption cross section is orders of magnitude higher than the other cross sections. The figure is taken from Ref. 83.

An X-ray beam that goes through a sample is strongly attenuated due to all the possible interactions between X-ray photons and matter. An X-ray beam with an initial intensity I_0^{ph} that travels a distance z within the sample has an intensity[84]:

$$I^{ph}(z) = I_0^{ph} \exp\left(-\mu_x z\right) = I_0^{ph} \exp\left(-\rho_a \sigma^{abs} z\right) \tag{4.1}$$

where μ_x is the linear X-ray absorption coefficient and σ^{abs} is the X-ray absorption cross section per atom. The two quantities are linked by ρ_a, the atomic number density, *i.e.* the number of atoms per unit of volume.

The photoelectric-absorption cross section σ^{abs} shows absorption edges at element-dependent distinctive energies, that arise from core-level electron excitations. The absorption edges are labeled K, L_1, L_2, L_3, M_1, M_2, etc. for photon-induced excitations from the $1s$, $2s$, $2p_{1/2}$, $2p_{3/2}$, $3s$, $3p_{1/2}$, etc. levels.

For electrons excited above the ionization potential, the final state is represented by a plane wave propagating in vacuum. For a fixed X-ray photon energy, one can study the kinetic-energy distribution of the photoelectrons, which gives rich information about the occupied core-level initial states. This technique, referred to as X-ray photoemission spectroscopy, is element specific as the binding energy of the core-level electrons depends on the element we consider. One can similarly retrieve information

about the valence band. X-ray photoemission spectroscopy is used to determine the composition and chemical properties of samples. In this thesis, we did not analyze the photo-electrons but focused our efforts on the absorption coefficient described below.

4.1.2. X-ray absorption spectroscopy detection techniques

Historically, absorption measurements were performed on ultra-thin samples by measuring the X-ray intensity that travels through the sample (see Fig. 4.2a). The corresponding transmitted intensity as a function of the photon energy shows dips at the absorption edges. There are two other detection modes for X-ray absorption: X-ray fluorescence and electron yield. The former consists in measuring the photons arising from the electron/core-hole recombinations, while the latter measures an electron current subsequent to the photon absorption (see Fig. 4.2b). In the center panel of Fig. 4.2b, we briefly describe how such an electron current can be induced. The absorption of an X-ray photon leaves a given atom with an unoccupied core-level state. The electronic relaxation of the atom leads to X-ray fluorescence or Auger electrons. In turn, the Auger electron, while propagating within the sample, induces secondary electrons through inelastic scattering. A proportion of the Auger and secondary electrons that have a kinetic energy larger than the sample's work function escape from the sample. The number of secondary electrons is proportional to the number of primary Auger electrons, that in turn is directly proportional to the sample's absorption. To measure the absorption intensity one can equivalently (i) count the electrons that leaves the sample or (ii) measure the electron current that goes from the ground to the sample (in order to balance the flow of out going electrons). Experimentally, method (i) can be realized by having an electron detector in front of the sample. In this case, one can only count the emitted electron within a limited solid angle, while method (ii) has no solid-angle constraint and can be experimentally easily implemented as sketched in Fig. 4.2b.

Since the Auger decay channel after the X-ray absorption dominates that of the X-ray fluorescence in the soft X-ray regime, electron-yield detection techniques usually lead to larger signals.[85] A typical electron-yield absorption spectrum for a Co sample is presented in Fig. 4.2b, and in the following, we will only consider X-ray absorption spectra in total electron yield mode.

We stated above that the number of emitted electrons is proportional to the X-ray absorption, but can we still link the electron yield to the X-ray absorption coefficient σ^{abs}? To answer this question, we write down the X-ray absorption using Eq. 4.1 in the limit of thin samples $d \ll 1/\mu_x$[84]:

$$I_0^{ph} - I^{ph}(d) = I_0^{ph} \left[1 - \exp\left(-\mu_x d\right) \right] \approx I_0^{ph} d\mu_x = I_0^{ph} \rho_a d\sigma^{abs}. \qquad (4.2)$$

From Eq. 4.2, we can see that the number of absorbed photons, and thus the electron-yield intensity is proportional to the X-ray absorption coefficient provided that $d \ll$
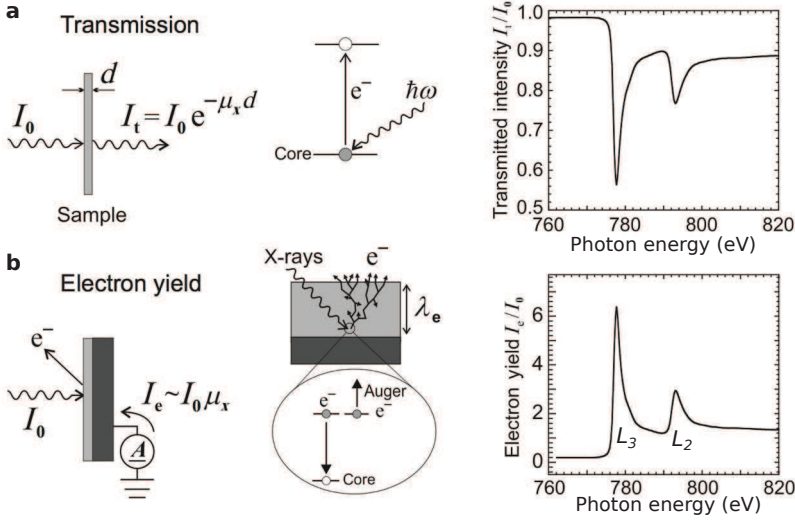
Figure 4.2. – **Two different common techniques for measuring X-ray absorption**. **a**, (Left) Typical transmission geometry where the proportion of X-rays that goes through the sample is measured. (Center) Schematic of a photon-induced core-level electron excitation that corresponds to an absorption event. (Right) Transmitted intensity as a function of the photon energy for a 10 nm Co-film sample. **b**, Experimental principle and methods to measure X-ray absorption spectra by (total) electron yield detection. (Left) Experimental geometry for total electron yield detection: the X-rays irradiate the sample and a picoammeter measure the current that goes from the sample to the ground. (Center) The absorption of photons induces core holes that may lead to Auger-electron emission. The inelastic scattering of primary Auger electrons produce a cascade of secondary electrons through inelastic scattering. A proportion of the Auger and secondary electrons escape from the surface; and electrons are flowing from the ground to the sample to keep charge neutrality. The total number of emitted electrons is proportional to the number of Auger electrons, that in turn is proportional to the absorption cross section. (Right) Electron yield intensity as a function of the photon energy for a Co sample. The X-ray absorption spectrum show two distinct peaks that correspond to the L_3 edge (transition from a $2p_{3/2}$ state) and the L_2 edge (transition from a $2p_{1/2}$ state). The figure is adapted from Ref. 84.

$1/\mu_x$. Fortunately, for electron-yield detection mode, Eq. 4.2 is not only valid for thin samples. Indeed 63 % of the electron-yield signal originates from the first 2 nm of the investigated sample that is usually much smaller than the X-ray penetration length $1/\mu_x$.[84–86] For transition-metal elements such as Fe, Co and Ni, the X-ray penetration length is about 500 nm below the L_3 edge, 20 nm at the L_3 edge and 80 nm after the L_3 edge.[84] Thus, the electron-escape length is indeed much shorter than the X-ray penetration length $1/\mu_x$. However, the situation can be different when

the absorption is measured at a grazing incidence angle θ. In this case, one should consider an effective X-ray penetration length $\cos(\theta)/\mu_x$ whose value can be in the order to that of the electron-escape length at an absorption edge. At an absorption edge, the X-ray intensity would rapidly decrease within the first 2 nm instead of staying constant to satisfy Eq. 4.2; and lead to measured absorption that underestimate the X-ray absorption cross section. In this thesis, we were careful to measure at incidence angles large enough to minimize this effect, known as the saturation effect.[86–89] Note that strictly speaking, the saturation effect can also occur at normal incidence.[86] Therefore, we must be careful when exploiting the amplitude of an adsorption edge.

In this thesis we focus on near edge X-ray absorption fine structure (NEXAFS) spectroscopy that consists in measuring the absorption coefficient while varying the photon energy in a small region around the absorption edge to fetch information about the unoccupied states. Theses unoccupied conduction states bear important information on electronic properties of materials and also their magnetic properties as will be shown below. Moreover, by changing the polarization of the X-rays, one can observe dichroic effects that can bring numerous additional information. In the following, we will look at the light-matter interactions using a quantum mechanical picture to understand and interpret the polarization dependence of the absorption spectra.

4.2. Interaction of polarized photons with matter

4.2.1. Derivation of the absorption cross section

In a one-electron picture, a photon of energy $E_p = \hbar\omega$ can bring a core electron to the continuum or a bound state. Within a quantum-mechanical description, the X-ray absorption cross section can be calculated by using the time-dependent perturbation approach. We consider an initial state $|i\rangle$ and final state $|f\rangle$, where both states contain an electronic and a photon part. In the following, we will only consider first-order processes, *i.e.* a direct transition from $|i\rangle$ to $|f\rangle$, without involving intermediate states. The transition probability per unit time T_{if} is given by Fermi's golden rule[84]:

$$T_{if} = \frac{2\pi}{\hbar} \left| \langle f | H_{int} | i \rangle \right|^2 \delta \left(E_i - E_f \right) \rho_f \left(E_f \right), \qquad (4.3)$$

where $\delta(E)$ is the delta function and $\rho_f(E)$ is the density of final states at an energy E. H_{int} is the electron-photon interaction Hamiltonian given by:

$$H_{int} = \frac{e}{m_e} \vec{p} \cdot \vec{A}, \qquad (4.4)$$

where e (m_e) is the charge (mass) of the electron, $\vec{p}$ the electron momentum operator and $\vec{A}$ the vector potential of the electromagnetic field. The total absorption cross

section is then simply obtained by normalizing the transition probability per unit time T_{if} to the incident photon flux Φ_0[84]:

$$\sigma^{abs} = \frac{T_{if}}{\Phi_0}. \tag{4.5}$$

Yet, by quantizing the electromagnetic field, and using the electric dipole approximation valid for $\vec{k} \cdot \vec{r} \ll 1$, *i.e.* the electric field is constant over the atomic volume; the X-ray absorption cross section for a transition from the electronic state $|a\rangle$ to electronic state $|b\rangle$ reads[84]:

$$\sigma^{abs} = 4\pi^2 \alpha_f \hbar\omega \left|\langle b|\vec{\epsilon} \cdot \vec{r}|a\rangle\right|^2 \delta\left[\hbar\omega - (E_b - E_a)\right]\rho_f(E_b), \tag{4.6}$$

where $\alpha_f = {e^2}/{4\pi\epsilon_0\hbar c}$ is the dimensionless fine structure constant, $\vec{\epsilon}$ is the unit photon polarization vector, E_a and E_b are the energies corresponding to the electronic states $|a\rangle$ and $|b\rangle$. A different quantity, referred to as the X-ray absorption resonance intensity I_{res}, which corresponds to the photon-energy integral of the cross-section, is expressed as[84]:

$$I_{res} = \mathscr{A} \left|\langle b|\vec{\epsilon} \cdot \vec{r}|a\rangle\right|^2, \tag{4.7}$$

with $\mathscr{A} = 4\pi^2 \alpha_f \hbar\omega$. $|a\rangle$ and $|b\rangle$ are volume normalized to one. From Eq. 4.7, we can see that the relevant terms for X-ray absorption are the transition matrix elements $|\langle b|\vec{\epsilon} \cdot \vec{r}|a\rangle|$ that we will briefly discuss in the following.

4.2.2. Transition matrix elements

For didactic reasons, we will keep the one electron picture, in which the initial state $|a\rangle$ corresponds to the core electron wave function and $|b\rangle$ is given by the valence electron wave function. We neglect here the interactions of the electrons with the core hole in the final state, and we suppose that $|a\rangle$ and $|b\rangle$ are atomic orbitals expressed as:

$$|a\rangle = |R_{n,l}(r); l, m_l, s, m_s\rangle \tag{4.8a}$$
$$|b\rangle = |R_{n',l'}(r); l', m_l', s', m_s'\rangle \tag{4.8b}$$

where $R_{n,l}(r)$ is the radial part of a shell with principal and orbital quantum number n and l, respectively. m_l, s and m_s are the magnetic, spin and secondary spin quantum numbers.

The electric dipole operator can be expressed $P_\alpha^q = \vec{\epsilon} \cdot \vec{r} = \vec{\epsilon_\alpha}^q \cdot \vec{r}$ where $\alpha = x, y, z$ is the direction of the electric field (photon's wave vector) for linearly (circularly) polarized light and $q = 0, \pm 1$ the spin angular momentum of the photon. $q = 0$ refers

to linearly polarized photons while $q = \pm 1$ refers to circularly polarized photons. If one expends the dipole operator into spherical harmonics, we can factorize the $|\langle b|P_\alpha^q|a\rangle|$ matrix elements in the following way (see complete description in Chap. 9 of Ref. 84):

$$\langle b|P_\alpha^q|a\rangle = \underbrace{\delta\left(m_s', m_s\right)}_{\text{spin}} \underbrace{\langle R_{n',l'}\left(r\right)|r|R_{n,l}\left(r\right)\rangle}_{\text{radial}} \underbrace{\sum_{m_l, m_l', p} a_{\alpha,p}^q \left\langle l', m_l'\big|C_p^{(1)}\big|l, m_l\right\rangle}_{\text{angular}}, \qquad (4.9)$$

where $C_m^{(l)}$ are the Racah's spherical tensor operators,[84] and $a_{\alpha,p}^q$ the coefficients to develop the electric dipole operator with Racah's spherical tensor operators ($\sum_p |a_{\alpha,p}^q|^2 = 1$).

From Eq. 4.9, we can see that the electric dipole operator does not act on the spin, and thus only transitions that conserve the spin are allowed. The radial part of Eq. 4.9 determines the strength of the transition. Moreover as the initial state is strongly localized to the core, X-ray absorption spectroscopy is an element-specific method. The angular part of Eq. 4.9 gives non-vanishing element for:

$$\Delta l = l' - l = \pm 1 \qquad (4.10\text{a})$$

$$\Delta m_l = m_l' - m_l = 0, \pm 1 \qquad (4.10\text{b})$$

$$\Delta s = s' - s = 0 \qquad (4.10\text{c})$$

$$\Delta m_s = m_s' - m_s = 0. \qquad (4.10\text{d})$$

Eqs. 4.10 are usually referred to as the dipole selection rules. The conservation of angular momentum implies that $\Delta m_l = 0$ for linearly polarized light while $\Delta m_l = \pm 1$ for circularly polarized light with angular momentum $\pm\hbar$. $\Delta l = \pm 1$ implies that a photon-induced excitation from a p orbital can only occur into a d or s orbital. The dipole selection rules (Eqs. 4.10) can also be expressed in the spin-orbit basis functions $|R_{n,l}(r); l, s, j, m_j\rangle$ that are needed for excitations from the $2p_{3/2}$ and $2p_{1/2}$ states:

$$\Delta l = \pm 1 \qquad (4.11\text{a})$$

$$\Delta j = 0, \pm 1 \qquad (4.11\text{b})$$

$$\Delta m_j = \pm 1, 0 \qquad (4.11\text{c})$$

$$\Delta s = 0. \qquad (4.11\text{d})$$

The value of Δm_j depends on the photon polarization: for circularly (linearly) polarized light $\Delta m_j = \pm 1$ ($\Delta m_j = 0$). For simplicity, the electric-dipole selection rules were derived using a one-electron picture. In reality, to calculate the absorption cross
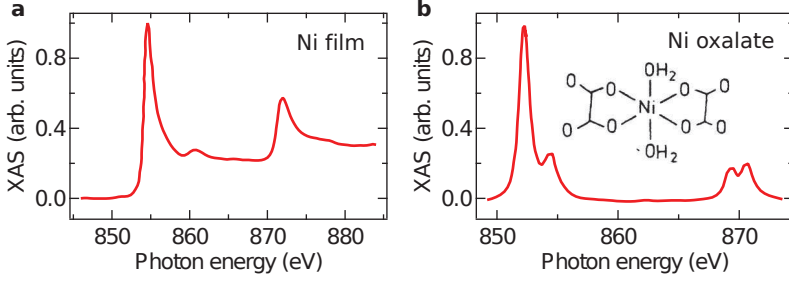
Figure 4.3. – **Multiplet features at the Ni $L_{3,2}$ edges**. XAS spectrum at the Ni $L_{3,2}$ edges for **a**, 13 ML Ni on Cu(100) and **b**, Ni oxalate. The inset show a molecular drawing of the Ni oxalate. The data are taken from Refs. 94 and 90.

section, one should take into account the other electrons in an electronic configuration picture (see Ref. 84). Nevertheless the selection rules are general and independent of the one-electron or the configuration pictures.

In the above calculations, we considered a final state $|b\rangle$ in a one electron picture. This is a good approximation, typically for metallic layers, when the final state is an extended state. In Fig. 4.3a, we represent a XAS spectrum at the Ni $L_{3,2}$ edges for 13 ML of Ni on Cu(100). On the spectrum, we clearly observe two pronounced peaks that correspond to the L_3 and L_2 absorption edges. However the XAS spectrum at the Ni $L_{3,2}$ edges for Ni oxalate exhibits additional pronounced peaks. The splitting of the L_3 and L_2 absorption edges into sub-peaks is referred to as multiplet splitting and mainly arises from the interaction of the excited electron with the core hole.[84, 90–92] The multiplet features depend on the symmetry and the ligand field of the investigated element. By simulating XAS spectrum including multiplet features using programs such that CTM4XAS,[93] it is potentially possible to retrieve information about the ligand field.

In addition, the X-ray absorption may depend on the X-ray photon polarization as suggested by the selection rules. This absorption dichroism, that we will briefly describe, can reveal structural and magnetic properties of the investigated sample.

4.3. X-ray magnetic circular dichroism

XMCD refers to different X-ray absorption spectra for left and right photon helicities due to the alignment of the magnetic moments. Alternatively, for a fixed circular photon helicity, the absorption depends on the magnetic orientation. The technique has been suggested by Erskine and Stern[95] in 1975 and pioneered by Schütz *et al.*[96] in 1987. An example on Fe metal is shown in Fig. 4.4, where the dichroism amplitude is important. We will see that the amplitude of the dichroism is directly proportional to the atomic magnetic moment, but we will first try to understand the origin of
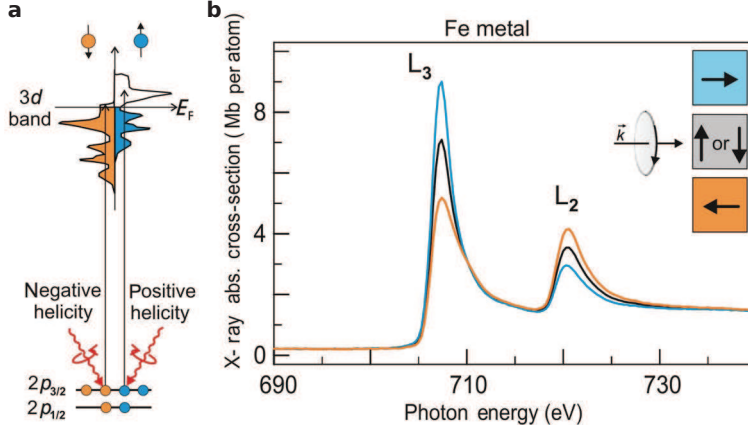
Figure 4.4. – **Illustration of the XMCD effect for Fe at the *L* edges**. **a**, Illustration of the spin-dependent density of states of bulk Fe. **b**, Experimental XAS spectra at the Fe $L_{3,2}$ edges for right photon helicity for two magnetic configurations of the sample. The figure is taken from Ref. 84.

XMCD in a two-step model. For simplicity, the explanations will be limited to the transition-metal elements.

4.3.1. Two-step model

In the first X-ray absorption step, the angular momentum of the incoming photon is transferred to the photoelectron since angular momentum must be conserved (see also section rules in Eqs. 4.10 and 4.11). As the electric-dipole operator does not act directly on the spin, the photon angular momentum should be converted into orbital momentum (see Eqs. 4.10). However, at the $L_{3,2}$ adsorption edges, the photoelectron arises from spin-orbit split $2p_{3/2}$ and $2p_{1/2}$ levels. As a consequence, for a proportion of photons, the angular momentum can be transferred to the electron spin (see Eq. 4.11) that leads to a spin polarization of the photoelectrons for a fixed photon helicity. Moreover, as the $2p_{3/2}$ and $2p_{1/2}$ levels have opposite spin-orbit coupling, the spin polarization of the photoelectrons arising from the $2p_{3/2}$ levels is opposite than that of the photoelectrons from the $2p_{1/2}$ levels. Changing photon helicities or the sample magnetization leads to an opposite spin polarization of the photoelectrons at a given absorption edge.

In the second step, the unoccupied states act as detector for the spin of the photoelectrons. Note that $p \rightarrow d$ transitions dominate by a factor larger than 20 the $p \rightarrow s$ transitions, and we will thus neglect the $p \rightarrow s$ contributions. In addition, we will see that the X-ray absorption is proportional to the number of holes in the d band. For magnetic materials, the unoccupied d states are split by exchange interactions
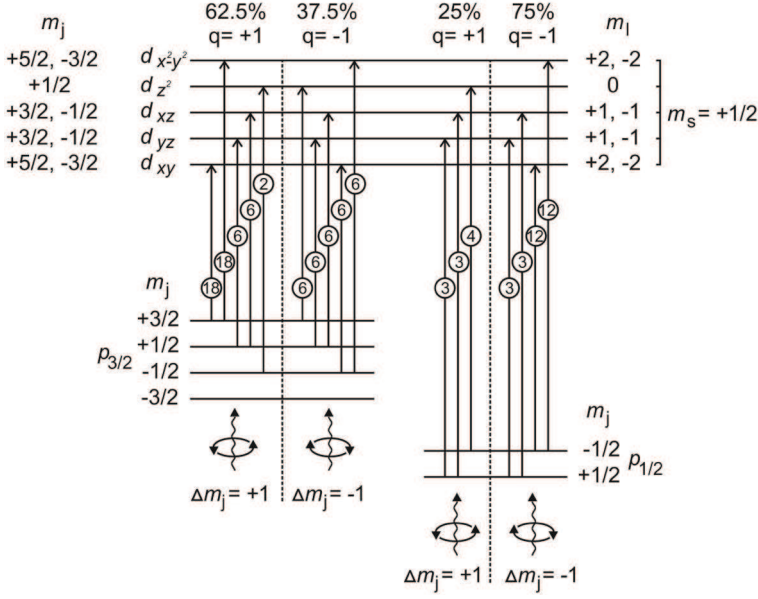
Figure 4.5. – **Polarization-dependent** $p \to d$ **transition probabilities**. The d orbitals are assumed to be split by exchange interactions and we consider that the spin-up (spin-down) sub-band is empty (full). The encircled numbers correspond to the angular part of Eq. 4.9 squared and are expressed in units of $\mathscr{AR}/90$ where $\mathscr{R}$ is the square of the radial part of the transition matrix element. The spin and photon angular momenta have same quantization axis. The figure is taken from Ref. 83.

and have unequal spin up and spin down populations. In turn, the absorption being proportional to the number of holes together with the unequal number of spin-up and spin-down holes explain why the unoccupied d states act a spin detector for the photoelectrons. For an optimal detection, the quantization axis for the angular momentum of the photons must be aligned with that of the spin momentum.

Above, we stated that, thanks to spin-orbit coupling of the $2p$ states, a proportion of spin angular momentum of the photons can be transferred to the electron spin. To be more quantitative about this statement, we go back to a one electron picture and solve the angular part of the matrix elements in Eq. 4.9. For simplicity, we assume that the spin-orbit coupling between the d orbitals is negligible. The results are presented in Fig. 4.5 for transitions from $2p$ states to unoccupied spin-up d states. Note that we only represented transitions with non-vanishing matrix elements, *i.e.* transitions that obey the selection rules. From Fig. 4.5 we observe that at the L_3 edge, X-ray photons with spin $q = 1$ ($q = -1$) give 62.5 % (37.5 %) of spin-up photoelectrons, while at the L_2 edge, X-ray photons with spin $q = 1$ ($q = -1$) give 25 % (75 %) of spin-up photoelectrons. For a completely filled (unoccupied) spin-down (spin-up) sub-band, the origin of the dichroism is straightforward: the L_3 (L_2) edge will have a higher

Figure 4.6. – **Application of the sum rules for a Ni film**. **a**, Helicities-averaged XAS spectrum, or white line, at the Ni $L_{3,2}$ edges (red line). The gray line represents the contribution of the continuum (ionization potential). The dashed black line represents the integration of the XAS spectrum on which the continuum is subtracted. **b**, Corresponding XMCD spectrum (red line) together with its energy integral (dashed black line). The sample is composed of 26 ML of Ni grown on W(110). The acquisition is performed at 30 K with an incidence angle of 20°. The figure is taken from Ref. 83.

absorption intensity for X-ray photons with spin $q = 1$ ($q = -1$). One can also see that the dichroism is of opposite sign at the L_3 and L_2 edges. Yet, for partially filled spin-up and spin-down sub-bands, the XMCD is non zero provided that the spin-up and spin-down populations are unequal. However, the resulting dichroism intensity is reduced. Note that the magnetic moment of the probed element is also reduced. In the next section, we will link the XMCD intensity to the spin and orbital magnetic moments.

4.3.2. Sum rules

In the two-step model, within a one electron picture and by neglecting the spin-orbit coupling, we illustrated that the XMCD intensity is related to the magnetic moment of the probed element. In 1993, Carra *et al.*[97] derived sum rules that quantitatively link the XMCD spectra at the $L_{3,2}$ edges to spin and orbital momenta. In 1995, Chen *et al.*[98] experimentally checked these sum rules and we will briefly discuss them below.

To ease the discussion, we will use the following notation. μ^+ and μ^- denote the X-ray absorption intensity for a given photon energy for positive and negative photon helicities, respectively. The white line is defined as $(\mu^+ + \mu^- + \mu_0)/3$ where μ_0 denotes the X-ray absorption intensity for linearly polarized photons with the electric field parallel to the magnetic field H.[99] For the study of transition-metal elements, which is the case in this thesis, one can simplify the definition and use the helicity-averaged XAS spectrum, defined as $(\mu^+ + \mu^-)/2$ (see Fig. 4.6). The integral of the white line over the L_j edge, is referred to as A_j and is expressed as:

$$A_j = \int_{L_j} \left(\frac{1}{2} \left[\mu^+ + \mu^- \right] - \mu_{continuum} \right) dE, \tag{4.12}$$

for $j = 2, 3$, where $\mu_{continuum}$ is the absorption from p states to states just above the vacuum level. Similarly, the integration of the XMCD intensity over the L_j edge is given by:

$$\Delta A_j = \int_{L_j} \left(\mu^+ - \mu^- \right) dE. \tag{4.13}$$

Note that the photon helicities may have different definitions. By convention, the XMCD is plotted such that XMCD intensity at the L_3 edge is negative for Fe, Co and Ni.

4.3.2.1. Charge sum rules

The charge sum rules link the white line intensity to the number of unoccupied d orbitals, or d holes, provided that the symmetry of the sample is higher than D_{2h}. Note that we are discussing about the number of d holes in the electronic ground state (initial state). The polarization-dependent integration of the white line over the $L_{3,2}$ edges is given by[84, 100]:

$$\left[A_3 + A_2 \right]_\alpha = C \left(N_h + N_Q^\alpha \right), \tag{4.14}$$

where $\alpha = x, y, z$ and $C = {}^2\mathscr{A}\mathscr{R}^2/15$ for $p \to d$ transitions.[84] N_h is the number of holes in the d band and N_Q^α is a quadrupole term that account for the anisotropy of charge density within the $3d$ shell and has a disappearing trace. Thus, if we average the white-line integral over three orthogonal directions, one obtain:

$$\frac{1}{3} \sum_\alpha \left[A_3 + A_2 \right] = C N_h. \tag{4.15}$$

Eq. 4.15 is also valid for a single measurement at the magic angle, *i.e.* an angle of 54.7° between the z axis and the photon-incidence vector.[100]

4.3.2.2. Spin sum rules

The spin sum rules link the XMCD integral over the $L_{3,2}$ edges to the magnetic spin moment m_{spin} and to the angle dependent intra-atomic dipole moment m_D^α that reflects the anisotropy of the spin density[84, 100]:

$$[\Delta A_3 - 2\Delta A_2]_\alpha = -\frac{C}{\mu_B}\left(m_{spin} + m_D^\alpha\right),\tag{4.16}$$

provided that the sample is magnetically saturated and for a symmetry of the sample higher than D_{2h}, where μ_B is the Bohr magnetron. Again, Eq. 4.16 can be considerably simplified by summing it over three orthogonal directions:

$$\frac{1}{3}\sum_\alpha [\Delta A_3 - 2\Delta A_2]_\alpha = -\frac{C}{\mu_B}m_{spin}.\tag{4.17}$$

Here also, by measuring at an incidence angle of 54.7° (between the z axis and the photon-incidence vector), a single measurement suffices.

4.3.2.3. Orbital sum rule

This last sum rule allows to link the orbital moment m_{orb}^α along the external magnetic-field direction α, provided that the sample is magnetically saturated[84, 100]:

$$[\Delta A_3 + \Delta A_2]_\alpha = -\frac{3C}{2\mu_B}m_{orb}^\alpha.\tag{4.18}$$

The angle-averaged magnetic moment m_{orb} may be determined by a single measurement at the magic angle previously defined.

4.3.2.4. Experimental determination of the spin and orbital moments

Experimentally, to extract the spin and orbital magnetic moments, the sample is positioned at the magic angle. The constant C is experimentally determined by using the charge sum rules (Eq. 4.15). This lead to the following equations for the spin and orbital moments:

$$m_s = -\frac{N_h \mu_B}{P_{circ}\cos(\theta)}\frac{\Delta A_3 - 2\Delta A_2}{A_3 + A_2}\tag{4.19a}$$

$$m_o = -\frac{2}{3}\frac{N_h \mu_B}{P_{circ}\cos(\theta)}\frac{\Delta A_3 + \Delta A_2}{A_3 + A_2},\tag{4.19b}$$

where P_{circ} denotes the degree of circular photon polarization (can be close to 100% when using undulators to generate the X-rays) and θ is the angle between the direction of the magnetic moments and the photon-incidence vector. In the following, using the data of Chen *et al.*,[98] we will apply the sum rules on *bcc* Fe. Note that the data extraction procedure is not perfect, and thus the magnetic quantities will slightly differ from that of Chen *et al.*[98] From Fig. 4.7, we can retrieve all the necessary information for Eqs. 4.19, except for the number of d holes in Fe that is taken equal to 3.39 from DFT-based calculations.[98] This leads to $m_s^{Fe} = 1.99\,\mu_{\mathrm{B}}$ and $m_o^{Fe} = 0.05\,\mu_{\mathrm{B}}$, that is very close to the values obtained by a different technique or calculations that range between $2.08\,\mu_{\mathrm{B}}$ and $2.20\,\mu_{\mathrm{B}}$ for the spin moment and between $0.04\,\mu_{\mathrm{B}}$ and $0.09\,\mu_{\mathrm{B}}$ for the orbital moment.[98] This example of application of the sum rules on *bcc* Fe show the great potential of the technique.

Note that in general, we acquire a set of at least 4 different spectra, *i.e.* a spectrum for each photon polarization and for each magnetization direction of the sample. This helps to remove eventual experimental artifacts. Note that the extraction of the spin moment is not possible for some elements, such as manganese, as the splitting of the $2p$ levels is not sufficient to correctly separate ΔA_3 and ΔA_2.
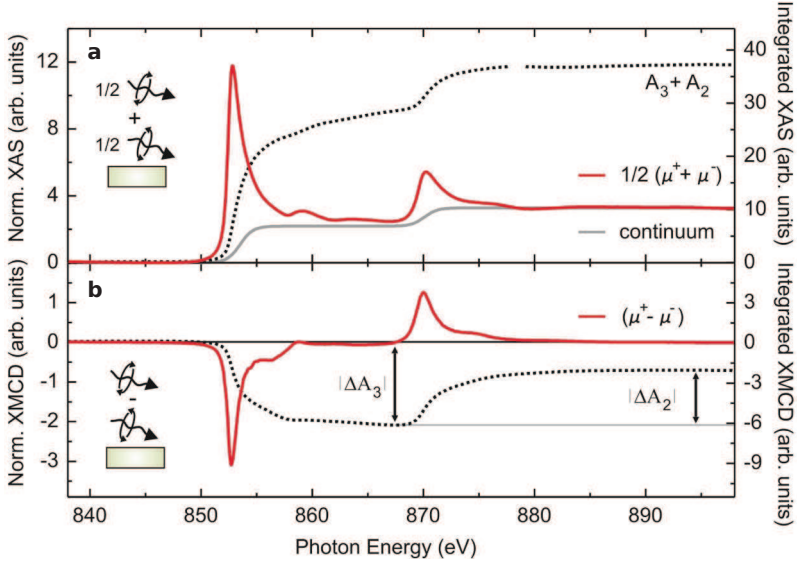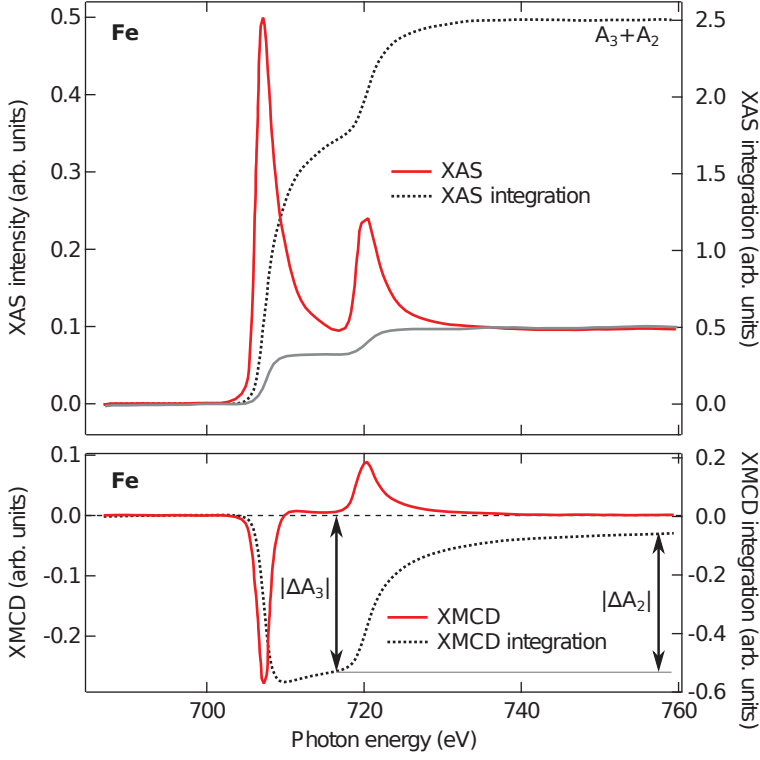
Figure 4.7. – **Application of the sum rules for a Fe thin film**. **a**, Helicities-averaged XAS spectrum at the Fe $L_{3,2}$ edges (red line) together with a two-step like function to remove contributions from the continuum (solid gray line). The integration of the XAS spectrum from which the continuum contributions are subtracted is also plotted (dashed black line). **b**, XMCD intensity (red line) together with the XMCD integration (dashed black line). Note that the shown XMCD data are corrected from the non perfect polarization of the photons (P_{circ}) and from the angle θ between the photon-incidence and magnetization directions. The data are taken from Ref. 98.

5

Scanning tunneling microscopy and spectroscopy

Scanning tunneling microscopy (STM) is a tool with an extremely high spatial resolution that mainly arises from the exponential dependence of the current on the tip-sample distance. In this chapter, after introducing the concept of STM, we briefly present two tunneling models that help to explain the signification of the measured tunneling currents. Scanning tunneling microscopes are not only imaging tools: we will see that it can be used for spectroscopy purposes. From the voltage derivative of the tunneling current, we can probe the density of states (DOS) of the sample as well as inelastic processes.

5.1. History and concept

The first scanning probe instrument dates back to 1972, when Young *et al.* designed a field-emission based "topografiner".[101] They applied a bias voltage of several volts between the tip and the investigated sample, and monitored a distance-dependent field-emission current. A feedback loop could maintain a constant field-emission current and thus a constant tip-sample distance. Although, the resolution of the instrument was limited, Young *et al.* proposed a real-space technique that, at the time of the discovery, was fundamentally different from the dominating diffraction techniques. In 1981, Binnig and Rohrer developed the first scanning tunneling microscope allowing unprecedented atomic resolution.[102, 103] Noways STM is widely used for surface-science studies.

The working principle is relatively simple (see Fig. 5.1). A bias voltage is applied between a very sharp metallic tip (ideally with only one atom at the apex) and the investigated surface. When the tip is brought close enough to the surface, a tunneling current, exponentially dependent on the vacuum-barrier thickness, flows between the tip and the sample. Typically, the tunneling currents range from $10\,\mathrm{pA}$ to $10\,\mathrm{nA}$ for
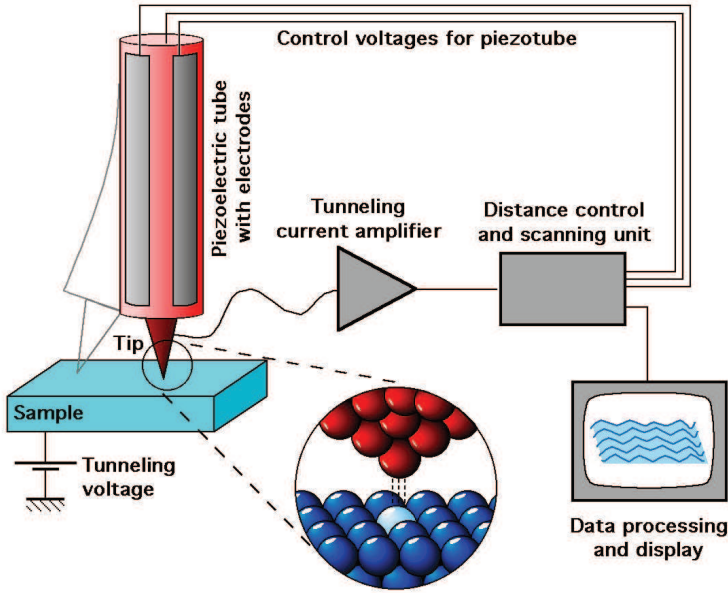
Figure 5.1. – **Schematic view of the STM working principle**. See text for description. Figure: Michael Schmid, TU Wien.

a tip-sample distance of a few angstroms and a bias voltage about $1\,\mathrm{V}$. Since the conducting tip is mounted on a piezoelectric scanner tube, it can be precisely moved in the three space directions by applying suitable voltages on the piezoelectric tube. The STM software samples the area we want to investigate into raster points. A STM topography can then be acquired using one of the two following modes.

- In the constant-height mode, the tip is scanning the surface and the tunneling current is measured at each raster point. Any protrusion (depletion) of the surface would then be revealed by an increase (decrease) of the tunneling current. The STM software then reconstructs the STM topography from the raster points.

- In the constant-current mode, the feedback loop maintains the tunneling current constant by regulating the voltage applied to the piezoelectric tube, and thus by regulating the tip-sample distance. When the tip is scanning the surface, the tip z position is recorded for each raster point, leading to the STM topography.

The constant-current mode allows to scan over protrusions while in constant-height mode, the tip may crash into it. Note that in constant-current mode, the tip can also possibly crash into protrusions for small feedback-loop gains. All the STM topographies presented in this thesis were acquired using the constant-current mode.

5.2. Theory of tunneling

Experimentally, the exact geometrical arrangement of the tip is not reproducible in a controlled way. It is therefore difficult to develop a reliable and general model that links the tunneling current to the STM topographies. Nevertheless, there are different approximate models that tentatively try to associate the tunneling current to the tip-sample distance and to the tip/sample electronic properties. In the following, we will briefly discuss a rather simple approximation, where we consider the tunneling through a one-dimensional square barrier, followed by the more advanced Bardeen approach.

5.2.1. One-dimension square barrier

Tunneling is of purely quantum-mechanical nature. Electrons are thus described by wave functions $\Psi(\vec{r})$ and the probability density of an electron to be located at $\vec{r}$ is obtained by squaring its wave-function value $\Psi^2(\vec{r})$. In the stationary regime, the wave function obeys the time-independent Schrödinger equation[104]:

$$-\frac{\hbar^2}{2m_e}\frac{\partial^2\Psi(\vec{r})}{\partial\vec{r}^2} + U(\vec{r})\Psi(\vec{r}) = E\Psi(\vec{r}), \tag{5.1}$$

where E is the energy of the electron in a potential $U(\vec{r})$, m_e the mass of the electron and $\hbar$ the reduced Planck constant. Tunneling exists because a particle has a certain probability to be located within the barrier and thus to go through it.

One of the simplest tunneling model for STM approximates the vacuum barrier between the tip and the sample by a one-dimension square barrier of height U_0 and thickness d (see Fig. 5.2). The left (right) side of the barrier would represent the tip (sample) with $U = 0$, or *vice versa*. Solving Eq. 5.1 in the left and right sides of the barrier, assuming an electron described by a plane wave of energy $E < U_0$, leads to standing waves with wave number $k = \sqrt{2m_e E}/\hbar$. The solution of Eq. 5.1 within the barrier is an evanescent wave with an inverse decay length $\kappa = \sqrt{2m_e(U_0-E)}/\hbar$. The electron wave functions $\Psi(x)$ and their derivatives $\frac{d\Psi(x)}{dx}$ in the three different regions (left side, barrier and right side) must be continuous at the edges of the barrier. For an electron going from left to right, and for $\kappa d \gg 1$ (thin enough barrier) the transmission probability to cross the barrier reads[104]:

$$T = \frac{16k^2\kappa^2}{\left(k^2+\kappa^2\right)^2}\exp\left(-2\kappa d\right). \tag{5.2}$$

From Eq. 5.2, we see that transmission probability of an electron through a barrier exponentially depend on the barrier thickness d. This simple model explains the exponential dependence of the tunneling current on the tip-sample distance. However, a STM topography does not necessarily represent the topography of a surface. Indeed,
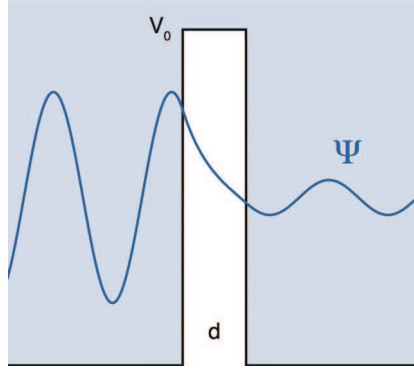
Figure 5.2. – **Tunneling through a one-dimension square barrier**. The square barrier has a height U_0 and a thickness d. The wave function Ψ of an electron arriving from the left side and described by a plane wave has a reduced but finite amplitude at the right side of the barrier. Note that only the real part of the wave function is plotted. The figure is taken from Ref. 105.

a variation of the local conductivity of the sample would lead to a different tunneling current, independently of the tip-sample distance. In the next section, we will describe a more elaborated model that takes into account the density of states (DOS) of the sample.

5.2.2. Bardeen's approach and the s-wave tip

Bardeen's approach[106] is based on the first-order time-dependent perturbation approximation. When the tip is brought close enough to the sample with a finite bias voltage V between the tip and the sample, the potential U in the barrier region becomes different from the potential of the free tip and the free sample. Instead of solving the Schrödinger equation for the whole system, we arbitrarily chose a planar region between the tip and the sample that separates the system into two subsystems. The tip (sample) subsystem has a potential U_T (U_S) different than that of the free tip (sample) system. The total potential U is given by the sum of U_T and U_S and the potentials are defined such that $U_T U_S = 0$ in the entire space. The wave functions of the sample subsystem are given by:

$$\left(-\frac{\hbar^2}{2m_e}\nabla^2 + U_S \right)\Psi_\mu = E_\mu \Psi_\mu \tag{5.3}$$

and the wave functions of the tip subsystem by:

$$\left(-\frac{\hbar^2}{2m_e}\nabla^2 + U_T\right)\chi_\nu = E_\nu\chi_\nu. \tag{5.4}$$

Yet, thanks to the overlap of the orbitals, an electron from a sample state Ψ_μ can transit into a tip state χ_ν, and the corresponding probability is given by the Fermi golden rule:

$$w_{\mu\nu}^{(1)} = \frac{2\pi}{\hbar}|M_{\mu\nu}|^2\delta\left(E_\mu - E_\nu\right). \tag{5.5}$$

$\delta\left(E_\mu - E_\nu\right)$ is the delta function that ensure energy conservation and thus a zero probability for $E_\mu \neq E_\nu$, and $M_{\mu\nu}$ is the matrix transition element that reads:

$$M_{\mu\nu} = \int_{\Omega_T} \chi_\nu^* U_T \Psi_\mu d\tau. \tag{5.6}$$

The orbital-overlap integral is only performed in the volume of the tip subsystem Ω_T as the potential U_T vanishes in the sample's subsystem. Eq. 5.6 can be rewritten as (see detailed calculations in Ref. 107):

$$M_{\mu\nu} = -\frac{\hbar^2}{2m_e}\int_\Sigma \left(\chi_\nu^*\nabla\Psi_\mu - \Psi_\mu^*\nabla\chi_\nu\right)\cdot dS \tag{5.7}$$

where the integration is performed over the subsystem-separation surface Σ.

For an applied voltage V, the tunneling current is obtained by integrating Eq. 5.5 over all the tip and sample states weighted by their occupation probability, and the result is multiplied by $2e$ to account for the charge of each electron and the spin multiplicity:

$$I = \frac{4\pi e}{\hbar}\sum_{\mu,\nu}\left[f\left(E_\mu - eV\right) - f\left(E_\mu\right)\right]|M_{\mu,\nu}|^2\delta\left(E_\mu - eV - E_\nu\right), \tag{5.8}$$

where $f\left(E\right) = \left(1 + \exp\left[\left(E - E_F\right)/k_BT\right]\right)^{-1}$ is the Fermi-Dirac distribution.

Within Bardeen's approach, the matrix elements $M_{\mu,\nu}$, and thus the tunneling current (see Eq. 5.8) depend on electronic and geometric properties of the tip. Tersoff and Hamman[108, 109] made assumptions on the tip geometry and on the symmetry of the wave functions, which allow to have an expression of the current that is mainly dependent on properties of the sample. They assumed the tip to be spherical at its apex with a radius curvature R centered at $\vec{r}_0$. They also made the hypothesis that among the numerous solutions, only the s-wave solutions are important. Under these assumptions and in the limit of low applied voltages and low temperatures, the tunneling current reads[109]:

$$I = 32\pi^3 \hbar^{-1} e^2 V \phi^2 \rho_T\left(E_F\right) R^2 \kappa^{-4} \exp\left(2\kappa R\right) \rho_S\left(\vec{r_0}, E_F\right). \tag{5.9}$$

The work function of the tip ϕ is supposed equal to that of the sample. E_F is the Fermi energy, $\kappa = \sqrt{2m_e\phi}/\hbar$ the inverse decay length, $\rho_T\left(E_F\right)$ the DOS of the tip at the Fermi energy and $\rho_S\left(\vec{r_0}, E_F\right)$ the local density of states (LDOS) of the sample at the Fermi level and at the position $\vec{r_0}$. From Eq. 5.9, we can see that, within this model, a constant-current STM topography correspond to the Fermi LDOS contour of the sample surface.

For larger sample voltage, the energy dependence of the sample and tip DOS have to be accounted, and the tunneling current is expressed as:

$$I = 32\pi^3 \hbar^{-1} e^2 \phi^2 R^2 \kappa^{-4} \exp\left(2\kappa R\right) \int_0^{eV} \rho_T\left(E_F - eV + \epsilon\right) \rho_S\left(\vec{r_0}, E_F + \epsilon\right) d\epsilon. \tag{5.10}$$

Bardeen's approach combined with Tersoff and Hamman s-wave tip model greatly helps to interpret the STM topographies. However, while this model was validated by numerical calculations, *e.g.* on Au(110), the model cannot explain the atomic resolution observed on some surfaces.[107] Indeed, the corrugation of the LDOS can be lower than the z precision of the STM. For a complete picture, the p or d orbitals should also be included. Moreover tip-sample interactions may also play a crucial role.

5.2.3. Semiclassical Wentzel, Kramers and Brillouin approximation

The derivation of the tunneling current using Bardeen's approach combined with Tersoff and Hamman s-wave tip model introduce a quantity $\rho_S\left(\vec{r_0}, E_F\right)$, the LDOS of the sample at the Fermi level and at the position $\vec{r_0}$. The distance dependence of the tunneling current is included in the LDOS ($\vec{r_0}$ is the position of the tip) but the expression is not convenient for the analysis of the electronic properties, *i.e.* the sample DOS. Moreover, it is assumed that only the s waves contribute to the current. The drawbacks of this model comes from the complicated form of the quantum matrix transition elements $M_{\mu\nu}$. In a semiclassical model, the latter is replaced by an effective tunneling transmission probability[110,111] $T(S, V, E)$ that depends on the tip-sample distance S, the applied voltage V and the energy E. A low temperatures ($k_B T \ll eV$) and considering only the electrons without momentum parallel to the surface, the density of tunneling current between two planar electrodes reads[110]:

$$J(S, V) = \frac{2\pi e}{\hbar} \left(\frac{\hbar^2}{2m}\right)^2 \int_0^{eV} T(S, V, E) \rho_S(E) \rho_T(E - eV) dE. \tag{5.11}$$

Note that $\rho_S(0)$ $(\rho_T(0))$ is the density of states of the sample (tip) at the Fermi edge. The tunneling transmission probability T for a trapezoidal tunnel barrier can be estimated in the one-dimensional semiclassical Wentzel, Kramers and Brillouin (WKB) approximation as[110]:

$$T(S,V,E) = \exp\left\{-2S\left[\frac{2m_e}{\hbar^2}\left(\bar{\phi} + \frac{eV}{2} - E\right)\right]^{1/2}\right\}, \qquad (5.12)$$

where $\bar{\phi} = (\phi_t + \phi_s)/2$ the average of the tip and the sample work functions.

5.3. Scanning tunneling spectroscopy

Scanning tunneling microscopes are not only capable of imaging samples surfaces but can also be used as spectroscopic tools. We usually assume that the tip has a flat energy-independent DOS. Thus, using the WKS approximation, first derivative of the tunneling current with respect to the applied voltage reads[110, 112]:

$$\frac{dI}{dV}(S,V) \propto e\rho_S(eV)T(S,V,eV) + \int_0^{eV} \frac{\partial T(S,V,E)}{\partial V}\rho_S(E)dE. \qquad (5.13)$$

The second term in Eq. 5.13 is usually neglected despite it can become important for large voltages.[112] In practice, if the tunneling background becomes important, the dI/dV spectrum is generally "normalized"[113] (for instance by dividing by the conductance), leading to a spectrum monitoring the variation of the sample DOS $\rho_S(eV)$. For molecular measurements, when the sample voltage allows for resonant tunneling into a molecular electronic level, a peak appears in the dI/dV spectrum. In turn, this is used to determine the energy of the highest-occupied molecular orbital and the lowest-unoccupied molecular orbital of a molecule adsorbed on a surface.

Scanning tunneling spectroscopy (STS) is usually performed by positioning the tip over the area of interest. The feedback loop is then turned off, and the sample voltage is swept. In order to increase the signal-to-noise ratio, the first and second current derivatives with respect to the sample voltage are usually acquired using a lock-in amplifier instead of numerical derivations. The sample voltage is modulated by a small sinusoidal voltage V_{LI} at a frequency ω. The amplitude of the resulting current at the same frequency ω is proportional to dI/dV. Note that the modulation voltage, in addition to Fermi-Dirac distribution at a given temperature, lead to a broadening of the spectroscopic features. The experimentally measured full with at half maximum (fwhm) of a spectroscopic peak is[42]:

$$\Delta_{\exp} = \sqrt{\Delta^2 + \Delta_T^2 + \Delta_{LI}^2} \qquad (5.14)$$

where Δ is the intrinsic fwhm of the spectroscopic feature, Δ_T and Δ_{LI} are the fwhm of the thermal broadening function and of the instrumental function, respectively. The broadening can be estimated using the following relations: $\Delta_{LI} = 1.73 eV_{LI}$ and $\Delta_T = 3.5 k_B T$ ($\Delta_T = 5.4 k_B T$ in the case of inelastic processes[42]).

5.4. Inelastic electron tunneling spectroscopy

In the previous part, we briefly introduced the ability of a scanning tunneling microscope to image surfaces and to reveal the local density of states of a sample. For inelastic electron tunneling spectroscopy (IETS), the electron are not only passively probing the sample, but are also inducing excitation processes within the sample. IETS has notably been used to probe vibration of individual molecules,[114] magnetic excitations of individual atoms or clusters,[79, 115–118] magnons[119, 120] and even phonons in superconducting metals.[105]

The principle of IETS is schematized in Fig. 5.3. An electron with an energy higher than that of the inelastic process ($E > E_{ie}$), can either tunnel directly from the tip to the sample, or transfer part of its energy for the inelastic process (see description of Fig. 5.3). Generally IETS are detected in the $dI/dV(V)$ curves where the opening of an inelastic channel leads to kinks for voltages $|V| = |E_{ie}/e|$; or in the $d^2I/dV^2(V)$ curves where the inelastic process is revealed by the presence of a pair of dip and peak for voltages $|V| = |E_{ie}/e|$. Note that Monturet and Lorente[121] showed that the elastic channel can also be importantly affected by the inelastic processes in the strong coupling regime.
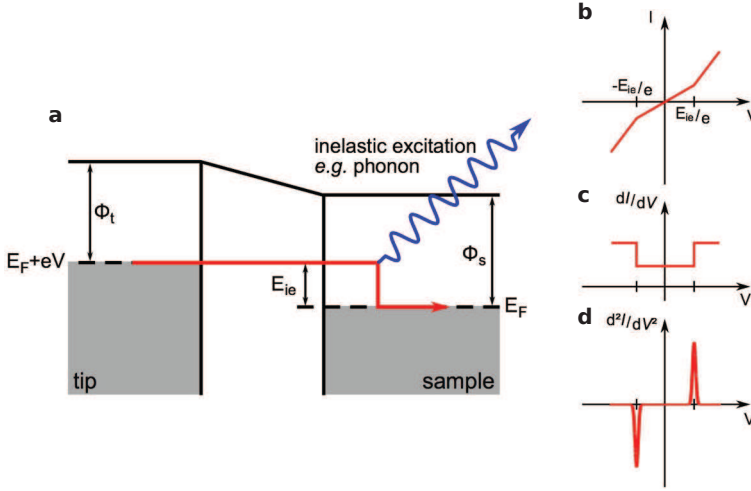
Figure 5.3. – **Principle of inelastic electron tunneling spectroscopy**.
a, Energy diagram of the tip and the sample illustrating an inelastic
excitation. When an electron has a sufficient energy to induce an inelastic
process ($E > E_{ie}$), the electron can either tunnel elastically from the tip
to the sample, or transfer part of its energy to occupy a energetically
lower unoccupied state. **b**, In a $I(V)$ curve, the opening of an inelastic
conduction channel is translated into a change in the slope for $|V| > |E_{ie}/e|$.
Inelastic excitation can be better detected in the **c**, $dI/dV(V)$ curve where
it appears as a kink and in the **d**, $d^2I/dV^2(V)$ as a pair of dip and peak.
The figure is taken from Ref. 122.

6
Methods and experimental setups

The surface and interface studies that we will describe in the next chapters required very high quality and contamination-free samples. Below, we will briefly introduce the methods we used to prepare the samples in ultra-high vacuum (UHV) conditions, followed by a brief description of the STM setups that were used to carry out this work. Finally, we will briefly describe the dichroism experimental installation for magneto-optical spectroscopy (DEIMOS) end station that was used for X-ray absorption spectroscopy (XAS) and X-ray magnetic circular dichroism (XMCD) studies.

6.1. Sample preparation

6.1.1. Ultra-high vacuum environment

The work presented in this thesis is devoted to studies on surfaces and interfaces. In order to have meaningful results, the preparation and the measurements of the samples were carried out in UHV environment at pressures about 10^{-10} mbar. Indeed, a brief exposure to air during only a few microseconds would lead to the sample surface covered with one monolayer of adsorbates.[105, 123]

To achieve these vacuum levels, we use a standard two-stage system: a primary pump reduces the pressure down to 1×10^{-2}–1×10^{-3} mbar, and turbo-molecular pumps further reduce the pressure. After each exposure to air, an out gassing of the stainless-steel chambers is necessary by baking it out to temperatures between 150 °C and 250 °C.

Once the UHV regime is achieved, we generally use an ion pump that suffices to maintain the vacuum level. During the STM and XAS measurements, the ion pump alone is used to maintain UHV conditions. In contrast to turbo-molecular pumps, ion pumps have the advantage to be motorless and thus do not induce mechanical noise.

In addition, the high magnetic fields that can be applied during the measurements is not prohibited for the ion pumps. Finally, we also use sublimation of titanium to the inner part of the chamber walls, what helps to temporarily further decrease the pressure.

6.1.2. Substrate preparation

In order to prepare contamination-free surfaces, we use a standard procedure to clean the substrates. First, the surface is bombarded by Ar^+ ions with a kinetic energy higher than $1\,keV$ for approximately one hour to remove the topmost layers. The substrate is then annealed to heal the bombardment-induced defects by mobilizing the surface atoms. The annealing temperature depends on the crystal to be cleaned. In the work presented in this thesis, we used Cu(100), Cu(111) and Au(111) substrates that we annealed between $450\,°C$ and $600\,°C$.

6.1.3. Metal and molecule sublimation

In this work, we deposited different metals (Co, Cu) and different molecules (manganese phthalocyanine (MnPc) and $Fe(phen)_2(NCS)_2$ (Fe-phen)) by molecular beam epitaxy on clean surfaces. For Co sublimation, we used a pure Co rod (99.99 %) that is heated by electron bombardment using an evaporation source similar to that described in Ref. 124. At the aperture of the evaporator, we measured a current, referred to as the flux, which is proportional to the sublimed partially-ionized Co. Typical parameters are $I_{em} = 12\,mA$, $HV = 900\,V$ and $I_{flux} = 40\,nA$, that leads to a sublimation rate about $0.17\,ML\,min^{-1}$ (see Tab. 6.1).

Material	Sublimation temperature	Typical sublimation rate
Co		$0.17\,ML\,min^{-1}$
Cu	$1080\,°C$	$0.22\,ML\,min^{-1}$
MnPc	$420\,°C$	$0.10\,ML\,min^{-1}$
Fe-phen	$170\,°C$ to $180\,°C$	$0.11\,ML\,min^{-1}$

Table 6.1. – **Sublimation parameters for the different sublimed materials**.

For Cu, MnPc and Fe-phen sublimation, we used Knudsen cells. The material we want to sublime is placed into a crucible that is surrounded by a filament. By injecting a current through the filament, the temperature of the crucible was increased up to the sublimation temperature (see Tab. 6.1). Note that we generally out gased the material we want to sublime. For MnPc and Fe-phen, the out-gassing time ranged from $24\,h$ to $72\,h$.

6.1.4. Tip preparation

The tip used for the STM measurements were electrochemically etched from a 0.3 mm tungsten wire using NaOH. After insertion in UHV, the tips were treated by several cycles of Ar^+ sputtering and flash-annealing by electron bombardment ($V = 1$ kV and emission currents up to 50 mA). This procedure helps to remove contaminations and oxides and promotes a more stable configuration of the tip apex.

6.2. Scanning tunneling microscope

The STM work on spin-crossover complexes (discussed in Part III) was performed using two home-built microscopes at the Physikalisches Institut in the group of W. Wulfhekel (Karlsruhe Institute of Technology): the Joule-Thomson and the 4K STMs. Growth and calibration studies for the work on spinterfaces (discussed in Part II) were realized using two *Omicron* variable-temperature microscopes. One is located at DEIMOS beamline at the source optimisée de lumière d'énergie intermédiaire du Lure (SOLEIL) synchrotron while the other one is located at institut de physique et chimie des matériaux de Strasbourg (IPCMS) in Strasbourg (group of E. Beaurepaire). Victor Da Costa and myself performed all the necessary preliminary tests on the *Omicron* STM located at IPCMS. Furthermore, with the help of Bernard Muller, Jacek Arabski, Arnaud Boulard and Eric Beaurepaire, we developed a complete fully-equipped preparation chamber connected to the STM chamber. In the following, I present generalities about STM and a brief description of the microscopes I used.

6.2.1. Generalities

From the underlying principles of scanning tunneling microscopy (see Chap. 5), we can expect to be sensitive to tip-sample-distance variations below the picometer range. The prerequisites for this very high sensitivity are the stabilization of the tip-sample distance against mechanical vibrations and the possibility to measure very low currents (picoampere range).

The mechanical stabilization is realized by a multi-stage damping system. Firstly, pneumatic insulators with laminar-flow damping suppress by more than one order of magnitude the external vertical and horizontal mechanical noise (for frequencies higher than 10 Hz). Secondly, the STM stage that is constructed to be very rigid in order to shift the resonant frequencies towards higher frequencies, hangs freely from springs. With these mechanical-noise filters, it is possible to reduce the mechanical vibrations down to a few picometers or lower.

Besides lowering the mechanical noise, one also needs to be able to control the positioning of the STM tip with sub-angstrom precision above the surface. This is accomplished by using a piezoelectric scanner tube that can be precisely moved laterally and vertically by using an adapted electronic controller. I used *Nanonis*

STM controller for the experiments done using low-temperature STM, and *Matrix* for the others. The electronics were operated via their corresponding computer programs and allowed us to acquire topographic images and to perform tunneling spectroscopy measurements. In addition to the piezoelectric scanner tube, the STMs have also slip-stick piezoelectric motors for coarse motion (sub-micron to millimeter range). Those motors are useful to approach the tip towards the surface when a sample is inserted, and for changing the probed area on a given sample.

For STM measurements, we used small tunneling currents that typically ranges from $10\,\mathrm{pA}$ to $10\,\mathrm{nA}$. In order to conveniently measure such small currents and to carry the signal to the corresponding electronics, we used a current-to-voltage converter placed as close as possible to the STM. We generally use a gain between $10^8\,\mathrm{V\,A^{-1}}$ and $10^{10}\,\mathrm{V\,A^{-1}}$. Note that the current-to-voltage converter acts as a low-pass filter, and the cutoff frequency depends on the gain we chose.

6.2.2. Joule-Thomson STM

A full description of the home-built Joule-Thomson STM used in this work can be found in Refs. 125, 126 (see Fig. 6.1). A temperature of $4.2\,\mathrm{K}$ is reached using a liquid-helium bath cryostat that is surrounded by a nitrogen tank allowing liquid-helium standing time exceeding one week. Temperatures below $800\,\mathrm{mK}$ can be reached using the Joule-Thomson stage with a mixture of $^4\mathrm{He}$ and $^3\mathrm{He}$ (see Fig. 6.1). A superconducting coil allowed to apply $1\,\mathrm{T}$ magnetic field normal to the sample surface. A new design of the coil now allows to reach magnetic fields up to $3\,\mathrm{T}$.[105]

The STM chamber is connected to a fully equipped preparation chamber that allows to clean crystals, deposit metals and molecules on surfaces, perform Auger electron spectroscopy (AES) and low energy electron diffraction (LEED) measurements to characterize the surfaces.

In this thesis, all the experiments with this Joule-Thomson STM were performed at $4.2\,\mathrm{K}$.

6.2.3. 4K STM

In Fig. 6.2, I show a schematic of the 4K-STM setup that is described in Refs. 122, 127, 128. The STM chamber is connected to a load lock to introduce new samples or tips from the air, and a preparation chamber. The base temperature of the STM stage is $4.2\,\mathrm{K}$ cooled by a liquid-helium bath cryostat positioned directly on top of the STM stage. Here also, the He cryostat is surrounded by a liquid-nitrogen tank to offer liquid-helium standing times about $72\,\mathrm{h}$.

The associated preparation chamber offers substrate-cleaning, metal- and molecule-deposition facilities. The surface preparation can be checked by AES, LEED and magneto-optical Kerr effect.
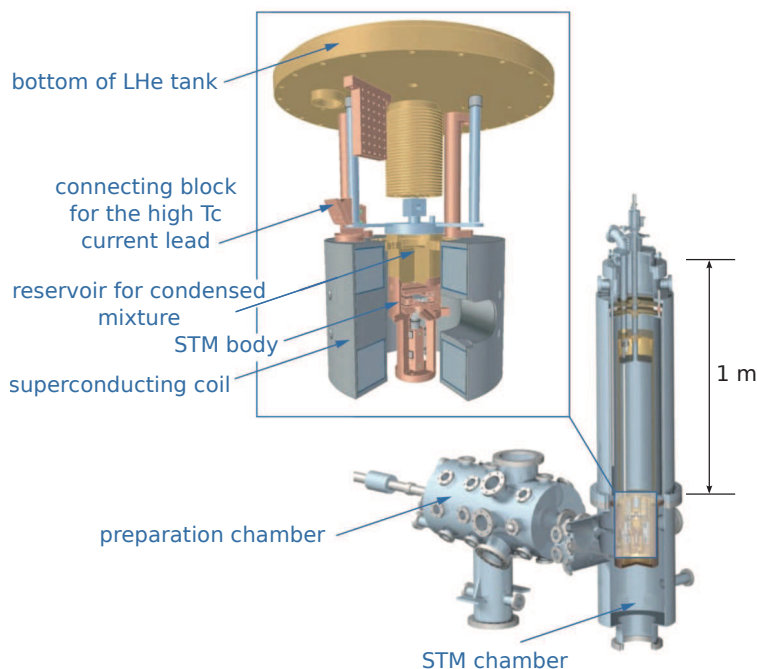
Figure 6.1. – **Technical drawing of the Joule-Thomson STM**. View of
the STM and preparation chambers. The inset magnifies the reservoir for
the condensed mixture on top of the STM stage. Note that the investi-
gated surfaces are facing downwards. The figure is taken from Ref. 105
and a full description can be found in Ref. 125.

6.2.4. Variable-temperature scanning probe microscopes

The variable-temperature scanning probe microscope (SPM) is a commercial micro-
scope commercialized by *Omicron*. In addition to STM measurements, the SPM lo-
cated at IPCMS allows to perform atomic force microscopy (AFM) studies in contact,
non-contact[129] and Q+ modes,[130, 131] as well as Kelvin probe force microscopy.[132, 133]
Using a helium flow and a heater at the back of the sample, the sample temperature
can range from 30 K to 350 K. However, as the tip is maintained at room temperature,
low-temperatures measurements limit the diffusion of adsorbates on surfaces but do
not increase the energy resolution.

A fully equipped preparation chamber is connected to the STM chamber located
at IPCMS (see technical drawing in Fig. 6.3), which has facilities to clean samples;
and to deposit metals and molecules (see home-built sample and tip holders in Fig.
6.4). There are also gas inlets to introduce different gases (*e.g.* oxygen) and a mass
spectrometer to accurately control the partial pressure of the injected gases. The
surfaces can be analyzed by (i) AES and LEED measurements or (ii) magneto-optical
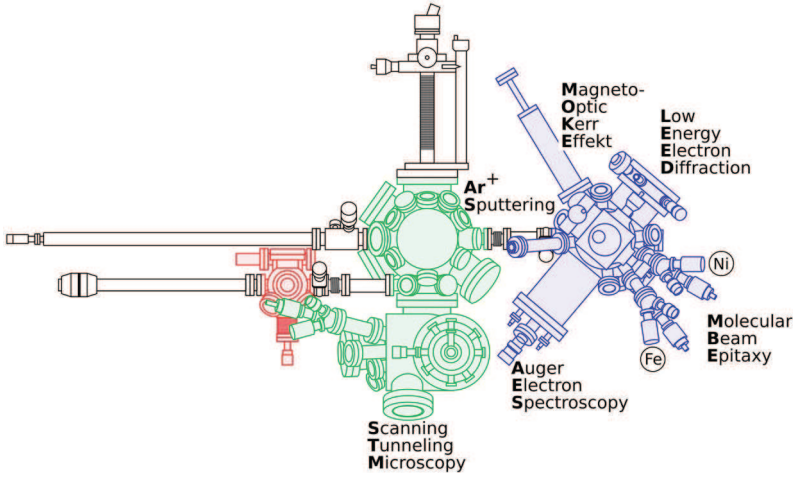
Figure 6.2. – **Top view of the 4K-STM setup**. The experimental setup is composed of three different chamber: the load lock (in red), the STM chamber (in green) and the preparation chamber (in blue). The figure is taken from Ref. 127.

Kerr effect measurements. (i) and (ii) cannot be used simultaneously as they are connected to the same flange.

The variable-temperature SPM located at DEIMOS beamline is also connected to a fully equipped preparation chamber that is described below.

6.3. Setup for X-ray absorption spectroscopy

The XAS measurements discussed in this thesis were realized at DEIMOS beamline at synchrotron SOLEIL. The X-rays are produced by the *HU-52* or the *EMPHU-65* undulators located in the storage ring.[134] The *HU-52* undulator can generate X-rays of all polarizations from 350 eV to 2500 eV. The newly installed *EMPHU-65* undulator was fabricated using electromagnets in addition to permanent magnets, which allows to rapidly switch from left to right circular polarizations (5 Hz repetition rate).[134] Note that the vertical field is produced by electromagnet while the horizontal field is still created by permanent magnets. The ability to flip rapidly from left to right circular polarizations makes the undulator an ideal source for measuring low XMCD and x-ray natural circular dichroism signals.

The X-rays are directed towards the end station using a bunch of optics described in Ref. 134. The end station has two superconducting coils that can provide ±7 T and ±2 T magnetic fields along and perpendicular to the X-ray beam, respectively. A variable-temperature insert can regulate the temperature of the investigated sample between 1.5 K and 370 K. The absorption signal can be measured by transmission,
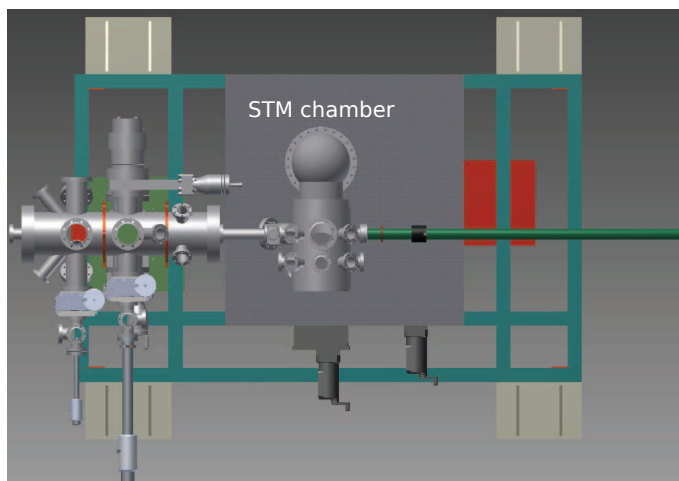
Figure 6.3. – **Top view of the multiprobe setup**. Technical drawing of the variable-temperature SPM together with its preparation chamber.
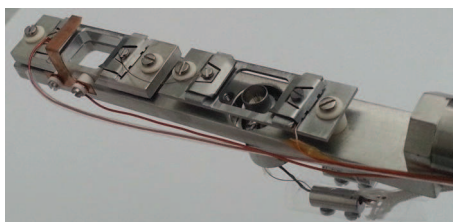
Figure 6.4. – **Photograph of a home-built manipulator**. On the left (right) side, we can observe a slot for tip (sample) holder.

fluorescence yield or total electron yield.[134] For all these modes, the currents are measured with *Novelec* electrometers connected to a counting card *NI-6602* from *National Instrument*. All the absorption spectra discussed in this thesis were acquired using the total electron yield mode. In addition, we used the *TurboScan* mode[135] that allows to faster acquire the XAS spectra.

The end station is connected to a glove-box and to a set of UHV chambers for *in situ* preparation of the samples. There are all facilities to deposit metals and molecules. To characterize the surfaces, the main preparation chamber offers AES and LEED. We also characterized surface and calibrate sublimation using the variable-temperature STM described above.

Part II.

Investigation of the MnPc/Co hybrid spinterface

Introduction to spintronics

Spintronics aims at exploiting the spin degree of freedom of an electron instead of or in addition to its charge[122, 136–142] . The topic emerged in the 80's by the discovery of giant magnetoresistance (GMR) that allows the realization of magnetic-field sensors and the study of a variety of spin-dependent phenomena. In the following we will focus on spin-transport properties that have already proven their potential in electronic technology, *i.e.* giant magnetoresistance and tunneling magnetoresistance. We will then discuss about the emerging field of organic spintronics.

7.1. Giant magnetoresistance

The groups of Albert Fert[143] and Peter Grünberg[144] discovered giant magnetoresistance (GMR) in Fe/Cr superlattices in 1988 and were awarded by the Nobel Prize in 2007. The magnetic Fe layers were AF coupled by interlayer exchange coupling through Cr spacers of variable thicknesses. The resistance of the sample is strongly modified by varying the strength of the in-plane external magnetic field (see Fig. 7.1). For low Cr-spacer thicknesses, the resistance of the sample can be reduced by a factor two by the application of the external magnetic field. Complementary studies revealed that the external magnetic field has the effect to magnetically align the magnetization of the Fe layers that are initially AF coupled. The conductance of the sample thus depends on the relative alignment of the magnetic layers.

Since 1988, the field emerged and it was found that two ferromagnetic electrodes sandwiching a non-magnetic metal suffice to have GMR devices. The ferromagnetic electrodes can have two different configurations depending on their relative magnetic alignment (see Fig. 7.2). As previously said, an external magnetic field can change the relative magnetic alignment of the electrodes. To explain GMR, we consider a
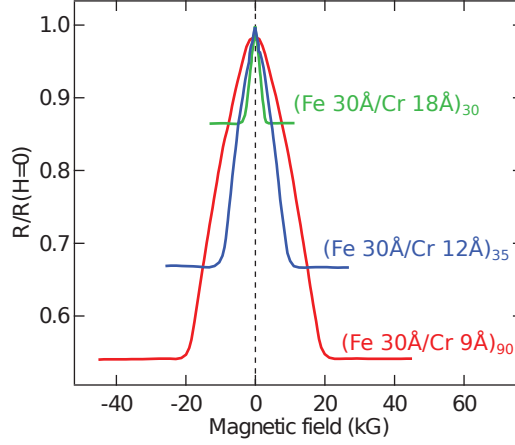
Figure 7.1. – **Giant magnetoresistance in Fe/Cr supperlattices**. Variation of the normalized resistance as a function of the external in-plane magnetic field for three different superlattices at 4.2 K. The data are taken from Ref. 143.

diffusive current without spin-flip scattering and also consider two spin-dependent current channels (two-channel current introduced by Mott).[145–147]

There are two different geometries of the GMR devices referred to as current in plane (CIP) and current perpendicular to plane (CPP). The physical mechanism involved in the two geometries are rather different, and we will briefly introduce them.

Baibich *et al.*[143] (see magnetoresistance results in Fig. 7.1) used CIP devices as they were easier to realize for technological reasons. In Fig. 7.2, we show typical CIP GMR devices in the two different magnetic configurations, together with equivalent electrical circuit of the device. The scattering probability of a conduction electron with a spin σ is roughly proportional to the number of empty states in the σ-spin sub-band at E_F. Hence, the scattering probability of a conduction electron is spin independent within the non-magnetic layer while within a magnetic electrode it depends on the relative orientation of the electron spin with the electrode magnetization (DOS of ferromagnetic electrodes are split by exchange interactions). When the magnetic configuration of the electrodes is parallel (see Fig. 7.2a), electrons from one of the spin channel are less subject to scattering than that of the other channel, and the associated resistance is then lower (see Fig. 7.2b; the lower spin channel has less scattering events and has thus a lower resistance). For an antiparallel magnetic configuration of the electrodes (see Fig. 7.2c), electrons from one spin channel have less scattering events in one electrode while electrons from the other spin channel have less scattering in the other electrode. This lead to the equivalent electric circuit presented in Fig.
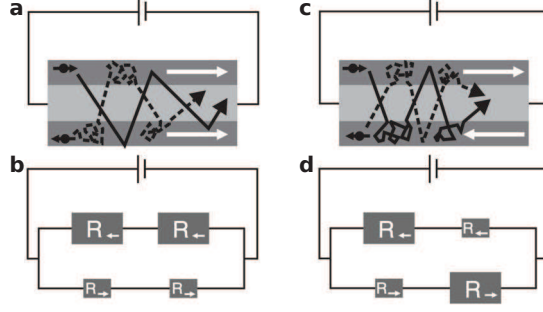
Figure 7.2. – **Schematic of current-in-plane GRM devices**. The GMR device is composed of two ferromagnetic electrodes (dark grey) that sandwich a non-magnetic spacer (light grey). The "trajectory" of two electrons with opposite spin orientation are represented by the solid black and the dashed black lines for **a**, a parralel and **c**, an antiparallel configuration of the magnetic electrodes. **b**, and **d**, represent the equivalent electronic circuit in a two-current model for respectively a parallel and an antiparallel configurations of the magnetic electrodes. The equivalent resistors are sized with the spin-dependent scattering probability of the electrons. The figure is taken from Ref. 148.

7.2d. In the present case, the resistance of the device is lower for a parallel magnetic configuration of the electrodes.[148]

For CPP geometry of the GMR devices, the physical mechanism is rather different. The geometry of the stacking is similar to that of Figs. 7.2a,c, but the voltage bias is applied between the two electrodes. The corresponding current in the first electrode is spin polarized (imbalance between spin-up and spin-down channel currents). When the current goes from one of the electrode to the non-magnetic-metal spacer, there is a spin accumulation at the interface that comes from non-equal spin-dependent DOS at E_F for the two materials (electrode and spacer).[148–150] The spin accumulation decays exponentially away from the interface and may be detected by the second electrode. Indeed, the reflection coefficient for an electron at the second interface depends on its spin σ due to spin-dependent band matching. Thus, the transmission probability is spin dependent at the second interface and depends on the magnetic orientation of the second electrode; the corresponding conductance/resistance varies accordingly.

7.2. Tunneling magnetoresistance

A usual tunneling magnetoresistance (TMR) device is composed of an ultrathin insulating layer sandwiched between two ferromagnetic electrodes. The resistance of such a device depends on the relative magnetic orientations of the electrodes, and the relative difference in resistance defines the TMR ratio:
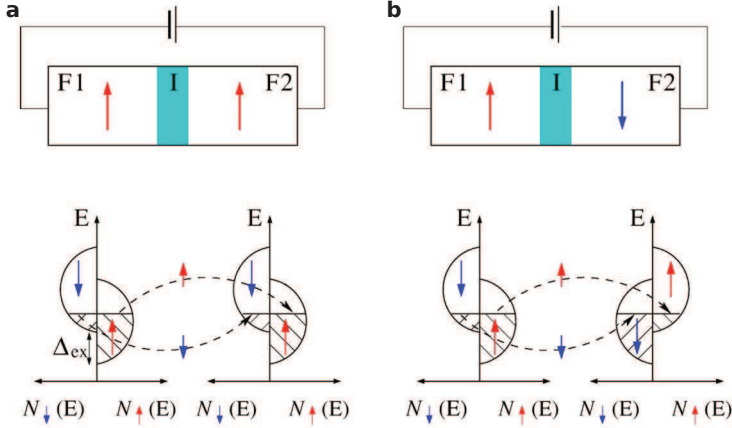
Figure 7.3. – **Schematic illustration of Julliere's model of TMR**. Illustration of electron tunneling in a tunnel junction composed of two ferromagnetic electrodes sandwiching an insulating layer. **a**, Parallel and **b**, antiparallel magnetic configurations of the electrodes with the corresponding spin-polarized DOS of the electrodes. Those DOS are split by Δ_{ex} due to exchange interactions. The figure is taken from Ref. 137.

$$TMR = \frac{R_{AP} - R_P}{min\left(R_{AP}, R_P\right)}. \tag{7.1}$$

The first realization of such a device was realized by Julliere[151] in 1975, which led to magnetoresistance at low temperatures. It is only about twenty years later that Moodera *et al.*[152] and Yaoi *et al.*[153] realized TMR devices working at room temperature with TMR ratios of a few percents (see Eq. 7.1). In 2004, Parkin *et al.*[154] and Yuasa *et al.*[155] considerably increased the TMR ratios by realizing epitaxial Fe/MgO/Fe magnetic tunnel junctions. This considerable increase of the TMR ratios in magnetic tunnel junctions are possible by a symmetry-dependent filtering of the evanescent states within the MgO barrier.[156–158] Nowadays, TMR values can exceed $1000\,\%$.[158, 159]

What is the actual mechanism behind TMR? First we recall that the DOS of the ferromagnetic electrodes are spin dependent due to the exchange interactions. The resulting DOS at the Fermi level E_F for spin-up electrons $N_\uparrow$ is usually different than that of the spin-down electrons $N_\downarrow$ (see Fig. 7.3). In the sketch in Fig. 7.3a that represents the spin-dependent DOS for a parallel magnetic alignment of the electrodes, the majority of the electrons at the Fermi level E_F have a spin up for both electrodes. For an antiparallel magnetic alignment of the electrodes, the first electrode has a majority of spin-up electrons at E_F while the second electrode has a majority of spin-down electrons at E_F (see Fig. 7.3b). Note that the nature of spin carriers at E_F also depends on the material. The transport of an electron from one

electrode to the other occurs via elastic tunneling (without spin flip in the absence of impurities or defects). Thus an electron from the spin-up (spin-down) band in the first electrode can only tunnel into the spin-up (spin-down) band of the second electrode. If one assume that (i) the tunneling transmission probability is the same for all the electrons; and (ii) the tunneling mainly involves the states at E_F, the tunneling rate for a given spin band is given by the product of the DOS at E_F. The conductance of the junction is then proportional to:

$$G \propto N_\uparrow^1 N_\uparrow^2 + N_\downarrow^1 N_\downarrow^2, \tag{7.2}$$

with N_σ^i the spin-σ DOS at E_F for the electrode i, and depends on the relative magnetic alignment of the electrodes. Referring to the DOS plotted in Fig. 7.3, one finds a higher conductance for the parallel magnetic alignment of the electrodes.

In his model, Julliere[3, 148, 151] goes further in the development and links the TMR ratio to the polarization of the electrodes:

$$TMR = \frac{R_{AP} - R_P}{R_{AP}} = \frac{2P_1 P_2}{1 + P_1 P_2}, \tag{7.3}$$

where $R_{AP(P)}$ is the resistance for a perfect antiparallel (parallel) configuration of the magnetic electrodes. The polarization of an electrode depends on the electronic structure of the material and on the experimental technique used to measure the quantity. We may express it as[3, 160, 161]:

$$P = \frac{N_M v_M^n - N_m v_m^n}{N_M v_M^n + N_m v_m^n}, \tag{7.4}$$

where N_σ is the density of states at the Fermi energy (E_F) for spin σ ($\sigma = M$ ($\sigma = m$) for majority (minority) electrons), and v_σ is the Fermi velocity of the electrons that depends on the spin σ. The n that weights the Fermi velocity depends on the device we are looking at. $n = 0$ for photoemission measurements and for tunneling, $n = 1$ for ballistic transport and $n = 2$ for diffusive transport.

For the expression of the TMR ratio (see Eq. 7.3), one should rather use effective electrode polarizations than bulk polarizations. Indeed, De Teresa et al.[162] have studied tunneling junctions with Co and $La_{0.7}Sr_{0.3}MnO_3$ (LSMO) electrodes sandwiching different insulating barriers: $SrTiO_3$, $Ce_{0.69}La_{0.31}O_{1.845}$ and Al_2O_3. From Eq. 7.3, we see that the TMR ratio is positive (negative) for a resistance higher in the anti-parallel (parallel) configuration. De Teresa et al.[162] found that, using the same magnetic electrodes, the TMR is positive with an Al_2O_3 barrier, while it is negative for $SrTiO_3$ and $Ce_{0.69}La_{0.31}O_{1.845}$ barriers. They ascribed these results to bonding effects localized at the electrode-barrier interface. Therefore, one should use an effective polarization P_{eff} that takes into account interface effects.

Above, we stated that the TMR ratio can be drastically improved by symmetry-

dependent filtering. From Eq. 7.3, we can see that the TMR ratio can alternatively be improved by increasing the electrode polarization. The spin polarization is maximum for electrodes that have only one spin carrier at the Fermi energy (see Eq. 7.4), which is the case for half-metals ferromagnets. In 2003, Bowen *et al.*[163] realized magnetic tunnel junctions using half metallic $La_{2/3}Sr_{1/3}MnO_3$ (LSMO) electrodes sandwiching a $SrTiO_3$ tunneling barrier, and measured huge TMR ratio reaching 1800% at $4\,K$.

7.3. Organic spintronics

In the last decades, the fruitful research in organic semiconductors (OSCs) has considerably progressed.[164] Products such as organic light-emitting diodes are commercially available, organic photovoltaic devices have already yields that can compete with the actual technology. In the last decade, OSCs have also interested the spintronics community who are together putting considerable efforts towards efficient and robust room-temperature organic spin valves.[1, 3, 148, 165–167] The increasing interest for spin-based devices with organic materials comes from the very long lifetime of the spin, typically larger than $10\,\mu s$,[1, 168, 169] which is orders of magnitude larger than in usual inorganic materials. Note that Warner *et al.* found an exceptionally long spin lifetime of $49\,ms$ at $5\,K$ in bulk phthalocyanine molecules.[2] These very long spin lifetimes in organic materials can be understood by the weak spin-orbit coupling found in carbon-based materials, since the strength of the spin-orbit interaction is proportional to the atomic number of the element to the power four (Z^4).[1, 148]

In the following, we will overview a few results on organic spin valves. These spin valves are strictly speaking not fully organic devices but rather metal/organic hybrid ones. There are usually composed of an organic active layer sandwiched between two magnetic inorganic electrodes, and are thus hybrid. To the best of my knowledge, there is no full organic spin valve yet, but recent achievements by Yoo *et al.*[170] go towards this direction. They replaced one of the usually inorganic magnetic electrode by an organic one (vanadium(TCNE: tetracyanoethylene)$_2$) and nevertheless observed a few percents of magnetoresistance at $100\,K$.

In 2002, Dediu *et al.*[171] reported the experimental injection in an organic spin-valve device. They designed a lateral device where an organic layer of sexithiophene is connected to two highly polarized manganite oxide (LSMO, $La_{0.7}Sr_{0.3}MnO_3$) electrodes. They observed a strong magnetoresistive response up to room temperature for both OSCs channel lengths of $100\,nm$ and $200\,nm$. However, as the magnetic-field-dependent measurements were limited, it was not straightforward that the observed magnetoresistance signal corresponds to GMR.

An important step forward in organic spintronic is from Xiong *et al.*[172] They used Alq_3 (*tris*(8-hydroxyquinoline)aluminium(III)) molecules, which were already popular in molecular electronics,[173] for the active organic layer in vertical spin valves. The $LSMO/Alq_3$ (100 to 200 nm)$/Co$ spin valve showed GMR with values up to 40% at $11\,K$ (see Figs. 7.4a,b) and the GMR survives up to around $200\,K$. Interestingly,
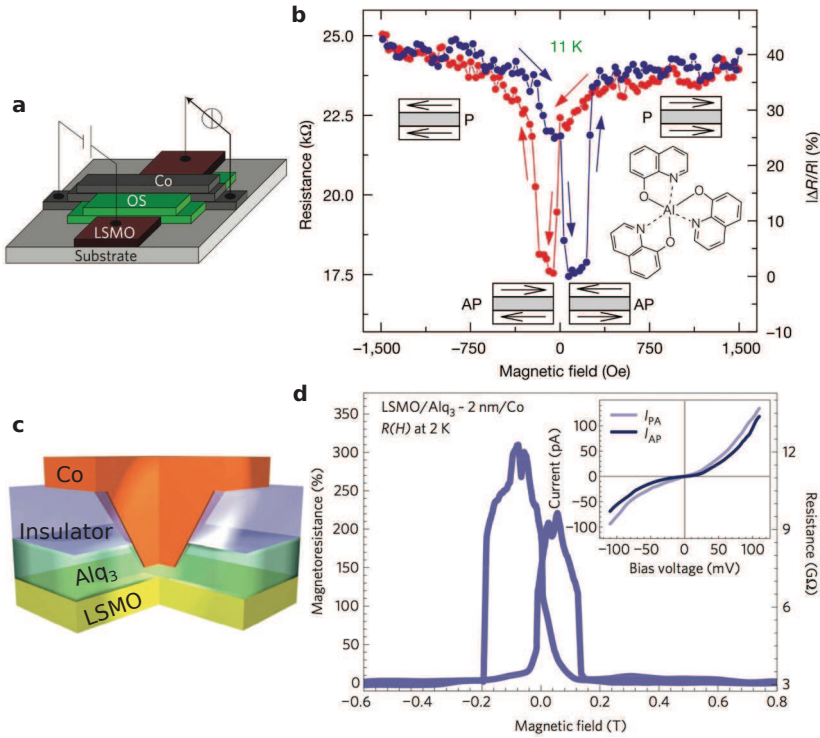
Figure 7.4. – **Magnetoresistance in Alq$_3$-based organic spin valves**.
a, Schematic of a typical vertical organic spin-valve device. The OSC
(here Alq$_3$) is sandwiched between a bottom LSMO and a top Co
electrodes. Magnetoresistance measurements are performed by apply-
ing a bias voltage between the magnetic electrodes and measuring
the current as a function of an external in-plane magnetic field. **b**,
Magnetoresistance loop of a spin-valve device such as presented in **a**
(LSMO(100 nm)/Alq$_3$(130 nm)/Co(3.5 nm)) at 11 K. The lower resistance
is obtained for an antiparallel magnetic alignment of the electrodes and
the device is thus defined as an inverse spin valve. **c**, Schematic of an
organic magnetic tunnel junction obtained by nanoindentation into the
organic layer before deposition of the top Co electrode. **d**, Magnetore-
sistance measurements of an organic magnetic tunnel junction (see **c**;
LSMO/Alq$_3$(2 nm)/Co) at 2 K and with a bias voltage of −5 mV. The
lower resistance is here obtained for a parallel magnetic alignment of the
electrodes, *i.e.* different from the device measured in **b**. The figure is
adapted from Refs. 4, 171, 172.

in contrast to standard spin-valve devices, this organic spin valve showed the lower resistance for an antiparallel configuration of the magnetic electrodes. Other studies from different groups validated this so-called inverse spin valve effect.[174–178] However, Santos *et al.*[179] have demonstrated that Co injects majority spin for the Co/Alq$_3$ interface, and LSMO is widely accepted as a majority injector.[1] Now, if one assume a tunneling transport between the magnetic electrodes with spin polarization P_1 and P_2, one would expect a positive magnetoresistance from the Julliere model (Eq. 7.3), in contradiction with the results in Fig. 7.4a,b. Note that we could still argue that P_1 and P_2 (see Eq. 7.4) are quantities that are not so well defined due to interface effects, and that Eq. 7.3 was demonstrated for tunneling transport across amorphous barriers (in contrast to the diffusive regime here).

Barraud *et al.*[4] realized similar Alq$_3$-based devices. However, the magnetic tunnel junctions are realized by a conductive-tip of an AFM that allows a precise control over the thickness of the Alq$_3$ spacer and allows to have nanometric-size junctions (see Fig. 7.4c). Moreover, they evidenced that the conduction of the electrons between the two magnetic electrodes occurs in the tunneling regime. The magnetoresistance measurements on such a device (see Fig. 7.4d) show huge TMR of about 300 % at 2 K and surprisingly with a positive sign. In order to explain the apparent discrepancy with the previous results, the authors propose the formation of spin-hybridization-induced polarized states arising from (i) a spin-dependent hybridization of the molecular orbitals of the first molecular layer with the electrode; and (ii) the shift of the energetic position of the molecular orbitals relative to the Fermi level by the interfacial dipole fields and image forces[180–186]; and because of the real part of the self-energy induced by the coupling.[4] In turn, they showed that these spin-hybridization-induced polarized states lead to an effective spin polarization of the electrode P^* that can be of opposite sign (compared to the spin polarization of the electrode in the absence of the molecules) provided that the molecule-substrate coupling is strong enough. They also indicated that due to disorder, only a few molecules would be coupled strongly enough to inverse the polarization of the interfacial molecular states. These interfacial states would nevertheless dominate the injection step. Finally, they tentatively explain the discrepancy on the magnetoresistance sign based on the local character of their measurements that do not involve molecules with inverted polarization of the interfacial molecular states in contrast to the measurements on large-area junctions.

Later, Sanvito[187] summarized the findings of Barraud *et al.*[4] in a simplified cartoon where different scenarii for the molecule-substrate interactions are proposed (see Fig. 7.5). In Fig. 7.5a, the molecule is isolated from the electrode and illustration of their respective DOS are represented. For simplicity, only the highest-occupied molecular orbital (HOMO) is considered for the molecule. The magnetic electrode has a spin-dependent DOS split by the exchange interaction, while the HOMO level of the molecule is spin independent. In this particular picture, the HOMO is located below the Fermi energy E_F and the transport through the molecule can thus only be tunnel-like (non resonant) with a spin polarization of the carriers that corresponds to the one of the electrode. When the molecule is closer to the electrode, such as depicted in Fig. 7.5b, the molecule-electrode coupling leads to two effects. (i) the molecular orbitals
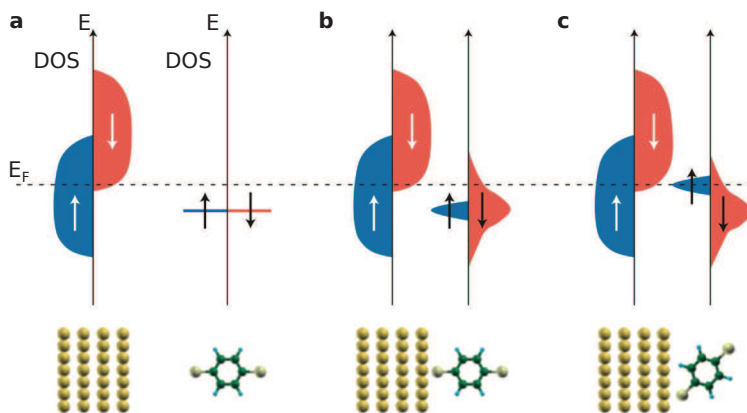
Figure 7.5. – **Schematic of the hybridization of a molecular orbital with a magnetic electrode**. **a**, The molecule (right) is sufficiently separated from the magnetic electrode (left) that they do not interact together. The spin-dependent DOS of the magnetic metal is split by the exchange interaction while the HOMO of the molecule is spin independent. **b**, When the molecule is close enough and interact with the magnetic electrode, the molecular orbitals are broadened with a spin-dependent broadening (see text). In the depicted case, the minority-spin molecular orbital crosses the Fermi edge E_F and the effective spin polarization is reversed compared to the case depicted in **a**. **c**, The interaction of the molecular orbitals with the extended states of the metal maybe also shift the energy position of the former (see text). The resulting spin-polarization sign is opposed to that of the case illustrated in **b**. The figure taken from Ref. 187.

become energetically wider. This is a consequence of the finite lifetime of the electrons in the molecular orbitals, as electrons may go to or come from the electrode. The broadening of a particular molecular orbital depends on how strongly the molecular orbital interacts with the extended electronic states of the electrode. In addition, the interaction may be spin dependent since the Fermi surfaces of majority and minority spins are different in magnetic metals; leading to a spin-dependent broadening of the molecular orbitals. In Fig. 7.5b, the minority-spin HOMO is much broader than the majority-spin one since the minority-spin HOMO interacts much more with the electrode than the majority-spin one. In this special case, the minority-spin HOMO crosses the Fermi level E_F, and the resulting polarization P changes sign with respect to the non-interacting case (Fig. 7.5a). (ii) An energetic shift of the molecular orbitals with respect to the Fermi energy (E_F) can appear when the molecule is brought close to the electrode.[3,4,187] In turn, it can again affect the spin polarization of the hybrid state at the Fermi level. In the case depicted in Fig. 7.5c, the sign of the spin polarization changes again and is now the same than that of the case described in Fig. 7.5a.

The work performed by Barraud *et al.*[4] and the cartoon in Fig. 7.5 suggest

that electronic and magnetic properties of the hybrid molecule-electrode interface are of fundamental importance and dictates the effective spin polarization as well as the spin-transport properties within spin-valve devices. One can then envisage custom-made chemistry to improve the performance of the spintronic devices. This has given birth to the *spinterface* science[187] that we introduce in the next chapter.

<div style="text-align: right; font-size: 3em;">*8*</div>

Phthalocyanine molecules and phthalocyanine-based spinterfaces

In the previous chapter, we have seen that the spin-polarized transport properties in hybrid metal-organic junctions highly depend on the metal-molecule interfaces. In turn, this strongly motivates the independent electronic and magnetic studies of magnetic metal-molecules interfaces, also referred to as spinterfaces. Planar phthalocyanine-based molecules appear as prototypical candidates as they may involve more molecular sites in the formation of the spinterface compared to three-dimensional molecules. In addition, it is possible to tune the electronic and magnetic properties of metal-phthalocyanine molecules by changing the central metallic ion, and subsequently probe the magnetic interactions with the (magnetic) substrate. In the first section, we briefly introduce the bulk properties of phthalocyanine molecules and in the second section, we discuss about the electronic and magnetic properties of phthalocyanine-based hybrid interfaces.

8.1. Phthalocyanine molecules

8.1.1. General information

Phthalocyanine (Pc) (from the greek naphtha and cyanide that respectively mean rock oil and dark blue) molecules were first reported in 1907 (metal-free Pc; H_2Pc).[188] Later in 1927, Swiss researcher accidentally synthesized CuPc (copper phthalocyanine) during an attempted preparation of 1,2-dicyanobenzene.[189] Since then, a huge number of different metal-phthalocyanine (referred to as MPc) were synthesized and studied in addition to an active usage of these Pc molecules in industries, mainly as dyes and pigments. MPc molecules present many applications in organic electronics for organic field-effect transistors,[190–192] diodes,[193] photovoltaics[194] and also for gas
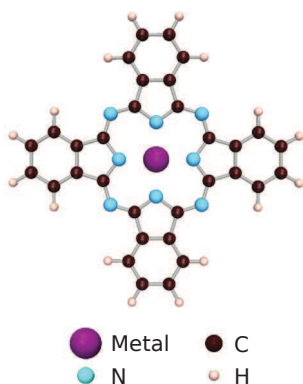
Figure 8.1. – **Representation of a MPc molecule**. The molecule has a square planar D_{4h} symmetry and the metal ion sits in the middle of the molecule.

sensors.[190] The Pc molecules are also known for their exceptionally strong thermal and chemical stability.[190] For instance, most of the Pc molecules do not decompose below 900°C in vacuum.

Pc molecules ($C_{32}H_{16}N_8$) are planar aromatic macrocycles consisting of four isoindole units and most of the MPc have a square planar D_{4h} symmetry (exception are found such as for PbPc and SnPc whose metal ion is out of the Pc molecular plane) as shown in Fig. 8.1.

8.1.2. Crystallographic structure

MPc and H_2Pc molecules are mainly found in two different crystallographic phases: α and β phases (see Fig. 8.2). The molecules stack into columns along the b axis and the main difference between the two phases is the stacking angle, which is defined as the angle between the normal of the molecular plane and the b axis in the (100) and (001) planes for respectively α and β phases. The respective stacking angles for the α and β phases are 26° and 45°. The different stacking angles lead to different apparent distances between the molecules along the b axis. For instance, the distance between two neighboring metal ion of MPc molecules depends on the crystallographic phase.

In most cases, large-size single crystals are in the β phase.[190] They usually have the shape of a 1 cm-long 0.1 cm-wide 0.01 cm-thick needle. When the molecules are evaporated under vacuum onto a substrate held at room temperature, the MPc molecules usually form polycrystalline films of the α phase.[190, 196] The films are of the β phase when the Pc molecules are deposited onto a substrate held at higher temperatures.[195, 197, 198] The α- to β-phase transition can also be irreversibly triggered by increasing the temperature of the Pc thin film. The crystalline phase of the thin
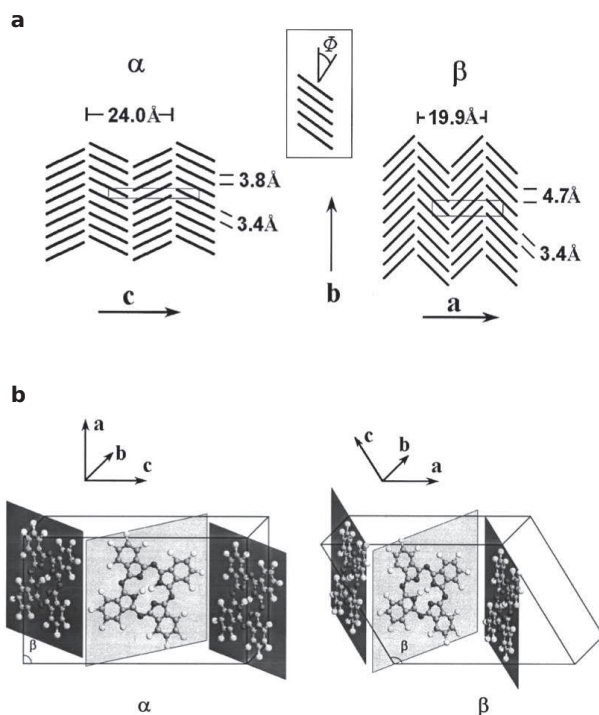
Figure 8.2. – α **and** β **phases of** H_2Pc. **a**, Schematic of the staking of H_2Pc molecules along the b axis in the α (left) and β (right) phases. The stacking angles defined as the angle between the normal of the molecular plane and the b axis (see inset) are 26° and 45° for the α and β phases, respectively. **b**, Schematic of molecular arrangement within the unit cell for α- (left) and β-phase (right) H_2Pc. For clarity, only half of the α-phase unit cell is represented. The figure is taken from Ref. 195.

film can additionally depend on the pressure[190, 199] under which the evaporation is carried out, and also on the "templating" of the substrate.[200–202]

Since the distance between the metal ions of two neighboring MPc molecules depends on their crystalline phase, the overlap of the metal orbitals also depends on the crystalline phase. In turn, the crystalline phase affects the electronic and magnetic properties of the MPc molecules.[200, 202]

8.1.3. Electronic structure of metal-phthalocyanine molecules

The occupation of the different molecular orbitals according to their symmetry can be of fundamental importance in order to describe the magnetic interactions between neighboring molecules. In Fig. 8.3 we report calculated orbital-energy levels of various
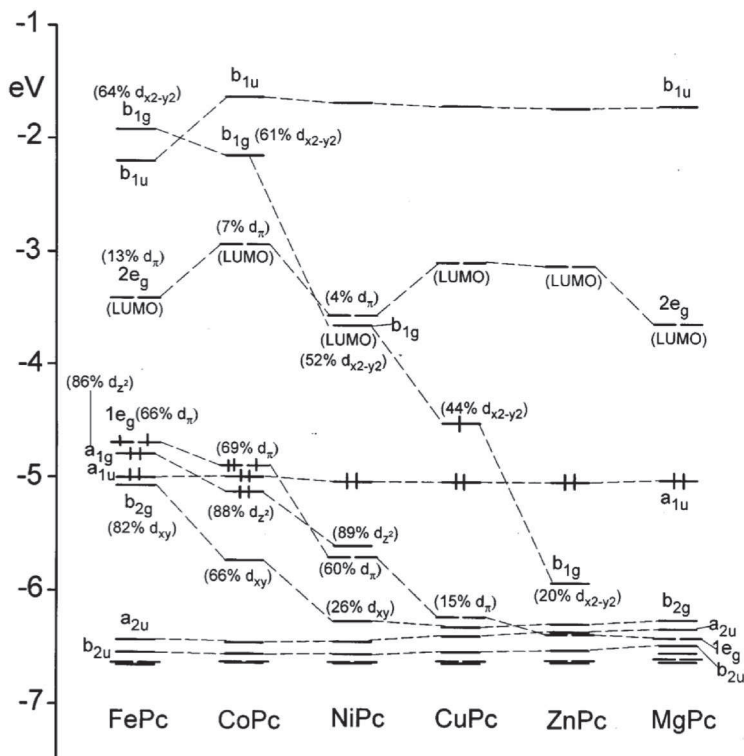
Figure 8.3. – **Calculated orbital energy levels of different MPc molecules**. The orbitals are labeled according to the irreducible representation D_{4h} (see text). The population of some orbitals are indicated in parentheses. The figure is taken from Ref. 203.

MPc molecules (M=Fe, Co, Ni, Cu, Zn and Mg) calculated by Liao *et al.*[203] As stated before in the previous section, these MPc molecules have a D_{4h} symmetry, and the molecular orbitals are thus labeled according to the irreducible representation of D_{4h}: a_{1g} (d_{z^2}), b_{1g} ($d_{x^2-y^2}$), e_g (d_{zx}, d_{yz}) and b_{2g} (d_{xy}).[203]

Referring to Fig. 8.3, we can observe that the nature of HOMO and lowest-unoccupied molecular orbital (LUMO) depend on the central metal ion of the MPc molecule. For Fe and Co central ions, the HOMO has the highest contribution from d_π orbitals ($1e_g$), while the LUMO has mainly contributions from the Pc ligand ($2e_g$). When increasing the "size" of the central ion, the d-like orbitals are pushed to lower energies, since the number of electrons increases as well.

For the situation that interest us the most, *i.e.* when the central ion is Mn, the arrangement of the molecular orbitals is similar to that of the FePc and CoPc. The spin-resolved DOS of a free MnPc molecule is shown in Fig. 8.4. In the spin-up channel, the HOMO and LUMO are a_{1u} and $2e_g$ orbitals, respectively. Both of
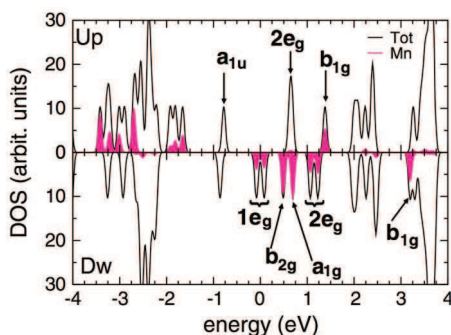
Figure 8.4. – **Calculated density of states of a free MnPc molecule**. The upper (lower) panel show the MnPc DOS for spin up (down). The shaded area represent the Mn *3d* contributions to the MnPc DOS. The calculations are performed by using the generalized gradient approximation (GGA) and by adding an Hubbard term to account for correlations. The figure is taken from Ref. 204.

these orbitals originate from the Pc ring. In the spin-down channel, both HOMO and LUMO have e_g contributions from the Mn ion. From the DOS of MnPc shown in Fig. 8.4, we can observe that the occupation of the metallic orbitals (shaded area) is imbalanced between the spin-up and spin-down channels, which gives rise to a net magnetic moment of $3.0\,\mu_B$ for MnPc.[139, 204]

8.1.4. Magnetic properties of metal-phthalocyanine molecules

The metal ions of MPc molecules can carry a magnetic moment and thanks to the stacking geometry of MPc, one can have magnetic correlations between the metal ions of MPc molecules along the b axis (see Fig. 8.2). The mechanisms involved for the magnetic correlations within molecular chains are still discussed and may depend both on the system and on the crystallographic phase.[200, 202, 205–210]

The metallic Mn ions within MnPc columns (see Fig. 8.2) in crystals or films of the α (β) phase exhibit antiferromagnetic (AF) (ferromagnetic (FM)) correlations at low temperatures.[205, 206] For both phases, AF and FM exchange interactions are competing. The FM correlations are supposed to be driven by superexchange through the overlap of the metallic orbital a_{1g} of one MnPc molecule and the ligand Pc orbital E_g of the neighboring molecule (see Figs. 8.5a and 8.5b). The AF correlations would also come from superexchange through the overlap of the metallic orbital e_g of one MnPc molecule with the Pc orbital E_g of a neighboring MnPc molecule (see Figs. 8.5c and 8.5d). Depending on the stacking angle, and thus on the crystallographic phase, the orbital overlaps are different (see Fig. 8.5) favoring AF and FM correlations for α and β crystallographic phases, respectively.[206]

Heutz *et al.*[200] realized CuPc thin films and studied their magnetic properties.
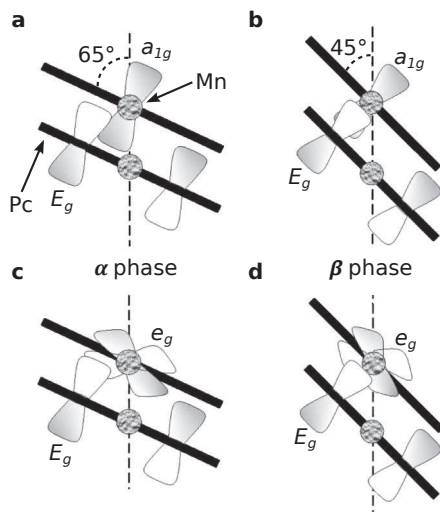
Figure 8.5. – **Schematic of the orbital overlaps for two adjacent MnPc molecules within a chain**. Schematic of the overlap between the metallic orbital a_{1g} and the Pc ligand orbital E_g for two adjacent molecules within a chain of the **a**, α and **b**, β phases. For MnPc, this overlap promotes FM correlations between the metallic centers. Schematic of the overlap between the metallic orbital e_g and the Pc orbital E_g in the **c**, α and **d**, β phases, responsible for AF correlations. The figure is adapted from Ref. 206.

CuPc films in the α phase on Kapton show antiferromagnetic correlations and they estimated a magnetic coupling energy, for neighboring molecules within the same columns, of $J_{AF}/k_B = 1.4$ K. Annealing the sample to 320 °C leads to a switch from the α to β phase. The magnetic measurements of the CuPc thin film in the β phase reveal a paramagnetic behavior. This simple example show how tiny difference in the molecular stacking lead to different magnetic properties of the CuPc thin films. They fabricated another CuPc thin film on a surface templated by PTCDA (3,4,9,10-perylenetetracarboxylic dianhydride). X-ray diffraction measurements reveal that the templated phase consists of α-phase columns where all the molecules are parallel to the surface.[200] The magnetic studies indicate antiferromagnetic correlation with an estimated coupling strength of $J_{AF}/k_B = 1.6$ K, *i.e.* slightly larger than for α-CuPc films.

Chen *et al.*[208] observed much lager AF correlations within CoPc molecules stacked into columns on Pb(111). Using STM they could experimentally determine the stacking structure of the molecules (see Fig. 8.6a). The first-ML molecule is lying flat onto the Pb(111) surface, and the second-ML CoPc molecule is lying on top of the first-ML one, rotated by 45°. The subsequent molecular layers are laterally shifted by 2 Å and the intermolecular vertical spacing is 3.5 Å. The Co ions within bulk CoPc
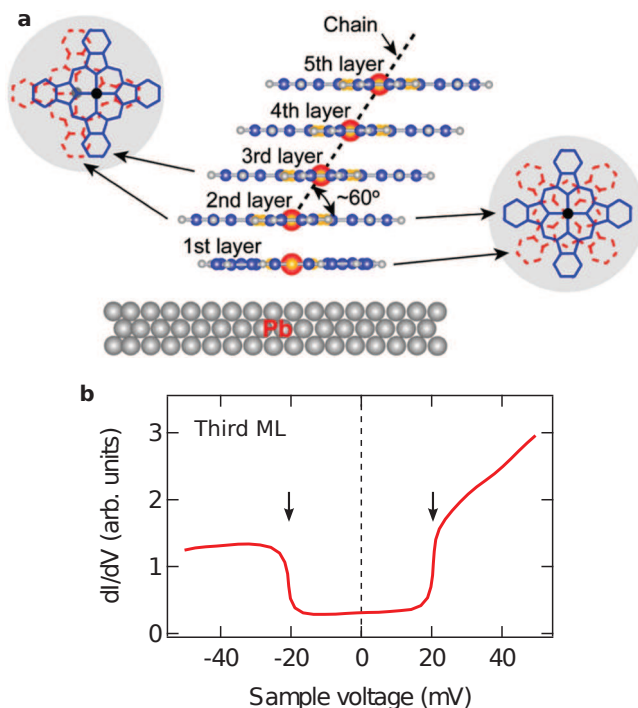
Figure 8.6. – **Antiferromagnetic correlations within CoPc columns on Pb(111)**. **a**, Sketch of the experimentally resolved stacking geometry of the CoPc molecules. The second-ML CoPc sits on top of the first-ML molecule, rotated by 45°. The subsequent CoPc molecule are laterally shifted by 2 Å and vertically separated by 3.5 Å. **b**, dI/dV curve obtained by STS on third molecular layer. The arrows indicate the threshold voltages for spin-flip events. The figure is adapted from Ref. 208.

have a spin $1/2$. However, the spin of first-ML CoPc on Pb(111) seems quenched as the STS data did not evidence a Kondo screening, neither a IETS-induced spin-flip excitations.[208] STS performed on second-ML CoPc evidence a Kondo resonance, while STS on third-, fourth- and fifth-ML manifest spin-flip processes (see Fig. 8.6b). From the STS spectra, they deduce a magnetic coupling energy about $J_{AF}/k_B = 208$ K (see Fig. 8.6b), that is order of magnitude higher than previous reports.

A complete structural and magnetic study of CoPc thin films and powder in the α phase by Serri *et al.*[202] showed AF correlations between 73 K to 106 K. They also performed *ab initio* calculations that predict AF correlations reaching 400 K within molecular columns for CoPc molecules stacked co-facially.

8.2. MnPc-metal hybrid interfaces

Several growth studies of the first monolayer (ML) of MPc molecules on flat metallic substrates using scanning tunneling microscopy[211, 212] or X-ray natural linear dichroism (XNLD) spectroscopy[213–216] revealed that the adsorbed MPc molecules lie flat on the investigated surfaces.

Yet, referring to the formation of hybrid spinterfaces discussed in Sec. 7.3, the electronic coupling of MPc molecules to the ferromagnetic substrate can lead to an energy shift and a spin-dependent hybridization of the molecular orbitals. The formation of the spinterface can have two outcomes concerning the magnetic properties of the molecules. (i) When the metallic center of MPc is paramagnetic, its magnetization can eventually be stabilized by the spinterface through spin-dependent hybridization of the molecular orbitals with the spin-split states of the ferromagnetic substrate. (ii) The spin-dependent hybridization and the energy shift of the molecular orbitals, in addition to eventual charge transfer between the substrate and the molecule, can lead to a spinterface-induced spin polarization of the molecule. Note that, strictly speaking, the spinterface-induced spin polarization is part of the molecule-substrate system and not the molecule alone.

X-ray magnetic circular dichroism (XMCD) measurements performed at room temperature evidenced a magnetic coupling between the paramagnetic center of MPc molecules and ferromagnetic substrates.[214, 215, 217–219] This was also observed by low-temperature spin-polarized STS experiments revealing a spin-polarized DOS near the Fermi level E_F on the Co metallic center of CoPc deposited onto a Co/Cu(111) substrate.[220] These two kind of experiments verify the point (i). Low-temperature spin-polarized STM experiments could, thanks to its high spatial resolution, show that the Pc ligands of MPc molecules on magnetic substrates were also spin polarized.[221, 222] Since the ligands of MPc have initially no spin polarization, the latter is induced by the interaction of the molecule with the substrate, verifying the point (ii). An excellent review of the magnetic coupling of MPc molecules on magnetic substrates can be found Ref. 223. It is also worth to note that Schmaus et al.[224, 225] constructed a GMR device out of a single molecule by contacting a H_2Pc molecule on Co/Cu(111) with a Co-coated tip. They measured a high magnetoresistance of 60 % interpreted by spin-dependent hybridization at molecule-metal interfaces, which demonstrates the exceptional potential of organic molecules for spintronic applications.

In the following, I will focus on the magnetic properties of MnPc molecules deposited on Co/Cu(100) and on Cu(100) substrates. I would like to stress that these results were obtained from my predecessors.[139, 226, 227] In Fig. 8.7, we represent X-ray absorption spectroscopy (XAS) and XMCD spectra at the Mn $L_{3,2}$ edges for MnPc molecules deposited on Cu(100) and Co/Cu(100) surfaces. The Mn L_3 edge of XAS and XMCD spectra for MnPc/Cu(100) (see Fig. 8.7a) show more pronounced peaked structures than that of the L_3 Mn edge of the spectra for MnPc/Co/Cu(100) (see Fig. 8.7b). Since the peaked structures reflect multiplet features that are highly sensitive to the oxidation state and to the strength and symmetry of the ligand field
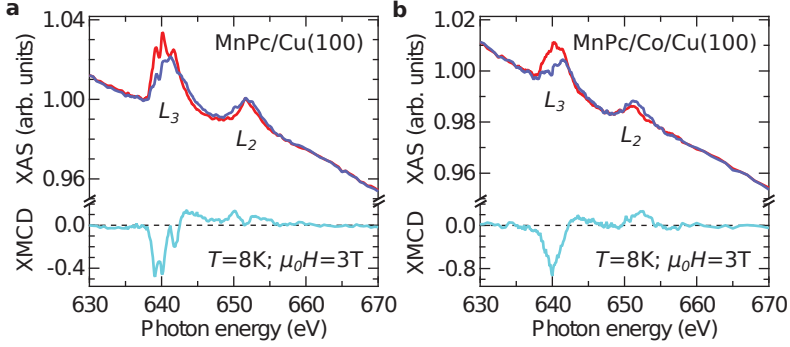
Figure 8.7. – **XAS and XMCD spectra at the Mn $L_{3,2}$ edges for MnPc on Cu(100) and Co/Cu(100) substrates**. XAS and the corresponding normalized XMCD spectra at the Mn $L_{3,2}$ edges for **a**, 1 ML MnPc on Cu(100) and **b**, 0.5 ML MnPc on Co/Cu(100). The spectra were acquired at $T = 8\,\mathrm{K}$ under an external magnetic field $\mu_0 H = 3\,\mathrm{T}$. The magnetic field is applied along the incoming direction of the photon, which makes an angle of 30° with the surface plane.

on the probed element (here the central Mn ion),[228] the Cu(100) and the Co/Cu(100) substrates seem to have different impact on the MnPc molecules (see Refs. 5, 7 for more details). The negative XMCD intensity at the L_3 Mn edges of MnPc on both substrates indicates that the central Mn ion carriers a magnetic moment and that it is aligned with the external magnetic field. Note that disordered orientation of the magnetic moments would lead to a zero XMCD intensity.

The Mn magnetic moments can be aligned by the external field and/or through interactions with the underlying substrate. However, the XMCD spectra presented in Fig. 8.7 were acquired at low temperature (8 K) and under a "high" magnetic field (3 T), which does not allow to distinguish between the two possible origins of the alignment of the Mn magnetic moments. Hence, additional measurements were carried out, such as element-specific magnetic hysteresis loops presented in Fig. 8.8. These loops were obtained by measuring the magnetic-field dependence of the XMCD intensity at the L_3 Mn edge. For MnPc/Cu(100) (see Fig. 8.8a), the unsaturated loop is similar to that of a paramagnetic ion, *i.e.* seems to follow a Brillouin function. Notably, in the absence of an external magnetic field, the XMCD intensity is zero. However, for MnPc/Co/Cu(100), the hysteresis loop obtained at room temperature saturates for low applied magnetic fields. In this case, a field-induced alignment of Mn paramagnetic moments can be ruled out since at room temperature and at the low applied magnetic fields, the proportion of aligned Mn magnetic moments would be negligible. A more careful observation at low magnetic fields shows that the Mn magnetization tracks that of the Co, implying a strong FM coupling between the Mn molecular sites and the Co substrate (see discussion in Ref. 5).

Yet, we know that the Mn center of MnPc is FM coupled to the underlying Co
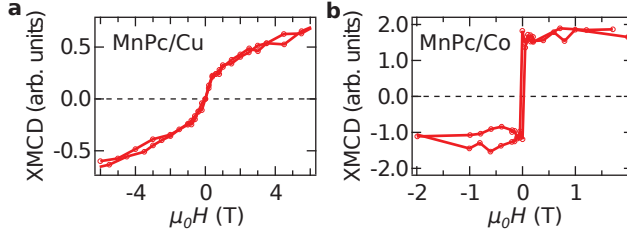
Figure 8.8. – **Magnetic hysteresis loop of the central Mn ion of MnPc molecules on Cu(100) and Co/Cu(100)**. Evolution of the XMCD intensity of the Mn L_3 edge (photon energy: 640 eV) as a function of the external magnetic field for MnPc molecules on **a**, Cu(100) and **b**, Co/Cu(100) substrates. The hysteresis loop of **a** and **b** were acquired at a temperature of 8 K and 300 K on a MnPc coverage of 2.5 ML and 1 ML, respectively.

substrate. What would be the potential of this spinterface in terms of spin-polarized transport (see Sec. 7.3)? To answer this question, at least partially, Djeghloul et al.[6] performed spin-resolved direct and inverse photoemission measurements of MnPc/Co. Following a well-established subtraction procedure discussed in Ref. 6, the contribution of the bulk Co is subtracted from the photomemission spectra. Thus, the resulting difference spectra shown in Fig. 8.9 only accounts for the DOS arising from surface-interface effects. The difference photoemission spectra indicate a positive spin polarization that reaches a surprisingly high value of 80 % close to E_F at room temperature. Considering that the Co DOS is higher for the minority-spin channel, the spinterface has a spin-polarization opposite to that of Co at E_F, in agreement with the predictions of Barraud et al.[4] inferred from magneto-transport measurements on another system.

Additional measurements showed that the second-ML (third-ML) of MnPc only contributes to 20 % (0 %) of the spin-polarized signal and thus reveals that the hybridization-induced spin-polarized states are confined to the interface. Furthermore, we also know that the interfacial spin-polarized states arise dominantly from the C and/or N molecular sites. Indeed, when the photon energy is increased from 20 eV to 100 eV, the photoionisation cross section for $2p$ states of free atoms decreases by one order of magnitude while that for $3d$ states stays almost constant. Thus, photoemission measurements with a photon energy of 100 eV involves mainly $3d$ photoelectrons and the resulting spin-resolved difference spectra show no spin polarization (see Ref. 6).

To summarize their findings, the first-ML of MnPc molecules strongly hybridize with the ferromagnetic Co substrate. The Mn central ion of MnPc is FM coupled to the Co substrate as revealed by density functional theory (DFT) calculations.[5] The N and C molecular sites have a small induced magnetization that is FM and AF coupled to the Co substrate, respectively.[6] In turn, this leads to a positive spin polarization of the spinterface close to E_F that reaches 80 %, whose sign is opposed to
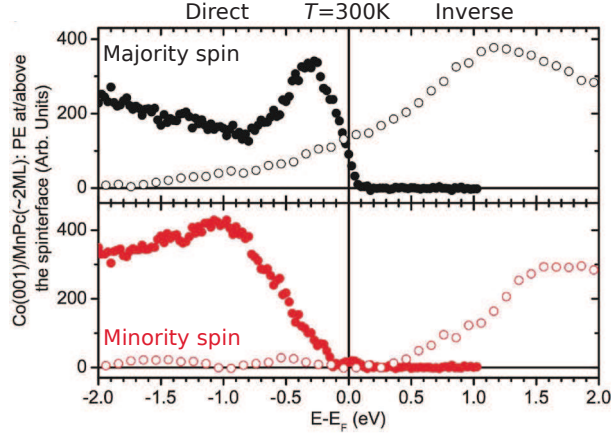
Figure 8.9. – **High spin polarization of the DOS near the Fermi level for MnPc/Co**. Spin-resolved difference spectra of direct (closed symbols) and inverse (open symbols) photoemission measurements at room temperature for MnPc molecules deposited on Co/Cu(100). The spin polarization at the Fermi energy E_F reaches $80\,\%$. The MnPc coverage is $2.6\,\mathrm{ML}$ and $2.0\,\mathrm{ML}$ for the direct and inverse photoemission spectra, respectively. The energy of the incoming photons is set to $20\,\mathrm{eV}$. The figure is adapted from Ref. 6.

that of the Co substrate. Note also that MnPc molecules on Cu(100) are also strongly hybridized but there is no evidence of an induced spin polarization and of a magnetic stabilization of the Mn central ion.

Recently, we evidenced that we can obtain highly spin-polarized spinterfaces just by depositing carbon on a ferromagnetic Co substrate (see Fig. 8.10). The spin-resolved photoemission spectra for $1.5\,\mathrm{ML}$ C on Co/Cu(100) after subtraction of the bulk Co contribution is very similar than that for $2\,\mathrm{ML}$ MnPc on Co/Cu(100) (see Fig. 8.9). Notably, the induced spin polarization at E_F is positive, *i.e.* opposite to that of Co. A complete STM, STS and XPS study reveal that the C is amorphous on the Co surface with mainly C-Co and sp^2 C-C bonds.[229] This highly spin-polarized carbon-based spinterface has a huge potential for spintronics applications. Apart from the low cost of carbon and the high spin polarization at E_F, the carbon forms a very dense and compact layer, which prevent metallic interdiffusion due to the counter electrode.

On the one hand, we know that the first-ML of MnPc is highly hybridized to the underlying FM Co substrate, what in turn stabilizes a FM coupling between the Mn molecular site and the Co substrate at room temperature. On the other hand, bulk MPc molecules can exhibit magnetic correlations within molecular chains at low temperature. In the next chapter, we will see what happens when we try to conciliate both points.
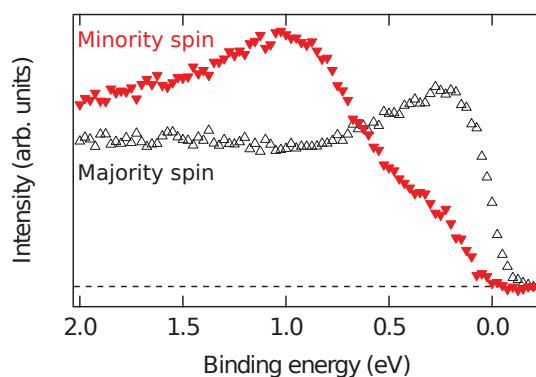
Figure 8.10. – **High spin polarization of the DOS near the Fermi level for C/Co**. Spin-resolved photoemission spectra for 1.5 ML C on Co/Cu(100) after subtraction of the bulk Co contributions.[6, 229] The spectra indicate a very high positive spin polarization at the Fermi level, similar to that represented in Fig. 8.9.

9

Room temperature magnetic order in molecular layers

In the previous chapter, we discussed about promising room-temperature spintronic properties that appear at the interface between a ferromagnetic (FM) metal and an organic molecular layer. Separately, molecular semiconductors, such as phthalocyanine-based molecules (see Sec. 8.1.4), may exhibit antiferromagnetic (AF) correlations well below room temperature (RT).

Can we advantageously use a molecular semiconductor with intermolecular magnetic correlations to build an efficient and robust spinterface; and what would be the impact of the spinterface on the magnetic properties of the molecules? We will try to partially answer this question by studying the magnetic properties of MnPc molecules on Co as a function of the MnPc thickness. The choice of this system is straightforward since in the previous chapter we have seen that MnPc on Co forms a relatively good spinterface, and bulk MnPc molecules can show magnetic correlations at low temperatures.[205, 206] In the following, we will describe the preparation of wedge-shaped samples with variable MnPc thicknesses and the study of the stacking geometry of MnPc on Co(100). Then, we will discuss the magnetic coupling of the first and subsequent MnPc layers, and finally show that MnPc on top of Co can induce exchange bias.

9.1. Investigated sample

For this study, different samples with different thicknesses were prepared. However, to ease the discussion of the results, we will focus on a unique sample that is schematized in Fig. 9.1. Note that the magneto-optical Kerr effect measurements were performed on a different sample since it was necessary to transfer the sample *ex situ*. The samples were prepared within the molecular beam epitaxy (MBE) environment of beamline
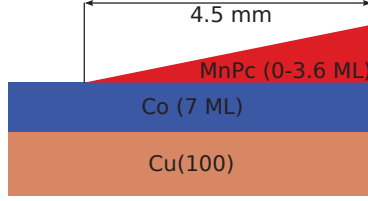
Figure 9.1. – **Schematic of the investigated sample**. The sample's stack is MnPc(0 to 3.6 ML)/Co(7 ML)//Cu(100). The MnPc wedge ranges over 4.5 mm.

DEIMOS at the SOLEIL synchrotron.[134] Clean and flat Cu(100) surfaces were prepared by several cycles of argon-ion sputtering (1 keV) and subsequent annealing to 820 K. 7 ML of Co were deposited onto Cu(100) at a pressure of 7.0×10^{-10} mbar relative to a base pressure of 3.0×10^{-10} mbar. We then annealed the stack at 370 K for 10 min in order to flatten the Co terraces.[127, 230] Finally, MnPc molecules were sublimed at 690 K onto the Co/Cu(100) sample at room temperature while a shutter was moved in front of the sample to craft a molecular wedge (see Fig. 9.1).

Different MnPc thicknesses could be measured by moving the sample along the wedge relative to the X-ray beam. We used the white-line integral at the Mn $L_{3,2}$ edges to determine the relative molecular thickness within the same sample. We used a combination of XAS, STM, Auger and quartz micro-balance measurements on the same reference samples to have an absolute thickness calibration (data not shown). Note that due to the finite size of the X-ray beam, the measurements were integrated over a thickness of about ±0.5 ML.

Moreover, the investigated sample had areas non-covered by MnPc molecules as depicted in Fig. 9.1. We acquired XAS spectra at the Mn $L_{3,2}$ edges over these areas and used them as background references that we systematically subtracted from the XAS spectra at the Mn $L_{3,2}$ edges. Note that all the following XAS measurements were performed under an angle of 40° between the surface and the photon-incidence direction.

9.2. Stacking geometry of MnPc on the Co substrate

As the stacking geometry of the MnPc molecules can strongly influence their magnetic properties, we use X-ray natural linear dichroism (XNLD) to determine the orientation of the planar MnPc molecules on Co/Cu(100), as a function of molecular thickness. In our experimental geometry,[134] the X-ray beam propagates horizontally towards the sample that is positioned vertically. The incoming X-ray beam makes an angle of 40° with the sample surface (see inset of Fig. 9.2b). The X-ray beam is linearly polarized and the polarization can be chosen vertically or horizontally.

The nitrogen molecular sites of MnPc have σ-like in-plane molecular orbitals;
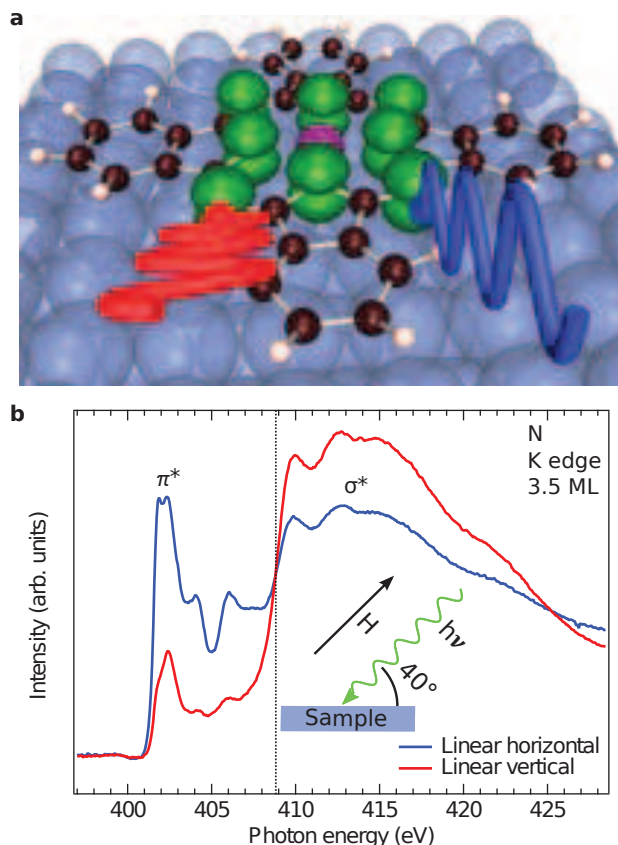
Figure 9.2. – **Principle of XNLD applied on MnPc molecules**. **a**, Schematic view of a MnPc molecule lying flat on a Co surface. Iso-density of the nitrogen π^* orbitals are represented in green to better visualize the interactions with X-rays with linear horizontal and vertical polarizations respectively represented in blue and in red. **b**, XAS spectra at the nitrogen K edge for 3.5 ML MnPc on Co. The spectra exhibit dichroism upon changing the linear polarization of the X-rays, reflecting a dominant flat adsorption of the MnPc molecules on Co (see text).

and out-of-plane orbitals (see for instance iso-density of the out-of-plane π^* orbitals represented in green in Fig. 9.2a). The unoccupied π^* and σ^* orbitals have different energies, and thus the transitions from the $1s$ core state to the π^* states and to the σ^* states occur for different photon energies. In addition, photon absorption is promoted within unoccupied orbitals that are spatially oriented parallel to the X-ray's electric field.[84, 85] Thus, by varying the orientation of the X-ray's electric field, one can eventually deduce the orientation of the MnPc molecular plane relative to the surface. This is illustrated by the schematic of a single MnPc molecule lying flat on the Co surface with incoming linear vertical (horizontal) X-rays represented in red (blue) (see

Fig. 9.2a), and the corresponding XAS spectra at the nitrogen K edge (see Fig. 9.2b). Note that to better visualize the XNLD effect on the MnPc molecule, the system represented in Fig. 9.2a is rotated by 90° compared to the system's orientation in the setup. In the actual experimental geometry (see inset of Fig. 9.2b), and for MnPc molecules lying flat on the surface, the linear horizontal polarization (represented in blue) is more efficient to probe core-state to π^*-state transitions, while the efficiency of core-state to σ^*-state absorption is higher for linear vertical polarization of the X-rays, in agreement with the spectra at the N K edge shown in Fig. 9.2b. It thus suggests that MnPc dominantly lies flat onto the Co surface for a molecular coverage of 3.5 ML. Note that (i) the situation would be reversed if the molecule stand up onto the surface with the molecular plane parallel to the incoming direction of the X-rays; and (ii) the XAS spectra are independent of the X-ray polarization for uniformly distributed orientation of the MnPc's molecular planes.

Note also that the technique we used for XNLD is different than the one usually used,[85, 213–216] *i.e.* probing the angular dependence of the XAS spectra at the nitrogen K edge acquired with linear horizontal photon polarization. The method gives similar results than angular-dependence measurements, but in former case the amplitude of the dichroism is limited.

In Fig. 9.3, we represent the XAS spectra at the nitrogen K edge acquired with linear horizontal (LH) and linear vertical (LV) photon polarization for MnPc coverages of 0.7 ML, 2.2 ML and 3.5 ML. To quantitatively determine the proportion of MnPc molecules that lie flat onto the substrate, we extracted the XNLD intensity for each MnPc thickness and normalized it to that found for 0.7 ML. This normalization is justified since the previous STM[211, 212, 231] and XNLD[213–216] studies of Pc molecules on flat metallic substrates show that at least the first-ML molecules lie flat on the substrate. Furthermore, we believe that only a flat adsorption of the molecule can promote the strong coupling of the Mn site of MnPc to the Co substrate and the apparent absence of paramagnetism within the first-ML MnPc on Co, which we will describe in the next section.

From 0.7 ML to 2.2 ML, the XNLD amplitude decreases only slightly. This shows that almost all first- and second-ML MnPc molecules lie flat. However, when the MnPc coverage is increased to 3.5 ML, the XNLD intensity decreases by about 30 % compared to that of 0.7 ML MnPc coverage. This XNLD-intensity decrease comes from a proportion of molecules that do not lie flat onto the surface.

9.3. Magnetic coupling of the first-ML MnPc onto Co

To determine the magnetic properties of MnPc on Co, we used the powerful element-specific XMCD technique (see Sec. 4.3). In Fig. 9.4a, we represent the XAS spectra measured at the Co $L_{3,2}$ edges for left and right photon helicities. The difference of the spectra for left and right photon helicities defines the XMCD intensity, which in
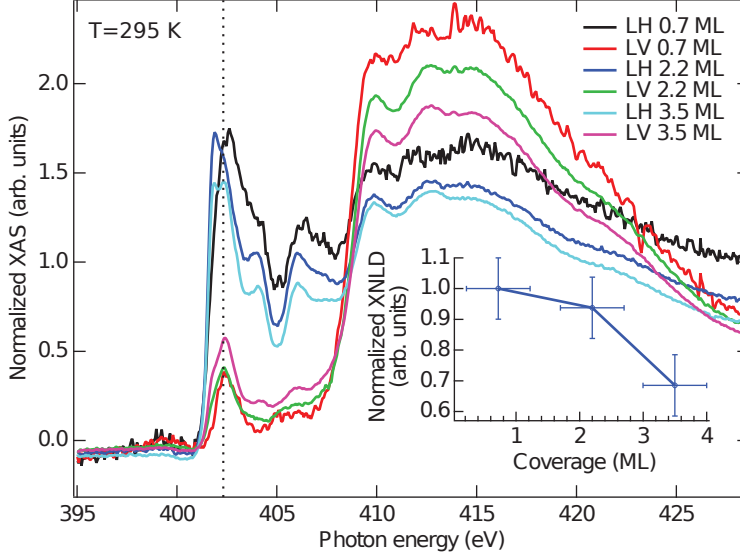
Figure 9.3. – **XNLD as a function of MnPc coverage**. XAS at the nitrogen K edge normalized by the white line intensity at 402.3 eV for different MnPc coverages. In the inset, we present normalized XNLD as a function of MnPc coverage. The normalization procedure is done by calculating $^{LH-LV}/_{LH+LV}$ at 402.3 eV and then dividing by the XNLD found for 0.7 ML.

Fig. 9.4a is negative (positive) at the Co L_3 (L_2) edge. This indicates an alignment of the Co in-plane magnetic moments along the external magnetic field of 0.1 T. The XMCD spectrum at the Mn $L_{3,2}$ edges for 0.7 ML MnPc on Co (see Fig. 9.4b) has similar signs than that at the Co $L_{3,2}$ edges. This infers an alignment of the Mn moments with that of Co. Yet, since a field-induced alignment of the Mn magnetic moments at room temperature in a low magnetic field would yield a negligible XMCD intensity, the XMCD spectrum presented in Fig. 9.4 evidence a FM coupling at room temperature of the Mn within MnPc to the underlying Co (see also Sec. 8.2), as seen in other systems.[214, 215, 217, 218]

9.4. Anti-ferromagnetic ordering of the MnPc molecules

In the previous section we observed a strongly magnetically coupled first-ML MnPc on Co allowing the formation of the spinterface. How does the magnetic coupling evolve beyond the hybrid interface? The initial naive picture is that the first-ML molecules strongly couple to the metallic substrate, and the subsequent molecular layers are de-
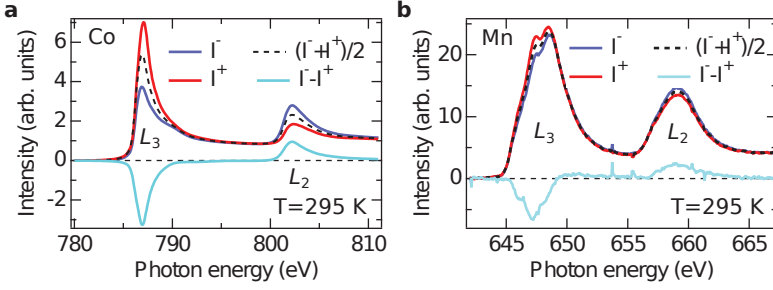
Figure 9.4. – **FM coupling of the first-ML MnPc onto Co**. **a**, XAS at the Co $L_{3,2}$ edges for left photon helicity (blue) and right photon helicity (red). The average of and the difference between left and right photon helicities defines the white line (dashed black) and the XMCD (sky blue), respectively. **b**, XAS and XMCD at the Mn $L_{3,2}$ edges for 0.7 ML MnPc on Co. Both measurements were acquired at 295 K in a magnetic field of $\mu_0 H = 0.1$ T using the experimental geometry depicted in the inset of Fig. 9.2b.

coupled, at least partially, from the substrate by the first-ML molecules. In this naive picture, the Mn molecular sites within the second and subsequent ML are uncoupled to the substrate, and are thus paramagnetic. Yet, the situation could be different since bulk MnPc molecules can have magnetic interactions between neighboring molecules provided that the molecular stacking is good enough.[200, 210]

In Fig. 9.5a, we show the thickness dependence of the XMCD spectra at the Mn $L_{2,3}$ edges. To better compare the XMCD spectra between them, each XMCD spectrum in Fig. 9.5a was divided by the white-line integral and are thus normalized to the MnPc thickness. The normalized XMCD spectra give information about the averaged magnetic quantities per molecule. Moreover, as the MnPc thickness is varied by changing the spot position over the MnPc wedge, the MnPc thickness span over ±0.5 ML due to the finite spot size of the X-ray beam. In the following we will consider two different experimental scenarii to distinguish between magnetically coupled and uncoupled paramagnetic molecules. Note that the magnetization of paramagnetic compounds follows a Brillouin function that describes the competition between the alignment of the paramagnetic moments along an external magnetic field H and the thermal fluctuations that tends to disorder the paramagnetic moments. As a result, for $\mu_0 H = 6.5$ T (referred to as high H or HH) and Mn paramagnetic ions, most of the paramagnetic moments are aligned at 4.8 K (here referred to as low temperature (LT)) while practically none are aligned at 295 K (referred to as RT). For $\mu_0 H = 0.1$ T (defined as low H or LH), only a negligible proportion of the paramagnetic moments are aligned along the field at LT and RT. In the first experimental scenario, we probe the impact of the strong magnetic coupling between the MnPc molecules and the Co substrate while excluding paramagnetic contributions using the RT-LH XMCD spectra acquired at RT and 0.1 T. In the second scenario, the LT-HH XMCD spectra were acquired at 4.8 K in an external magnetic field of 6.5 T, which leads to an
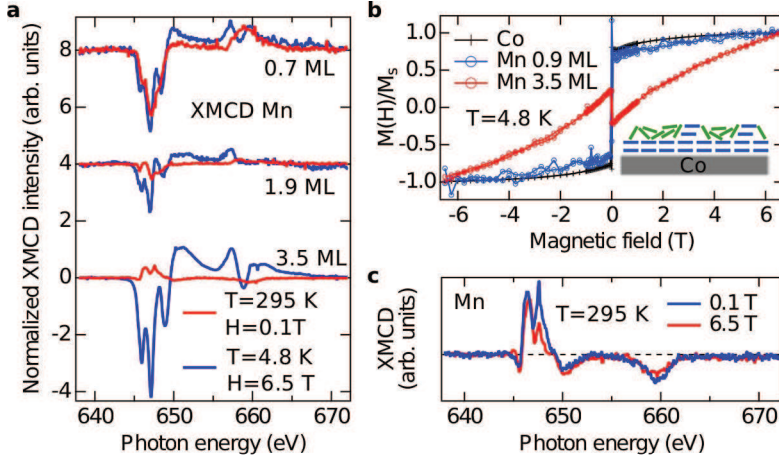
Figure 9.5. – **AF ordering of MnPc molecules onto Co**. **a**, XMCD at Mn $L_{3,2}$ edges for MnPc coverages of 0.7 ML, 1.9 ML and 3.5 ML; and normalized by the quantity of probed MnPc, *i.e.* by its white line integral. For every coverage a pair of XMCD is represented, one at 295 K in a magnetic field of 0.1 T to probe the robustness of the magnetization and one at 4.8 K in a field of 6.5 T to align the uncoupled paramagnetic moments. **b**, Normalized magnetization of Co and Mn as a function of the external magnetic field at 4.8 K. The magnetization is deduced from the XMCD intensity at 786.8 eV and 647.0 eV for Co and Mn, respectively. The inset schematizes the stacking of 3.5 ML MnPc on Co where only a few proportion of third- and fourth-ML molecules are forming molecular columns with the underlying molecules. **c**, XMCD of MnPc at a molecular coverage of 3.5 ML at RT for two different magnetic fields demonstrating the robustness of the effect.

alignment of almost all the paramagnetic Mn moments in addition the Mn moments coupled to the Co substrate. To first order, the difference between the LT-HH- and RT-LH-XMCD spectra represent the magnetic signal due to the paramagnetic Mn centers.

At 0.7 ML MnPc thickness, the RT-LH- and LT-HH-XMCD spectra have similar shapes and amplitudes (see Fig. 9.5a). At low temperature, the magnetic-field dependence of the XMCD amplitude at the Mn L_3 edge follows that of Co (see Fig. 9.5b) demonstrating that all the Mn center within first-ML MnPc are magnetically FM coupled to underlying magnetic Co. At 1.9 ML MnPc thickness, the RT-LH-XMCD spectrum differs both in shape and in amplitude from that obtained at 0.7 ML MnPc thickness. Particularly, we monitor a four-fold decrease in the XMCD intensity at the Mn L_3 edge at RT. The four-fold intensity decrease cannot be explained in terms of a second-ML MnPc magnetically decoupled from the first-ML MnPc, as the intensity drop would be at most two fold. In contrast, the experimental data are consistent with an AF ordering of Mn sites of the second-ML MnPc molecules relative to the
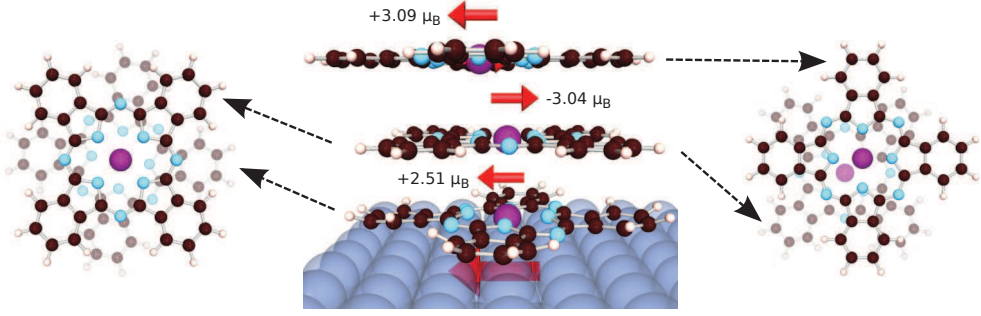
Figure 9.6. – **Adsorption geometry and magnetic properties of the MnPc stacking on Co**. Molecular column composed of three MnPc molecules on Co. Left inset shows the second-ML molecule on top of the semi-transparent first-ML MnPc. Right inset represents the relative alignment of the third-ML MnPc on top of the semi-transparent second-ML molecule. The red arrows indicate the orientation of the spin moments. Other molecular stacking are considered in Appendix A.2.3.

Mn sites of the first-ML MnPc molecules, in agreement with theoretical calculations discussed below (see also Appendix A.2.3). The LT-HH-XMCD spectrum exhibit a larger amplitude than the RT-LH-XMCD spectrum, revealing a small contribution from paramagnetic Mn centers. We believe that the paramagnetic contributions come from structural disorder within the third- and fourth-ML MnPc (see inset of Fig. 9.5 and discussion in Sec. 9.2) that contribute to our measurements at (1.9 ± 0.5) ML MnPc thickness due to an imperfect layer-by-layer growth. At 3.5 ML MnPc thickness, the paramagnetic contribution of the Mn centers within MnPc considerably increases as revealed by the difference between the LT-HH- and RT-LH-XMCD spectra. In addition, the magnetic-field dependence of the Mn magnetization (see Fig. 9.5b) has a Brillouin-like behavior for large magnetic fields. This corroborates the picture presented in the inset of Fig. 9.5b with mostly uncoupled and thus paramagnetic molecules on top of two AF-coupled MnPc layers.

Interestingly, at 3.5 ML thickness, the RT-LH-XMCD spectrum at the Mn L edges is of opposite sign than that at the Co L edges. Moreover, the Mn field-dependence magnetization loop at low magnetic field $(\mu_0 H \pm 0.1\,\mathrm{T})$ presented in Fig. 9.5b exhibits an opposite circulation to that of Co. This implies an anti-alignment of the mean Mn magnetic moments relative to the Co moments. Note that we can exclude any contamination-induced sign reversal since the Co XMCD spectra retain similar shape and same sign for all investigated MnPc thicknesses (not shown). To explain the initially surprising mean Mn moment antiparallel to that of Co, Fatima Ibrahim and Mebarek Alouani performed *ab initio* calculations on different systems (see Appendix A.2.3). The energetically most favorable calculated system is shown in Fig. 9.6. Note that the stacking geometry of the first two molecules depicted in Fig. 9.6 is similar to that for CoPc on Pb reported by Chen *et al.*[208] The calculations indicate that the 3.1 μ_{B} Mn moment of the free MnPc molecules is reduced to 2.51 μ_{B}

when the MnPc molecule is adsorbed onto Co. The variation of the magnetic moment is due to the formation of the spinterface and the transfer of one electron from the substrate into the Mn ion. This is in agreement with the XAS spectra at the Mn $L_{3,2}$ edges presented in Appendix A.1. The Mn ion within the second-ML MnPc carries a magnetic moment of $3.04\,\mu_B$ in an opposite direction to that of the first-ML Mn site. The calculated magnetic-coupling strength between the Mn sites of first- and second-ML MnPc is about $33\,\text{meV}$ ($E_F - E_{AF} = 33.1\,\text{meV}$), but highly depends on the stacking geometry we consider (see Appendix A.2.3). However, since we observed the AF magnetic coupling at room temperature, the calculated coupling strength of $33\,\text{meV}$ seems reasonable, and much stronger than the $J_{AF} \approx 18\,\text{meV}$ reported by Chen *et al.* for a molecular column of 5 CoPc on Pb.[208] The sign reversal of the RT-LH-XMCD spectrum for 3.5 ML MnPc thickness (see Fig. 9.5a) thus reflects the larger magnetic moment of the Mn site of the second-ML molecule compared to that of the first-ML MnPc. The third- and fourth-ML MnPc have a dominant paramagnetic contribution but we believe in the existence of a few magnetically coupled MnPc columns composed of three or more molecules, in agreement with a large proportion of flat-absorbed molecules for 3.5 ML revealed by the XNLD results in Sec. 9.2. Note that we do not compare more quantitatively the experimental and theoretical Mn magnetic moments as the XMCD sum rules[84] cannot yield accurate values of the Mn spin moment due to the low spin-orbit coupling of that element.[209, 232]

Note also that there is a key difference between the experiments of Chen *et al.*[208] and Serri *et al.*[202] on CoPc; and the measurement we presented above. In the former, they observed AF correlation within CoPc columns with coupling strength up to $18\,\text{meV}$, while we report the observation at room temperature of an AF molecular ordering that is stabilized by a ferromagnet (Co), *i.e.* a molecular spin is blocked by exchange with Co at the end of the molecular columns.

9.5. Exchange bias induced by MnPc

We have an AF molecular ordering of MnPc on top of a FM layer. Can this unusual AF molecular ordering pin the underlying Co substrate, as would some other inorganic AF layers? To demonstrate this cornerstone of spintronics called exchange bias (EB),[13, 14, 23, 233] we prepared samples in a UHV chamber with the following stack: Au(15 ML)/MnPc(50 ML)/Co(20 ML)//Cu(100). Since the samples were transported *ex situ*, the gold layer is used to cap the sample and to prevent its contamination. We then performed magneto-optical Kerr effect (MOKE) measurements in a home-built variable-temperature multi-functional cryostat with a 670 nm laser and a photoelastic modulator.

In Fig. 9.7a, we present a magnetic hysteresis loop of the previously described sample at $T = 250\,\text{K}$. While the measurements are done along an easy axis of the Co(100), the magnetization does not switch abruptly and we can monitor some kinks at low magnetic fields. This can arise from i) surface anisotropy[234] eventually due to step edges and ii) a small rotation of the Co easy axis along the easy axis of the
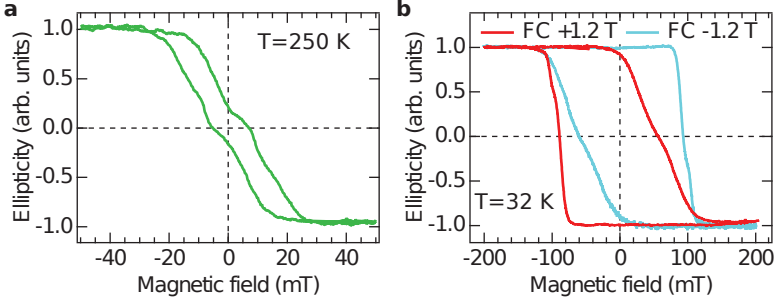
Figure 9.7. – **Exchange bias induced by MnPc**. **a**, Magnetic hysteresis loop on Au(15 ML)/MnPc(50 ML)/Co(20 ML)//Cu(100) acquired at 250 K. **b**, MOKE measurement on the gold capped MnPc/Co bilayer after cooling down to 32 K in a in-plane magnetic field of −1.2 T (cyan) and 1.2 T (red). Each hysteresis loop is field-shifted in the direction opposed to that of the field during the cooling process, characteristic of EB.

MnPc molecules. On the same sample, when the sample is cooled from RT to 32 K in an external magnetic field $\mu_0 H = 1.2$ T, the measured magnetic hysteresis loop shifts towards fields in a direction opposite to that of the in-plane magnetic field applied during the cooling (see Fig. 9.7b). When the field applied during the cooling process is in the opposite direction, *i.e.* $\mu_0 H = -1.2$ T, the magnetic hysteresis loop shifts towards positive fields. This is characteristic of EB.

In Fig. 9.8a, we present two magnetic hysteresis loops on Au(15 ML)/MnPc-(50 ML)/Co(20 ML)//Cu(100) at 32 K after cooling in an external magnetic field of 1.2 T and 0.2 T. Since the two hysteresis loops coincide, we can conclude that both field amplitudes are sufficient to induce EB of identical amplitude. We then present in Fig. 9.8b the temperature dependence of the EB after cooling in a magnetic field of 0.2 T. The EB strength linearly decreases with increasing temperature, and vanishes around 100 K.

We now discuss the underlying conditions that are fulfilled to observe exchange bias. First, the MnPc molecular layers have to provide additional magnetic anisotropy to pin the Co layer. In Appendix A.2.2, we show that the theory predicts an additional anisotropy, at least for the first-ML MnPc on Co. Second, there must be AF domains/columns that do not track the underlying Co layer below 100 K, otherwise there would be no field shift in the hysteresis. Yet, this second point is not fulfilled for AF-ordered two-molecule-long columns on Co that mostly follow the Co magnetic referential (see Fig. 9.5b). We thus believe that the AF-ordered MnPc columns responsible for EB are composed of at least 3 molecules. We note that our XMCD measurements cannot be conclusive on this points. Indeed, XMCD is not an adequate technique to probe long-range AF ordering; and the experiment is averaging over AF-ordered MnPc columns (that produce a low XMCD signal) with the uncoupled paramagnetic molecules. Note that we observed a correlation between the increase of the paramagnetic contribution in the XMCD spectra (see Fig. 9.5a) and
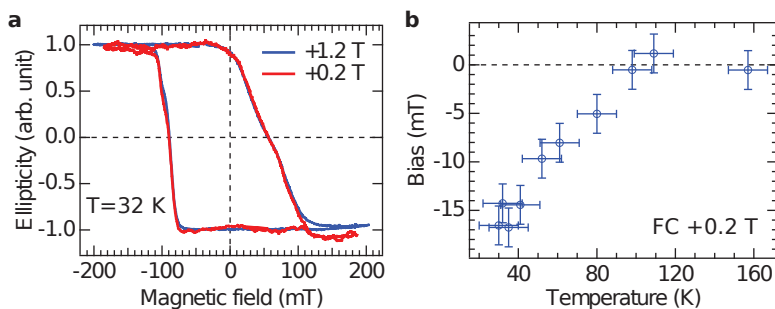
Figure 9.8. – **Temperature dependence of the MnPc-induced exchange bias**. **a**, MOKE measurements on Au(15 ML)/MnPc(50 ML)/Co(20 ML)//Cu(100) at 32 K after cooling the sample from RT in a field of 1.2 K (blue) and 0.2 K (red). **b**, Temperature dependence of the exchange bias. For each data point the sample was cooled down from RT in a magnetic field of 0.2 T.

the decrease of structural order within the MnPc layer revealed by XNLD (see Fig. 9.3) with increasing MnPc thickness. Therefore, we infer that only a small proportion of third- and fourth-ML MnPc lie flat on the surface and form longer AF-ordered columns (see inset of Fig. 9.5b and Sec. 9.2). In turn, this few proportion of molecules that form longer AF-ordered columns, non-detected in our XMCD measurements due to experimental limitations, are responsible for the observed EB with thicker MnPc layer. To support this assumption, our *ab initio* calculations show a preferred AF ordering of the third-ML MnPc molecule (see Appendix A.2.3).

9.6. Partial conclusion

In this chapter, we have shown that the first-ML MnPc on Co is FM coupled to the underlying Co substrate. Our combined experiments and theory reveal that the first and subsequent molecular layers are AF coupled at room temperature provided the molecules lie flat on the surface and form molecular columns. Conversely, the AF ordering of the molecular columns can pin the underlying Co layer and lead to EB below 100 K.

In this system, the interactions between the molecular AF columns are weak. This represents a key difference with other conventional EB systems. Future studies could eventually link the thus-far phenomenological blocking temperature[235] to the length and density of molecular AF columns. These results are also important for the organic-spintronics field. From a magnetoresistive-device point of view, one could use the spinterface to freeze the magnetic referential within a molecular layer to promote efficient spin-polarized transport within the organic layer, tuned by suitably engineered (magnetic) interactions within molecular columns. Alternatively, molecule-induced EB open the path towards fully molecular magnetoresistive devices.

10

Metal/molecule spinterface stabilized by interlayer exchange coupling

In the precedent chapters, we have shown that the hybrid magnetic-metal/molecule interfaces, referred to as spinterfaces, can be strongly spin polarized close to the Fermi level. Additionally, we observed that the spinterface sets the magnetic referential and stabilizes a magnetic ordering within the molecular layer. The influence of the spinterface on the magnetic properties can thus propagate within the molecular layer. Alternatively, if the magnetic properties of a magnetic metal propagate through a non-magnetic-metal spacer, can the non-magnetic-metal/molecule interface lead to the formation of a spinterface? One of the biggest advantage would be the larger choice of the molecular deposition technique and thus a larger choice of molecular candidates. Indeed, the non-magnetic-metal layer could protect the ferromagnet from the potentially adverse impact of adsorbed impurities inherent to wet molecular deposition techniques. The magnetic coupling of a molecule to ferromagnetic substrate through a non-magnetic spacer that we propose here, has been widely studied for inorganic systems, where interlayer exchange coupling (IEC) can magnetic couple two ferromagnetic layers through a non-magnetic spacer.[34]

In this chapter, we will first discuss the theoretical predictions of a MnPc molecule on Co(100) separated by up to 3 ML of Cu. Then, after a description of the investigated sample, we will experimentally evidence, using XMCD spectroscopy, a magnetic coupling of MnPc to the Co layer through the Cu spacer by interlayer exchange coupling. Finally, we will estimate the effective exchange field due to interlayer exchange coupling and discuss about spin-polarized transport perspectives.

10.1. Theoretical predictions

Fatima Ibrahim and Mebarek Alouani performed the following *ab initio* calculations using the methods described in Appendix A.2.1. They used a supercell composed of 3 atomic layer of *fcc* Co (8×8 atoms per layer) and a MnPc molecule separated by d_{Cu} ($d_{Cu} = 0, 1, 2, 3$) layers of Cu. They used the lattice parameter for *fcc* Co and Cu of 0.36 nm and included van der Waals interactions in the calculations.[7]
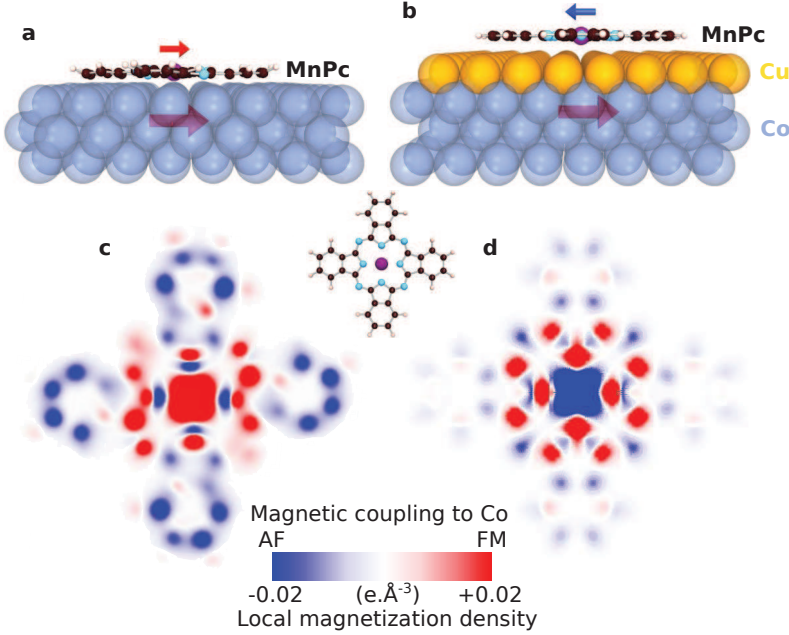
Figure 10.1. – **Magnetization of MnPc due to interlayer exchange coupling**. Calculated Co/Cu(d_{Cu})/MnPc structure for **a**, $d_{Cu} = 0$ ML and **b**, $d_{Cu} = 1$ ML. The arrows indicate the calculated direction of magnetization of the Co substrate and of the Mn center within MnPc. Magnetization map of a single MnPc molecule **c**, on Co and **d**, on Cu(1 ML)/Co. A single MnPc molecule is represented in the center of the figure to better interpret the magnetization maps.

From the *ab initio* calculations, we now focus on the magnetic interactions between the Mn center within a MnPc molecule and the Co/Cu(100) substrate separated by up to 3 ML of Cu. We recall that for $d_{Cu} = 0$, we experimentally and theoretically (see Chap. 9) found a ferromagnetic (FM) coupling between the Mn ion of a MnPc molecule and the Co(100) substrate. When 1 ML of Cu is inserted between the MnPc molecule and the Co(100) substrate, the coupling switches to antiferromagnetic (AF). Additionally, the Mn magnetic moment m_{Mn} of 2.54 μ_B for MnPc directly adsorbed onto Co increases to 2.78 μ_B when 1 ML Cu is inserted (see Figs. 10.1a-b and Tab.

Magnetic moments	$d_{Cu} = 0\,\mathrm{ML}$	$d_{Cu} = 1\,\mathrm{ML}$	$d_{Cu} = 2\,\mathrm{ML}$	$d_{Cu} = 3\,\mathrm{ML}$
Mn (μ_B)	+2.54	-2.78	+2.79	+2.8
N_nn (μ_B)	+0.01	+0.1	-0.1	-0.1
N_fn (μ_B)	+0.1	-0.04	+0.05	+0.01
C (μ_B)	-0.22	+0.08	-0.18	-0.21
Total Energies	$d_{Cu} = 0\,\mathrm{ML}$	$d_{Cu} = 1\,\mathrm{ML}$	$d_{Cu} = 2\,\mathrm{ML}$	$d_{Cu} = 3\,\mathrm{ML}$
$\Delta E = E_{AF} - E_{FM}$ (eV)	-0.437712	+0.11546299	-0.03491001	-0.0036827
$\mu_0 H_{ex}$ (T)	+1490	-360	+110	+12

Table 10.1. – **Calculated magnetic properties of MnPc/Cu(d_{Cu})/Co(100)**. Calculated spin moments of the different sites of MnPc on Cu(d_{Cu})/Co(100) as a function of d_{Cu}. N_nn (N_fn) denotes the nitrogen atoms that are the nearest (far) neighbors to the Mn ion. The magnetic moment of Co is positive (not shown).

10.1). For 2 and 3 ML Cu, the coupling between the Mn ion within MnPc and the Co substrate is FM, while $m_{Mn} = 2.8\,\mu_\mathrm{B}$ (see Tab. 10.1).

The C and N sites of a MnPc molecule on Co exhibit an adsorption-induced magnetic moment that is also coupled to the substrate (see Fig. 10.1c and Tab. 10.1). Inserting Cu layers between MnPc and Co do not significantly alter the magnetic moments of the MnPc molecular sites (see Fig. 10.1d and Tab. 10.1). In order to estimate the strength of the magnetic coupling, we calculated the system by imposing either FM or AF alignment of Mn within MnPc and Co as a function of the Cu-spacer thickness. The difference in total energy between FM and AF alignments gives an indication about the strength of the coupling. We transpose the energy difference into an effective exchange field H_{ex} using : $\mu_0 H_{ex} = {-\Delta E}/{2\mu_{Mol}}$ where μ_{Mol} is the molecule's average magnetic moment. As shown in Tab. 10.1, the effective exchange field H_{ex} strongly decreases when Cu is inserted, as direct exchange is replaced by interlayer exchange. However, for 3 ML Cu between MnPc and Co, we still have a substantial calculated IEC-induced exchange field of 12 T (see Tab. 10.1).

10.2. Investigated sample

To experimentally check the IEC-induced magnetic coupling of MnPc to Co through the Cu spacer, we fabricated samples such as presented in Fig. 10.2. Within the same sample, we have a Co/Cu/Co/Cu(100) stack, referred to as spintronic reference whose IEC-oscillation periods with the Cu-spacer thickness d_{Cu} are known and well
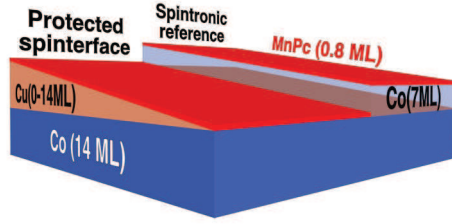
Figure 10.2. – **Investigated sample for the interlayer exchange coupling study**. Schematic of the sample used to study the IEC-induced coupling of MnPc to Co through a Cu spacer. On one side, referred to as the protected spinterface, the sample stack is MnPc(0.8 ML)/Cu(0 < d_{Cu} < 14 ML)/Co(14 ML)/Cu(100). On the other side of the sample, referred to as the spintronic reference, the stack is composed of MnPc(0.8 ML)/Co(7 ML)/Cu(0 < d_{Cu} < 14 ML)/Co(14 ML)/Cu(100).

referenced[34]; and a MnPc/Cu/Co/Cu(100) stack referred to as protected spinterface to probe the IEC-induced magnetic stabilization of MnPc.

To fabricate the sample, we cleaned a Cu(100) single crystal by repeated cycles of Ar-ion sputtering and annealing to 750 K. The first layer of Co was deposited on the sample held at room temperature and post annealed at 380 K for 10 min to flatten the surface. We crafted a Cu wedge from 0 to 14 ML by moving a shutter in front of the sample during the Cu deposition. During Cu deposition, the sample was held at 170 K to limit interdiffusion. The top Co layer on the spintronic reference stack, and the MnPc layer were deposited on the sample held at room temperature.

We calibrated MnPc and Co thicknesses using quartz microbalance, Auger microscopy and STM microscopy. We used quartz microbalance and STM microscopy for Cu-thickness calibration, and we fine tuned the calibration measuring the IEC-oscillation periodicity on the spintronic reference stack found using XMCD.

10.3. Magnetic coupling of Mn within MnPc to Co through Cu

We measured the magnetization of the Mn ion within MnPc to reveal the magnetic coupling of MnPc to the Co substrate through Cu. To do so, we measured the XMCD at the Mn L edges for different Cu thicknesses. Note that the spin sum rule cannot yield quantitative information about the Mn spin moment since the Mn L_3 and L_2 edges are overlapping.[236] However, we can track changes in the Mn magnetization by measuring the XMCD intensity at the Mn L_3 edge. Note also that all the following XAS measurements were performed under an angle of 40° between the surface and the photon-incidence direction.
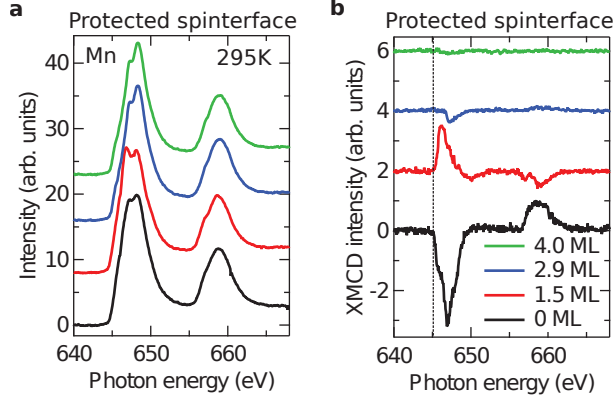
Figure 10.3. – **XAS and XMCD at the Mn $L_{3,2}$ edges of MnPc on Cu(d_{Cu})/Co(100) for different Cu thicknesses**. **a**, White line spectra at the Mn $L_{3,2}$ edges of MnPc on Cu(d_{Cu})/Co(100) for d_{Cu} = 0 ML, 1.5 ML, 2.9 ML and 4.0 ML. **b**, XMCD spectra at the Mn $L_{3,2}$ edges of MnPc on Cu(d_{Cu})/Co(100) for the Cu thicknesses enumerated in **a**. The spectra were acquired at 295 K in 0.1 T, and are vertically shifted for clarity.

In Fig. 10.3a, we present XAS spectra at the Mn $L_{3,2}$ edges of MnPc on Cu(d_{Cu})/Co(100) (protected spinterface structure) acquired at 295 K in 0.1 T for selected Cu thicknesses d_{Cu}. The Mn L_3 adsorption edge shifts and is altered when the adsorption surface is changed from Co to Cu.[5] In Fig. 10.3b, we show XMCD spectra at the Mn $L_{3,2}$ edges at 295 K in 0.1 T on the protected spinterface structure for the Cu thicknesses selected in Fig. 10.3a. Note that the 0.1 T external magnetic field was used to increase the electron yield, that in turn increase the signal-to-noise ratio. Additionally from the 0.1 T magnetic field, we know and confirmed by XMCD measurements (not shown) that the 14 nm-thick Co layer is saturated. For d_{Cu} = 0 ML, *i.e.* for MnPc molecules directly adsorbed on Co(100), we found the usual negative sign of the L_3 edge and positive sign of the L_2 edge, indicating a FM coupling between the Mn ion within MnPc and the Co substrate (see Ref. 5 and Chap. 9). Yet, when the MnPc molecules are separated by 1.5 ML Cu from the Co(100) substrate, the XMCD spectra at the Mn $L_{3,2}$ edges is reversed, which corresponds to an AF alignment of the Mn and Co magnetic moments. For 2.9 ML and 1.5 ML, the XMCD at the Mn L_3 edge is negative again, though with decreased intensities, and implies a return to FM coupling. Note that the XMCD integral is different from zero for the different thicknesses, suggesting the presence of a non-negligible orbital moment. However care must be taken as the XAS spectra in Fig. 10.3a suggest different oxidation state for the Mn ion and a mixing of the oxidation states would prevent us to apply the sum rules.

These results are impossible in the absence of a strong IEC-induced effective exchange field H_{ex}. Indeed, for T = 295 K and an external magnetic field of 0.1 T, the

proportion of paramagnetic Mn moments that are aligned with the external magnetic field would lead to a negligible positive XMCD intensity at the Mn L_3 edge. Furthermore, the reversed Mn XMCD spectrum for 1.5 ML of Cu spacer cannot be explained in terms of MnPc molecules in direct contact to the Co, which could arise from an imperfect growth of the Cu spacer. Alternatively, these results are consistent with an IEC-induced coupling of the Mn ion within MnPc molecules to the Co substrate through Cu and in agreement with the theoretical prediction discussed in Sec. 10.1. Note that for $d_{Cu} = 1.5\,$ML the XMCD spectrum at the Mn edge arises from MnPc molecules sitting on 1 or 2 ML of Cu. However, the measured mean Mn magnetization dominantly comes from MnPc on Cu(1 ML)/Co(100) as the magnetic-coupling strength rapidly decreases with increasing Cu thickness.

To more systematically evaluate the impact of the Cu-spacer thickness d_{Cu} on the magnetic coupling between the Mn ion within MnPc and the Co(100) substrate, we extract the XMCD intensity at the Co and Mn L_3 edge by measuring helicity- and magnetic-field-dependent absorption before and at each edge over the Cu wedge. This technique allows to perform a large number of measurements but yields only a qualitative thickness dependence of the IEC-induced magnetic coupling as the Mn L_3-edge XMCD evolves with increasing Cu thickness (see Fig. 10.3b). In Fig. 10.4a, we present the Co L_3-edge XMCD as a function of the Cu-spacer thickness at 295 K in 0.1 T on the spintronic reference structure. For low Cu thicknesses, the magnetizations of both Co layers are aligned along the external magnetic field yielding the usual negative XMCD at the L_3 edge.[98] With increasing Cu thickness, the XMCD intensity changes sign for d_{Cu} = 6.9 ML, what suggest an IEC-induced AF alignment of the Co layers.[34, 237, 238] We also observed pronounced changes for $d_{Cu} \approx 9.5\,$ML and $d_{Cu} \approx 12.2\,$ML, which do not yield opposite sign. The absence of sign reversal can come from: (i) the temperature and the external magnetic field that work against an IEC-induced AF configuration; and (ii) the finite size of the X-ray beam that can compensate otherwise opposite signals, particularly for weak IEC for large Cu thicknesses.

We qualitatively reproduce the Co XMCD as a function of the Cu-spacer thickness by using the analytic expression of IEC (see gray line in Fig. 10.4a)[34] :

$$J_{IEC} = \frac{A_l}{d_{Cu}^2}\left[\sin\left(\frac{2\pi d_{Cu}}{\Lambda_l} + \phi_l\right) + \frac{A_l}{A_s}\sin\left(\frac{2\pi d_{Cu}}{\Lambda_s} + \phi_s\right)\right]. \qquad (10.1)$$

A negative (positive) J_{IEC} indicates an AF (FM) coupling. Λ_s and Λ_l are the short and long oscillation periods that we fixed to the widely reported values of 2.7 ML and 5.6 ML, respectively.[237–239] We also fixed the ratio A_s/A_l to 1.2 as done by Ref. 237. We fitted the data presented in Fig. 10.4a with Eq. 10.1 and the best fit was found for ϕ_s = 1.15 rad and ϕ_l = −3.34 rad, which depend on the nature of the entire stack.[240] Note that we do not observe XMCD sign reversal for $d_{Cu} \approx 4.2\,$ML as expected from Eq. 10.1. This AF configuration is seldom observed most likely due to roughness of the Cu interlayer.[241] The evolution of the XMCD at the Mn L_3 edge on the spintronic reference structure mimics that of the Co XMCD since the Mn ion
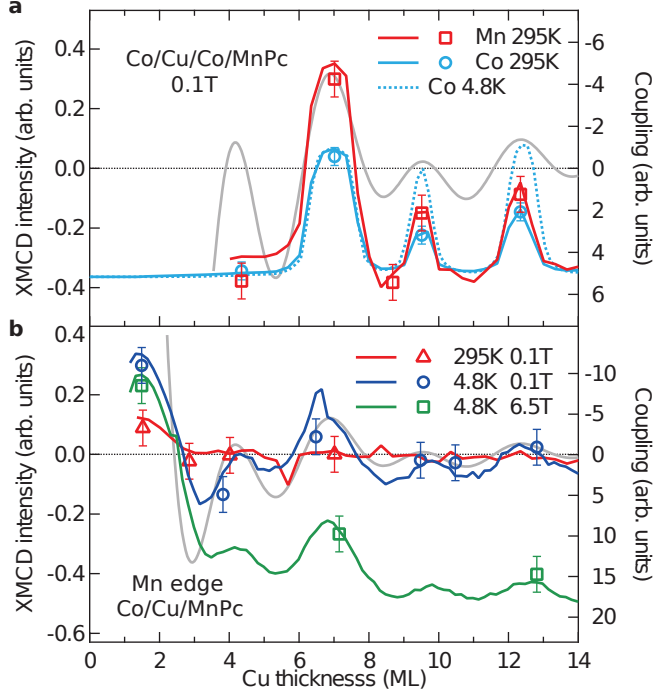
Figure 10.4. – **Oscillations of the interlayer exchange coupling with the spacer thickness for the spintronic reference and the protected spinterface structures**. **a**, Cu-thickness dependence of the XMCD spectra at the Co L_3 edge (786.0 eV) at 295 K and at 4.8 K; and at the Mn L_3 edge (646.8 eV) in $\mu_0 H = 0.1$ T on the spintronic reference structure. **b**, XMCD intensity at the Mn L_3 edge as a function of the Cu thickness on the protected spinterface structure for different temperatures and magnetic fields. The makers represent the XMCD intensity extracted from XMCD spectra used to scale and position the measurements limited to the XMCD intensity of the given edge (continuous line). The Mn XMCD spectra were multiplied by 65 to have XMCD intensities comparable to that of Co. The theoretical Cu-thickness dependence of the magnetic coupling energy J_{IEC} described by Eq. 10.1 is represented in full gray and scaled on the right axes.

within MnPc is FM coupled to the underlying Co. In turn, this demonstrates that IEC switches the top Co layer's magnetization.

Having calibrated the IEC response as a function of Cu thickness using the well known spintronic reference, we now examine the evolution of the XMCD intensity at the Mn L_3 edge as a function of the Cu-spacer thickness on the protected spinterface structure. At 295 K in 0.1 T, the Mn XMCD oscillates with increasing Cu thickness d_{Cu} at the same periodicity than J_{IEC} with decreasing amplitude (see Fig. 10.4b).

For the same measurement performed for T = 4.8 K, the Mn XMCD oscillations are stronger and span over a larger Cu-thickness range. This is expected from the paramagnetic Mn sites whose magnetization follows a Brillouin function. Indeed, the Mn XMCD tracks the mean Mn magnetic moment aligned along the photon incident-vector referential that is essentially dictated by the effective field $H_{eff} = H_{ex} + H$ and the temperature T through a Brillouin function. In turn, H_{ex} is directly linked to J_{IEC} that is expected to decrease with the Cu thickness as $1/d_{Cu}^2$. At 4.8 K increasing the external magnetic field from 0.1 T to 6.5 T only shifts the Mn XMCD towards larger negative values as a larger proportion of Mn magnetic moments are aligned along the field, and thus to the magnetization of the Co layer (see Fig. 10.4b).

10.4. Estimation of the coupling strength

From the previous section, we know that the paramagnetic Mn within MnPc on Cu/Co(100) is magnetically stabilized by IEC. The XMCD intensity, and thus the Mn magnetization, depends on the strength of the effective exchange field H_{ex} that is Cu-thickness dependent; and on the temperature. In this section, we want to estimate H_{ex} for given Cu-spacer thicknesses.

The proportion of Mn magnetic moments aligned in the direction of an external magnetic field H at a given temperature T is given by a Brillouin function:

$$B_J\left(\frac{\mu_0 H}{T}\right) = \frac{2J+1}{2J}\coth\left(\frac{2J+1}{2J}\frac{g\mu_B J}{k_B}\frac{\mu_0 H}{T}\right) - \frac{1}{2J}\coth\left(\frac{1}{2J}\frac{g\mu_B J}{k_B}\frac{\mu_0 H}{T}\right) \quad (10.2)$$

where J is the total angular momentum quantum number that we consider equal to $S = 3/2$, g the Landé factor taken equal to 2, μ_B the Bohr magneton and k_B the Boltzmann constant.

On the protected spinterface structure, the Mn magnetic moments not only feel the external magnetic field H but also the effective exchange field H_{ex} coming from the interlayer exchange coupling through the Cu layer. Thus, the total effective magnetic field applying on the Mn magnetic moments is the sum of the two fields: $H_{eff} = H + H_{ex}$. H_{eff} can be opposed to the external magnetic field H thanks to IEC, and lead to an anti-alignment of the Mn magnetic moment with the external magnetic field. For the Brillouin function (Eq. 10.2) of paramagnetic Mn on the protected spinterface, we can thus replace the external field H by the total effective magnetic field H_{eff}. In the following we will investigate the field (H) and temperature (T) dependence of the Mn magnetization for two different Cu-spacer thicknesses and fit the data with a modified Brillouin function $B_J\left(\mu_0[H+H_{ex}]/T\right)$.

In Fig. 10.5, we show XMCD spectra at the Mn $L_{3,2}$ edges for different magnetic fields and temperatures for Cu thicknesses of 1.5 ML and 7 ML on the protected spinterface structure. For d_{Cu} = 1.5 ML, the XMCD spectrum indicates an anti-
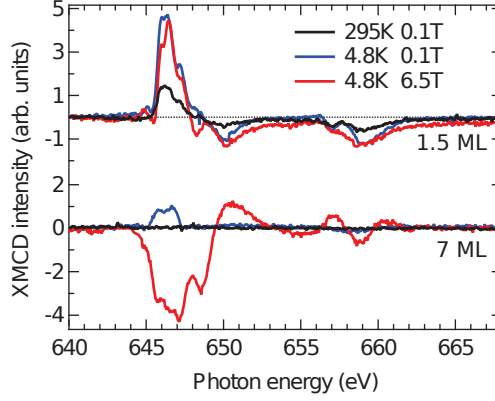
Figure 10.5. – **Field and temperature dependence of the XMCD at the Mn $L_{3,2}$ edges for MnPc on Cu/Co(100)**. XMCD spectra at the Mn $L_{3,2}$ edges acquired for different magnetic fields, temperatures and for Cu thickness of 1.5 ML (upper panel) and 7 ML (lower panel).

alignment of the Mn magnetic moments with the applied magnetic field (and with the underlying Co magnetization) at any investigated temperatures and fields. Notably the XMCD spectra acquired at 4.8 K in 6.5 T reveals an effective exchange field H_{ex} lower (larger negative values) than −6.5 T. For d_{Cu} = 7 ML, we observe no noticeable dichroic signal at room temperature, while at 4.8 K the XMCD spectra indicate a switch from an AF to a FM alignment when increasing the external magnetic field from 0.1 T to 6.5 T. This unveil an effective exchange field H_{ex} between 0.1 T and 6.5 T for a Cu thickness of 7 ML.

We extract the XMCD intensities at the Mn L_3 edge of the different XMCD spectra presented in Fig. 10.5, and fit the XMCD intensities with a modified Brillouin function $B_J\left(\mu_0 H + H_{eff}/T\right)$ (see Fig. 10.6). Note that here we assume that H_{ex} is independent of the temperature T. The free parameters of the fit are $H_{ex}^{1.5\,\mathrm{ML}}$ and $H_{ex}^{7\,\mathrm{ML}}$ that represent the effective exchange field for Cu thicknesses of 1.5 ML and 7 ML, respectively. For d_{Cu} = 1.5 ML, we found a strong effective exchange field of $\mu_0 H = (-78 \pm 35)\,$T. For d_{Cu} = 7 ML, the effective exchange field is quite reduced but still negative $\mu_0 H = (-0.8 \pm 0.5)\,$T as expected from Eq. 10.1. Note that the uncertainties associated to the effective exchange fields are relatively high and arises from the limited number of points in Fig. 10.6. We believe that this approach to measure the effective exchange fields can lead to accurate values provided that the number of experimental points is high enough.
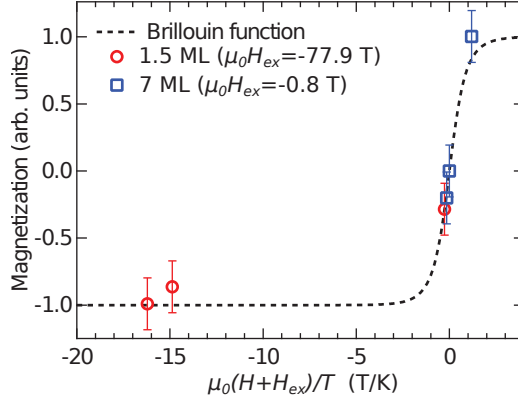
Figure 10.6. – **Estimation of the effective exchange field**. Results of
the fit of the field- and temperature-dependent XMCD intensities at the
Mn L_3 edge (spectra presented in Fig. 10.5) with a Brillouin function in
which the external applied magnetic field is replaced by the effective field
$H_{eff} = H + H_{ex}$.

10.5. Spin polarization close to the Fermi energy

As most of the molecule-deposition techniques use solvents that usually alter the
properties of the FM layer and the interface, the molecular candidates to craft room-
temperature spinterfaces were, until now, drastically limited. Note that oxide FM
layer are resilient to oxidation but cannot generate an efficient spinterface at room
temperature. Nevertheless, protected spinterfaces may be fabricated by depositing
molecules through "wet" techniques onto a noble-metal spacer, such as Au that can
sustain QWSs[34] while remaining impervious to oxidation. We thus believe that pro-
tected organic spinterfaces are conceptually superior to standard spinterfaces.[6] In this
vein, we theoretically consider the spintronic performance of a MnPc/Cu(d_{Cu})/Co(100)
protected spinterface. To do so, we examined the DOS within $E_F - 25 < E(\text{meV}) <
E_F + 25$, *i.e.* the DOS that contributes to transport at room temperature. In Tab.
10.2, we report the evaluated spin polarization P from the integrated DOS close to the
Fermi level. For $d_{Cu} = 0$ ML, we found the already reported large positive polariza-
tion.[6] Yet, for $d_{Cu} = 1$ ML, there is nearly no states in the spin ↑ channel, leading to
a surprisingly large negative polarization of −98 %. For $d_{Cu} = 2$ ML, the polarization
turns back to positive (+30 %) and even increases to 75 % when adding an additional
Cu layer ($d_{Cu} = 3$ ML). Note that in all cases, the spin polarization mainly arises
from the C sites.

The spin-polarized DOS integrated from $E_F - 25$ meV to $E_F + 25$ meV will con-
tribute to the spin-polarized transport across the interface as weighed by the molecule's
hybridization to the underlying Cu surface. To evaluate this aspect, we show in Fig.
10.7 spin-polarized spatial maps of MnPc on Cu(d_{Cu})/Co(100) for $d_{Cu} = 0$ ML, 1 ML,
2 ML and 3 ML. We can observe that the Cu DOS is changing with increasing Cu
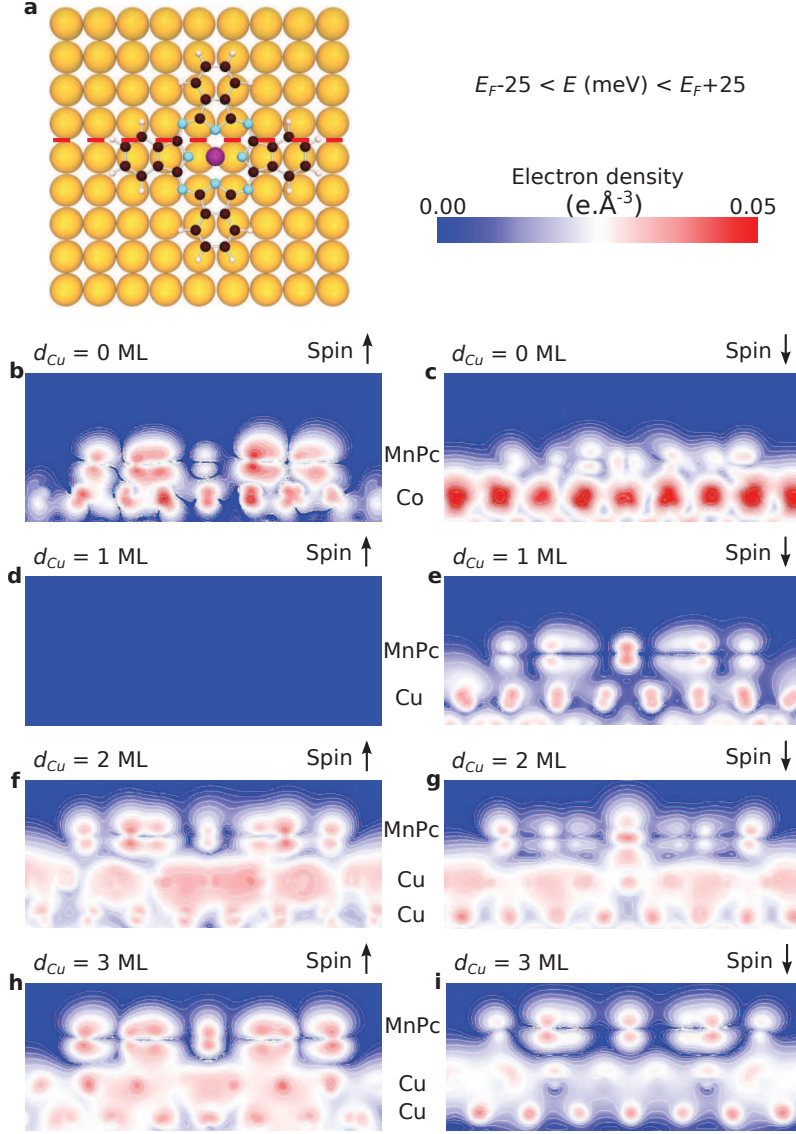
Figure 10.7. – **Spin-polarized spatial maps of the Co/Cu/MnPc protected spinterface**. **a**, Top view of a calculated MnPc molecule on Cu(d_{Cu})/Co(100). **b-i**, Spin-dependent spatial charge-density maps, taken along the red dashed line represented in **a**, for different Cu thicknesses. The maps show how the numerous N and C sites of MnPc on Cu(d_{Cu})/Co(100) exhibit a highly spin-polarized DOS close to E_F. Furthermore the molecule hybridization to the surface is spin dependent. The maps are in e.Å^{-3}.

Spin polarization	$d_{Cu} = 0\,\mathrm{ML}$	$d_{Cu} = 1\,\mathrm{ML}$	$d_{Cu} = 2\,\mathrm{ML}$	$d_{Cu} = 3\,\mathrm{ML}$
z-P ($E_F \pm 25\,\mathrm{meV}$) (%)	+65.8	-98.3	+30.0	+74.0
pl-P ($E_F \pm 25\,\mathrm{meV}$) (%)	-69	-99.2	+17.0	+51.1
Total P ($E_F \pm 25\,\mathrm{meV}$) (%)	+50.2	-98.4	+29.3	+73.3

Table 10.2. – **Calculated spin polarization of MnPc/Cu(d_{Cu})/Co(100) close to E_F.** pl-P (z-P) are evaluated from the integrated spin-dependent planar (z) DOS from $E_F - 25\,\mathrm{meV}$ to $E_F + 25\,\mathrm{meV}$.

thickness, which in turn modulates the spin-dependent hybridization between the metal surface and the MnPc molecule. For instance, for $d_{Cu} = 2\,\mathrm{ML}$ (see Fig. 10.7d-e) the hybridization is rather similar for both spin channels, while for $d_{Cu} = 3\,\mathrm{ML}$ (see Fig. 10.7h-i) the molecule hybridization to the metal surface is strongly asymmetric. This shall promote a spin-polarized transport across the interface that is higher than that inferred from DOS considerations alone.

10.6. Partial conclusion

In this chapter, we have experimentally and theoretically shown that MnPc can be magnetically coupled to a FM Co layer through a Cu spacer by IEC. The IEC-oscillation period is found to be the same than that of the Co/Cu/Co spintronic reference structure. In addition, we observed oscillation for low Cu thicknesses that are usually not visible for standard IEC systems.

Compared to other IEC studies using ultra-thin paramagnetic layers (Fe[242] or Pd[243]), our use of Mn paramagnetic centers with low-susceptibility allows to directly estimate the IEC strength (see Sec. 10.4). More generally, this probing of IEC using paramagnetic centers within a molecular cage deposited atop the FM-metal bilayer offers important advantages. The molecular cage that contains the paramagnetic center hinders (for ML coverage) clustering of the paramagnetic centers that would modify the effective paramagnetic properties. In addition, the molecular cage refrain the paramagnetic center to interdiffuse within the spacer layer (here Cu). The absence of magnetic interactions between the paramagnetic centers also circumvents possible competitions between several effective exchange fields H_{ex} on terraced Cu surface. We believe that this last point is the reason for the observation of IEC oscillations at low Cu thicknesses (see Fig. 10.4) compared to standard IEC systems. These aspects thus underscore an interesting opportunity to further explore the physics of IEC and QWS in systems whose understanding has thus far been tainted by growth challenges,[244] notably by directly measuring the IEC strength.

In this part, we investigated metal-molecule spinterfaces using phthalocyanine-based molecules. These spinterfaces show promising properties for spin-polarized

transport, and thus for magnetoresistance-based devices. Alternatively, we have shown that the spinterface can stabilize an AF order within a molecular semiconductor, and lead to exchange bias. In the next part, we will study functional molecules on metallic surfaces, which can conceptually conduct to superior magnetoresistance-based devices. Indeed, by changing the molecular state of the molecules composing the organic layer with external triggers, we could change the spin-filtering properties of the organic layer as well as the spinterfaces within the same device.

Part III.

Investigation of organic functional molecules on surfaces: spin-crossover molecules

11

Introduction to functional molecules

Molecular electronics aim at building electronic components from a single molecule by combining the expertise of chemistry and physics. The desired electronic function should in a first step be encoded into a single molecule, and in a second step the single-molecule device should be connected to electrodes. There are multiple advantages of such an approach and we will only enumerate three of them. First, the properties and/or functions of the molecule can be optimized by subtle changes of the molecular structure. Second, as carbon is an abundant element, carbon-based single-molecule devices can in principle be produced at low costs. Third, the long spin lifetime in carbon-based elements, due to low spin-orbit coupling, make them interesting for the nascent field of molecular spintronics,[3] where the spin degree of freedom is used in addition to the charge.

In 1974, Aviram and Ratner[245] proposed a theoretical description of a rectifier out of a single molecule. The community then realized the great potential of molecular electronics and many possible functions were identified such as molecular resistors, diodes, switches/memories, capacitors, field-effect transistors and even unimolecular amplifiers.[246,247] In the following we will focus the discussion on molecular switches[248,249] as there is, a priori, no need to integrate these molecules in an electronic circuit to observe the different stable states.

11.1. Molecular switches

Molecular switches are typically molecules that present a bistability, *i.e.* the molecules present two stable states separated by an energy barrier (see Fig. 11.1). One state is the ground state, while the other state is a metastable state with a higher energy. Ideally for the stability of the molecular switch, the energy barrier necessary to overcome for switching between the states is much larger than the thermal energy $k_B T$. There
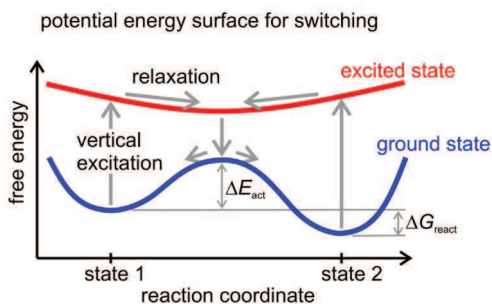
Figure 11.1. – **Schematic of the typical potential energy surface of a two-state molecular switch**. The x axis is the reaction coordinate, *i.e.* a quantity that describe the passage between the two states, such as a distance between two atoms. The potential energy of a bistable molecule presents two minima separated by a potential barrier along the reaction coordinate. The two minima correspond to molecular states; one of the state is the ground state, while the other state is usually metastable with a higher energy. Switching the molecule from one state to another can be achieved by overcoming the potential barrier, or by bringing the molecule into an excited state, that eventually relaxes into the other spin state. Figure is taken from Ref. 248.

are usually two different ways to switch the state of the molecule. (i) One brings the molecule into an excited state, which in turn eventually relaxes into the other state. (ii) The molecule overcomes the potential barrier for instance by transferring energy to the molecule or by modifying the potential landscape with an electric field.

When such molecular switches are deposited on surfaces or connected to electrodes, the electronic coupling between the molecule and the substrate influences the molecule's properties. There are two possible outcomes depending on the strength of the electronic coupling. In the case of a weak electronic coupling, the molecule keeps its switching property that is then referred as an intrinsic property, while in the case of strong electronic coupling, the molecule can lose its functionality. Interestingly, the reverse phenomenon is also possible, *i.e.* a non-switchable molecule may develop a switching property once deposited onto the surface. The switching property is then referred to as extrinsic.[248] In the rest of this thesis, we will focus on systems with intrinsic switching properties.

Within a single-molecule switch, what distinguishes the two different states? One may divide the molecular switches into two different categories: conformational and charging/redox switches. For conformational switches, the two states of a molecular switch correspond to two different isomers of the molecule. Both states are thus differentiated by the three-dimensional structure of the molecule. For charging/redox switches, a molecule gains or loses an electron leading to a different charge state of the molecule.[248] Note that the two charge states may present minor conformational

changes but the above categories remain clear since the charge of conformational switches do not change.

Yet, provided that the state of the molecular switch can be easily read, *e.g.* if the molecular states have different conductance, the molecule can possibly be used as a memory element. The memory element would have advantageous properties with respect to the size of the element (in the order of the nanometer) and the stability of the states over time that depends on the height of the energy barrier.

11.2. Stimuli

There is a wide variety of external stimuli that are known to operate molecular switches[248]:

Current Electrons traveling through a molecular switch in a given state may have sufficient energy to excite the molecule into an excited electronic or vibrational level, which in turn relaxes into the other state.[248, 250] In the cases where the energy of the electrons is not sufficient to bring the molecule to the appropriate excited state or to overcome the energy barrier, the latter can be "climbed" by subsequent excitations into higher vibrational levels of the molecule, *i.e.* the switching process involves several electrons.[251]

Electric field When an external electric field is applied, the latter can couple to the dipoles within the molecule, and the resulting torque can eventually drive the switching (Stark effect). Note that a strong electric field can even induce a dipole moment in the molecule, which in turn couples to the field.

Light The absorption of a photon of sufficient energy can bring a switchable molecule to an excited state (such as depicted in Fig. 11.1). The molecule in the excited state relaxes either back to the ground state or to a metastable state (the two minima in Fig. 11.1). In a certain percentage of cases, this lead to switching.

Redox potential An external gating can change the relative position of the molecular orbitals with respect to the Fermi level. Thus, by varying the gating voltage, it is possible to change the charge state of a molecular switch.[248]

Temperature The potential barrier between the two states of a molecular switch can eventually be overcome by thermal energy, provided that the barrier height is low enough. Note that the temperature can also drastically change the stability of the molecular switch, *i.e.* the lifetimes of the molecular states decrease upon heating.

11.3. Towards spin-crossover molecules

We recall that the work on phthalocyanine molecules on magnetic substrates (see previous chapters) shows promising properties for spin-valve devices. In such devices,

the Pc molecules, where the spin lifetime is expected to be long, would be sandwiched between two magnetic electrodes. The molecular-junction conductance would then depend on the relative orientation of the magnetic-layer magnetization, leading to a 2-state junction. Yet, if the molecular tunneling barrier is composed of functional molecules, such as a molecular switch with state-dependent conductance, the molecular junction would have 4 states. One would then drastically increase the density of the memory bits.

Arguably, the best molecular-switch candidate would be spin crossover (SCO) molecules. Indeed, as we will discuss in Chap. 12, SCO molecules present two different spin states corresponding to two different conformations that can be addressed by various stimuli (temperature, pressure, magnetic field, light, electric field). The many possible stimuli known for bulk SCO molecules make them very appealing. In addition, we can speculate that the different conformations lead to different conductance, and that the two different spin states lead to different spin coupling and spin filtering properties within a junction.

Since at the time of the study, there were almost no report of ultra-thin films of SCO molecules, and since SCO molecules also have a great potential for many technological applications (see Sec. 12.4), we will first study SCO molecules on non-magnetic surfaces. In the next chapters, after introducing the SCO phenomenon and the $Fe(phen)_2(NCS)_2$ (Fe-phen) molecule (Chap. 12), *i.e.* the SCO complex that we want to study, we will discuss about the first-monolayers growth of Fe-phen on different surfaces (Chap. 13) and the identification and spin-state switching of Fe-phen on various surfaces (Chap. 14). Finally, we will investigate the surprising spin-state coexistence that we observe at low temperature (Chap. 15).

Spin-crossover molecules

Spin crossover (SCO) complexes can be found in nature, such as in minerals.[252] It also plays a fundamental role in the biological functions of a number of haem derivatives.[253] In particular hemoglobin that carries the oxygen from the lungs to the muscles is known to change its spin state upon adsorption of oxygen, and leads to an increased efficiency of oxygen transport.[254]

In 1931, Cambi *et al.* reported the first SCO arising from a synthesized molecule.[255] Since then, the field has considerably grown and the number of SCO complexes drastically increased.[256–262]

In next chapters of the manuscript, we will present the results obtained on the $Fe(phen)_2(NCS)_2$ SCO molecule, molecule that we introduce in the first section of this chapter. We will then discuss about the thermodynamic picture of SCO as well as the different SCO triggers reported in the literature. Finally, we will discuss about possible technological applications of SCO-based devices.

12.1. $Fe(phen)_2(NCS)_2$ molecules

12.1.1. General information

Cis-bis(thiocyanato)bis(1,10-phenanthroline)-iron(II) molecule that is more generally referenced as $Fe(phen)_2(NCS)_2$ (Fe-phen), is among the first synthesized Fe^{2+} complex exhibiting SCO. It was initially reported by Baker et al.[263] in 1964 and then widely studied in the bulk powder form.[264–268]

Fe-phen is composed of a Fe^{2+} ion surrounded by two phenanthroline (phen) and two thiocyanate groups as represented in Fig. 12.1a. The ligands induce an electric field on the Fe^{2+} ion and the ligand-field theory in the octahedral case predicts the
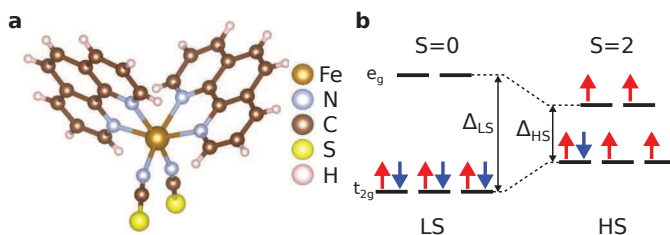
Figure 12.1. – **Single Fe-phen molecule and electronic configuration**. **a**, Model of a single Fe-phen molecule composed of a central Fe^{2+} ion surrounded by two phenanthroline groups and two thiocyanate groups. **b**, Simplified electronic configuration of the six d electrons of the Fe ion in the LS and HS states.

splitting of the five $3d$ orbitals into e_g and t_{2g} orbitals (see Chap. 2). Note that here the anti-bonding orbitals e_g^* are referred to as e_g. SCO complexes present two stable configurations with different ligand-field strength. In the low-spin (LS) state, the ligands are closer to the metallic ion, giving rise to a large ligand field. The electrons then occupy only the t_{2g} orbitals leading to a total spin state S=0. In the high-spin (HS) state, the ligands are further away from the metallic ion resulting in a lower ligand field, and thus a lower energy splitting Δ_{HS} between e_g and t_{2g} orbitals. Δ_{HS} becomes lower than the electron-pairing energy and leads to an electronic configuration with a total spin state S=2 (see Fig. 12.1b).

The geometry of the molecule is modified upon spin transition, especially the Fe-N bond lengths and angles. In the HS state, the Fe-N (phen) bonds are in average about 0.15 Å larger than the Fe-N (NCS) bonds. Moreover, the N-Fe-N bond angle connecting the two nitrogen atoms of a single phenanthroline to the central Fe ion is about 76° in the HS state to compare to the 90° required for a perfect octahedron. In the LS state, the N-Fe-N bond angles are approaching 90°. Furthermore, the Fe-N (phen) bonds are shortened by about 0.20 Å, and Fe-N (NCS) bond lengths are reduced by 0.10 Å. The decreased Fe-N bond lengths is the result of the population of the non-bonding t_{2g} orbitals at the expense of the anti-bonding e_g orbitals.

12.1.2. Crystal structure

The Fe-phen molecules can be synthesized by following one of the two reported methods:

- **Extraction method**: Removal of a phen group from $[Fe(phen)_3](NCS)_2 \cdot H_2O$.[269, 270]

- **Precipitation method**: Addition of phen groups to $Fe(py)_4(NCS)_2$ or to $Fe(NCS)_2$[269, 271]

Both methods lead to the same crystal structure but the extraction method is known to have less HS residues at low temperature as well as a sharper thermal spin

	HS state	LS state
a (Å)	13.1612 (18)	12.7699 (21)
b (Å)	10.1633 (11)	10.0904 (25)
c (Å)	17.4806 (19)	17.2218 (30)
Volume (Å^3)	2338.2	2219.0

Table 12.1. – Crystallographic parameters for the HS and LS states of Fe-phen.[266]

transition. The differences in the completeness and sharpness of the spin transition is ascribed to different crystal qualities, the best quality obtained with the extraction method.[265, 266, 271]

The crystal system is orthorhombic, and each unit cell contains two right- and two left-handed enantiomers of the chiral Fe-phen molecule. The space group is Pbcn and is independent of the spin state of the molecule.[266] The lattice constants and the volume of the unit cell is reported in Tab. 12.1 for both spin state. The volume of the unit cell is found to decrease by about 5 % upon spin transition from the HS to the LS state.

In Fig. 12.2, we represent the stacking of the molecules along the b and c axes. The molecular pattern along the b axis consists of the same molecule simply being translated. The structure along the c axis can be obtained by performing a glide reflection (mirror plane perpendicular to the c axis) together with a rotation of π. This configuration allows to have $\pi-\pi$ interactions between the phenanthroline groups, such as represented by dashed double arrows in Fig. 12.2. For the last dimension, the b-c plane is reproduced and translated by $\frac{1}{2}a + \frac{1}{2}b$.[266, 272]

The prototypical Fe-phen molecule was chosen as the candidate molecule to investigate SCO at the single molecule level since (i) it has been well studied in the bulk form, (ii) the low spin state is non-magnetic with a total spin $S = 0$, (iii) successful sublimation was reported for this molecule.[274] The Fe-phen molecules for this work were synthesized by Guillaume Rogez following the extraction-method procedure described by Akabori *et al.*[270]

12.2. Thermodynamics of spin-crossover complexes

12.2.1. Definition of the thermodynamic quantities

In this section, we are interested in a thermodynamic picture of spin crossover as it helps to understand the effect of temperature, pressure and even magnetic field on SCO complexes.
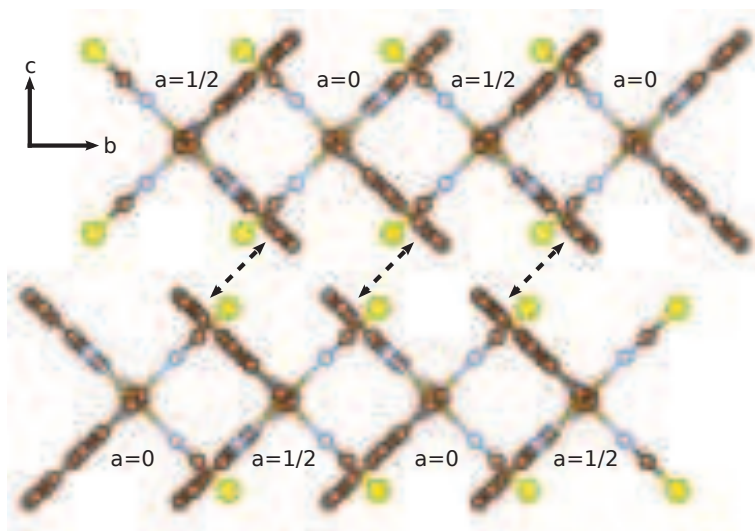
Figure 12.2. –   **Bulk structure of Fe-phen**. The unit cell contains four
molecules and is repeated once along the b axis. The figure has been
created with VESTA[273] using the crystallographic data from Gallois *et
al.*[266]

As we will impose the temperature and the pressure applied onto the system, the
Gibbs free energy is the good thermodynamic quantity to use to predict the reaction
direction. In the present case, we let the system evolve between the HS and LS states,
and thus we are interested in the relative difference in Gibbs free energy:

$$\Delta G(T,p) = G_{HS}(T,p) - G_{LS}(T,p) = \Delta H - T\Delta S. \qquad (12.1)$$

ΔH and ΔS correspond to the variation of molar enthalpy and molar entropy,
respectively. The above formula is valid if one considers the molecules as independent
quantities (no cooperativity) and it follows that the thermodynamic stable state is
the one that has the lowest Gibbs free energy.

The variation of enthalpy between the HS and LS states originates mainly from
the energy difference between the lowest spin-orbit ligand-field states of the HS and LS
multiplet, respectively. In addition, there are intra- and inter-molecular vibrational
contributions but in a much lower proportion.[257, 275]

ΔS refers to the difference in entropy between the HS and the LS states, and
can be also separated between electronic and vibrational contributions. The electronic
contribution originates from the electronic degeneracy that can be separated into spin
and orbital degeneracies. The spin degeneracy is expressed as:

$$\Delta S_{el}^{spin} = R\left[ln\left(2S+1\right)_{HS} - ln\left(2S+1\right)_{LS}\right]. \tag{12.2}$$

So, for Fe^{2+} in an octahedral symmetry with $S = 2$ ($S = 0$) for the HS (LS) state, ΔS_{el}^{spin} is equal to $13.38\,\mathrm{J\,K^{-1}\,mol^{-1}}$. In practice there is no orbital degeneracy as any orbital degeneracy would be lifted by a symmetry reduction caused by the Jahn-Teller distortion.[276]

Sorai and Seki[277] performed precised calorific measurements on Fe-phen, and pointed out that the electronic contribution to the total entropy variation is only about one third, and the remaining entropy variation arises from vibrational contributions (with $\Delta S_{vib} > 0$). Upon spin crossover, the metal-ligand bond lengths are modified such that the phonon modes are changed and have different stretching frequencies. In turn it explains the large spin-state dependence of the vibrational entropy.[275, 277]

Both ΔH and ΔS are positive[275, 277–280] such that at $T = 0\,\mathrm{K}$, $\Delta G = \Delta H$ and the LS state is thermodynamicaly preferred over the HS state. From Eq. 12.1, we can see that when the temperature is increased, ΔG is reduced and can become zero at $T_{1/2} = \Delta H/\Delta S$ referred to as the transition (or critical) temperature. At $T_{1/2}$, the two spin states are equienergetic in terms of Gibbs free energy and thus have equal probability to be populated. When the temperature is further increased, ΔG becomes negative favoring the HS state. The $T\Delta S$ term in Eq. 12.1 modulates the difference in Gibbs free energy between the HS and LS states, and thus, the entropy is often referred to as the driving force of the spin transition.[275, 278, 279]

12.2.2. Spin crossover in a crystal and cooperativity

When we consider spin crossover in a crystal, there is an additional entropy term compared to Eq. 12.1, arising from a coexistence of HS and LS molecules in the crystal. In addition, we recall that the spin crossover changes the volume of the unit cell, such that a spin transition that occurs at a given position of the crystal can induce the transition to its neighbor by elastic interactions. This elastic effect that can also be seen as an internal pressure, is in general referred to as cooperativity.[281, 282]

In 1972, Slichter and Drickamer[283] were the first to introduce an *ad hoc* cooperative term Γ, as well as a mixing entropy term S_{mix} in the Gibbs free energy G to model SCO in solids. In addition, we define p_{HS} (p_{LS}) the molar fraction of molecules in the HS (LS) states in order to account for the possibility to have both spin states into the crystal. The Gibbs free energy then reads:

$$G = p_{LS}G_{LS} + p_{HS}G_{HS} - TS_{mix} + \Gamma p_{HS}\left(1 - p_{HS}\right). \tag{12.3}$$

The mixing entropy term has the following expression[283]:

$$S_{mix} = -R\left(p_{LS}\ln p_{LS} + p_{HS}\ln p_{HS}\right). \tag{12.4}$$
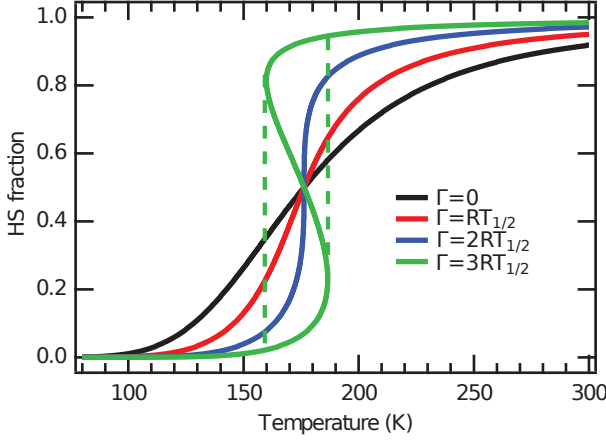
Figure 12.3. – **Proportion of high-spin molecule as a function of temperature**. The different temperature-dependent proportions of HS molecules were calculated using Eq. 12.6 considering different values for the cooperative term Γ. We used $\Delta H = 8600 \, \text{J mol}^{-1}$ and $\Delta H = 48.78 \, \text{J mol}^{-1} \, \text{K}^{-1}$ corresponding to the enthalpy and entropy variation of Fe-phen.[277]

We recall that $\Delta G = \Delta H - T\Delta S$, and the energy origin can be chosen such that $G_{LS} = 0$. Eq. 12.3 can then be expressed as:

$$G = p_{HS}\Delta H + \Gamma p_{HS}\left(1 - p_{HS}\right) - RT\left[p_{HS}\frac{\Delta S}{R} - \left(1 - p_{HS}\right)\ln\left(1 - p_{HS}\right) - p_{HS}\ln p_{HS}\right]. \tag{12.5}$$

At a given temperature and pressure, the equilibrium of the system is reached when $\left(\partial G/\partial p_{HS}\right)_{T,p} = 0$, which allows us from Eq. 12.5 to have a correlation between the temperature of the system and the molar fraction in the HS state p_{HS} at the equilibrium[278, 279, 283]:

$$T = \frac{\Delta H + \Gamma\left(1 - 2p_{HS}\right)}{R\ln\left(\frac{1 - p_{HS}}{p_{HS}}\right) + \Delta S}. \tag{12.6}$$

In Fig. 12.3, we calculated the proportion of HS molecules using Eq. 12.6 and considering particular values for the cooperative term Γ. We note that the transition temperature, *i.e.* the temperature $T_{1/2} = \Delta H/\Delta S$ at which half of the molecules are in their HS state, is independent of the cooperative term that is used. When no cooperativity is considered, the population of HS is dictated by a smooth Gibbs-Boltzmann statistic. When cooperativity is turned on, with $\Gamma < 2RT_{1/2}$ corresponding

to weak inter-molecular interactions, the transition is more abrupt than the previous case, but still relatively smooth. For the special case of $\Gamma = 2RT_{1/2}$ the derivative dT/dp_{HS} is zero at $p_{HS} = 0.5$ and positive everywhere else. This leads to an abrupt transition such as represented in blue in Fig. 12.3. For even larger inter-molecular interactions, *i.e.* $\Gamma > 2RT_{1/2}$, $T = f(p_{HS})$ presents two extrema, that should be interpreted as the opening of a thermal hysteresis loop such as represented by dashed green lines in Fig. 12.3.

The simple thermodynamic model developed by Slichter and Drickamer[283] that we just derived is very helpful to understand the temperature dependence of the HS population. In 1974, Sorai and Seki expanded the model and considered nucleation of SCO domains in the material.[277] Later, in 1982, Spiering *et al.*[281, 284] considered the elastic energy coming from the interaction between the SCO complexes modeled as rigid spheres.

More recently, and by means of *ab initio* calculations, Kepenekian *et al.*[285, 286] have shown that in addition to elastic forces, there are huge contributions coming from the Madelung field to the cooperative term. Their findings also reveal that the electrostatic contributions arising from the crystal environment (*i.e.* Madelung field) can stabilize the HS or the LS state of the molecule. Although they only considered internal electrostatic contributions, the concept can, in principle, be expanded with external contributions (*e.g.* an applied electric field) to trigger the spin transition.[287, 288]

12.3. Triggers

The thermodynamic model discussed in the previous section, helped to understand the effect of temperature upon the spin transition. Using the same model, we can foresee that pressure, electric and magnetic fields can also trigger the spin-crossover phenomenon, provided that the correct ingredients are included in the Gibbs free energy. In addition, the crossover can be induced by non-equilibrium processes occurring for instance when the complexes are illuminated with light or X-rays. In the following, we will review the different SCO triggers and when possible, present the data for the Fe-phen molecule.

12.3.1. Temperature

Temperature is the historical SCO trigger[255] and remains the most common perturbation to induce SCO.[258] Fe-phen molecules can be switched from a LS state at low temperatures into a HS state when the temperature is increased above 176.3 K.[277] Shi *et al.*[274] have shown an interesting study where they sublimed Fe-phen in order to make a 280 nm-thin-film Fe-phen sample. The magnetometry measurements revealed that the spin transition curves, *i.e.* the HS proportion of molecules as a function of temperature, are very similar between the bulk (powder) and thin film (see
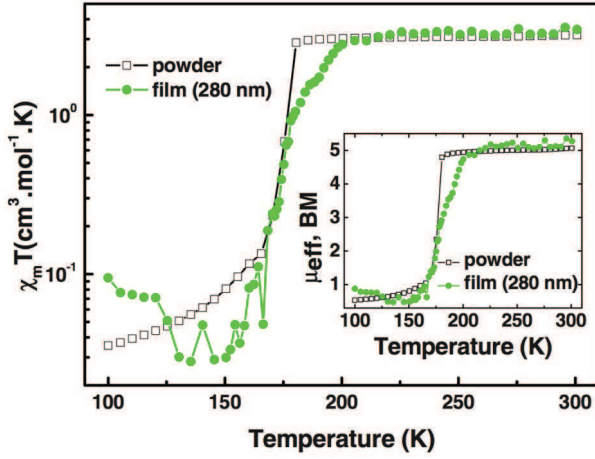
Figure 12.4. – **Magnetic susceptibility as a function of temperature for bulk (empty square) and** $280\,\text{nm}$**-thin-film (full circle) Fe-phen**. The figure is taken from Ref. 274.

Fig. 12.4). It is, to my knowledge, the first observation of spin transition in sublimed SCO molecules.

12.3.2. Pressure

In Sec. 12.2, we discussed about the origin of the difference in enthalpy ΔH, when the system is at atmospheric pressure. If the pressure is different from its atmospheric value, the work done by the pressure forces must be added to the variation of internal energy U[279]:

$$\Delta H = \Delta U + p\Delta V. \tag{12.7}$$

$\Delta V = V_{HS} - V_{LS} > 0$ represents the variation of volume upon transition from HS to LS. We can note that ΔV can be approximated as independent of the pressure. Indeed, Jeftic $et\ al.$[289] carried out a study on $[\text{Fe(ptz)}_6](\text{PF}_6)_2$ and have estimated that the pressure-induced variation of the metal-ligand bond length is $\approx -6 \times 10^{-4}\,\text{Å\,kbar}^{-1}$, and thus negligible. In addition, they checked that the variation of the ligand field with the pressure is negligible in comparison to $p\Delta V$. Thus, when the pressure of the system is increased, ΔH is increased as well, going towards the stabilization of the LS state.

There are many studies reporting the influence of the pressure on SCO, and in most of the cases the measurements consisted on acquiring different spin-transition curves at different constant pressures.[290–294] The effect of the pressure is then directly
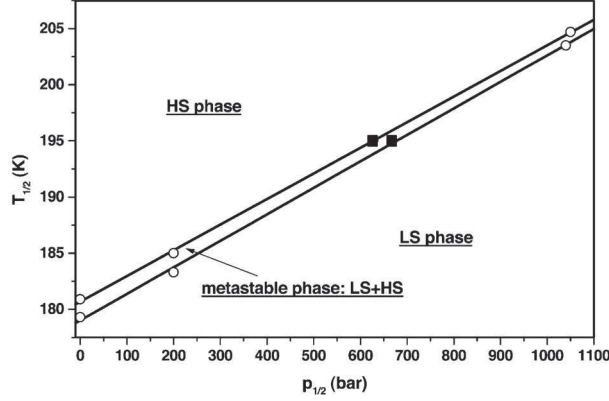
Figure 12.5. – **Spin-transition temperature as a function of applied pressure for Fe-phen**. The spin-transition curve exhibits a thermal hysteresis so that the upper (lower) fitted line corresponds to the increasing (decreasing) spin-transition temperature. The figure is taken from 290.

read on the shift of the transition temperature $T_{1/2}$. For Fe-phen, Bousseksou *et al.* reported that the shift of $T_{1/2}$ with pressure is of $(23.0 \pm 0.4)\,\mathrm{K\,kbar^{-1}}$ (see Fig 12.5).

12.3.3. Magnetic field

The susceptibility χ of a paramagnetic ion given by the Curie's law is[295] (in SI units):

$$\chi = \frac{\mu_0 n m_{eff}^2}{3 k_B T},\qquad(12.8)$$

with μ_0 the vacuum permeability, n the number of paramagnetic centers per unit volume, $m_{eff} = g\mu_B\sqrt{J(J+1)}$ an effective magnetic moment per magnetic center, k_B the Boltzmann constant and T the temperature. In the presence of an external magnetic field $B = \mu_0 H$, the corresponding variation of energy per unit volume is[295, 296]:

$$E_V(B) = -M.B = -\chi\frac{B^2}{\mu_0}.\qquad(12.9)$$

The magnetic susceptibility of the HS state $\chi^{HS} > 0$ is about two orders of magnitude higher than in the LS state χ^{LS}.[296] It results from Eq. 12.9 that the application of an external magnetic field B favors the HS state of the SCO molecules and E_V^{LS} can be neglected in comparison to E_V^{HS}. The energy variation of the HS state can be inserted into the Gibbs free energy $G(p_{HS}, T)$ (Eq. 12.3) and leads to[296]:

$$G(p_{HS}, T, B) = G(p_{HS}, T) + p_{HS} E_m^{HS}(B), \tag{12.10}$$

where $E_m^{HS}(B) = \frac{E_V^{HS}(B)}{\rho_m}$ is the variation of energy per mole, with ρ_m the molar density of the HS Fe-phen. p_{HS} is the proportion of molecules in the HS state.

Qi *et al.*[296] derived Eq. 12.10 and found that the transition temperature of a SCO complex is shifted by:

$$\Delta T_{1/2} = -\frac{\chi_m}{\mu_0 \Delta S} B^2 \tag{12.11}$$

in the presence of an external magnetic field B. $\Delta S = S_{HS} - S_{LS}$ correspond to the variation of entropy upon spin transition as discussed in the previous section and $\chi_m = \chi/\rho_m$ the molar magnetic susceptibility. Thus the shift of the transition temperature is quadratic with the external magnetic field, such has experimentally observed by Lejay *et al.*[297] Moreover using an effective magnetic moment of $m_{eff} \approx 5.2\,\mu_B$ for Fe-phen,[265] Eq. 12.11 predicts a spin-transition-temperature shift of $-0.119\,\text{K}$ at $B = 5.5\,\text{T}$ for Fe-phen in good agreement with the experimentally observed shift of $-0.115\,\text{K}$ in a field of $B = 5.5\,\text{T}$.[296] Note that despite the relatively good agreement between theory and experiments, the temperature shifts with reasonable magnetic fields are very small.

Instead of looking at the influence of the transition temperature $T_{1/2}$ on the applied magnetic field, Bousseksou *et al.*[298,299] have measured the variation of the HS proportion of Fe-phen (p_{HS}) when applying magnetic pulses of $32\,\text{T}$ (see Fig. 12.6). Since the thermal spin transition is rather abrupt, and that the theoretical magnetic-field-induced energy shift of the transition temperature is about $1.8\,\text{K}$,[298] the temperature of the powder sample was chosen to be on the ascending or descending part of the thermal hysteresis. They have shown that the HS proportion of the molecules can be increased upon application of an external magnetic field (see right panels in Fig. 12.6). The HS-proportion increase is irreversible (reversible) when the sample's temperature is on the ascending (descending) part of the thermal hysteresis. They attribute this difference to the kinetic barrier originating from cooperative effects responsible for the thermal hysteresis, and the limited effective transition temperature shift compared to the hysteresis width of $1.2\,\text{K}$.

12.3.4. Light

12.3.4.1. Introduction

In 1982, McGravey and Lawthers[300] reported on the first observation of laser-pulse-induced transition from the singlet LS ($^1A_1$) to the quintet HS ($^5T_2$) state of Fe^{2+} complexes in solution. The relaxation rate of the meta-stable HS state was in the nano to microsecond timescale for temperatures between 220 to 320 K. Latter, in 1984, Decurtins et al.[301] reported light-induced LS to HS transition on solid SCO
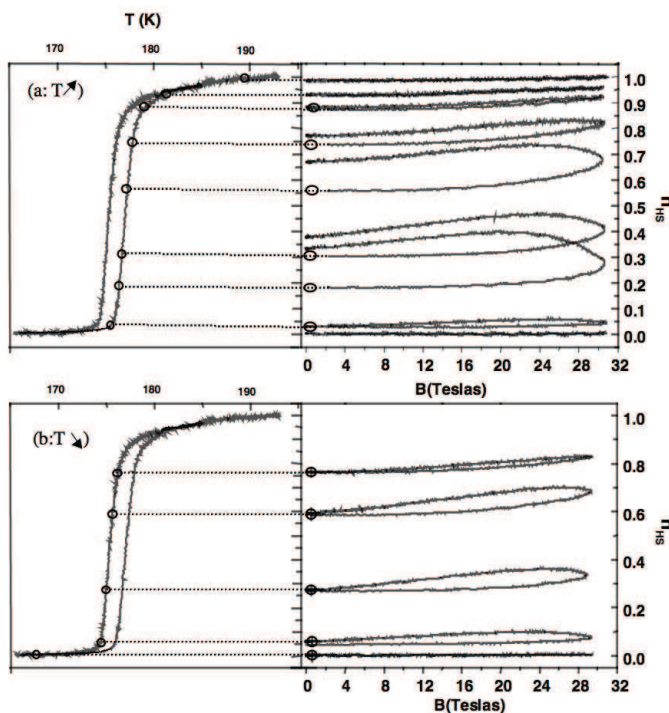
Figure 12.6. – **Effect of magnetic pulses on the HS proportion of Fe-phen molecules.** The upper (lower) panel reports on the magnetic pulses effect on the increasing (decreasing) part of the thermal hysteresis. The figure is taken from Ref. 290.

complexes. They have shown that the meta-stable HS state can have a lifetime of several hours provided that the powder is cooled down below 50 K. Thus, at cryogenic temperatures, the SCO system can be trapped into the HS state by application of light, leading to the term: light-induced excited spin-state trapping (LIESST). Since then, many studies have been carried out and the photo-switching mechanism seems to be general to the Fe^{2+} SCO complexes.[257, 292, 302]

12.3.4.2. Mechanism

In Fig. 12.7 a simplified scheme of the Fe^{2+} electronic states is represented. The transitions from the singlet $^1A_1$ (LS) ground state to the $^1T_1$ or to the $^1T_2$ states can be achieved by application of light with an adequate energy. These exited states exhibit a fast relaxation to the triplet $^3T_1$ state, that in turn can relax either to the $^1A_1$ (LS) ground state or to the $^5T_2$ (HS) metastable state. Radiative relaxation from the $^5T_2$ (HS) to the $^1A_1$ (LS) state is forbidden and thus explains the long lifetime of the metastable HS state at low temperatures.
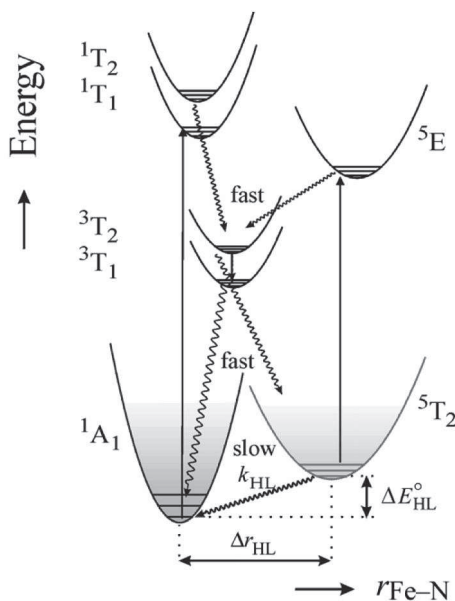
Figure 12.7. – **Scheme of the electronic states of a Fe²⁺ ion of a SCO complex.** The $^1A_1$ $(^5T_2)$ state corresponds to the LS (HS) state. The figure is taken from Ref. 257.

The reverse effect, *i.e.* light-induced population of the LS state from the trapped HS metastable state is also possible[303] and referred to as reverse LIESST. In this case, the absorption of a photon with an adequate energy can induce the transition from the $^5T_2$ (HS) to the ^5E state that eventually relaxes into the $^1A_1$ (LS) state. We note that, while LIESST can induce a complete conversion of the SCO system from LS to HS state, the reverse LIESST can only induce partial transition from HS to LS state. Indeed, there is a spectral overlap between the $^5T_2 \to ^5E$ transitions and the spin forbidden transitions: $^1A_1 \to ^3T_1$ and $^1A_1 \to ^3T_2$.

The above described mechanism can be different if the metal-ligand charge transfer (MLCT) states have similar energies than the ligand-field states, which is typically the case when the ligands have extended π-systems.[302] The LS to HS transition would then occur through the singlet ^{1}MLCT and triplet ^{3}MLCT states within some picoseconds.[304–312]

12.3.4.3. Relaxation and LIESST

The relaxation from the metastable HS to the LS state is accompanied by changes in the metal-ligand distances of the SCO complex. Intermediate metal-ligand distances are more energetic for the system and thus represent an energy barrier to overcome for spin transition. When the temperature of the system is sufficiently low, only tunneling
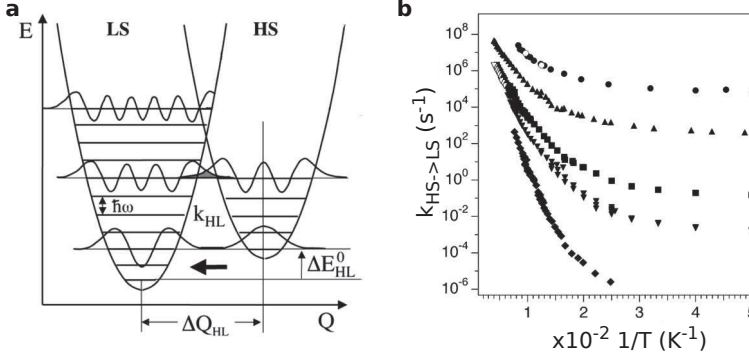
Figure 12.8. – **Relaxation model. a**, Energy potential well of the HS and LS states. The Q coordinate is related to the metal-ligand distance. **b**, HS-to-LS relaxation rate as a function of inverse temperature for different SCO complexes: $[Zn:Fe(ptz)_6](BF_4)_2$ (filled diamonds), $[Mn:Fe(pic)_3]Cl_2EtOH$ (filled upside down triangle), (open up- side down triangle) $[Fe(pic)_3]Cl_2EtOH$,[314, 315] $[Zn:Fe(mepy)_3tren](PF_6)_2$ (filled squares), $[Zn:Fe(py)_3tren](PF_6)_2$ (filled triangles), $[Mn:Fe(bpy)_3tren](PF_6)_2$ (filled circles).[316, 317] The figure is adapted from Ref. 302.

through the barrier can lead to a relaxation to the LS state, and consequently the light-induced HS metastable can have a relatively long lifetime, typically tens of hours. Buhks *et al.*[302, 313] developed a theory in which they describe the HS-to-LS relaxation by a radiationless nonadiabatic multiphonon process.

If the temperature is sufficiently low, typically below $\approx 40\,\mathrm{K}$, such that only the HS vibrational ground state is occupied, the relaxation rate is given by.[302]

$$k_{\mathrm{HS}\to\mathrm{LS}}\,(T \to 0) = \frac{2\pi}{\hbar^2\omega}\beta^2_{\mathrm{HS}\to\mathrm{LS}}|\langle\chi_n|\chi_0\rangle|^2, \tag{12.12}$$

where $\hbar\omega$ represents the vibrational quanta, $\beta_{\mathrm{HS}\to\mathrm{LS}} = \langle\Phi_{\mathrm{LS}}|H_{SO}|\Phi_{\mathrm{HS}}\rangle$ is the electronic coupling matrix element of the LS (Φ_{LS}) and HS (Φ_{HS}) electronic wave functions by the spin orbit coupling.[302] $|\langle\chi_n|\chi_0\rangle|^2$ is the Franck-Condon factor given by the overlap of the vibrational functions of the nth (ground) vibrational state of the LS (HS) state, where $n = \Delta E^0_{HL}/\hbar\omega$ corresponds to the zero-point energy difference (see Fig. 12.8a). The model assumes similar harmonic potential for the HS and LS state. The relaxation rate $k_{\mathrm{HS}\to\mathrm{LS}}\,(T \to 0)$ that we find, is independent of the temperature.

When the temperature is increased, the population of HS vibrational levels evolves, and the Franck-Condon factor becomes temperature dependent:

$$F_n(T) = \frac{\sum_m |\langle\chi_{m+n}|\chi_m\rangle|^2 e^{m\hbar\omega/k_BT}}{\sum_m e^{m\hbar\omega/k_BT}}, \tag{12.13}$$

so as the relaxation rate:

$$k_{\text{HS}\to\text{LS}}\left(T\right) = \frac{2\pi}{\hbar^2\omega}\beta_{\text{HS}\to\text{LS}}^2 F_n(T). \tag{12.14}$$

At sufficiently low temperatures, the HS-to-LS relaxation rate $k_{\text{HS}\to\text{LS}}$ is temperature independent, and leads to the plateau at the right of Fig. 12.8b. When the temperature is increased, additional vibrational levels of the HS state are occupied leading to a temperature-dependent relaxation rate. Since (i) the HS excited vibrational levels have better overlap with vibrational levels of the LS state and (ii) the number of possible transitions is increased, the relaxation rate increases with increasing temperatures.

The magnitude of the relaxation rate highly depends on the investigated complex. For instance, in Fig 12.8b, in the low temperature regime $k_{\text{HS}\to\text{LS}}$ ranges from $10^{-6}\,\text{s}^{-1}$ to $10^6\,\text{s}^{-1}$ depending on SCO complex under consideration. A different number of parameters can have an impact on the relaxation rate, such as the hapticity (describes the coordination of a ligand to a metal center) of the ligands that can modify the height of the energetic barrier between the HS and the LS state, as well as the transition temperature $T_{1/2}$ of the SCO complex that is directly linked to the energy difference between the potential wells of the HS and LS state $n = \Delta E_{HL}^0/\hbar\omega$. Note that in this model, we neglected any influence from cooperative effects between the molecules. If one wishes to include them, the relaxation rate $k_{\text{HS}\to\text{LS}}(T, p_{\text{HS}})$ will not only depend on the temperature, but also on the HS proportion (p_{HS}).[282, 318, 319]

At low temperatures, the HS-to-LS relaxation rate can be low enough so that the light-induced metastable HS state has a sufficiently long lifetime to be observed without pump-probe techniques. The HS metastable state is considered as trapped, and leads to the term light-induced excited spin-state trapping (LIESST). In some cases, the trapping is so efficient that the only way to relax in an acceptable timescale is to increase the temperature of the system, and thus to increase the relaxation rate as described in the above discussion. For a system prepared in the HS metastable state at low temperature, T_{LIESST} defines the temperature at which the light-induced effect is erased. Moreover, since the definition of T_{LIESST} can depend to experimental parameters, *e.g.* the sweeping rate of the temperature, Létard *et al.* developed a procedure to unambiguously determine T_{LIESST}.[319, 320]

There is a general wish in the community to find complexes with the highest T_{LIESST}, *i.e.* $T_{\text{LIESST}} >$ room temperature.[319, 321] Indeed, for temperatures lower than T_{LIESST}, the spin transition can be triggered by light through the LIESST and reverse-LIESST effects. This represent an interesting aspects for application perspective provided that T_{LIESST} is close enough to room temperature. Since the HS-to-LS relaxation rate $k_{\text{HS}\to\text{LS}}$ depends on the transition temperature $T_{1/2}$, as well as on the hapticity of the ligands, T_{LIESST} depends on the same parameters. For SCO complexes of same halipticity number, the T_{LIESST} temperature is inversely proportional to the transition temperature $T_{1/2}$.[319, 320] Nowadays, the record of T_{LIESST} temperature is 145 K[319, 322] obtained for $\text{Na}_{0.37}\text{Co}_{1.37}^{\text{II}}[\text{Fe}^{\text{III}}(\text{CN})_6]_{0.89}[\text{Fe}^{\text{II}}(\text{CN})_6]_{0.11}\bullet 4.8\text{H}_2\text{O}$, which
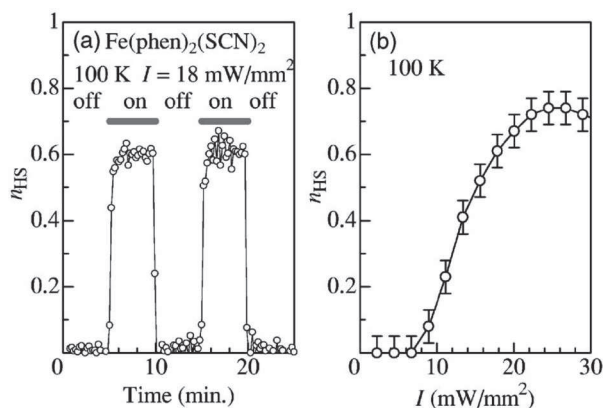
Figure 12.9. – **Photoexcitation of Fe-phen at** 100 K. **a**, Proportion of HS molecules as a function of time, with and without light irradiation. **b**, Impact of the laser-light intensity on the proportion of HS molecules. The figure is taken from Ref. 325.

is still well below room temperature. An alternative is to trigger the spin transition with light within the thermal hysteresis, taking benefit of the long lifetime of HS and LS due to cooperativity.[323, 324]

12.3.4.4. LIESST on Fe-phen

In the precedent parts, we have seen the principle of light-induced transition from LS to HS state, as well as the relaxation process of the metastable HS state. Here, we intend to illustrate these principles in the case of the Fe-phen molecule.

Kato *et al.*[325] have realized a nice experiment in which they monitor the proportion of Fe-phen molecules in the HS state as a function of time. In addition, a 532-nm-laser light with variable intensity is directed onto the molecules and can be switched on or off. In Fig. 12.9a, we can see the evolution of the HS proportion as a function of time acquired at 100 K while the laser light is alternatively switched on and off. In the absence of light, at the origin of time, the Fe-phen molecules are in their LS state. When the laser is turned on, there is about 60 % of the molecules that switch into the HS state within approximately 10 seconds. The proportion of HS molecules stays constant as long as the photo-excitation is maintained reflecting an equilibrium between the continuous light-induced excitation and the HS-to-LS relaxation. The HS proportion decreases to zero within 10 seconds once the laser is switched off.

In Fig. 12.9b, the influence of the light intensity on the proportion of HS molecules is represented. A threshold intensity of about $6 \, \mathrm{mW \, mm^{-2}}$ is necessary to observe the photoexcitation. Kato *et al.*[325] suggest that the presence of the threshold is due to cooperativity effects. The proportion of HS molecules then increases
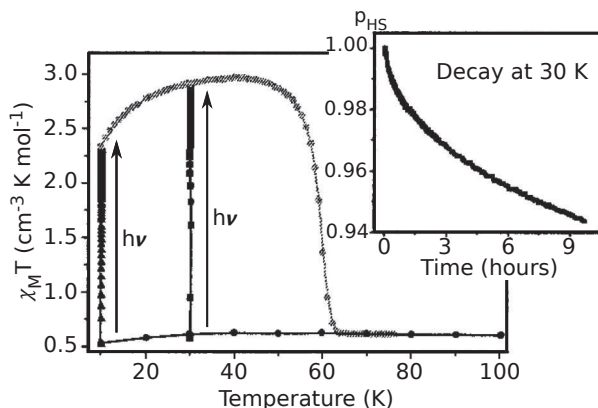
Figure 12.10. – **LIESST on Fe-phen.** Magnetic susceptibility representing the proportion of HS molecules as a function of temperature with and without light irradiation. Light irradiation was performed at 10 (triangle) and 30 K (square) on a sample with molecules in the LS state. The photo-induced HS molecule relaxes into the LS state when increasing the sample temperature above 62 K. In the inset, the proportion of HS molecules as a function of time at a temperature of 30 K. The figure is adapted from Ref. 268.

porportionaly to the laser intensity, and can reach about 80% for a laser intensity of $20\,\mathrm{mW\,mm}^{-2}$.

When the temperature is decreased below T_{LIESST}, the metastable HS state is trapped with a long lifetime.[326] Marchivie *et al.*[268] irradiated a single Fe-phen crystal at 10 and 30 K with an intensity of $0.05\,\mathrm{mW\,mm}^{-2}$ (Fig. 12.10). At both temperatures, the irradiation led to a successful LS-to-HS transition with a laser intensity lower than the $6\,\mathrm{mW\,mm}^{-2}$ threshold found by Kato *et al.*[325] The difference comes from the very low HS-to-LS relaxation rate in the present case that can be neglected in front of the photo-induced-transition rate. In the inset of Fig. 12.10, we can see the HS-to-LS decay at 30 K once the laser irradiation is switched off. The metastable HS-state lifetime is of the order of tens of hours. In order to reset the sample in a reasonable timescale, *i.e.* a sample without HS molecules, one need to increase it's temperature above $T_{\mathrm{LIESST}} = 62\,\mathrm{K}$.[268, 320]

The study of Marchivie *et al.*[268] also revealed the photo-induced HS state (referred to as HS-2) is different from the thermal-induced HS state (HS-1). The difference mainly lies in the Fe-N bond lengths and the volume of the unit cell while the distortion parameter seems unaffected.

12.3.5. X-rays

In 1997 Collison *et al.*[267] observed an effect similar to LIESST: the trapping of metastable HS molecules induced by soft X-rays, leading to the term soft X-ray induced excited spin-state trapping (SOXIESST). However, the experiment is different from the previous one since the excitation is produced by the X-rays needed for spin-state detection. In order to clarify the things, we will first present how one can read the spin state of the molecules with X-rays and in a second part, we will discuss about the dynamic of the SOXIESST effect.

In 1992, Cartier Dit Moulin *et al.*[327] observed that, for Fe^{2+} SCO complexes, the spin state of the molecules can be read via X-ray absorption spectroscopy (XAS) measurements performed at the L edges of Fe. Indeed, the L-edge XAS is sensitive to the unoccupied density of states that differs from the HS to the LS state. The difference is mainly visible at the Fe L_3 edge where the main peak shifts by about 1.5 eV toward higher energies when going from HS to LS state.[267, 280, 327–334] In Fig. 12.11a, we present Fe L edge XAS spectra of Fe-phen molecules in the LS and in the HS state, that we acquired on a Fe-phen powder sample on DEIMOS beamline (synchrotron SOLEIL).[134, 135, 333]
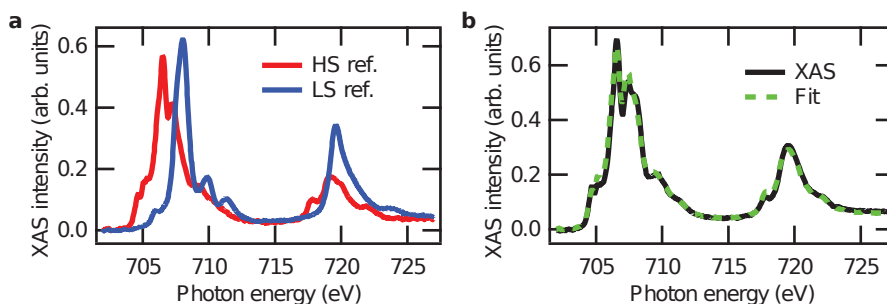
Figure 12.11. – **XAS on the Fe L edge of Fe-phen powder. a**, LS and HS reference spectra acquired at 100 and 300 K, respectively. **b**, XAS spectrum acquired at 30 K where a proportion of molecules are in the metastable HS state due to the X-rays. The experimental spectrum can be reproduced by a linear combination of the LS and HS reference spectra (22 % LS and 78 % HS) that allows to extract the proportion of HS molecules: 78 %. See Refs. 280, 333 for more details.

One can observe intermediate spectra when the molecules are excited (see Fig. 12.11b). We have shown that these spectra can be reproduced by the sum of HS- and LS-reference spectra with adequate weighting. In turn, the weighting coefficients allows us to extract the proportion of molecules that are in the LS and in the HS state.[331–333] The proportion of HS molecules can thus be directly read from the Fe L-edge XAS spectrum provided that we have clear HS and LS references. The detection technique is very powerful, but one needs to constantly check the integrity
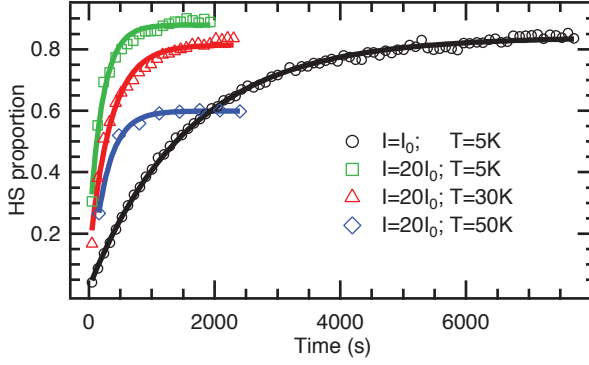
Figure 12.12. – **SOXIESST dynamic of Fe-phen powder at different temperatures and different photon flux.** We can observe that for a given photon flux, the lower the temperature, the higher the final proportion of HS molecules. Additionally, for identical temperatures, the HS population is slower when the photon flux is reduced. Every dynamics were fitted with Eq. 12.15 and are represented in solid lines. $I_0 = 6.1 \times 10^8$ photons/s/mm^2, see Refs. 280, 333 for more details.

of the molecules since the X-rays can damage the molecules.[267, 328, 333] This is done be checking the reproducibility of the LS- and HS-reference spectra over time.

Thanks to recent experimental improvements on beamline DEIMOS,[134, 135] we were able to measure a XAS spectrum within one minute instead of about 20 minutes, allowing us to perform slow dynamic studies. For a fixed temperature, we have studied the evolution of the proportion of HS Fe-phen molecules as a function of time (see Fig 12.12a). We note that the saturation value depends on the measurement temperature and on the photon intensity. The time needed to reach the saturation value is of the order of thousands of seconds. The data can be fitted by the following mono-exponential function[280, 333]:

$$p_{\text{HS}} = \frac{k_1}{k_1 + k_2} \left[1 - \exp\left(-\left(k_1 + k_2\right)t\right)\right] \tag{12.15}$$

derived from the following master equation:

$$\frac{dp_{\text{HS}}}{dt} = k_1 \left(1 - p_{\text{HS}}\right) - k_2 p_{\text{HS}}. \tag{12.16}$$

k_1 represents the soft X-ray-excitation-induced transition rate and k_2 the temperature-dependent relaxation rate from the HS to the LS state. The fit of the experimental data with Eq. 12.15 allows to extract k_1 and k_2, and the thermal evolution of the relaxation rate is discussed in detail in Ref. 333.

The origin of the X-ray-induced transition remains unknown. We verified that SOXIESST is a non-resonant excitation process by irradiating the sample at different photon energies before measuring successive spectra at the L_3 edge, suggesting a different mechanism than LIESST. Moreover, the secondary electrons of the photo-absorption process have energy of a few eV compatible with the transitions present in LIESST, and thus may be the SCO trigger.

Note that Vanko et al.[335] reported that the SCO can also be induced by more energetic hard X-rays.

12.3.6. Electric field and current

We have seen in Sec. 12.2.2, that the electrostatic contributions arising from the crystal environment can have a crucial role for the cooperativity. Kepenekian et al.[285, 286] have shown that the crystal field can stabilize a given spin state. From these findings, one can speculate that an external electric field can possibly favor a given spin state, and thus induce a spin transition. However, due to experimental limitations, the application of an external electric field is often associated with a flow of electrons. Those electrons have typically an energy of about 1 eV, if injected through a tunnel barrier, and thus can possibly induce a spin transition with a mechanism similar to the photo-excitation. Since it is experimentally not always possible to distinguish between electric-field- and current-induced transitions, both triggers are presented here separated in two parts: SCO complexes placed in a device or onto a surface.

12.3.6.1. SCO molecular junctions

At first, the theoretical work performed by Baadji et al.[336] is of great importance. They pointed out that, in general, the HS and LS states of a molecule may have different polarizabilities and eventually different permanent electrical dipoles. An external electric field would then modify the relative energy difference between the two spin states, and eventually induce a spin crossover. They then performed an ab initio DFT study on polar magnetic molecules and have shown that electric field of about $1.5\,\mathrm{V\,nm^{-1}}$ can favor the triplet to the singlet state. In turn, they showed that if the molecule is sandwiched between two gold electrodes, the critical electric field can be reached with an applied bias of about 1 V, which is experimentally accessible.

Draghetti and Sanvito[337] performed a similar theoretical work on a Co-dioxolene complex, which exhibit valence tautomeric interconversion.[338] The effect is somewhat similar to SCO but the spin state transition is accompanied with (or due to) the change of the oxidation state of the metallic cation. They have shown that an electric field of $0.5\,\mathrm{V\,nm^{-1}}$ is sufficient to drift the transition temperature by about 100 K, and that the direction of the electric field determines the favored spin- and thus oxidation-state configuration.

Later, in 2012, Baadji and Sanvito[339] calculated the transport properties on
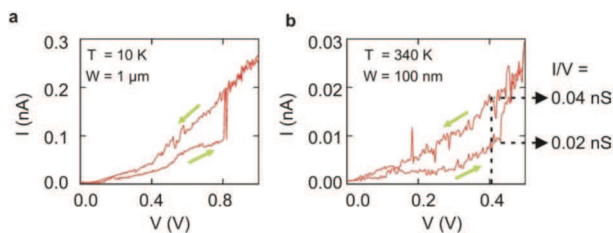
Figure 12.13. – **I-V characteristics on a single nanoparticle. a**, Current-
voltage curve acquired at low temperature (T = 10 K) on Fe-based SCO
nanoparticles bridged between two 1 μm-width gold electrodes. **b**, Same
measurements performed at T = 340 K on a single nanoparticle sandwiched
between two 100 nm-width gold electrodes. In both panels, we observe a
conductance jump ascribed by the authors to a transition from the LS to
the HS state when increasing the voltage. The figure is taken from Ref.
341.

the $[FeL_2]^{2+}$ (L=2,2':6,2"-terpyridine) SCO complex attached to two gold electrodes.
They observed a relative variation of the resistance up to 3000% when the spin state
of the molecule is changed. These findings are really important since it predicts that
the spin state of a SCO molecule can, in principle, be electrically detected. Moreover,
the huge relative variation of the resistance makes SCO complexes good candidates
for applications. Some interesting reviews on SCO transport properties can be found
in Refs. 259–261, 340.

Concerning the experimental reports, Prins *et al.*[341] reported in 2011, the possi-
bility to electrically address the spin state of a SCO nanoparticle. The nanoparticle
is composed of a SCO $[Fe(trz)_3(BF_4)_2]$ (trz = triazole) core coated with a surfactant
shell, with a total diameter about 11 nm. The latter is placed in between two gold
electrodes and the I-V characteristics revealed conductance jumps at low and room
temperature (see Fig. 12.13a-b), ascribed to a transition from a low-conductance
LS state at low voltages to a high-conductance HS state at higher voltages. How-
ever, the origin of the spin-state transition could not be experimentally determined.
Note that conductance measurements performed by Rotaru *et al.*[342, 343] on a similar
complex $[Fe(Htrz)_2(trz)](BF_4)$ (Htrz = 1H-1,2,4-triazole) revealed a high (low) con-
ductance state for the LS (HS) molecules, and thus the conductance and spin-state
correspondence is not straightforward.

Osorio *et al.*[344] in 2010 constructed a three-terminal device with two molecules
of $[Mn(terpy-O-(CH_2)_6-SAc)_2]^{2+}$ in between two gold electrodes. By varying the
gate-voltage, they could reduce the terpyridine moiety. The resulting strengthened
ligand field in turn favored a LS state of the Mn ion. In 2011, Meded *et al.*[287, 340]
investigated a single molecule of $[Fe^{II}(bpp)_2]^{2+}$ [bpp: 2, 6-bis(pyrazol-1-yl) pyridine]
in a combined theoretical and experimental study. On one hand, the *ab initio* DFT
calculations showed that the molecule with two extra electrons favors a HS state
configuration. On the other hand, three-terminal transport measurements through
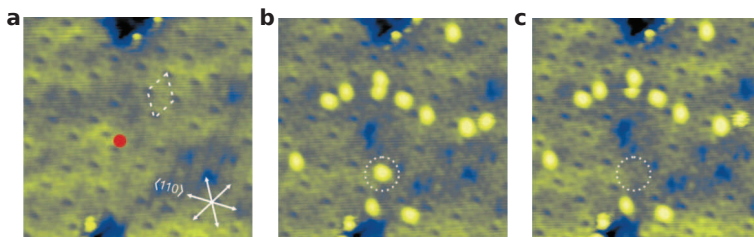
Figure 12.14. – **STM topographies revealing spin transition of SCO complexes. a**, Topography of a 14 nm wide area. The second-layer molecules appear in yellowish and are prepared in the LS state. The tip is afterward positioned on top of the red dot. **b**, Topography of the same location than **a** but recorded after a voltage pulse. The brighter molecules correspond to molecules switched into the HS state. Selective reverse switching can be performed by placing the tip on top of a HS molecule (*e.g.* the encircled HS molecule) and increasing the tunneling current to 0.5 nA with a voltage of 1.8 V for about 0.5 s. The topography acquired afterwards is presented in **c** where the encircled molecule is now in the LS state. The figure is taken from Ref. 347.

a single molecule show indication of a spin transition induced by the gate-voltage-controlled charging of the ligands. Note that in the above two examples, the electric field has an indirect role on the spin-state of the central cation.

12.3.6.2. SCO molecules on surfaces

SCO molecules on surfaces are of great interest for future applications, since it allows for down-scaling the systems. Scanning tunneling microscope (STM) is probably the best suited equipment to investigate these systems, since it allows for probing electrical properties of selected single molecules and eventually induce a spin transition with the help of the tunneling electrons or the electric field produced by the tip.

In 2009, Alam *et al.*[345, 346] reported a room temperature STM investigation of SCO complexes on a highly-oriented pyrolytic graphite (HOPG) surface. Single molecules or clusters composed of two to three molecules form 1D-chain structure, and current-imaging tunneling spectroscopy (CITS) measurements revealed two conductance states for the beads. They ascribed the low- and high-conductance states to HS and LS states, respectively. In addition, the conductance state of some molecules/clusters appeared to switch between successive CITS maps.

There is also a very nice study performed by Gopakumar *et al.*[347] concomitant with the study we will present in the next chapters. They sublimated two monolayers or $[Fe(bpz)_2(phen)]$ (phen=1,10-phenanthroline, bpz=dihydrobis(pyrazolyl)-borate) on a Au(111) substrate. The spin state of the molecules could be determined by the presence (HS) or absence (LS) of a Kondo resonance in the scanning tunneling spectroscopy (STS) spectra. Furthermore, if the molecules are initially in the LS

state, they were able to switch a proportion of the molecules into the HS state by application of a voltage pulse of 3 V (see Fig 12.14). On the next topography, the HS molecules appear by 2 Å–4 Å higher. The selective reverse transition was also possible by increasing the tunneling current with a voltage $V > 1.5$ V. Since the time needed for the HS-to-LS transition is inversely proportional to the current, the authors suggest that the transition mechanism involves charge injection into the unoccupied orbitals.

Zhang *et al.*[348] performed an alternative original study. They used the electric field to control the electric polarization of the ferroelectric substrate, and observed evidence of spin transition in the [Fe(H$_2$B(pz)$_2$)$_2$(bipy)] thin film deposited on top.

12.4. Technological applications

We have seen that different physical triggers can induce spin transition. Moreover, each spin state of a SCO complex has given optical, magnetic and electrical properties. The various spin-state-dependent properties that can be addressed by various stimuli make SCO complexes promising candidates for technological applications. Some of these applications are discussed in interesting reviews[349–351] and we will present few of the potential applications in the following.

Information storage

Molecular-memory unit out of a single molecule or out of a limited number of molecules are appealing since it would allow increasing the actual memory density. Molecular candidates have to present distinct switchable and readable states, robust against uncontrolled external perturbations from the environment, and the information has to remain over time in the absence of the trigger. The switchable states of the molecules can be of different origins: charge storage, conformational or positional shifting and physical transformation.[350, 352]

SCO complexes are very interesting in respect to the various possibilities to read the spin state (optical, magnetic or electric reading) as well as the different possibilities to write the information. However, a single isolated SCO molecule is impractical since the spin transition follows a Boltzmann approach, and the information would be erased as soon as the trigger is turned off. Consequently, if one wish to obtain a memory device out of SCO complexes, one need to look for SCO complexes with a hysteresis effect.[350] Nowadays, it is possible to synthesize SCO molecules exhibiting thermal hysteresis of about 40 K close to room temperature (*e.g.* Fe(Htrz)$_2$(trz)](BF$_4$)[342]) by increasing the inter-molecular interactions, and thus making SCO complexes suitable for memory applications.[353]

An alternative application has been proposed by Mahfoud *et al.*[354] where the transition is irreversible. They sublimed a thin film of [Fe(HB(pz)$_3$)$_2$] on a gold substrate and observe an irreversible conductance drop during the first heating as-

sociated to a phase change. They proposed to exploit this two orders of magnitude conductance drop to build read-only memories.

Temperature and pressure sensors

The SCO is usually accompanied by a pronounced thermochromism that has been used for thermochromic paints.[355, 356] Moreover, when SCO molecules switch their spin state as a consequence of a temperature or pressure variation, the result can be easily read from the color of the complex. By chemically tuning the SCO molecules, one can in principle, chose the transition temperature or (high) pressure. Their color would then change if the temperature or the pressure cross a given threshold value, making them suitable for sensors.

One could also use the synergy between the spin transition and a dehydration-re-hydration process, observed in some cases in polymeric SCO systems[350] such as [Fe-(hyetrz)$_3$](anion)$_2 \bullet 3H_2O$ [hyetrz=4-(2'-hydroxyethyl)-1,2,4-triazole, anion = 3-nitro-phenylsulfonate].[357] The first spin transition from LS to HS occurs around 370 K and is associated with a dehydration process. The inverse transition is only possible if the sample is cooled below approximately 100 K. Such compounds are interesting for threshold-temperature sensors with a memory.

Display devices

The thermochromism properties of SCO complexes can be employed to realize SCO-based display devices. Kahn and Martinez[349] have presented the principle of such devices: they suggest using a matrix of resistive dots on an alumina substrate. Electrodes are arranged in rows and columns, which allow addressing a given resistive dot. A layer of SCO complexes is then deposited on top of the resistive-dot matrix, ideally using an ink consisting of the SCO material and a resin that would protect the SCO complexes against the environment. When a given resistive dot is addressed, it locally increases the temperature, and eventually induce a spin transition of the SCO material located on top of the dot if the temperature exceed $T_{1/2} \uparrow$. In turn, the SCO material on top of the dot, that represents a single pixel, changes its color.

If one use a SCO material with a thermal hysteresis, the pixel information remains even when the resistive dot is turned off. To erase the pixel, one can activate a Peltier element to decrease the temperature below $T_{1/2} \downarrow$. The principle is presented in Fig. 12.15. A similar prototype device can be found in Ref. 350.

Micro actuator

The SCO phenomenon is accompanied by a variation of the unit-cell volume of about 5 % to 10 %, which gives potential to SCO complexes to transform different forms of energy (thermal, electric, light, ...) into motion.[351] Shepherd *et al.*[358] designed and
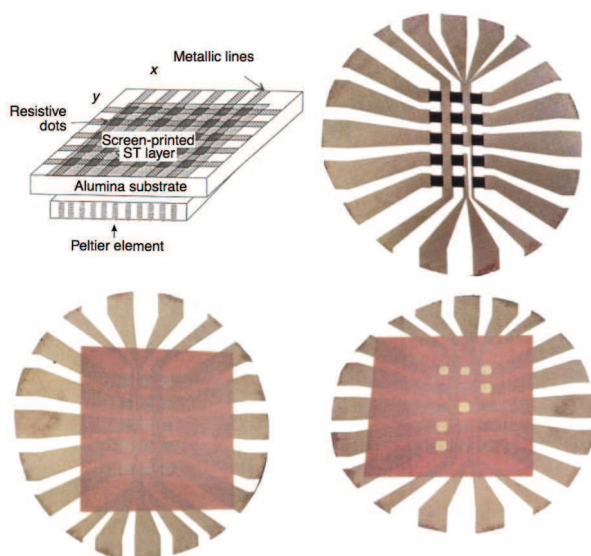
Figure 12.15. – **Principle of a SCO-based display.** Electrodes and resistive dots are printed onto an alumina substrate. The resistive dots can be addressed through columns and rows (top). The SCO molecules are deposited on top, ideally by using a screen-printing technology, and mixed with a resin that protect the SCO complexes against the environment (bottom left). When a current pass through a given resistive dot, the temperature is locally increased above $T_{1/2} \uparrow$ inducing a color change of the molecules (bottom right). The new color remains as long as the temperature stays within the thermal hysteresis loop. To erase, Peltier elements can locally lower the temperature below $T_{1/2} \downarrow$. The figure is taken from Ref. 349.

constructed a micro actuator based on SCO materials, and monitored micrometer motion upon thermal- and light-induced SCO (see Fig. 12.16). The bilayer stip they developed is composed of a layer of inert material and a layer of SCO molecules. By selecting adequate SCO materials, and an inert metal layer with an adequate strain, one can possibly tune the amplitude of the SCO-based actuator.

Based on their findings, we propose to use the bilayer strip in the three following situations:

- Cryogenic environment

- Electric protection

- Photo detection

In cryogenic environments in which one wish to reach sub-Kelvin temperatures, the sub-Kelvin part must be efficiently shielded and thermally decoupled from the room-temperature environment. A liquid-helium tank that is separated by high vac-
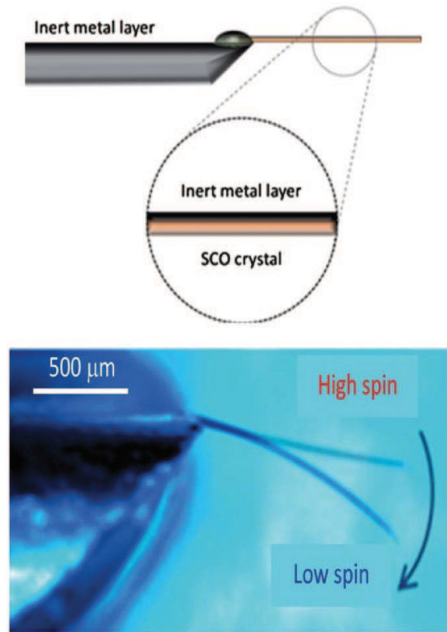
Figure 12.16. – **SCO-based cantilever prototype.** (Top) Bilayer strip composed of a thin film of aluminum and the SCO complex Fe(3-CNpyridine)[Au(CN)$_2$]$_2 \bullet$2/3H$_2$O. (Bottom) Highlight of the SCO-induced actuation of the bilayer cantilever by optical microscopy image. The figure is taken from Ref. 351.

uum from the sub-Kelvin element usually performs the thermal shielding. On one hand the thermal decoupling ensure that the sub-Kelvin element does not thermalize with liquid-helium tank, on the other hand it drastically increase the time needed to cool down the sub-Kelvin element from room temperature. This problem could be solved by using SCO-based strips with high thermal conductivity that would connect the sub-Kelvin element to the liquid-helium tank, ensuring a fast cooling process of the sub-Kelvin process. When the temperature would reach a value slightly above liquid-helium temperature, the SCO would switch and suppress the thermal contact, restoring the good thermal decoupling of the sub-Kelvin element.

Many scientists are working on the miniaturization of the electronic components. Another challenging task is to extract the heat produced by these nanometric components that can eventually damage the circuits. A possibility to protect the circuit against overheat would be to use a conductive bilayer strip to bring the current to the chip. If the temperature of the chip and strip increases above a given threshold, the SCO complexes switch and remove the electrical contact to the chip, protecting the later from overheating.

Most if not all the photodetector sensors are based on photodiodes. The light is

absorbed and converted into an electric signal. However, the photodiode surface must be large enough to have a detectable electronic signal. Moreover the photodiode are usually operated in photoconductive mode that gives rise to dark current, *i.e.* the current that pass through the photodiode in the absence of light. One may use SCO-based strips, downsizable to nanometer scale, to detect light. The light, if present, would induce a spin transition that would move the strip such that it can close an electric circuit, the "ON state". In absence of light, the electronic is open and in the "OFF state".

13

Growth of Fe(phen)$_2$(NCS)$_2$

In the previous chapter, I presented different properties and different triggers for SCO molecules in their bulk form. Crafting SCO (ultra-)thin films would allow to build SCO-based devices and would help answering the following questions:

- How does the size/dimension of the SCO system affect its properties? Indeed, when the size of the SCO system decreases, the surface to bulk ratio increases, and one may have to consider surface energy terms, that may eventually favor a HS instead of a LS state.

- How does the molecule-substrate interface influence the physical properties of the future SCO-based electronic devices. Does the molecule-substrate interactions prevent the switching of the SCO complex? Moreover, we have seen that inter-molecular interactions, referred to as cooperativity, allow one to have a homogeneous spin state in the system. We might be wondering on how the molecule-substrate interaction affects the cooperativity, and thus the spin-state homogeneity.

- How do the properties of the SCO complex evolve in the lower limit of a single molecule?

13.1. Realizing SCO films

A lot of efforts have been performed to deposit SCO complexes on surfaces using different techniques:

Langmuir-Blodgett Langmuir-Blodgett films can be realized by transferring a single layer of molecules from a liquid-air interface onto a surface. In 1988, Ruaudel-Teixier *et al.*[359] were the first to realize Langmuir-Blodgett SCO films using an amphiphilic derivative of Fe-phen. Many other SCO films have been realized us-

ing Langmuir-Blodgett-based deposition[340, 360, 361] but the serious disadvantage of the technique is the requirement of amphiphilic molecules.

Surface-assisted molecular self-assembly For this technique, there is an alternate deposition of cations and anions that leads to the formation of a three-dimensional spin-crossover coordination polymer.[340, 362] The advantage of this technique is the purity of the film (no amphiphile) but it drastically reduces the choice of SCO molecules.

Drop casting Drop cast of a solution on a substrate leaving the SCO molecules on the surface when the solvent evaporates.[340, 345, 363, 364] This very simple technique leads to non-uniform films with almost no control on the thickness. Moreover, the purity of the sample is questionable since the solvents can be retained in the thin film.

Spin coating Dropping a solution containing SCO complexes on a spinning substrate increases the uniformity and the control of the final film thickness.[340, 365, 366] However, traces of solvents can still remain in the film and there is usually a lack of molecular order inherent to the technique.[367]

Thermal sublimation Subliming SCO complexes in (ultra-high) vacuum allows the *in situ* realization of solvent- and contamination-free thin films with an accurate control of the thickness.

It results that thermal sublimation is the most suitable technique to perform ultra-thin films and to work at the single molecule level. However, thermal sublimation drastically limits the number of SCO candidates, since the molecules should be of low molecular weight, thermally stable, neutral and should not include solvent molecules in the molecular lattice.[260] Intuitively, thermal stability is the most difficult point to fulfill. Indeed, the delicate coordinate covalent bonds between the metallic ion and the ligands, whose lengths are affected upon spin transition, may not sustain the temperature required for sublimation. To the best of my knowledge, only six SCO complexes are reported to be sublimable:

- Fe(phen)$_2$(NCS)$_2$ (with phen = 1,10-phenanthroline)[274, 288, 331, 368]

- Fe(H$_2$B(pz)$_2$)$_2$(phen) (with H$_2$B(pz)$_2$ = bis(hydrido)bis(1H-pyrazol-1-yl)borate and phen = 9,10-phenanthroline)[347, 369–371]

- Fe(H$_2$B(pz)$_2$)$_2$(bipy) (with H$_2$B(pz)$_2$ = bis(hydrido)bis(1H-pyrazol-1-yl)borate and bipy = 2,20- bipyridine)[334, 369, 370, 372, 373]

- Fe(HB(pz)$_3$)$_2$ (with pz = pyrazolyl)[354]

- Fe(NCS)$_2$L (L: 1-6-[1,1-di(pyridin-2-yl)ethyl]- pyridin-2-yl-N,N-dimethylmethan-amine)[332]

- Fe{[Me$_2$Pyrz]$_3$BH}$_2$ (Me = Methyl and Pyrz = Pyrazolyl)[280]

The realization of a 250 nm Fe-phen thin film by thermal sublimation reported by Shi *et al.*[274] in 2009 represents the first successful sublimation of SCO complexes. There were no other SCO complexes known to be sublimable at the time I started the SCO

study, and it thus partially explains the choice of Fe-phen as the SCO candidate for the ultra-thin film and single-molecule investigations that I will present. I would like to note that the fragility of the SCO complexes is a serious limitation for thermal sublimation, and demands us to check the integrity of the molecules once deposited onto the surface.

Concerning the substrate, most of the investigations were carried out using copper single crystals since they are conducting, can be relatively well cleaned in UHV environment and present large atomically flat terraces. In the following, I will describe the growth of Fe-phen molecules from single molecules to ultra-thin films on copper substrates with (100) and (111) surfaces.

13.2. Fe-phen growth on a Cu(100) substrate

A lot of efforts have been carried out to find the appropriate sublimation parameters, which are summarized in Sec. 6.1.3. We were then able to precisely control the deposited thickness of molecules such as to obtain samples with submonolayer Fe-phen coverage. Fig. 13.1a display a high-quality STM topography of isolated Fe-phen molecules on Cu(100). Each molecule shows two lobes (see for instance the single molecule encircled in Fig. 13.1a). Because of the strong affinity of S to the Cu substrate, the NCS groups bind to the substrate and the two phen groups point upwards as depicted in Fig. 13.1b. The two phen groups of a single molecule are seen as two lobes on the STM topography. In addition, the molecules adsorb along two different axes differing by 90° reflecting the underlying 4-fold symmetry of the substrate.
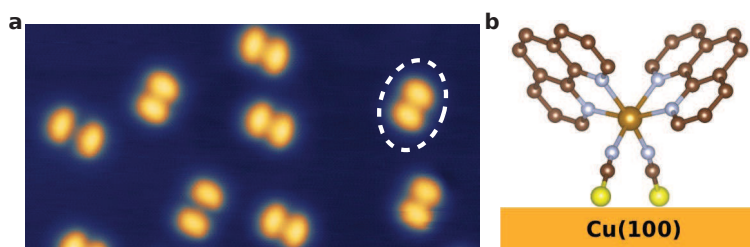
Figure 13.1. – **Isolated molecules on Cu(100)**. **a**, Topography of single Fe-phen on Cu(100). A single Fe-phen molecule appears as two bright lobes corresponding to its two phenanthroline groups. A single molecule is encircled for clarity. Image size is $17\,\text{nm} \times 8.5\,\text{nm}$ ($V=30\,\text{mV}, I=2\,\text{nA}$). **b**, Model of a single Fe-phen on top of Cu schematizing the adsorption geometry of the single molecules.

Figures 13.2a-d display medium-scale topographies of Fe-phen on Cu(100) with coverages ranging from 0.1 to 1.8 monolayers (ML) and indicate a layer-by-layer (Frank-van der Merwe) growth mode. As previously mentioned (13.1), the molecules
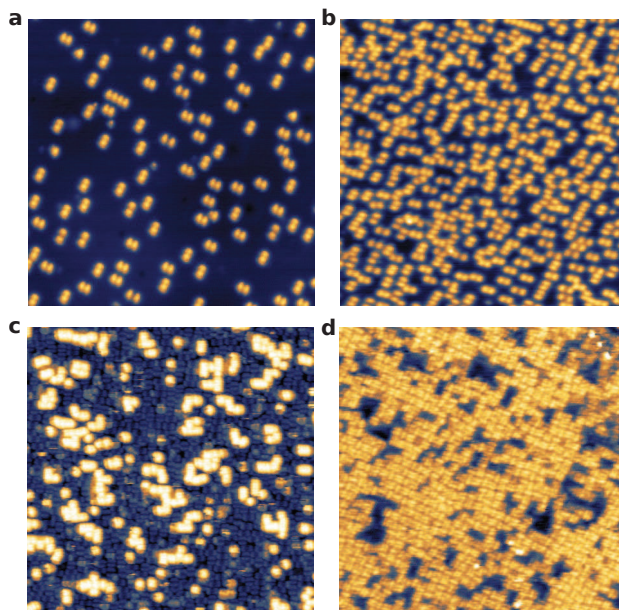
Figure 13.2. – **Layer-by-layer growth of Fe-phen on Cu(100)**. STM to-
pographies of Fe-phen on Cu(100) at different coverages. We can observe
that the molecules are rather isolated at sub-ML coverages of **a**, 0.1 ML
(V=0.1 V,I=1.1 nA) and **b**, 0.4 ML (V=1.0 V,I=15 pA), while they form
molecular clusters at a higher coverage of **c**, 1.4 ML (V=1.0 V,I=250 pA).
When the coverage if further increased to **d**, 1.8 ML (V=1.8 V,I=100 pA),
the molecules form short-range-ordered structures. The blueish (yel-
lowish) areas represent **a-b** the Cu substrate (first-ML molecules) or
c-d the first-ML molecules (second-ML molecules). Images sizes are
40 nm × 40 nm.

are rather isolated for a low Fe-phen coverage of 0.1 ML (Fig 13.2a). Increasing the
Fe-phen coverage to 0.4 ML (Fig. 13.2b) does not change the situation as we observe
only very little clustering inherent to the occupation of the surface by the molecules.
The isolated character of the molecules in contrast to their packed bulk structure (see
Sec. 12.1.2) suggest a blocking of molecular diffusion onto the Cu(100) surface. In
turn, it may reflect a diffusion energy barrier that is higher than the room-temperature
thermal energy. However, the second-ML Fe-phen can diffuse on top of the first ML
leading to the formation of second-ML islands as seen in Fig. 13.2c. When the Fe-
phen coverage is further increased to 1.8 ML, islands grow further and coalesce to form
short-range-ordered molecular structures (Fig. 13.2d). Since no significant molecular
diffusion is observed at the measurement temperature ($T \approx 4$ K), any molecular dif-
fusion must take place during and after deposition at room temperature, which leads
to a molecular arrangement that is frozen upon subsequent cooling. In addition, we
infer that the diffusion energy barrier reflects the coupling of the molecules to the un-
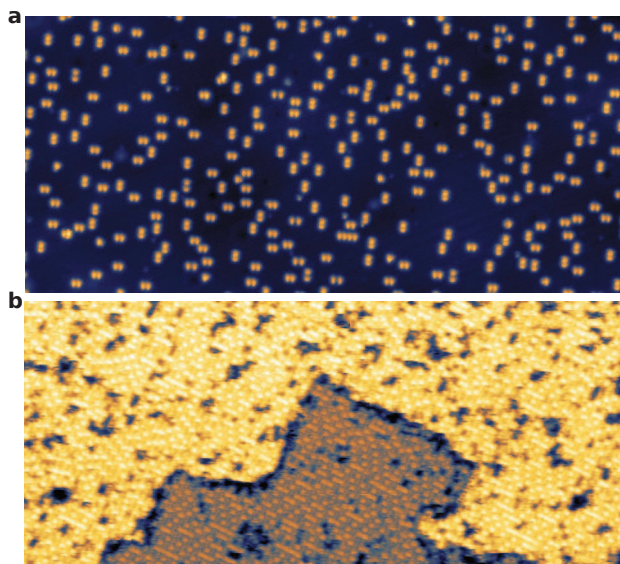
Figure 13.3. – **Large-scale topographies of Fe-phen on Cu(100)**. STM topographies of **a**, isolated first-ML Fe-phen (V=100 mV,I=2 nA) and **b**, second-ML Fe-phen (V=0.6 V,I=150 pA) on Cu(100). **a**, The topography reveals a relatively homogeneous and almost contamination-free Fe-phen deposition. **b**, The height difference between the yellowish and the orangish levels does not allow to distinguish between atomic and molecular steps. However the steps are mainly in two orthogonal directions and form relatively straight lines in contrast to the shapes of the holes. This suggests that the steps observed in the topography correspond to atomic steps of the underlying copper substrate. On both levels, we can observe a mixture of dense and depleted molecular areas. Images sizes are 110 nm × 50 nm .

derlying substrate or molecular layers, and thus indicates that second-ML molecules are less coupled to the underlying substrate compared to the first-ML molecules.

Large-scale topographies on first- and second-ML Fe-phen on Cu(100) shown respectively in Fig. 13.3a and 13.3b, confirms the layer-by-layer growth. In the topography of the second ML, we observe dense and depleted areas of molecules. In addition, both topographies reveal a relatively homogeneous molecular deposition at the 100 nm scale and almost contamination free samples.

The dense areas of the second-ML molecules present short-range-ordered structures (see Fig. 13.2d and 13.3b). In order to describe and understand these structures, we first depict how the molecules lie onto Cu(100). Figure 13.4a shows a single Fe-phen molecule sitting on the Cu(100) substrate via its NCS groups. The long axis of the molecule is along the [0$\bar{1}$1] crystallographic axis of the underlying copper and a single molecular model is scaled and superimposed onto the STM image. For low
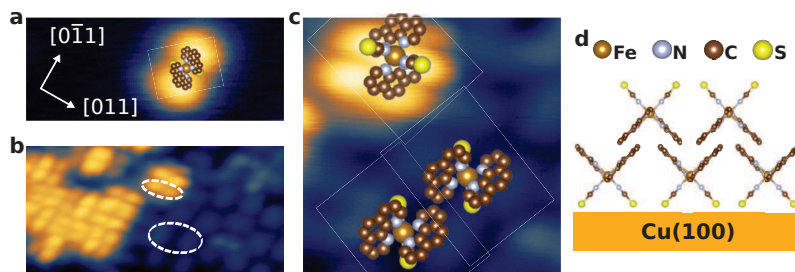
Figure 13.4. – **Adsorption geometry of first- and second-ML Fe-phen on Cu(100)**. **a**, Model of a Fe-phen molecule scaled and superimposed onto the topography of an isolated molecule. **b**, STM image of 1.4 ML Fe-phen on Cu(100). Single first- and second-ML molecules are encircled for clarity and clearly indicate the different apparent sizes of the molecules. Note that the first-ML molecules are identified by suitably modifying the image contrast. **c**, Zoomed STM topography of **b**, with scaled and superimposed molecular models that point out the different adsorption geometry for first- and second-ML Fe-phen molecules. **d**, Schematic of the proposed adsorption geometry for first- and second-ML Fe-phen on Cu(100). Image sizes are **a**, 6.6 nm × 2.7 nm (V=0.2 V,I=180 pA), **b**, 9.0 nm × 4.5 nm (V=0.6 V,I=200 pA), **c**, 3.1 nm × 3.1 nm (V=0.7 V,I=70 pA). The molecular models were created using VESTA[273] and the X-ray diffraction data from Ref. 266.

tunneling currents that we use here, STM only probes the outermost part of the broad π orbitals of the phenanthroline groups that are pointing away from the surface. In turn, this explains the significantly increased apparent size of the Fe-phen molecule deduced from the topography compared to the size inferred from the model molecule. The apparent size of the first-ML molecules remains larger than that of the model even when the coverage is increased to 1.4 ML such that the occupation of the first layer is maximum (Figs 13.4b and 13.4c). Nevertheless, the situation is different for the second-ML molecules whose apparent size is slightly smaller. They also exhibit a different shape that suggests a different adsorption geometry. Based on the bulk structure of Fe-phen[266,272,374] (see also Sec. 12.1.2) and on STM experiments performed on other SCO complexes,[347,373] we propose that the second-ML molecules lie upside down compared to first-ML molecules. The phen groups of the first-ML (second-ML) molecules would then point upwards (downwards) such as to enable $\pi-\pi$ interactions also present in the bulk form (Sec. 12.1.2).

The possibility of the second-ML Fe-phen molecules to diffuse, in addition to the inter-molecular interactions between molecules of the second ML, leads to the formation of small region where the molecules are ordered (Fig. 13.5). A molecular pattern composed of three molecules, represented in the left inset to Fig. 13.5, is often reproduced in the ordered areas. Other structures, such as the one emphasized in the inset to Fig. 13.5, rarely appear and may thus be energetically less favorable.
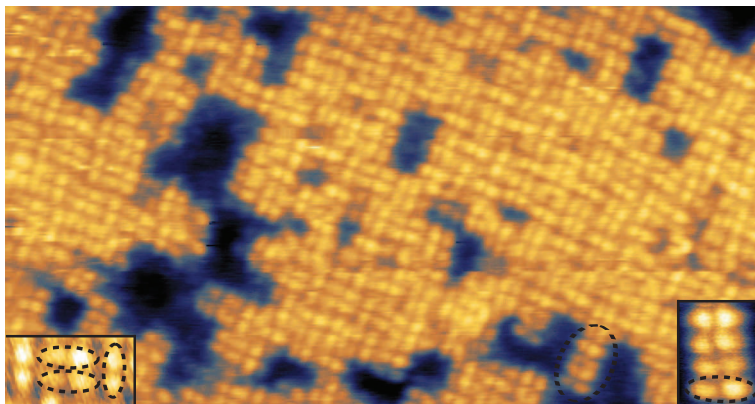
Figure 13.5. – **Molecular structure of the second-ML Fe-phen molecules on Cu(100)**. STM topography of the second-ML Fe-phen molecules on Cu(100) revealing dense and depleted areas of molecules. The bottom left inset shows the three-molecule pattern commonly seen in the dense and ordered areas. Other molecular structures seldom appear, such as the one presented in the bottom right inset: molecules with same orientation are sitting next to each other, so as to form a chain-like molecular structure. Image size is $27.6\,\text{nm} \times 14.5\,\text{nm}$ (V=0.6 V,I=115 pA). Inset sizes are (left) $2.8\,\text{nm} \times 1.6\,\text{nm}$, (right) $1.6\,\text{nm} \times 2.1\,\text{nm}$.

13.3. Fe-phen growth on a Cu(111) substrate

Since the geometry of molecular adsorption is closely related to the substrate symmetry, the growth of Fe-phen was also investigated on a Cu(111) substrate. Figure 13.6a shows a topography of 0.1 ML of Fe-phen deposited onto a Cu(111) surface. The molecules look similar to those on a Cu(100) substrate (see Fig. 13.3a), which suggests a similar adsorption geometry. Here too, Fe-phen molecules are isolated on the surface due to the absence of molecular diffusion at room temperature, due to the strong coupling to the substrate. STM topographies of Fe-phen at coverages of 0.6 ML (Fig. 13.6b) and of approximately 1.8 ML (Fig. 13.6c) indicate a layer-by-layer growth in analogy to the growth of Fe-phen on Cu(100) (Figs. 13.2 and 13.3). However, the second-ML Fe-phen looks much more dense on Cu(111) than on Cu(100) substrates. Indeed, in Fig. 13.6a we can observe dense areas almost free of depletion zones in contrast to Fe-phen on Cu(100) (Fig. 13.3b). These large areas of high molecular density may arise from a lower diffusion barrier of the second-ML molecules on a Cu(111) substrate compared to the one on a Cu(100) substrate. Since second-ML molecules diffuse onto the corrugated potential landscape originating from the first-ML molecules, the lower diffusion barrier on Cu(111) is corroborated by the very regular and homogeneous first-ML-molecule positioning onto the Cu(111) surface (Fig. 13.6b) to compare to the molecule positioning onto the Cu(100) surface (Fig. 13.2b). The less dense areas of the second-ML Fe-phen on Cu(111) are dendrite
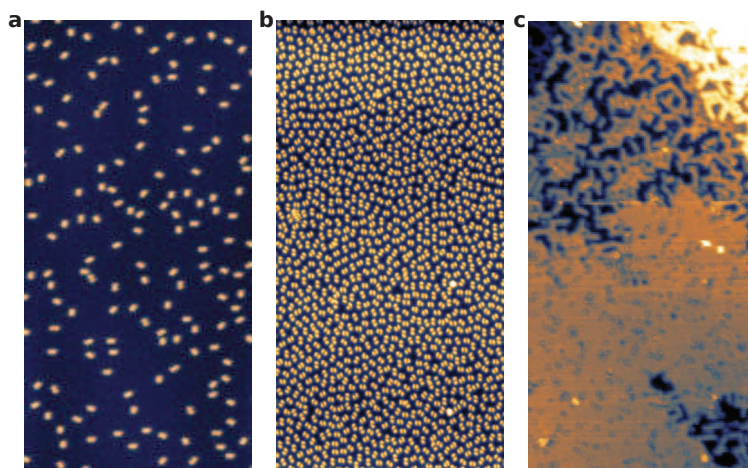
Figure 13.6. – **Layer-by-layer growth of Fe-phen on Cu(111)**. Large-
scale STM topography of Fe-phen molecules on Cu(111) at different cover-
ages: **a**, 0.1 ML (V=0.3 V,I=30 pA), **b**, 0.6 ML (V=1.0 V,I=50 pA) and **c**,
approximately 1.8 ML (V=0.85 V,I=230 pA). The topographies indicate
a layer-by-layer and contamination-free growth of Fe-phen on Cu(111).
Image sizes are 55 nm × 110 nm.

like, and one can speculate that these areas turn into organized dense zones when
the coverage is further increased. Additionally, Figs. 13.6a-c also indicate an almost
contamination-free deposition.

The molecular topography presented in Fig. 13.7a indicates a 6-fold symmetry
with 6 different orientations of the molecules on the substrate. This suggests two
different adsorption sites that are three-fold degenerate due to the three-fold symmetry
of the substrate. Increasing molecular coverage up to 1.9 ML leads to a layer-by-layer
growth of the molecules as previously mentioned. On the surface, areas consisting
of dense ordered structures coexist with areas with chains of molecules as shown in
Fig. 13.7b. Similarly to the Cu(100) case, the second-ML molecules look different
from the first-ML molecules, in agreement with the adsorption geometry proposed in
Fig. 13.4c. A zoomed image of the chain structure is shown in the upper inset to
Fig. 13.7b. In the one-molecule-wide chain, the molecules sit next to each other to
favor $\pi - \pi$ interactions of the phenanthroline groups. The molecules in the second
layer form a densely packed layer according to a molecular pattern that is presented
in the lower inset to Fig. 13.7b. The ordered molecular structure is composed of 4
pairs of molecules, which reduces the 6-fold symmetry of the first layer to the 2-fold
symmetry of Fe-phen.
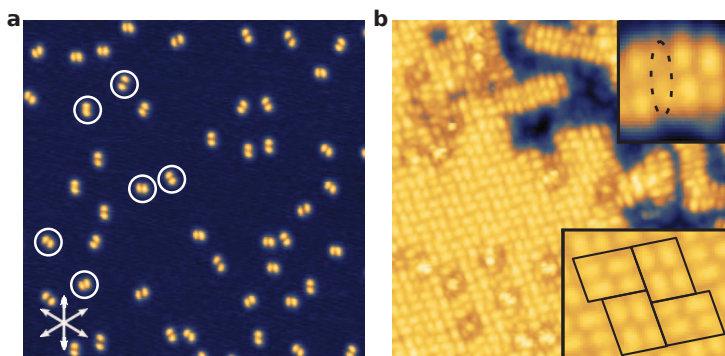
Figure 13.7. – **Adsorption geometry of first- and second-ML Fe-phen on Cu(111)**. Topographies of a **a**, 0.1 ML sample revealing 6 different orientations of the molecules (molecules in the 6 different orientations are encircled in white), **b**, 1.8 ML showing ordered densely-packed areas (lower inset) in contrast to chain-like structures of the molecules in less dense-areas (upper inset). For clarity, a single molecule is encircled in the upper inset, and pairs of molecules are surrounded by a parallelogram in the lower inset. Image sizes are **a**, 45 nm × 45 nm (V=0.15 V, I=150 pA), **b**, 18 nm × 18 nm (V=0.6 V, I=200 pA), (upper inset) 2.0 nm × 2.1 nm, (lower inset) 3.9 nm × 3.1 nm.

13.4. Partial conclusion

In this chapter, I have shown STM topographies that reveal a successful and almost contamination-free Fe-phen deposition onto Cu(100) and Cu(100) substrates, that is reinforced by XAS measurements presented latter. Note that part of these growth results were published in Ref. 288. On both substrates, we observe a layer-by-layer growth of Fe-phen, which is of fundamental importance to realize SCO-based devices. With the help of high-resolution STM images, we could propose the adsorption geometry of the molecules: the first-ML molecules have their NCS (phen) groups towards (away from) the surface, while the second-ML molecules are lying upside-down. In addition, the diffusion energy barrier of the first-ML molecules seem much higher than that of the second-ML molecules, which suggest that the first-ML is much more coupled to the substrate than the second-ML. In turn, the different couplings have an impact on the spin state of the molecules, which will be discussed in the next chapter.

14

Spin-state switching with a STM tip

In the previous chapter, we have shown that we can successfully sublime Fe-phen molecules onto Cu surfaces. In bulk, Fe-phen molecules are either in the HS state with a total spin S=2 or in the LS state with S=0, depending on the external physical parameters (see Chap. 12). In turn, the size of the molecules, as well as the density of states are expected to be spin-state dependent. In the following, the measurements are performed at cryogenic temperatures ($T \approx 4$ K) and low pressure ($p < 1 \times 10^{-11}$ mbar), we would thus expect the bulk Fe-phen molecules to be in their LS state. However, the reduction of the system size and the interactions with the substrate should be taken into account. It results that the properties of the Fe-phen molecules on surfaces can be totally different from that of Fe-phen bulk molecules. In this chapter, we will see that both spin states of the first-ML Fe-phen molecules coexist on the surface and the spin state of a given first-ML molecule can be identified from topography and/or spectroscopy data. The spin-state identification is followed by spin-state-switching attempts on first-ML molecules. We will see that while the strong molecule-substrate electronic coupling prevents the switching when the molecules are deposited onto a Cu(100) surface, the spin-state switching is possible by inserting an insulating CuN layer between the molecules and the Cu(100) substrate. Finally, we will discuss about the spin-state of the second-ML Fe-phen molecules on Cu(100) and Cu(111); and voltage-induced topographic changes that we tentatively ascribe to a spin transition.

14.1. Spin-state identification of first-ML Fe-phen on Cu(100)

Figure 14.1a displays a high-resolution topography of isolated Fe-phen molecules on Cu(100). As previously mentioned, there are two orientations of the molecules coming from the 4-fold symmetry of the underlying substrate. In addition, we can observe
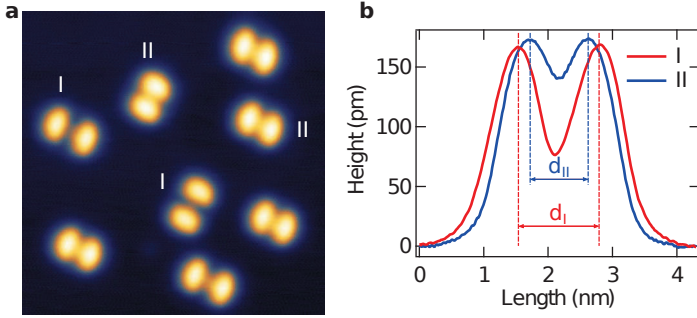
Figure 14.1. – **Two different conformations for Fe-phen molecules on bare Cu(100)**. **a**, STM topography of isolated first-ML Fe-phen molecules with two different conformations denoted I (HS) and II (LS). Image size is $13\,\text{nm} \times 13\,\text{nm}$ ($V=30\,\text{mV}, I=1\,\text{nA}$). **b**, Height profiles for molecules in conformation I and II extracted from image **a**.

two different conformations of the molecules depending on the interlobe distance. The molecules in the conformation labeled I are characterized by an interlobe distance of $d_\text{I}=1.29\,\text{nm}$ which is quite larger than the interlobe distance of $d_\text{II}=0.92\,\text{nm}$ for molecules in conformation II (see height profiles in Fig. 14.1b). Note that the interlobe distances for both conformations can vary slightly when using different STM tips since the STM image results from a convolution of the surface topography and the tip shape.

In bulk, the Fe-N bond length and the unit-cell volume are larger in the HS state. Since conformation I is larger than conformation II, we can tentatively ascribe the molecules in conformation I as being in the HS state, in agreement with *ab initio* calculations.[375] However, we cannot be conclusive on this point considering that (i) the measured interlobe distances are strongly affected by the local density of states and (ii) the interaction of the molecule with the substrate could lead to different electronic configurations in the Fe ion than those of bulk Fe-phen, which in turn would lead to different spin states.

In order to provide further insights into the spin state of the Fe-phen molecules, we performed scanning tunneling spectroscopy (STS) measurements on molecules of both conformations. The tunneling conductance, sensitive to the local density of states, measured atop a conformation II molecule's center reveals only minor variations. In contrast, the differential tunneling current atop a conformation I molecule's center exhibits a strong increase near the Fermi edge (Fig. 14.2b). The resonance can be fitted with a Fano function revealing a Kondo temperature $T_K \approx 317\,\text{K}$, a q-factor of 6.1 and a Coulomb repulsion shift of $5.7\,\text{meV}$ (see Sec. 3.3). The dI/dV map presented in Fig. 14.2c shows that the Kondo resonance is located at the expected position of the Fe ion, and is only present for the molecule in conformation I. A Kondo resonance is caused by a many-body state that arises from the screening of an "impurity" spin by the substrate conduction electrons, and is thus a signature of unpaired spins. Since
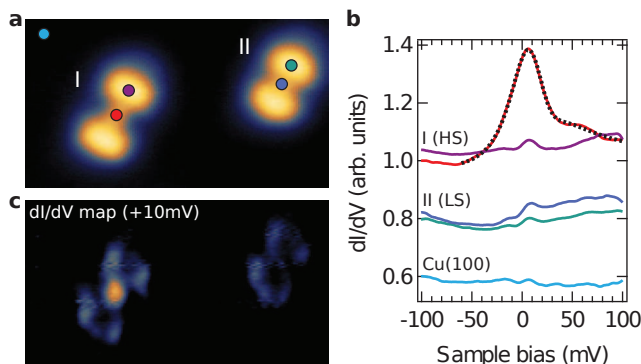
Figure 14.2. – **Spectroscopy of Fe-phen molecules on bare Cu(100)**. **a**, STM topography of isolated first-ML Fe-phen molecules in conformations I and II. **b**, dI/dV spectra recorded on the center and the lobe of two molecules in different conformations. The colors indicate the location, where the spectra were acquired and are marked as colored dots of **a**. **c**, dI/dV map acquired at 10 mV imaging the same area than **a**, showing the position of the dI/dV resonance at the center of the molecule in conformation I (HS). Image sizes are 6.7 nm × 2.7 nm. The spectra were acquired with a voltage modulation of 3 mV at a frequency of 723 Hz.

we ensured that the spin states of Fe-phen molecules are not altered upon adsorption onto Cu(100) (see next paragraph), we can ascribe the molecular conformations I and II as the HS ($S=2$) and the LS ($S=0$) states, respectively.

As described in Chap. 4, X-ray absorption spectroscopy (XAS) is an element-specific spectroscopic method that is sensitive to the electronic structure with chemical selectivity. Since the electronic structure of the metallic ion depends on the spin state, XAS can, in principle, resolve the spin state of Fe-phen. We carried out XAS measurements on an *in situ* prepared sample of ≈2 ML Fe-phen onto a Cu(100) substrate. In addition, we measured bulk Fe-phen powder that we use as a reference. During the measurements, we ensured that the X-ray intensity was low enough in order to avoid deterioration of the molecules. Furthermore, no external illumination except for the X-rays was applied to avoid light-induced excited spin-state trapping (see Sec. 12.3.4). We first present the XAS measurements at the Fe L edges on Fe-phen powder that we use as a reference to analyze the thin-film data. The measurement performed at 200 K, *i.e.* above the transition temperature of Fe-phen ($T_{1/2} \approx 175$ K), gives a reference spectrum for the molecules in the HS state (top panel of Fig. 14.3a), while the measurement acquired at 100 K gives a LS reference spectrum (middle panel of Fig. 14.3a). The L_3 edge of the HS reference XAS spectrum is characterized by a dominant peak located at 706.6 eV and a satellite peak located at 707.4 eV, while the L_3 edge of the LS reference spectrum has a dominant peak at 708.1 eV. This is in good agreement with previous studies on Fe-phen powder.[267, 327] Interestingly, the L_3 edge in the XAS spectrum of 2 ML Fe-phen on Cu(100) (bottom panel of Fig. 14.3a)
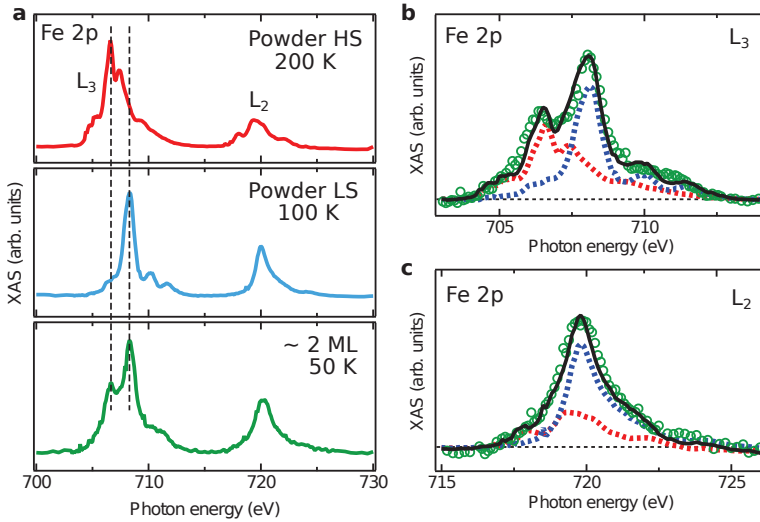
Figure 14.3. – **Coexistence of HS and LS states of Fe-phen molecules on Cu(100) revealed by XAS**. **a**, XAS performed at the Fe L edges on Fe-phen powder reference sample at 200 K (HS state, top panel), at 100 K (LS state, middle panel) and on 2 ML Fe-phen on Cu(100) at 50 K (bottom panel). The main peak of the L_3 edge is located at different energies for the HS (top) and the LS (middle) Fe-phen molecules. The 2 ML-thin Fe-phen film (bottom) seems to have HS and LS contributions. Reproduction of the XAS (solid black) **b**, L_3 and **c**, L_2 edges of 2 ML Fe-phen on Cu(100) (green circles) using a linear combination of the HS (46%, red) and the LS (54%, blue) reference spectra obtained on the powder sample.

has two dominant peaks located at 706.6 eV and 708.1 eV suggesting a coexistence of both spin state, in agreement with the STM study. In order to be more quantitative, in Figs. 14.3b and 14.3c we reproduced the XAS spectrum of the 2 ML Fe-phen using a linear combination of the HS and LS reference spectra. The weighting coefficient can be used to deduce the proportion of HS molecules (46%) and the proportion of LS molecules (54%).[333] Note that a Fe ion with a different ligand field (*e.g.* in a molecule with broken ligands) or in a different oxidation state (e.g. due from a charge transfer with the substrate) than that of bulk Fe-phen would lead to different XAS spectra. Hence, the XAS results ensure that (i) the molecules are intact on the surface, (ii) the spin states of the molecules are not altered by the substrate and (iii) molecules in HS and in LS states surprisingly coexist on the surface.

To further reinforce the validity of the non-altered spin moments of Fe-phen on Cu(100) we performed X-ray magnetic circular dichroism (XMCD) measurements, as this sensitive technique can reveal the spin and orbital magnetic moments of a specific element. The XMCD spectrum is obtained by taking the difference between XAS spectra obtained for left- and right-circularly polarized photons. In turn, the
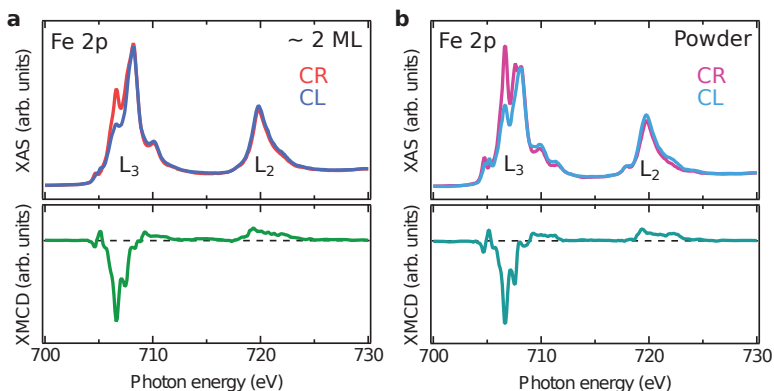
Figure 14.4. – **Comparison of XMCD spectra of bulk and** 2 ML **Fe-phen**. XAS and corresponding XMCD spectra of **a**, 2 ML Fe-phen on Cu(100) measured at 1.5 K and 6.5 T and **b**, Fe-phen powder reference sample acquired at 4.0 K and 6.5 T. CR (CL) stands for the circular right (circular left) photon helicity of the incoming X-rays. The zero of the XMCD spectra is represented by the black dotted lines.

XMCD intensity is directly linked to the magnetic moment of the investigated element provided that the paramagnetic centers are aligned with an external magnetic field. This requires measurements at low temperatures and high magnetic fields. Note that at low temperatures, bulk Fe-phen molecules are sensitive to the soft X-ray induced excited spin-state trapping (SOXIESST) effect[267, 333] (see Sec. 12.3.5), so that a proportion of the Fe-phen molecules initially in the LS state are excited into the HS state by the X-rays, and remain trapped in the HS state. XAS and XMCD measurements performed at low temperatures and high magnetic field on 2 ML and on bulk Fe-phen molecules are shown in Fig. 14.4a and 14.4b, respectively. The XAS spectra are relatively different since the proportion of HS molecules is different in both samples. However, the XMCD spectra are similar. Considering that only molecules in the HS state have a net magnetic moment on the Fe ion, the similar XMCD spectra indicate identical HS states for bulk and 2 ML Fe-phen molecules, in agreement with the previous results. Note that we can, in principle, extract the spin and orbital magnetic moment by applying the sum rules on the XMCD spectra (see Sec. 4.3.2), but it would lead to wrong quantities since we do not have only HS molecules.

To conclude the section, the combined STM and XAS studies allow to unambiguously claim that (i) the Fe-phen molecules are intact on the Cu(100) surface, (ii) the spin states are not altered by the substrate and (iii) HS and LS molecules coexist onto the Cu(100) surface and can be identified using STM topography and/or spectroscopy. At the time of the study, this last point was very surprising since Fe-phen bulk molecules would be in their LS state at $T \approx 4$ K, and we will thus further investigate the spin-state coexistence in the next chapter. However, another challenging

question remains: does the SCO property of the molecules subsist once deposited onto the surfaces?

14.2. Selective and deterministic switching of a single molecule

We first discuss the spin-state-switching attempts on single isolated molecules since the spin state of a given single molecule can be identified by the topographic and/or spectroscopic data. Moreover, as the hybridization of a single molecule with the substrate can strongly influence the molecular properties, the spin-state-switching study is carried out using two different substrates, Cu(100) and CuN/Cu(100). Molecules deposited onto Cu(100) are expected to hybridize more than the one deposited onto CuN/Cu(100) due to the different electron density near the Fermi level. Note that the work presented in this section has been published in Ref. 331.

14.2.1. Single-molecule switching attempts on Fe-phen on Cu(100)

Following the spin-state identification of Fe-phen on Cu(100) detailed in the previous section, we now would like to switch the spin state of a selected molecule. In the literature, a common way to trigger a molecular switch using a STM is to perform current-voltage curves.[250,376–378] In figure 14.5, we show a current-voltage curve acquired atop the center of a HS molecule. The $I(V)$ curve shows a typical tunneling background with no abrupt current variation and the curves acquired for two different voltage-sweeping directions match perfectly. There is thus, no sign of a spin transition of the Fe-phen HS molecule. The same experiment performed atop a LS molecule's center and with different tip-molecule distances also suggest the absence of a spin transition (not shown).

Now we have to consider that there is possibly no conductance change of Fe-phen molecule upon spin transition, although a conductance change is expected for SCO complexes due to the conformational transition.[339] In that case, the tunneling current atop a HS molecule would be the same than that atop a LS molecule, and we would thus not be able to monitor a spin transition in a current-voltage spectrum. However, thanks to the discussion in the previous section, we know that the spin state can be identified by topographic data. In Fig. 14.6, at a fixed current, we continuously scanned a single Fe-phen molecule along its long axis to monitor the interlobe gap of a molecule, and thus its spin state, while gradually increasing the sample voltage. Since we do not observe a sharp change in the topography for measurements atop a HS (Fig. 14.6a) and atop a LS (Fig. 14.6b) molecule, we can conclude that there is no voltage-induced spin transition. Additional measurements were performed at higher voltages, for negative sample voltages and for different tunneling currents leading to the same conclusion (not shown).
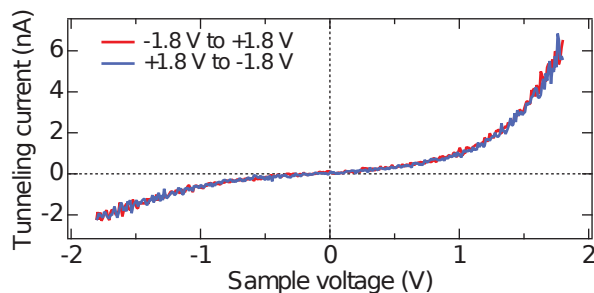
Figure 14.5. – **Current-voltage curve acquired atop the center of a single Fe-phen HS molecule on Cu(100)**. The spectrum exhibits a normal tunneling background with no sign of a spin transition. The feedback loop is opened at 1.8 V and 6 nA.
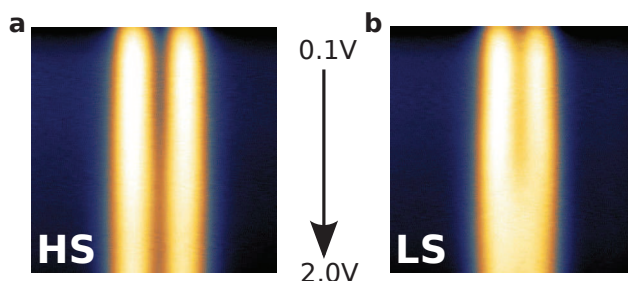
Figure 14.6. – **Evolution of the interlobe distance of a single Fe-phen molecule on Cu(100) with increasing sample voltage**. Sample-voltage dependencies of the STM height profile for the **a** HS and the **b** LS states. Image widths are 6.0 nm.

We additionally tried to switch the spin state of a Fe-phen molecule on Cu(100) by applying high sample voltages (up to 4 V) and high tunneling currents (up to 1 µA), both in continuous and pulsed mode, without any sign of success. The only possible way we found to switch the spin state of Fe-phen on Cu(100) is to perform a lateral tip manipulation on the molecule. In Fig. 14.7, we present the modification of the adsorption site of a LS Fe-phen molecule through a tip induced lateral manipulation of the molecule (see Figs. 14.7a and 14.7b for topographies before and after the tip manipulation, respectively). The topography of the manipulated molecule presents a larger interlobe distance than before the manipulation, suggesting a transition into the HS state. However, the final orientation of the molecule is tilted by about 45° compared to the usual orientations of Fe-phen molecules (see Fig. 14.7b), so that the conclusion of a final HS state is not straightforward.

We infer that the impossibility to electronically switch the spin state of Fe-phen on Cu(100) with the above tunneling conditions is due to a too strong electronic (chemical) coupling of Fe-phen with the Cu substrate.
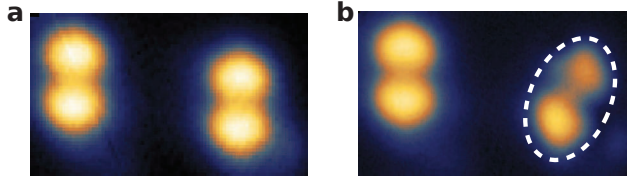
Figure 14.7. – **Lateral tip manipulation on a LS Fe-phen molecule on Cu(100)**. Topographies **a** before and **b** after a tip induced lateral manipulation of a LS Fe-phen molecule. For clarity, the manipulated molecule is encircled in **b**. Image sizes are $4.8\,\text{nm} \times 2.8\,\text{nm}$.

14.2.2. Spin-state switching of single Fe-phen molecules on CuN/Cu(100)

In order to reduce the electronic interaction between the molecule and the substrate, that we believe to be responsible for the impossibility to switch the spin state of the Fe-phen molecules on Cu(100), we inserted a CuN monolayer between Fe-phen and the Cu(100) substrate. The insulating CuN layer helps to significantly reduce the adsorption energy and the ensuing hybridization.[375,379] The preparation of the CuN layer is discussed in the appendix B. In Fig. 14.8a, we present a topography of two Fe-phen molecules on CuN/Cu(100), which suggest an adsorption geometry with the NCS groups towards the surface, similarly to Fe-phen on Cu(100). Additionally, we observe two different conformations of the Fe-phen molecules. The topographic differences between the two conformations mainly reside at the center of the molecules, where the apparent height of the two conformations slightly differs (see Figs. 14.8a and 14.8b). The difference in STM topographies between the two conformations is not as obvious as that of Fe-phen on Cu(100), which might be due to the electronic decoupling of the Fe-phen molecules with the substrate. dI/dV spectra near the Fermi level on the center of both conformations reveal a Kondo resonance only for the conformation with the highest apparent size at the center. The dI/dV spectrum atop a Fe-phen molecule in the other conformation shows only weak spectroscopic features (see Fig. 14.8c), that are very similar to those present in the spectrum acquired atop bare CuN. By analogy to the measurements performed on Fe-phen onto Cu(100) (see Sec. 14.2.1), we ascribe the molecular conformation with (without) a Kondo resonance to the HS (LS) conformational state. A Fano fit on the Kondo resonance yields a Kondo temperature of $T_K^{CuN} \approx 105\,\text{K}$ ($q = 4.9$ and Coulomb shift of $5.5\,\text{meV}$) that is significantly lower than that previously found on HS Fe-phen on Cu(100) ($T_K^{Cu(100)} \approx 317\,\text{K}$). This is expected from a weaker electronic hybridization of Fe-phen molecules on CuN/Cu(100) compared to Cu(100).

The dI/dV spectra presented in Fig. 14.9 reinforce the statement of the reduced electronic hybridization of Fe-phen/CuN compared to that of Fe-phen/Cu(100). Indeed, spectroscopic features in addition to the Kondo resonance, indistinguishable on the spectra taken on single Fe-phen molecules on Cu(100) become visible on the
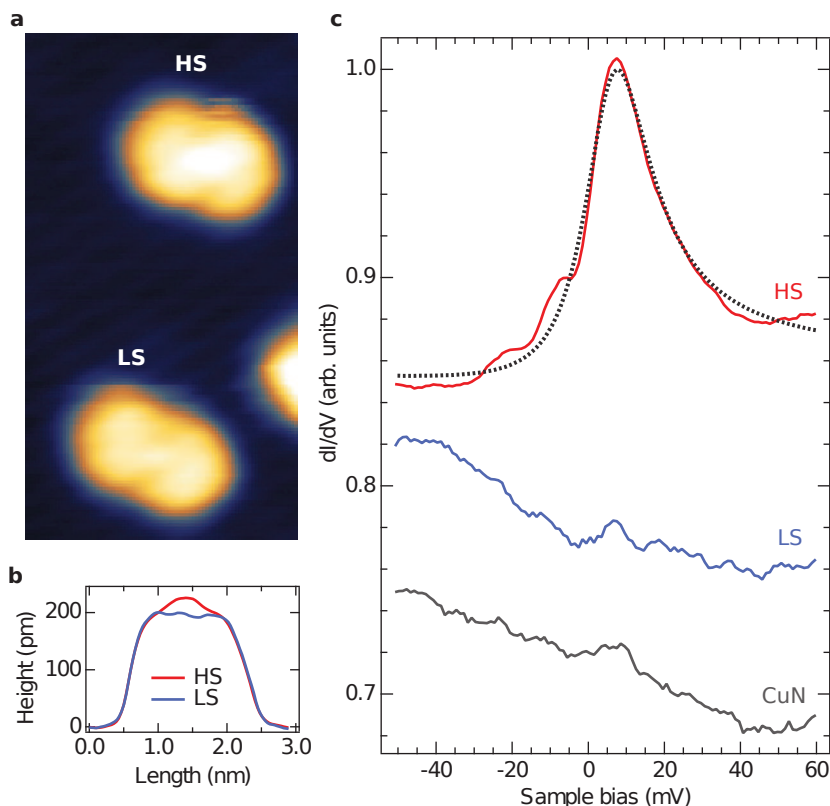
Figure 14.8. – **Identification of the two conformations of Fe-phen on CuN/Cu(100)**. **a**, STM topography of the two observed conformations of isolated Fe-phen molecules on the CuN/Cu(100) surface and **b**, the corresponding height profiles along the long axis of the molecules highlighting the difference between the two conformations. **c** dI/dV spectra acquired at the center of the molecules for the two conformations and on bare CuN/Cu(100). The spin-state assignment of the two conformations is based on the presence/absence of the Kondo resonance. The latter is fitted with a Fano function represented by a dotted black line. Image size is $3.0\,nm \times 5.5\,nm$ ($V=0.1\,V$,$I=100\,pA$). The spectra were acquired with a voltage modulation of $3\,mV$ at a frequency of $723\,Hz$.

spectra acquired on Fe-phen/CuN. Those molecular states are however still rather broad indicating short lifetimes. From the observed widths of the peaks in the dI/dV spectra of Fe-phen/CuN, and using the Heisenberg uncertainty principle, one can roughly estimate the molecular states' lifetime between $2\,fs$ and $5\,fs$. These short lifetimes indicate that, although the CuN partially electronically passivates the surface, the molecule/substrate hybridization is still rather strong. In turn, this excludes the possibility of a charged state of the molecule.
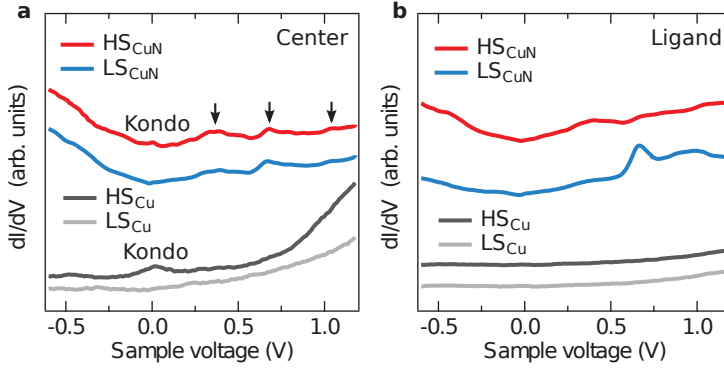
Figure 14.9. – *dI/dV* **spectra on Fe-phen molecules for both spin states on CuN/Cu(100) and Cu(100)**. **a**, *dI/dV* spectra taken on top of Fe-phen molecules' center. The Kondo resonance is distinguishable for molecules in the HS state on both substrates. The arrows indicate the position of additional spectroscopic features that are observed when the molecules are on the CuN/Cu(100) surface (peaks located at 0.35, 0.7 and 1.0 eV). **b**, *dI/dV* spectra acquired on the top of the ligand of Fe-phen molecules on CuN/Cu(100) and Cu(100) surfaces. The spectra were acquired with a voltage modulation of 10 mV at a frequency of 723 Hz.

We additionally observe that the *dI/dV* spectra acquired on top of the ligands of Fe-phen/CuN reveal spectroscopic features that are different for the HS and LS conformations (see Fig. 14.9b). This is in agreement with theoretical predictions of electronic differences between the HS- and the LS-state molecules.[272]

We recall that we observed the two spin states of Fe-phen molecules when deposited onto Cu(100) and the apparent failure of the switching attempts was explained by a too strong molecule-substrate coupling. Here, for Fe-phen on CuN/Cu(100), the reduced Kondo temperature and the better resolved molecular orbitals in *dI/dV* spectra indicate a reduced molecule-substrate hybridization. We can thus expect to be more fortunate and successfully switch the spin state of single Fe-phen molecules on CuN/Cu(100). In Fig. 14.10a, we show current-voltage curves acquired with the STM feedback loop opened atop the center of a Fe-phen molecule on CuN/Cu(100). In contrast to the same experiment performed on Fe-phen/Cu(100) (see Fig. 14.5), the cyclic *I(V)* curve indicates a hysteresis with two different conductance states. For a molecule initially in the high-conductance state (in red), sweeping the sample voltage up leads to an abrupt current decrease at $V \approx 1.2$ V that corresponds to a switch to the low-conductance state (in blue). From this low-conductance state, a current increase (negative current) appears at $V \approx -0.8$ V when sweeping the sample voltage down. This current jump is associated to the transition from the low- to the high-conductance state. Repeated cyclic *I(V)* measurements were performed and indicate a fully reversible conductance-state switching.
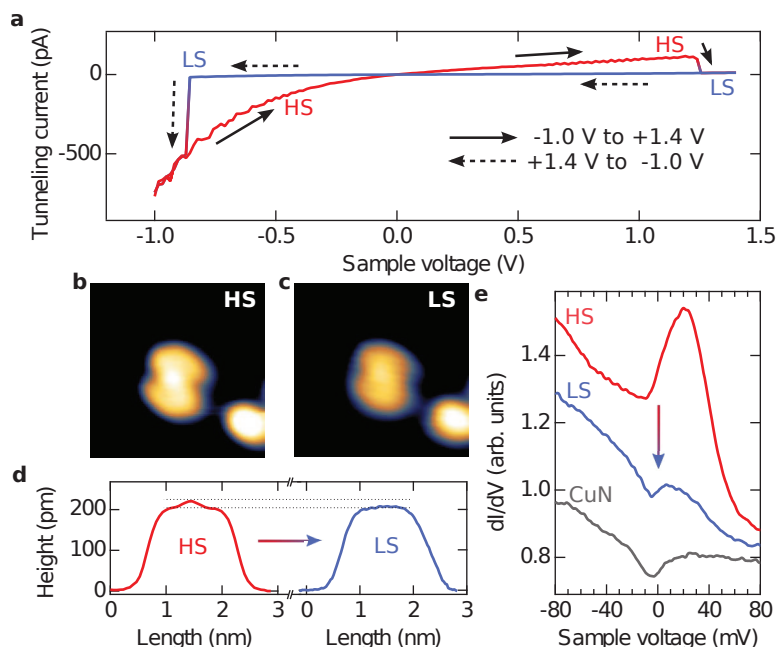
Figure 14.10. – **Spin-state and conductance switching of single Fe-phen molecules on CuN/Cu(100)**. **a**, $I(V)$ curve of an isolated single Fe-phen molecule recorded on the center of the molecule. The curve clearly shows two conductance states with a hysteretic behavior (tunneling conditions for tip stabilization: $V=1\,V$, $I=100\,pA$). The single Fe-phen molecule is imaged in both conductance states. The high (red) and low (blue) conductance states correspond to the molecule in the **b**, HS and in the **c**, LS states, respectively. **d**, Height profiles of the STM topographies presented in **b** and **c** along the long axis of the molecule to better visualize the spin state of the molecule. **e**, dI/dV spectra of the single Fe-phen molecule in both conductance states. A Kondo resonance is observed only for the molecule in the high conductance state. Topographic and spectroscopic data clearly reveal that the high (low) conductance state correspond to the HS (LS) state of the single molecule. Image size are $3.7\,nm \times 3.7\,nm$ ($V=0.1\,V, I=100\,pA$). The dI/dV spectra were acquired with a voltage modulation of $3\,mV$ at a frequency of $723\,Hz$.

Since a change in the molecular conformation can induce a conductance switching in the $I(V)$ curve,[376] such as in Fig. 14.10a, we now identify the conformational state in the high- and low-conductance states. Figs. 14.10b and 14.10c represent STM topographies of the same isolated Fe-phen molecule in the high and low-conductance states, respectively. For the molecule in the high-conductance state (Fig. 14.10b), we can observe a bright protrusion at the center of the molecule, which is absent when the molecule is in the low-conductance state (Fig. 14.10c). The conductance-state

dependence of the STM topographies can also be monitored on the height profiles along the long axis of the molecule (Fig. 14.10d). In addition, the apparent two different molecular conformations have totally different spectroscopic features near the Fermi energy in the dI/dV spectra (see Fig. 14.10e). Indeed, there is a Kondo resonance when the molecule is in its high-conductance state, and the resonance is turned off when the molecule is switched into its low-conductance state. We additionally checked that the conductance-switching events do not alter the STM images and the dI/dV spectra of the surrounding molecules to exclude the possible artifact of STM tip changes. We also note that the Kondo resonance used to monitor the SCO is not caused by a charge transfer or unpaired spins on the organic ligands as in the case of other switchable Kondo reports.[287, 380, 381] This is supported by the Kondo resonance being located on the center of molecule corresponding to the position of the central Fe ion. To summarize, an isolated single Fe-phen molecule in the high-conductance (low-conductance) state is imaged with a small (no) protrusion at the center of the molecule and show a Kondo resonance (no spectroscopic features) in the dI/dV spectra near the Fermi level. By referring to the spin-state identification described in Fig. 14.8, we can ascribe the high-conductance (low-conductance) state of the Fe-phen molecule on CuN/Cu(100) to the HS (LS) state. This Fe-phen/CuN system falls into the general category of memristive devices,[382–384] where the conductance of the device can be electronically altered in a reversible way.

Here, for Fe-phen on CuN/Cu(100) the intrinsic SCO property is expressed by a nanoscale memristive behavior. The spin state of an isolated single Fe-phen molecule can be electronically addressed and the corresponding spin state can be read from the molecular-junction conductance. We propose to test the bistable deterministic nature of this SCO-based single-molecule memory device by applying a suitable train of voltage pulses. In Fig. 14.11a, we show voltage-pulse induced spin-state switching of the Fe-phen molecule sitting on CuN/Cu(100) under the STM tip. The subsequent spin state can be read from the current level. The investigated Fe-phen molecule is initially prepared into its HS state and the STM feedback loop is opened once the tip was stabilized over the center of the molecule. A 3 s-long voltage pulse of 1.5 V produces a current drop associated to the switching of the molecule from the HS to the LS state. The reverse switching (from LS to HS) is possible by applying a voltage pulse of −1.2 V. A similar experiment is shown in Fig. 14.11b to demonstrate the deterministic nature of the switching process. The Fe-phen is prepared into its HS state, and we apply two consecutive voltage pulses of the same polarity. While the spin state of the Fe-phen molecule switches with the first voltage pulse, the second pulse leaves the spin state of the molecule unchanged. Only a pulse of an negative polarity can switch the molecule back into its HS state. It results that by applying a voltage pulse of positive (negative) polarity, the Fe-phen molecule will end in its LS (HS) state, independently of the initial spin state of the molecule. We note that the voltage-pulse induced switching has been repeated about one hundred times without any sign of fatigue demonstrating the robustness of this SCO-based single-molecule memristor. In addition, no spontaneous switches were observed even after tens of
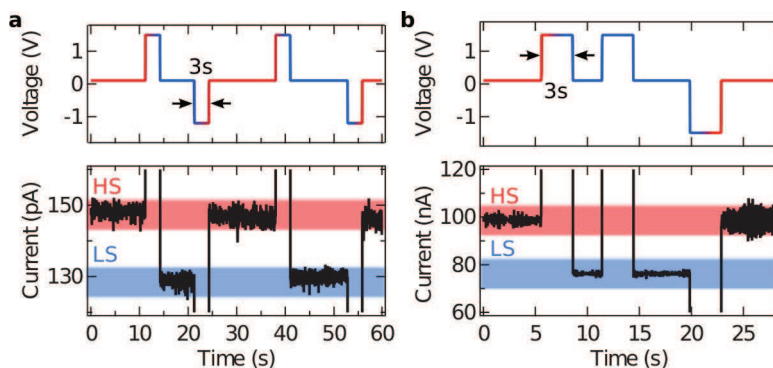
Figure 14.11. – **Spin-state switching of Fe-phen on CuN induced by voltage pulses**. **a**, Train of voltage pulses and the corresponding tunneling current for the STM tip positioned on top of a Fe-phen molecule on CuN/Cu(100). The spin state of the Fe-phen molecule is read from the tunneling current with an applied voltage of 0.1 V. For this particular molecule-tip distance, the Fe-phen molecule in the HS (LS) state leads to a tunneling current about 150 pA (130 pA) for $V = 0.1$ V. A 3 s-long voltage pulse of 1.5 V (−1.2 V) induce a HS→LS (LS→HS) transition. The tip was initially stabilized at 0.1 V and 150 pA and the subsequent measurements performed with an opened feedback loop. **b**, Similar experiment than in **a** that demonstrates the deterministic nature of the switching. Two consecutive voltage pulses of the same polarity were applied. The first positive pulse switches the Fe-phen molecule from the HS to the LS state, while the second positive pulse does not change the spin state. The molecule can be switched back into its HS state only by applying voltage pulse of negative polarity (third pulse). The tip was initially stabilized at 0.1 V and 100 pA.

hours of repeated STM imaging at low bias voltage ($< \pm 0.5$ V). It results that the lifetime of both spin states is remarkably long at the observation temperature.

14.2.3. Switching mechanisms

Following the description of successful spin-state-switching events of Fe-phen molecules on CuN/Cu(100), we now want to gain further insight into the switching mechanisms. We have thus further examined the real-time traces of the tunneling current during the voltage pulse used to induce the spin-state switching. For a Fe-phen molecule initially in its HS state, the current trace within a positive voltage pulse exhibits a small stepwise reduction after a time delay (time delay of 1.3 s in the example shown in Fig. 14.12a). A stepwise increase of the current's absolute value is visible after a given delay within a negative voltage pulse that triggers a transition from LS to HS (see Fig. 14.12b with 0.4 s time delay). Thus, the switching event does not occur instantaneously but rather after a significant time delay.
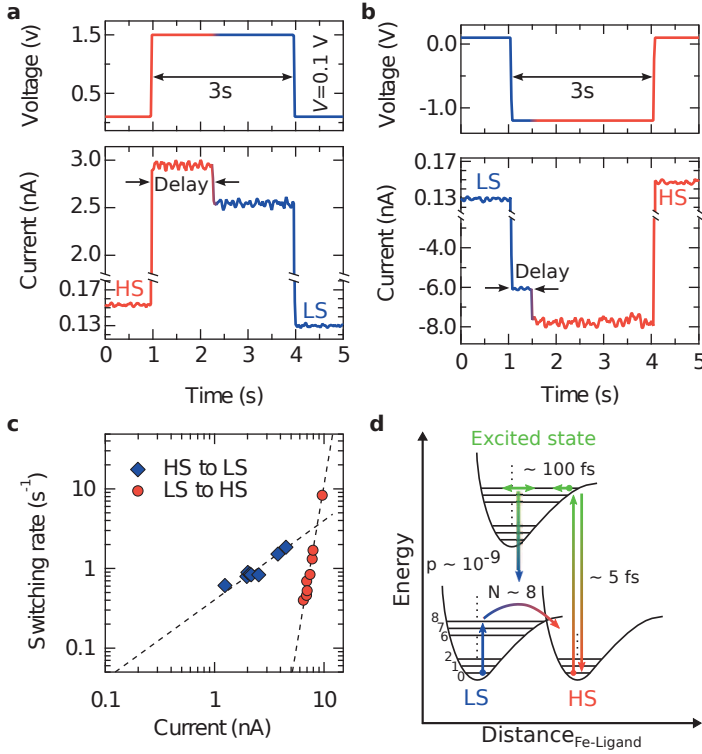
Figure 14.12. – **Proposed mechanism for the spin-state switching of Fe-phen on CuN/Cu(100)**. **a**, (**b**) Real-time voltage and current traces of a voltage-pulse induced HS to LS (LS to HS) transition. The voltage pulse of $1.5\,\mathrm{V}$ ($-1.2\,\mathrm{V}$) is applied for $3\,\mathrm{s}$ and the spin-state of the Fe-phen molecule is read from the tunneling current at a voltage of $0.1\,\mathrm{V}$. The HS to LS (LS to HS) transition is witnessed during the pulse by a small decrease (increase) of the current after a delay of $1.3\,\mathrm{s}$ ($0.4\,\mathrm{s}$). **c**, Observed switching rate (defined as one over the switching delay) as a function of the tunneling current during the voltage pulse. The tip is initially stabilized at $0.1\,\mathrm{V}$ and $100\,\mathrm{pA}$ and the different currents are obtained by slightly varying the intensity of the voltage pulse. The dashed lines indicate the results of power-law fits of the switching rate as a function of the current. **d**, Schematic of the proposed spin-state-switching mechanism in both directions. While, the switching from the HS to the LS state is a one electron process ($N \approx 1$) and involves an excited state, the reverse switching (from LS to HS) is a higher order process ($N = 8$) that can involve the population of intermediate vibrational levels (heating).

In Figs. 14.12a and 14.12b, the observed time delays are respectively $1.3\,\mathrm{s}$ and $0.4\,\mathrm{s}$ and are thus different. We performed similar experiments in a more systematic way and reported the corresponding averaged switching rates, defined as the inverse of the time delay, as a function of the tunneling current during the voltage pulse before the transition (see Fig. 14.12c). Note that the amplitude of the voltage pulse is varied between $1.1\,\mathrm{V}$ and $1.5\,\mathrm{V}$ in order to modify the tunneling current. The evolution of the switching rate with the tunneling current depends on the switching direction. Both HS→LS and LS→HS switching rates versus current presented in Fig. 14.12c with logarithmic x-y scales, can be fitted with a linear function. This shows that, for the current-window invested here, a simple power law relates the switching rate r to the current I: $r \propto I^N$. On one hand, we find that $N \approx 8$ for the LS→HS transition, suggesting a high-order process involving population of vibrational levels (heating) by inelastic scattering of the tunneling electrons,[114, 376] in competition with the heat transfer to the substrate. Note that the electric field produced by the STM tip could also be the mechanism behind the LS→HS transition. On the other hand, for HS→LS transition, the switching rate is proportional to the current ($N \approx 1$). This indicates that, although the probability per electron to switch the spin-state of the Fe-phen molecule is low (on the order of 10^{-9}), the switching is induced by single-electron processes. We note that, the dI/dV spectrum acquired on the center of a HS Fe-phen molecule (see Fig. 14.9a) reveals the presence of an unoccupied orbital located approximately at $1\,\mathrm{V}$. Hence, the voltage-pulse induced HS to LS transition with voltage above $1.0\,\mathrm{V}$ can involve the charging of an unoccupied state for a short time, that in turn modify the effective ligand field felt by the Fe-ion.

In the following, considering the power laws that relate the switching rate to the current, we discuss the broad feature of a model for electrical spin-state switching in analogy to that of optical switching. When an electron excites the molecule from the HS to the excited state at $1.0\,\mathrm{eV}$ (see Fig. 14.12d), the positions of the atomic cores are initially not changed owing to their slow relaxation. The effective ligand field felt by the Fe-ion in the excited state can favor Fe-N bond lengths closer to that of the LS state. If the lifetime of the excited state were relatively long, the excited state would relax into its vibronic ground state. The ensuing electronic relaxation of the excited state would leave the Fe-phen molecule in its LS state (see Fig. 14.12d). However, from the dI/dV spectrum (see Fig. 14.9) on the center of a HS Fe-phen molecule, we can estimate a $5\,\mathrm{fs}$ lifetime of the excited state at $1.0\,\mathrm{eV}$, and thus relatively short. Yet, typical vibration times of vibronic excitations are in the range of $10\,\mathrm{THz}$, that corresponds to periods of about $100\,\mathrm{fs}$. Thus, the transition from the excited to the LS state is possible only in the low-probability case that the excited state survives about $100\,\mathrm{fs}$. A simple calculation reveals that, for a $5\,\mathrm{fs}$ electronic lifetime and a $10\,\mathrm{THz}$ vibration frequency, the switching probability P is about 2×10^{-9} ($P = \exp\left(-100/5\right)$). This model is in agreement with the HS→LS switching rate proportional to the current ($N \approx 1$) and explains the low success rate for switching. Using a thicker insulating layer than CuN can in principle drastically increase the switching probability, since the switching probability scales exponentially with the excited charged state's lifetime

that would be increased. Interestingly, the energy of the excited state observed in STS (about 1 eV) lies close to that needed for $^5T_2 \rightarrow {}^5E$ optical transition (1.49 eV).[257]

14.3. Dynamical switching of second-ML molecules

In the previous section, we have shown that we can switch the spin state of single Fe-phen molecules provided that they are sufficiently decoupled from the substrate, *e.g.* by an intermediate CuN insulating layer. Similarly, Gopakumar *et al.*[347] reported successful switching events of second-ML $Fe(bpz)_2(phen)$ decoupled from the Au(111) substrate by the first ML (see also Sec. 12.3.6.2). Both experiments motivated us to study the spin state of the second-ML molecules on Cu(100) and Cu(111) substrates. We evidenced strong topographic modifications when varying the sample voltage, which we attribute to a dynamical spin transition in agreement with a simple model based on tip-induced electric-field effect.

14.3.1. Second-ML molecules on a Cu(100) substrate

We recall that, as described in Sec. 13.2, the second-ML molecules on Cu(100) are lying upside down compared to first-ML molecules, with the sulfur ions pointing upwards. In Fig. 14.13a, we show a high-resolution STM image of second-ML molecules on Cu(100). When molecules of same orientation are compared, the distance between the lobes appears to be similar suggesting an uniform spin state for the molecules of the second ML. This suggestion is reinforced by the discussion about the dynamic spin-state switching (below) and about spin-state coexistence (see Sec. 15.1.2).

In the Sec. 14.1, we showed that the spin state of first-ML molecules on Cu(100) can be directly read from the observed distance between the lobes in the STM topography. Here, we are reluctant to deduce the spin state of second-ML molecules directly from the topography, since the second-ML molecules are upside down compared the first-ML molecules. As HS and LS molecules should differ in their density of states, we performed STS on a sample of 1.4 ML Fe-phen on Cu(100). As a reference, we carried out STS atop the center of a first-ML HS molecule (see Fig. 14.13b). The differential spectrum shows clear distinctive peaks at −1.8 eV, −1.0 eV and −0.6 eV. Except for the peak at −0.6 eV that could originate from the Cu substrate, the experimental spectrum is in very good agreement with the Fe-ion density of states of a first-ML HS Fe-phen molecule on a Cu(100) substrate.[375] Note that no peak can be recognized for positive sample voltage (unoccupied orbitals) due to the strong tunneling background.

The differential conductance spectrum acquired atop a second-ML molecule's center is similar to the spectrum of a HS molecule in direct contact to the substrate (see Fig. 14.13). We thus tentatively ascribe the second-ML molecules as being in the HS state. We note that the peak at −1.8 eV of the first-ML molecule is slightly shifted towards lower energies compared to the second-ML molecule. This shift most
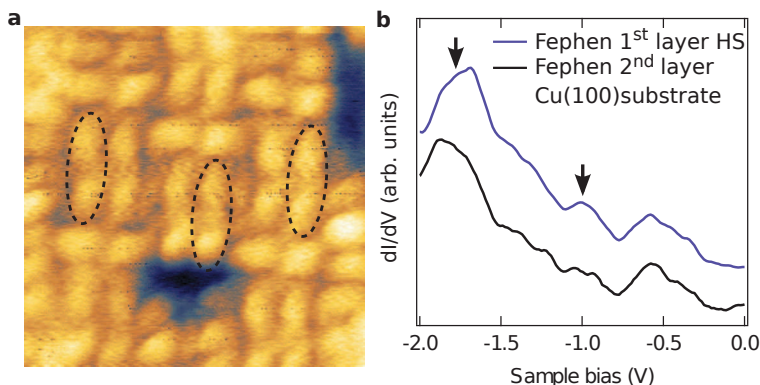
Figure 14.13. – **Spin-state identification of second-ML Fe-phen on Cu(100)**. **a**, STM topography of second-ML Fe-phen molecules that suggest an identical spin state for all the molecules. Black ellipses indicate single molecules for clarity. **b**, Differential conductance dI/dV spectra taken on a sample of 1.4 ML of Fe-phen on Cu(100) atop first- and second-ML molecules. Gueddida and Alouani[375] performed *ab initio* calculations of the first-ML molecules. The resulting density-of-states peaks are indicated by arrows for clarity. For clarity, the spectrum atop a second-ML molecule is multiplied by a factor 4, and smoothed to remove unphysical variations. Image size is 4.4 nm × 4.4 nm (V=0.3 V, I=140 pA). The spectra were acquired with a voltage modulation of 15 mV at a frequency of 723 Hz.

probably reflects the reduced influence of the substrate on the second-ML molecules compared to the first ML. Hence, despite the negative results on first-ML molecules on Cu(100), it might nevertheless be possible to trigger the spin transition of the second-ML molecules with the STM tip.

In Figs. 14.14a and 14.14b, we present STM topographies of second-ML Fe-phen molecules on Cu(100) acquired at 0.40 V and 0.70 V, respectively. The apparent distance between the two lobes of a single molecule shrinks with increasing sample voltage, in contrast to similar experiments performed on first-ML molecules on Cu(100) (see Fig. 14.6). Subsequent topographies of the same area acquired at 0.40 V reveal that the interlobe distance increases again, and the molecule returns to its initial state (see appendix C). Zoomed STM topographies of a pair of second-ML Fe-phen molecules taken at low and higher voltage are shown in Figs. 14.14c and 14.14d, respectively. The corresponding extracted STM height profiles along the long axis of a molecule is shown in Fig. 14.14e and clearly evidence the change in the molecular shape. We note that, at negative voltages, we do not observe topographic changes (not shown).

What is the origin of the topographic changes that we observe? Since the STM is sensitive to the local density of states, the variation of the interlobe distance with the applied sample voltage could originate from an abrupt change in the orbitals
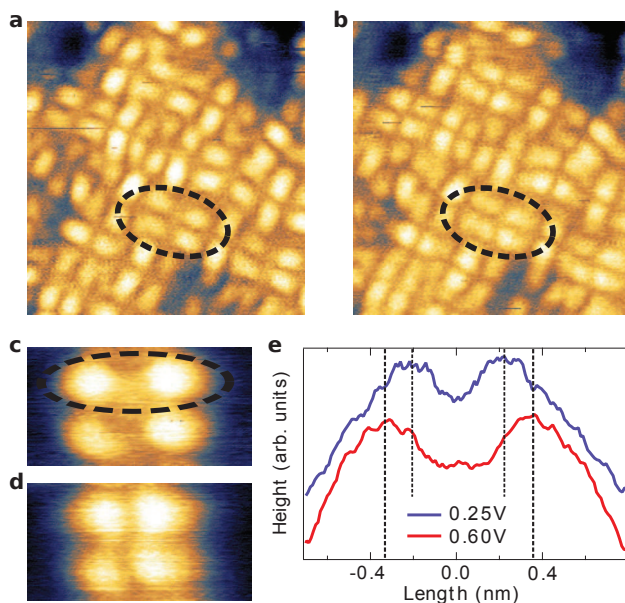
Figure 14.14. – **Voltage-induced topographic changes of second-ML Fe-phen molecules on Cu(100)**. Topographies of second-ML Fe-phen molecules on Cu(100) at **a**, low voltage (0.40 V) and **b**, higher voltage (0.7 V). The apparent distance between the lobes decreases with increasing voltage. For clarity, a pair of Fe-phen molecules is encircled in both topographies. Zoom on a pair of Fe-phen molecules at **a**, low voltage (0.25 V) and at **b**, higher voltage (0.60 V), evidencing the apparent interlobe distance shrinking with increasing voltage. A single molecule is indicated by a black ellipse for clarity. **e**, Height profiles for the upper molecule in topographies **c** (blue) and **d** (red) along the long axis of the molecule. The height profile in blue is vertically shifted for clarity. Image size are **a**, 5.50 nm × 5.80 nm (V=0.40 V, I=1.75 nA), **b**, 5.50 nm × 5.80 nm (V=0.70 V, I=1.75 nA), **c**, 2.40 nm × 1.25 nm (V=0.25 V, I=130 pA), **d**, 2.40 nm × 1.25 nm (V=0.60 V, I=130 pA).

probed by the tip at different energies. In this case, as the STM topography is closely related to the integrated local density of state from the Fermi energy to the sample voltage V, one would rather expect an expansion of the lobes with increasing sample voltage. Alternatively, the topographic changes could originate from the expected spin transition from the HS (low voltage) to the LS (higher voltages) state. In this scenario, why do we not observe the metastable LS state at low voltages like for first-ML single molecules? To answer this question, we have to briefly discuss the outcome of Chapter 15 in which the spin-state coexistence is investigated in details. We will see that, the spin-state coexistence of first-ML molecules, *i.e.* the presence of an energy barrier between the HS and the LS states, possibly comes from the adsorption site (S-Cu bonding). In the present case, it is reasonable to think that the phen-phen

bonding between first- and second-ML molecules leads to a much lower energy barrier between the two spin states. The molecule in the excited state (here LS) would thus more easily returns to its ground state (here HS).

We carried out additional measurements in order to get further insights about the origin of the observed voltage-induced topographic changes. Since it is difficult, from the topographies shown in Fig. 14.14, to precisely detect the voltage at which the topographic changes occur, we developed a different experiment protocol. The acquisition software is set such that the investigated molecule is continuously scanned along its long axis while increasing the sample voltage. This leads to images such as shown in Fig. 14.15a, where we observe an evolution of the height profiles with increasing sample voltage in contrast to the same experiment performed on first-ML molecules (see Fig. 14.6). From the acquired STM image, we extract averaged height profiles for a given sample voltage (see Fig. 14.15b for the extracted height profile at V =0.1 V), and fitted with a double Gaussian function:

$$Ae^{-\left(\frac{x-x_1}{\sigma_1}\right)^2} + Be^{-\left(\frac{x-x_2}{\sigma_2}\right)^2} + const. \tag{14.1}$$

The fitting of the extracted height profile with Eq. 14.1 (see *e.g.* Fig. 14.15b) allows extracting the positions x_1 and x_2 of the two lobes. In Fig. 14.15, we represent the bias voltage dependence of the distance between the lobes defined as $d(V) = x_2(V) - x_1(V)$. The interlobe distance is maximal at low voltages (about 7.6 Å), and is more or less constant until 0.5 V. The interlobe distance $d(V)$ then smoothly decreases with increasing sample voltage and ends with a plateau at ≈ 6.0 Å. The interlobe distance and the position of the two plateaus can slightly vary with different tips, but the shrinking is always about 25%. We note that no variation of the interlobe distance is observed for negative sample voltage (not shown). The voltage-dependence of the interlobe distance is then fitted with a sigmoid function in order to extract the threshold voltage V_{Th} at which half of the shrinking occurs.

A set of voltage-dependent STM height profiles such as in Fig. 14.15a was recorded for different set-point currents. The height profile extraction and the fitting procedures were then repeated for each of the acquired STM images. In Fig. 14.15d, we show the current dependence of the threshold voltage V_{Th}. It results for larger tunneling current, larger threshold voltages are needed.

As previously mentioned, the topographical changes could originate from a sharp variation in the local density of states (orbital). However, we would rather expect an increasing interlobe distance with increasing sample voltage due to the density-of-states integration, inherent to STM topographies. In addition, the threshold voltage varies with the tunneling current (see Fig. 14.15d), while the energy position of the orbital should stay independent of the tunneling current. Exceptions are found by Gopakumar *et al.*,[385, 386] who observed an electric-field induced shift of the HOMO and LUMO of phtalocyanine molecules. However, the shift is modeled with a capacitor interface and the shift is towards the Fermi level with increasing current. Yet, referring to Fig. 14.15d, the orbitals would be shifted towards higher energy with
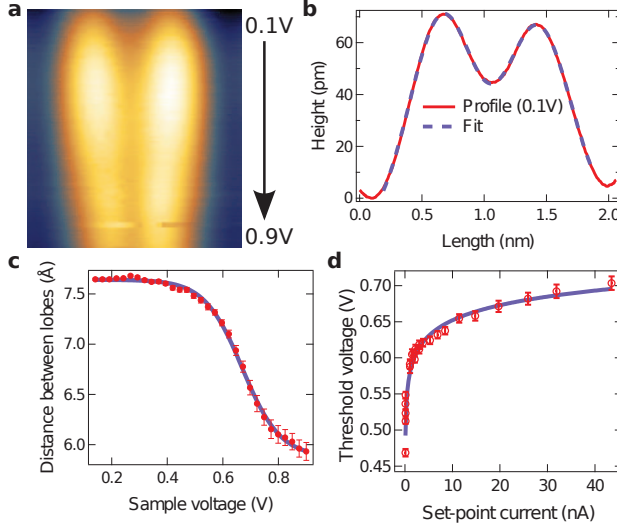
Figure 14.15. – **Voltage and current dependence of the interlobe distance of second-ML Fe-phen molecules on Cu(100)**. **a**, Evolution of the STM height profile of second-ML Fe-phen on Cu(100) with increasing sample voltage. The image width is 2.06 nm ($I = 25.9$ nA). **b**, Extracted STM height profile at 0.1 V from the STM image of pannel **a**. The solid red line corresponds to the profile and the dashed blue line represents the fit using Eq. 14.1. **c**, Distance between the lobes extracted from the fit of **b** as a function of the sample voltage (red points) together with a fit using $d(V) = base + {}^{max}/_{1+\exp\left(\frac{V_{Th}-V}{rate}\right)}$ (solid blue; fitting parameters: $base = 7.641 \pm 0.008$, $max = -1.763 \pm 0.025$, $V_{Th} = 0.670 \pm 0.003$ and $rate = 0.068 \pm 0.002$). **d**, Current dependence of the threshold voltage V_{Th} (red data points) on a set of data like that of pannel **a**.

increasing tunneling current (*i.e.* electric field), which does not fit with capacitor model proposed by Gopakumar et al.[385, 386] At this point of the study, we conclude that the topographical changes are unlikely to be caused by orbital changes. On the other hand, the experimental data can be nicely explained by considering a dynamic switching between the two spin states that we propose to discuss in the next section.

14.3.2. Dynamic-switching mechanisms

The evolution of the distance between the lobes for second-ML Fe-phen molecules on Cu(100) with varying sample voltage could reflect the expected spin transition. The molecule would go from the HS state at low voltages, characterized by an interlobe distance ≈ 7.6 Å, to the LS state at higher voltages with a distance between the lobes ≈ 6.0 Å. In that case, one would expect the spin transition, expressed by the change in the interlobe distance, to be rather abrupt such as for first-ML Fe-phen

on CuN/Cu(100)[331] in contrast to the smooth transition that we observed (see Fig. 14.15c). In addition, in Fig. 14.15c, we observe intermediate interlobe distances while it is unlikely to observe that many excited spin states with sufficiently long lifetimes at the energies we probe. In order to solve this apparent discrepancies, we propose that the observed distance between the lobes represents a time-averaged distance that corresponds to the molecule spending α proportion of time into its HS state and $1-\alpha$ proportion of time in the LS state. The distance between the lobes can then be expressed as:

$$d = \alpha(d_{HS} - d_{LS}) + d_{LS}. \tag{14.2}$$

In this scenario, we have to assume that the investigated molecule switches its spin state back and forth and has time to switch many times during the measurement time of a single STM height profile (that is about 8 s). Considering the switching in both directions, the derivative of the time proportion in the HS state α is given by:

$$\frac{d\alpha(t)}{dt} = -\alpha k_{HS \to LS}(I,V) + (1-\alpha)k_{LS \to HS}(I,V). \tag{14.3}$$

$k_{HS \to LS}(I,V)$ and $k_{LS \to HS}(I,V)$ are the switching rates (or transition rates) from HS to LS (LS to HS). In the stationary regime $d\alpha(t)/dt = 0$; Eq. 14.3 leads to:

$$\alpha(I,V) = \frac{k_{LS \to HS}(I,V)}{k_{LS \to HS}(I,V) + k_{HS \to LS}(I,V)}. \tag{14.4}$$

For a given current and voltage, Eq. 14.4 describes how, as expected from our initial hypothesis, the molecule can spend a given proportion of time in the HS state (α) and the rest of the time in the LS state ($1 - \alpha$). This lead to an averaged interlobe distance given by Eq. 14.2 that depends on the proportion of time spent in the HS state (α). Eq. 14.4 also describes how the proportion of time spent in the HS state α depends on the competition between the current- and voltage-dependent switching rates ($k_{HS \to LS}(I,V)$ and $k_{LS \to HS}(I,V)$). In addition, the competition between the current- and voltage-dependent switching rates would explain the observed tunneling current dependence of the voltage threshold V_{Th} (see Fig. 14.15d). We note that, within this formalism, the points of Fig. 14.15d represent the set of I and V satisfying $\alpha = 1/2$ and thus corresponds to equal switching rates ($k_{HS \to LS}(I,V) = k_{LS \to HS}(I,V)$).

The rapid switching between the two spin states that we propose to have observed may involve different mechanisms. In the following, we describe two mechanisms that we believe the most relevant for this system.

(i) As briefly introduced previously, we believe in the existence of a potential-energy barrier between the two spin states that originates from the molecule adsorption site. The barrier is supposed to be much lower in the present case (second-ML molecules), where we have phen-phen bonding between first- and second-ML
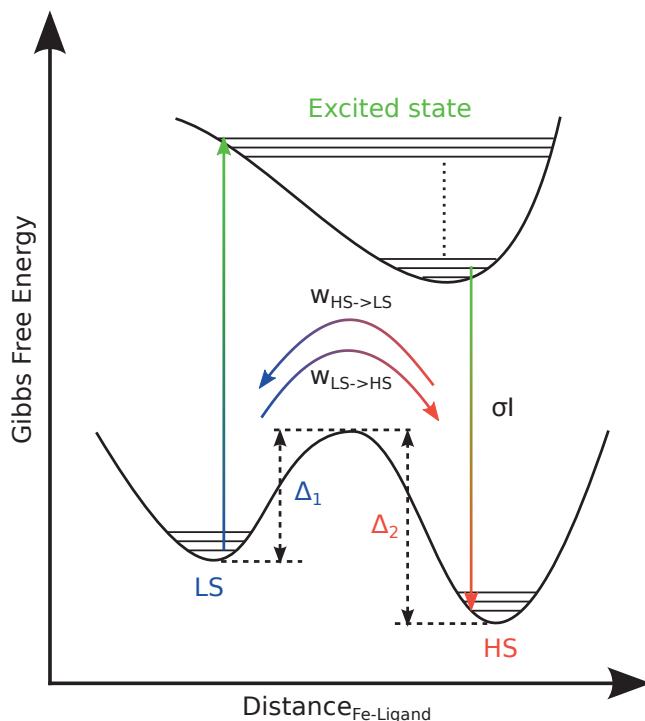
Figure 14.16. – **Suggested switching mechanisms for second-ML Fe-phen molecules on Cu(100)**. The HS state has the lowest Gibbs free energy since the HS state seems to be the ground state in this system. The energy barrier between the two spin states is supposed low enough to allow switching given by the transition-state theory; and can be modified, for example, through the Stark effect when an electric field is applied. Moreover, there is possible LS to HS transition through an excited state with an overall cross section σ. This single-electron process is such as presented in Ref. 331.

molecules, compared to the first-ML case involving S-Cu bonding. It results that, although the measurements are carried out at low temperatures ($\approx 4.8\,\mathrm{K}$), we should consider "direct switching" through the barrier as a possible spin-state switching mechanism. The corresponding switching rates are given by the transition-state theory (Arrhenius law). The potential-energy barrier as well as the "direct switching" mechanism are schematized in Fig. 14.16. $w_{HS\rightarrow LS}$ ($w_{LS\rightarrow HS}$) is the switching rate given by the transition-state theory for transition from HS to LS (LS to HS). Those switching rates exponentially depend on the barrier heights (Δ_1 and Δ_2). Since an electric field can shift the Gibbs free energy of the HS and the LS states through the Stark effect,[287, 336, 337, 387, 388] the former can thus modify the apparent barrier heights (Δ_1 and Δ_2), and in turn alter the switching rates ($w_{HS\rightarrow LS}$ and $w_{LS\rightarrow HS}$).

(ii) Referring to Sec. 14.2.3 and Refs. 331, 347, the switching could also be induced by an electron injection into an unoccupied molecular orbital, and should thus be considered (see Fig. 14.16). We assume here that the single-electron processes trigger switching from the excited (LS) to the ground (HS) state. The corresponding switching rate is σI where σ represents the inelastic-process overall probability and I the tunneling current. We note that, in Sec. 14.2.3 and in Ref. 331, we demonstrated that the switching rate from the excited to the ground state is proportional to the tunneling current for Fe-phen on CuN/Cu(100). However, the ground state was LS in contrast to the HS ground state found in the present case.

Mechanisms (i) and (ii), in agreement with our phenomenological explanations, would lead to current- and voltage-dependent switching rates that have the following form: $k_{LS \to HS}(I, V) = w_{LS \to HS}(I, V) + \sigma I$ and $k_{HS \to LS}(I, V) = w_{HS \to LS}(I, V)$. In the following, we will show that the picture of a dynamic spin transition governed by these two mechanisms is in agreement with the results presented in Fig. 14.15d. We note that we exclude single-electron-process switching from HS to LS as there would be no more agreement with the experiment data.

Within the scope of the transition-state theory, the switching rates read:

$$
\begin{aligned}
w_{LS \to HS}(I, V) &= \nu_0 \exp\left(-\frac{\Delta_1(I,V)}{k_B T}\right) \\
w_{HS \to LS}(I, V) &= \nu_0 \exp\left(-\frac{\Delta_2(I,V)}{k_B T}\right),
\end{aligned}
\tag{14.5}
$$

where ν_0 is the attempt frequency, Δ_1 and Δ_2 are, as previously defined, the potential-energy barrier to overcome for LS to HS and HS to LS transitions, respectively. For simplicity, we assume the attempt frequencies to be the same for both switching directions. In the presence of an electric field $\vec{E}$, the Stark effect adds a potential energy to the HS and the LS states in the form[389]:

$$
E_{HS(LS)}^{Stark} = -\vec{\mu}_{HS(LS)} \cdot \vec{E} - \frac{1}{2}\alpha_{HS(LS)}\vec{E}^2,
\tag{14.6}
$$

with $\vec{\mu}_{HS(LS)}$ the static dipole moment and $\alpha_{HS(LS)}$ the polarizability tensor of second-ML Fe-phen in the HS (LS) state. The Gibbs free energy difference between the LS and the HS states is then expressed as:

$$
\Delta_2 - \Delta_1 = G_0 - (\vec{\mu}_{LS} - \vec{\mu}_{HS}) \cdot \vec{E} - \frac{1}{2}(\alpha_{LS} - \alpha_{HS})\vec{E}^2,
\tag{14.7}
$$

with G_0 the difference in Gibbs free energy between the LS and the HS states in the absence of external electric field ($\vec{E} = \vec{0}$). We are not able to perform the following calculations using Eq. 14.7 and we will thus consider two different cases: (i) the electric-field-induced height difference of the potential barrier mainly arises from the difference in the static dipole moments ($(\vec{\mu}_{LS} - \vec{\mu}_{HS}) \cdot \vec{E} \gg \frac{1}{2}(\alpha_{LS} - \alpha_{HS})\vec{E}^2$); and (ii) from the

difference of the polarizabilities $((\vec{\mu}_{LS} - \vec{\mu}_{HS}) \cdot \vec{E} \ll \frac{1}{2}(\alpha_{LS} - \alpha_{HS})\vec{E}^2)$. Moreover, the electric field coming from the STM tip is approximated with the simple expression of the electric field between two parallel conducting plates $\vec{E} = -V/d_{tip-sample}$. Since the distance $d_{tip-sample}$ between the STM tip and the sample decreases logarithmically with increasing tunneling current, $\vec{E}$ is developed to the first order. The resulting electric field is then simply proportional to the applied sample voltage $\vec{E} \propto V\vec{i}$ ($\vec{i}$ is a unitary vector colinear to $\vec{E}$). Eq 14.7 then reads:

$$\begin{aligned} \Delta_2^{(i)} - \Delta_1^{(i)} &= G_0 - \gamma^{(i)}V, \\ \Delta_2^{(ii)} - \Delta_1^{(ii)} &= G_0 - \gamma^{(ii)}V^2. \end{aligned} \tag{14.8}$$

We can thus express Eq. 14.4 as:

$$\begin{aligned} \alpha^{(i)} &= \frac{1 + \frac{\sigma}{\nu_0}\exp\left(\frac{\Delta_1}{k_B T}\right)I}{1 + \exp\left(-\frac{G_0 - \gamma^{(i)}V}{k_B T}\right) + \frac{\sigma}{\nu_0}\exp\left(\frac{\Delta_1}{k_B T}\right)I}, \\ \alpha^{(ii)} &= \frac{1 + \frac{\sigma}{\nu_0}\exp\left(\frac{\Delta_1}{k_B T}\right)I}{1 + \exp\left(-\frac{G_0 - \gamma^{(ii)}V^2}{k_B T}\right) + \frac{\sigma}{\nu_0}\exp\left(\frac{\Delta_1}{k_B T}\right)I}. \end{aligned} \tag{14.9}$$

Equation 14.9 provides, for a set of current and sample voltage, the proportion of time that a second-ML Fe-phen molecule under the STM tip spend into its HS state. For constant tunneling current, Eq. 14.9 predicts a decreasing time spent in the HS state α with increasing sample voltage (V), in agreement with the decreased averaged distance between the lobes observed in the experiments presented in Figs. 14.15a,c. We recall that the voltage threshold V_{Th} corresponds to the voltage at which half of the shrinking occurs, and thus is reached for $\alpha = 1/2$. Within our interpretation of dynamic switching of the second-ML Fe-phen molecules on Cu(100), the threshold voltage V_{Th} has the following expression:

$$\begin{aligned} V_{th}^{(i)} &= \frac{G_0}{\gamma^{(i)}} + \frac{kT}{\gamma^{(i)}}\ln\left(1 + \frac{\sigma}{\nu_0}\exp\left(\frac{\Delta_1}{k_B T}\right)I_{sp}\right), \\ V_{th}^{(ii)} &= \sqrt{\frac{G_0}{\gamma^{(ii)}} + \frac{kT}{\gamma^{(ii)}}\ln\left(1 + \frac{\sigma}{\nu_0}\exp\left(\frac{\Delta_1}{k_B T}\right)I_{sp}\right)}. \end{aligned} \tag{14.10}$$

We then fit the current dependence of the voltage threshold with its analytic expression as expressed in Eq. 14.10 using the two approximations of the difference in Gibbs free energy of the LS and HS states ((i) and (ii)). Fig. 14.17 represents the experimental data points together with the fits using approximations (i) and (ii). We note a very good agreement between the experimental data points and our
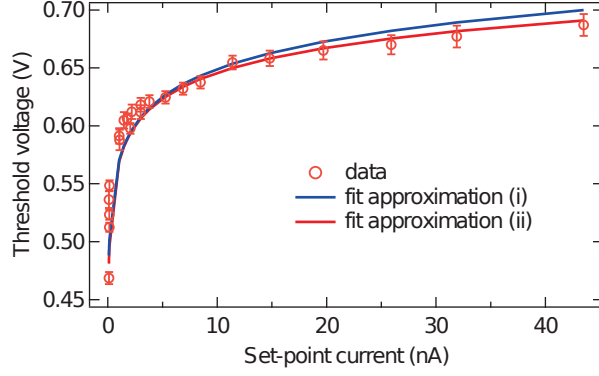
Figure 14.17. – **Compatibility of the switching model of second-ML Fe-phen with the experimental data**. Current dependence of the voltage threshold (see Fig. 14.15d) together with fits using Eqs. 14.10. There is a good agreement between the experimental data and the model. The best agreement is obtained when using approximation (ii), valid in the case of high electric fields. The fitting parameters are shown in Tab. 14.1.

simple dynamic-switching model. We can see that, while both approximations lead to an overall agreement with the experimental data, the discrepancy is smaller when using approximation (ii). Yet, referring to Eq. 14.7, the apparent better agreement using approximation (ii) can be understood as the electric fields we use have very high values, in the order of $1\,GV\,m^{-1}$. However, the discrepancy of the fit using approximation (ii) is so small that we have to consider the two cases.

The fitting parameters are reported in Tab. 14.1. The uncertainties of the fitting parameters is unfortunately important, and we can thus only account for the magnitude of $G_0 \approx 1\,meV$, which corresponds to the difference in Gibbs free energy between the LS and the HS states in the absence of an electric field for $T \approx 4\,K$. The $G_0 \approx 1\,meV$ that we found here for second-ML Fe-phen molecules on Cu(100) is much lower than the $170\,meV$ energy difference between the HS and the LS state calculated by Gueddida and Alouani[375] on the free Fe-phen molecule. At the temperature of the measurements ($T \approx 4\,K$), this is consistent with the presence (absence) of the proposed dynamic switching between the two spin states for second-ML (bulk) Fe-phen molecules.

14.3.3. Second-ML molecules on a Cu(111) substrate

The voltage-induced topographic changes of second-ML Fe-phen molecules on Cu(100) are consistent with a dynamic switching from a HS state at low voltages to a steady-state combination of HS and LS at higher sample voltages. The dynamic switching model is based on the reasonable assumption of the existence of a small potential-

	$\frac{G_0}{\gamma}$	$\frac{k_B T}{\gamma}$	$\frac{\sigma}{\nu_0} \exp\left(\frac{\Delta_1}{k_B T}\right)$	χ^2	G_0 (meV)
Approx. (i)	0.31 (0.19)	0.034 (0.003)	2000 (9000)	0.0212	≈ 3
Approx. (ii)	0.15 (0.13)	0.04 (0.63)	65.99300 (8×10^{-5})	0.0203	≈ 1

Table 14.1. – Fitting parameters obtained by fitting the current dependence of the threshold voltage using Eqs. 14.10 for the two different approximations.

energy barrier between the two spin states and a small difference in the Gibbs free energy of the HS and the LS states (G_0). The height of the potential-energy barrier and G_0, both originating from the adsorption sites of the molecule, are possibly modified when the symmetry of the underlying substrate is modified. We are wondering if the voltage-induced topographic changes survive for second-ML Fe-phen molecules on Cu(111).

We recall that the adsorption geometry of second-ML Fe-phen on Cu(111) is similar than that of second-ML Fe-phen on Cu(100) (see Sec. 13.3), *i.e.* the phenanthrolines groups towards the first-ML molecules and the NCS groups facing upwards. Figs. 14.18a and 14.18b show topographies acquired with low and higher sample voltage, respectively. Similarly to second-ML Fe-phen on Cu(100), the apparent morphology of the second-ML molecules is modified upon changing the sample voltage. The distance between the lobes of a given second-ML Fe-phen molecule is larger at low voltage than that at higher voltage. The zoomed STM topographies at low and higher sample voltage (see Figs. 14.18c and 14.18d) confirm the apparent shrinking of the lobes with increasing sample voltage. Note that, similarly to the second-ML Fe-phen molecules on Cu(100), the process is fully reversible and we do not observe topographical changes for negative sample voltage (see Appendix D).

The voltage-dependent topographies of Fig. 14.18 and complete topography sets presented in Appendix D show voltage-induced topography changes, similar to that found for second-ML Fe-phen on Cu(100). In turn, it can be consistent with a dynamic switching from the HS state at low voltages to a steady-state combination of HS and LS states at higher voltages. We note that our data sets on second-ML Fe-phen molecules on Cu(111) is quite reduced compared to the one on second-ML Fe-phen molecules on Cu(100). Evolution of the STM height profile of second-ML Fe-phen on Cu(111) with increasing sample voltage, such as presented in Fig. 14.15 for a Cu(100) substrate, for different tunneling currents, could have been really interesting. We could expect a relative variation of the difference in Gibbs free energy between the HS and the LS states (G_0), provided that the adsorption sites of the second-ML Fe-phen on Cu(111) slightly differ than that on Cu(111).
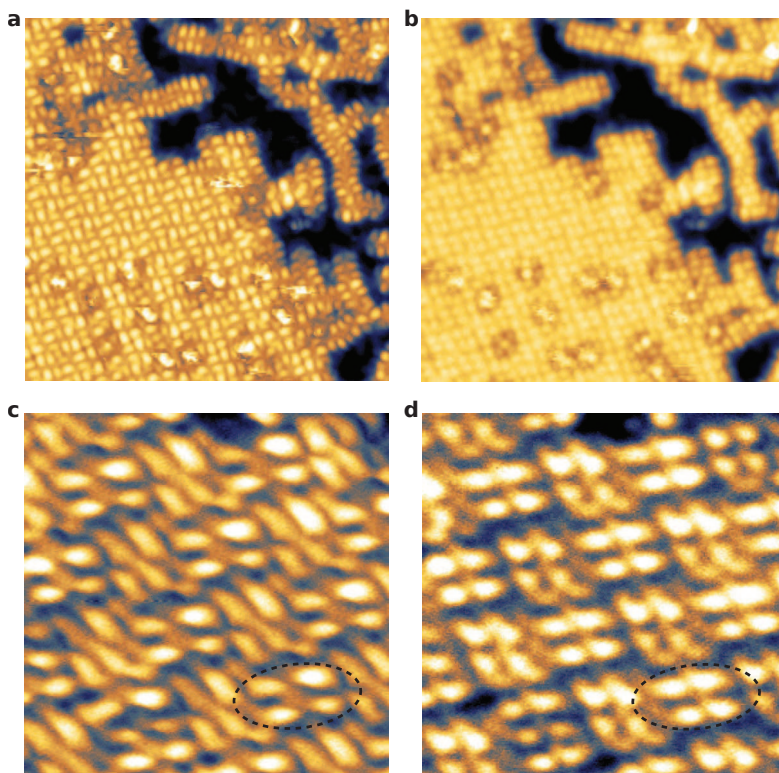
Figure 14.18. – **Voltage-induced topographic changes of the second-ML Fe-phen molecules on Cu(111)**. STM topographies of second-ML Fe-phen molecules on Cu(111) at **a**, low voltage (0.30 V) and **b**, higher voltage (1.00 V). The apparent morphology of the molecules is clearly changed when the sample voltage is varied. **c** and **d** are zoomed topographies at respectively low (0.40 V) and higher voltage (0.90 V). A pair of second-ML Fe-phen moelcules is encircled for clarity. Image size are **a**,**b** 18.1 nm × 18.1 nm (I=110 pA) and **c**,**d** 5.5 nm × 5.5 nm (I=210 pA).

14.4. Partial conclusion

In this chapter, we successfully identified the spin state of isolated single Fe-phen molecules adsorbed on Cu(100). The spin state can be identified by reading the distance between the two phen groups from the STM topography, or from scanning tunneling spectroscopy measurements near the Fermi level. The HS (LS) state of the single Fe-phen molecule on Cu(100) is characterized by the largest (smallest) interlobe distance in the STM topography and by the presence (absence) of a Kondo resonance in the STS spectra. The STM measurements, reinforced by XAS and XMCD measurements, indicate thus a surprising coexistence of the two spin states

of Fe-phen at the temperature of investigation ($T \approx 4\,\mathrm{K}$). The spin-state coexistence will be further investigated in the next chapter.

The attempts to induce a spin transition on a single Fe-phen molecule on Cu(100) by applying strong currents and electric fields (voltage) were unsuccessful. We could only possibly switch the spin state by lateral manipulation of the Fe-phen molecule with the STM tip, but the final adsorption site of the molecules makes the conclusion doubtful. However, by introducing an interfacial CuN layer between the molecule and the Cu(100) substrate, *i.e.* by partially electronically decouple the molecules from the substrate, one can switch the Fe-phen spin state and read the state of the molecule from the molecular-junction conductance. We show that the switching is selective, deterministic and robust. A complete study of the current dependence of the switching rate allowed us to identify two different switching mechanisms. For transition from the HS to the LS state, a single electron process that is possibly the charging of an unoccupied orbital causes the transition. The reverse transition is a higher order process and may originate from vibrational heating or from the electric field produced by the tip.

In the last section, we evidenced voltage-induced topographic changes for second-ML Fe-phen molecules on Cu(100) and Cu(111). While these changes are unlikely to originate from the probing of different molecular orbitals, we show that there are consistent with a dynamic switching of second-ML molecules from the LS state at low voltages to a steady-state combination of HS and LS at higher voltages. The dynamic switching model we developed, based on a few assumptions, remarkably fits the experimental data.

<p align="right">15</p>

Spin-state coexistence

15.1. Investigation of the spin-state coexistence

In the last years, many groups have fabricated and studied thin spin-crossover films with thicknesses ranging from 5 nm to 1000 nm.[274, 354, 368–370, 372, 390] These different studies report temperature-dependent effects ascribed to the expected spin transition, similarly to bulk compounds. However, when the film thicknesses are strongly reduced the behavior of the spin-crossover complexes seems to be modified. In the following, I will briefly introduce the spin-state-coexistence observation in four experimental reports on ultra-thin SCO films.

In the STM study by Gopakumar *et al.*[347, 371] concomitant to our study, and already partially discussed in Sec. 12.3.6.2, a bilayer of $Fe(H_2B(pz)_2)_2$(phen) (with $H_2B(pz)_2$ = bis(hydrido)bis(1H-pyrazol-1-yl)borate and phen = 9,10-phenanthroline) on Au(111) experience a controllable spin-state coexistence. Indeed, when the second ML is initially in the LS state, they can switch a proportion of the molecules into the HS state by applying a voltage pulse with the STM tip. The metastable HS-state molecules can be monitored in the following STM topographies indicating a lifetime of at least tens of minutes.

Pronschinske *et al.*[373] investigated a bilayer of $Fe(H_2B(pz)_2)_2$(bipy) (with H_2-$B(pz)_2$ = bis(hydrido)bis(1H-pyrazol-1-yl)borate and bipy = 2,20-bipyridine) on a Au(111) sample using a variable temperature STM. They can identify the spin state of the molecules by monitoring the topographic contrast and by measuring the electronic gap in STS experiments. Similarly to our work, they observe a spin-state coexistence at low temperature, and they show that the proportion of HS molecules stays constant with increasing temperatures. They suggest that the spin-state coexistence helps to form a dense ordered structure.

Interestingly, Warner *et al.*[334] investigated the same molecule for submonolayer

coverages on Au(111) using XAS. They observe an increase of the proportion of HS molecules with increasing temperature, and under illumination at low temperatures. According to their study, a small proportion of the molecule can experience a temperature and light-induced spin transition, while the spin-state of the other molecules is fixed. At low temperatures, in the absence of illumination, the proportion of HS molecules in about 50%, indicating a spin-state coexistence.

In contrast, Bernien *et al.*[332] observed a complete thermal spin transition on submonolayer $Fe(NCS)_2L$ (L: 1-6-[1,1-di(pyridin-2-yl)ethyl]- pyridin-2-yl-N,N-dimethyl-methanamine) deposited onto a highly oriented pyrolytic graphite substrate. The XAS measured at low temperatures indicate molecules only in the LS state, and thus the absence of spin-state coexistence. We can however note that the transition width is about 115 K, and hence much larger than in the bulk.

Considering the above discussion, it seems that spin-state coexistence appears at the molecule-substrate interface and has origins from the substrate. In addition, it looks like the spin-state coexistence depends on the considered molecule/substrate pair. In the following we show, using the same SCO molecule, the substrate and the coverage dependence of the spin-state coexistence. In turn, this will help to describe a possible origin of the effect.

15.1.1. Substrate dependence

In Sec. 14.1, by using a combination of STM and XAS techniques, we identified the spin state of single first-ML Fe-phen molecules on Cu(100). From topographic measurements, the molecules in the HS state have a larger interlobe distance than that of the molecules in the LS state. In Fig. 15.1a, we present a topography of first-ML Fe-phen molecules on Cu(100). There is clearly a spin-state coexistence since we observe Fe-phen molecules in the HS (dashed red ellipse) and LS (solid blue ellipse) states. If one change the symmetry of the surface, *i.e.* by using a Cu(111) substrate, the adsorption geometry of the first-ML Fe-phen molecules on Cu(111) is similar than that of first-ML Fe-phen on Cu(100) (see Sec. 13.3). The topography of first-ML Fe-phen molecules on Cu(111) presented in Fig. 15.1b reveal first-ML molecules with two different conformations (with different interlobe distances). The STS measurements performed on both conformations are consistent with the one on Cu(100) (see Fig. 15.2a), *i.e.* molecules in the HS (LS) state exhibit the largest (smallest) interlobe gap and are characterized by the presence (absence) of a Kondo resonance (see Fig. 15.2a). In turn, this demonstrates that the spin-state coexistence survives the surface-symmetry change. Identical measurements performed on first-ML Fe-phen molecules deposited onto a Au(111) substrate (see topography in Fig. 15.1c and spectroscopy in Fig. 15.2b) indicate that i) the molecules have the same adsorption geometry than on Cu(100) and Cu(111) substrates; and ii) the spin-state coexistence remains.

In conclusion, the spin-state coexistence remains on the three different metallic substrates that we investigated. However, the electronic coupling between the molecules and the substrate, and more particularly, the sulfur-metal bonds are rela-
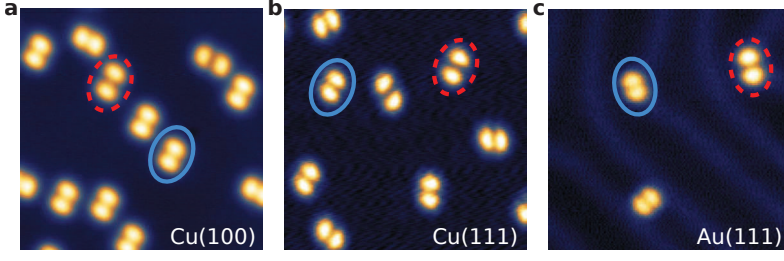
Figure 15.1. – **Substrate dependence of the spin-state coexistance**. Topographies of submonolayer Fe-phen coverage on **a**, Cu(100) (V=0.8 V,I=50 pA) **b**, Cu(111) (V=0.1 V,I=550 pA) and **c**, Au(111) (V=−0.2 V,I=200 pA) substrates. On each topography, a HS (LS) Fe-phen molecule is encircled in dashed red (solid blue) for clarity. Image sizes are 14.1 nm × 14.1 nm.
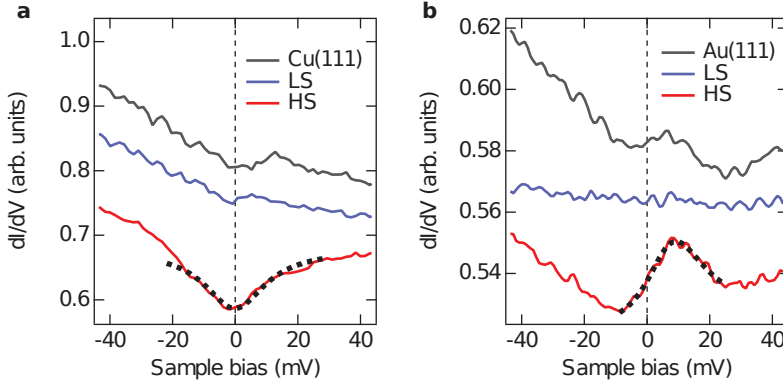
Figure 15.2. – **Spectroscopy of Fe-phen on Cu(111) and Au(111)**. dI/dV spectra recorded on the center of HS (red), LS (blue) and on the substrate for Fe-phen on **a**, Cu(111) and **b**, Au(111) surfaces. The fitting of the spectra of HS Fe-phen on Cu(111) (Au(111)) with a Fano function reveal a Kondo temperature $T_K \approx$137 K ($T_K \approx$133 K), a q-factor of 0 (4.5) and a Coulomb repulsion shift of −0.1 meV (6.8 meV). The spectra were acquired with a voltage modulation of 3 mV at a frequency of 723 Hz.

tively strong for the three substrates. This is further reinforced by the unsuccessful spin-state-switching attempts on the first-ML Fe-phen molecules deposited on these three substrates (see Sec. 14.2.1). However, introducing an insulating CuN layer between the first-ML Fe-phen molecules and the Cu(100) substrate, helps to electronically decouple the molecules from the substrates, and most probably helps to reduce the bonding of the sulfur ion to the surface. In this case, the spin-state switching is possible (see Sec. 14.2.2) and both spin states have long lifetimes (no spontaneous transition observed after tens of hours). We thus have a "controllable" spin-state coexistence of Fe-phen on CuN/Cu(100). One can already foresee that the bonding of

the molecule on the substrate is a key element for the spin-state coexistence. One can also speculate that using a highly oriented pyrolytic graphite substrate as in Ref. 332, one can eventually suppress the spin-state coexistence.

15.1.2. Coverage dependence

As discussed in the previous section, the molecule-substrate bonding seems to be an important parameter for the spin-state coexistence. One may also be wondering about the influence of intermolecular interactions on the spin-state coexistence. Indeed, a molecule in the HS state is typically 5% larger than the same molecule in the LS state (see Sec. 12.1.2) leading to intermolecular elastic interactions that can influence the spin state of the neighboring molecules (this is referred to as cooperativity, see Sec. 12.2.2).

In order to gradually increase the intermolecular interactions, and since molecular diffusion is absent for submonolayer coverages, we investigated different Fe-phen coverages on Cu(100) and Cu(111) substrates at 4 K. For a Fe-phen coverage of 0.1 ML, Cu(100) and Cu(111) surfaces promote the coexistence of the spin states as depicted respectively in Fig. 15.3a and Fig. 15.3b. Referring to Figures 15.3c and 15.3d, this coexistence subsists also at 0.5 ML coverage. However, this coexistence is not present for molecules that form the second ML on Cu(100) and Cu(111) as seen in the respective Fig. 15.3e and Fig. 15.3f. Indeed, as discussed in Sec. 14.3, there seems to be no variation in the interlobe gap when two molecules of same orientation are compared. We infer that a coexistence of spin states is sustained in the first-ML molecules while the second-ML molecules appear to be fixed into a dominant spin state. The first layer would act as a decoupling layer from the substrate,[347] so as to increase intermolecular effects within the second layer such as cooperativity.

For the investigated submonolayer coverages, we try to be more quantitative by extracting the proportion of HS molecules from high-resolution large-scale STM topographies (not shown). The resulting proportion of HS molecules as a function of the coverage on a Cu(100) substrate is presented in Fig. 15.3g. The plot contains only a few data points but it is rather clear that there is no direct correlation between the HS proportion and the coverage of molecules. Furthermore, we note that the HS proportion seems to adopt the two discrete values of 5 or 30 %. This suggests that the spin-state coexistence originates from the properties of the system rather than from a low-temperature frozen spin state, in agreement with the study reported by Pronschinske *et al.*[373]

Based on the discussion in Sec. 14.3, we tentatively ascribe the second-ML Fe-phen molecules on Cu(100) and Cu(111) in their HS state at low positive and for negative sample voltages. We extrapolate that at zero voltage, in absence of external stimuli, the second-ML Fe-phen molecules on Cu(100) and Cu(111) are in their HS state, in contrast to bulk Fe-phen molecules which are in the LS state at $T \approx 4$ K. The dominant HS state for second-ML molecules is consistent with the thermodynamic model developed by Félix *et al.*[391] In their model for nanoparticles, the Gibbs free
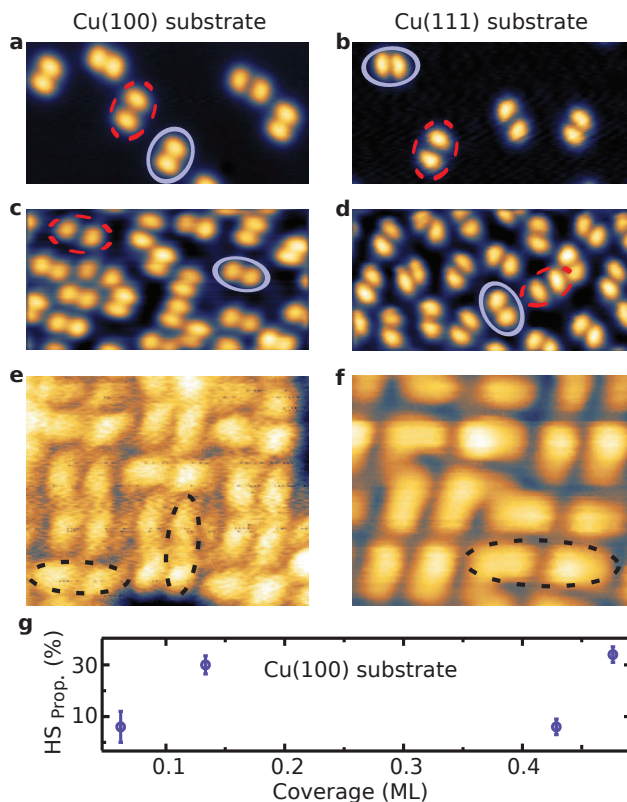
Figure 15.3. – **Coverage dependence of the spin-state coexistence**. Constant-current topographies for different Fe-phen coverages and substrates: 0.1 ML on **a**, Cu(100) (V=0.80 V, I=500 pA) **b**, Cu(111) (V=0.10 V, I=200 pA) and 0.5 ML on **c**, Cu(100) (V=0.80 V, I=500 pA) **d**, Cu(111) (V=0.60 V, I=10 pA). Image sizes are 14.0 nm × 7.0 nm. In panels **a-d**, examples of HS and LS molecules are respectively indicated by dashed red and solid blue ellipses. **e**, 1.8 ML of Fe-phen on Cu(100) (V=0.30 V, I=140 pA), **f** Fe-phen (1.9 ML) on Cu(111). Image sizes are 3.8 nm × 3.1 nm and 2.7 nm × 2.2 nm, respectively. In panels **e-f**, examples of second-ML molecules are indicated by black ellipses. **g**, Proportion of HS molecules as a function of coverage. Each point corresponds to a different sample, and we used between 500 and 4000 molecules on each sample to determine the proportion of HS molecules. As described in the text, the coexistence of the spin states remains at submonolayer coverages but, in this regime, no direct correlation is found between the HS proportion and the coverage.

energy has a supplementary term accounting for the spin-state-dependent surface energy. They show that for small enough nanoparticles, *i.e.* when the proportion of the "surface molecules" is no more negligible in front the "bulk molecules", the model predicts the existence of a non-thermally switchable residual fraction of molecules. The residual fraction of molecules can in the HS state and reach values up to 100 %, provided that the difference between the HS and LS surface energies is sufficiently negative.

The dominant HS proportion of the second-ML molecules is also reinforced by the previous XAS measurements (see Sec 14.1). Indeed, on one hand, a detailed analysis of the topographies on first-ML Fe-phen molecules on Cu(100) reveals a proportion of HS molecules between 5 % and 30 %. On the other hand, the XAS study of approximately 2 ML Fe-phen on Cu(100) (see Sec. 14.1 and Ref. 331) indicate a much higher proportion of HS molecules of 46 %. Yet, if we assume that the spin state of the first-ML molecules remains unchanged upon adsorption of the second-ML molecules, simple algebra calculations suggest that the second-ML Fe-phen molecules are dominantly in their HS state, in agreement with our assignment.

15.2. Possible origin of the spin-state coexistence

In the previous section, we observed a spin-state coexistence for the first-ML molecules that are directly anchored to the surface. Since a bulk or free Fe-phen molecule would be in its LS state at $T \approx 4\,\text{K}$, there is an additional interaction that prevents the metastable HS state of a proportion of the first-ML Fe-phen molecules to relax into the LS state. By varying the molecular coverage, we showed that there is no direct correlation between the spin-state coexistence and the intermolecular interactions for first-ML Fe-phen molecules. Thus, the interactions that refrain the HS state to relax into the LS state for a portion of first-ML Fe-phen molecules most probably arises from the substrate. Moreover, as the SCO is related to geometric modifications, the precise adsorption site of the molecule and the strong bonding of sulfur on copper should be crucial.

In Figs. 15.4a and 15.4b, we show topographies of first-ML Fe-phen molecules, respectively in the HS and in the LS states, on an atomically resolved Cu(100) surface. From the topographies, we cannot identify the adsorption site of the sulfur ions on the corrugated Cu(100) surface as they are hidden by the phenanthroline groups. However, we can read that the Fe ion of the first-ML Fe-phen in the HS state is positioned on top of a hollow site, while the Fe ion is on top of a bridge site for the first-ML Fe-phen in the LS state. These spin-state-dependent positions of the Fe-ion relative to the corrugated Cu(100) surface, as well as the spin-state-dependent distance between the two sulfur ions of a Fe-phen molecule,[266] suggest different adsorption sites for both spin states. In the following, we interpret the spin-state-coexistence and the switching results assuming a spin state that depends on the adsorption site.

The spin state of a first-ML Fe-phen molecule would be fixed by the adsorption
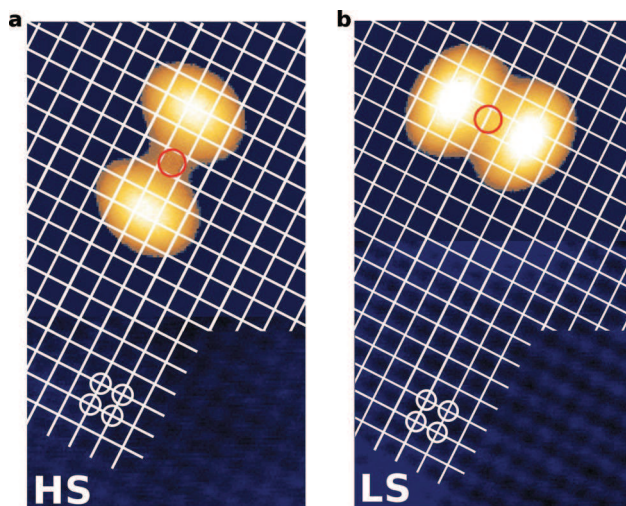
Figure 15.4. – **Adsorption site of first-ML Fe-phen on Cu(100)**. To-
pographies of single **a**, HS Fe-phen and **b**, LS Fe-phen molecules atop an
atomically resolved Cu(100) surface revealing the adsorption site of the
molecule. The Fe ion of the HS and LS molecules is sitting on top of a
hollow and bridge sites, respectively. For clarity, four Cu atoms are en-
circled and intersections of lines represent the center of Cu atoms. Image
sizes are $2.8\,\text{nm} \times 5.0\,\text{nm}$.

site when the molecule is adsorbed on Cu(100). In turn, switching the spin-state of
the molecule would require a sufficient energy to change the adsorption sites. Since
we do not observe additional molecular conformations, any intermediate adsorption
site, between that of the HS and LS states, is energetically less favorable and thus
represents a potential-energy barrier to overcome for switching the spin state of a first-
ML molecule. In the absence of external stimuli, this potential barrier prevents the
metastable HS state to relax into the LS ground state, and would explain the existence
of the spin-state coexistence. Moreover, the unsuccessful switching attempts on first-
ML Fe-phen on Cu(100) discussed in Sec. 14.2.1 could be explained by an insufficient
energy transferred to the system in order to modify the adsorption site of the molecule.
Indeed, one can expect that the energy required to change the adsorption site is rather
important, as the sulfur-copper bond is rather strong. We note that, applying even
larger sample voltages than that used in Sec. 14.2.1 often results in the destruction
of the molecule as the Fe-N bonds of the Fe-phen molecule might not withstand the
energy applied to the system. However, if we change the adsorption site of a first-ML
Fe-phen molecule initially in the LS state, through *e.g.* lateral manipulation with the
tip of the STM, the final spin state of the molecule seems modified (see Sec. 14.2.1).

For second-ML Fe-phen on Cu(100) or Cu(111), the adsorption geometry of the
molecules suggests $\pi - \pi$ interactions between the phenanthroline groups of first- and
second-ML molecules. We believe that this drastically reduced bonding strength com-

pared to that of sulfur-copper bonds leads to a quite reduced potential-energy barrier between the two spin states. In turn, the lower potential barrier no more refrain the metastable state to relax into the ground state and leads to the disappearance of the spin-state coexistence. Furthermore, as we believe the potential barrier to be relatively small, switching the spin state of second-ML Fe-phen molecules would require little energy compared to that needed for first-ML Fe-phen molecules on Cu(100) or Cu(111), in agreement with the experimental observations (see Secs. 14.2.1 and 14.3). Note that the HS ground state of the second-ML molecules is most probably induced by the geometry of the system through the position and orientation of the phenanthroline groups, *i.e.* a special adsorption site that is energetically favored.

For intermediate heights of the potential-energy barrier between the two adsorption sites, such as for first-ML Fe-phen on CuN/Cu(100) where the sulfur-copper bond strengths are reduced, the spin-state coexistence is still present but becomes "controllable". Indeed, the spin state of a first-ML Fe-phen molecule on CuN/Cu(100) can be switched using reasonable current and voltage values; and both spin states have long lifetimes (see Sec. 14.2.2).

15.3. Partial conclusion

Spin-state coexistence is observed for the first-ML Fe-phen molecules and survives on different substrates such as Cu(100), Cu(111), Au(111) and CuN/Cu(100). For first-ML Fe-phen molecules on Cu(100), the proportion of HS molecules does not seem to be correlated to the Fe-phen coverage. Instead, we presume that commensurability considerations between the sulfur-sulfur distance of a single Fe-phen molecule, which drives the spin state of the Fe-ion site, and the corrugated potential landscape of sulfur adsorption sites promoted by the underlying Cu(100) substrate, shall pin the spin state. This is in agreement with STM topographies of HS and LS Fe-phen molecules, where we observe a spin-state-dependent position of the Fe-ion relative to the underlying Cu(100) surface. In turn, this would explain the spin-state coexistence observed for first-ML Fe-phen molecules.

In contrast, second-ML Fe-phen molecules are adsorbed on a weaker energy-potential landscape from the underlying blanket of phenanthroline orbitals of the first-ML Fe-phen molecules. This relaxes any commensurability constraints on the adsorption geometry of the second-ML Fe-phen. This suppresses the spin-state coexistence as any metastable spin-state would relax into the ground spin state.

Although these results were obtained with Fe-phen molecules, we believe that they can be generalized for other SCO complexes on different surfaces.

16

Conclusions

Understanding the physics occurring at the molecule-metal hybrid interfaces is of fundamental importance for the development of organic spintronics devices. We therefore focused our study on molecule-ferromagnetic hybrid interfaces using archetypal phthalocyanine molecules, followed by a study of the interaction of functional spin-crossover molecules on metallic surfaces.

In the first part of this thesis, we studied MnPc molecules deposited on a magnetic Co/Cu(100) substrate with MnPc coverage varying from sub ML to 3.5 ML. Using X-ray absorption techniques, notably X-ray natural linear dichroism, in combination to STM measurements, we could determine that the first- and second-ML molecules lie flat on the Co surface, while most of the third- and fourth-ML do not. Since MnPc molecules preferentially stack into columns,[200] we believe that the molecules lying flat on the surface form small molecular columns. We then studied the magnetic coupling between the Mn ion within MnPc and the Co substrate for sub ML coverage using X-ray magnetic circular dichroism. For sub-ML coverage, the measurements reveal a ferromagnetic coupling between the Mn ion and the Co, in agreement with previous studies on the same system[5] and on similar systems.[215, 217, 218] For larger MnPc coverages, the XMCD measurements in combination to *ab initio* DFT calculations evidenced antiferromagnetic correlations at room temperature between the Mn centers of neighboring MnPc molecules within molecular columns. In turn, by performing magneto-optical Kerr effect measurements, we have shown that the AF ordering of the MnPc molecules on top of the ferromagnetic Co surface leads to a shift of the Co magnetic hysteresis loop, *i.e.* exchange bias, for temperature below 100 K. Exchange bias is a cornerstone of spintronic that was still unreported for molecular systems. In that sens, this first observation of a molecule-induced exchange bias constitutes a breakthrough in the field of molecular spintronics. As a perspective of this work, we can investigate the magnetic impact of MnPc molecules on ferromagentic polycrystalline substrates that are more practical for realization of devices and for large-scale production. Additionally, we can look for a complete set of molecules that can in-

duce exchange bias. Hashim Jabbar has already started investigations towards these perspectives and the results are promising. Alternatively, the magnetic order within the molecular layer may strongly affect the spin-polarized transport properties.[392] We can imagine that the latter can be enhanced by an adequate engineering of the magnetic interactions within the molecular layer.

Separately, we have studied the magnetic coupling between MnPc and Co through a Cu-spacer layer by interlayer exchange coupling. We fabricated a wedge sample with variable Cu thickness ranging between 0 and 14 ML. On one side of the sample, we had the spintronic reference system composed of the Co/Cu/Co/Cu(100) stack, while the stack on the other side of the sample was MnPc/Cu/Co/Cu(100) that we referred to as the protected spinterface. Using a combination of XMCD and DTF calculations, we evidenced a room-temperature magnetic coupling between MnPc and Co through 1 ML, 2 ML and 3 ML of Cu. The coupling is antiferromagnetic for 1 ML of Cu and ferromagnetic for the other thicknesses. At low temperature (4.8 K), we can observe an oscillatory magnetic coupling between the Mn center within MnPc and the Co separated by up to 12 ML. The period and phase of the oscillatory exchange coupling correspond to that of the spintronics reference system, as expected for interlayer exchange coupling. From this qualitative but systematic measurements, we could also observe an antiferromagnetic coupling for 4 ML Cu on the protected spinterface while it is absent on the spintronic reference stack. This oscillation, despite its prediction, is generally not present in the inorganic-based systems what is usually attributed to roughness issues at the interfaces.[376] This shows that the system we investigated, *i.e.* Mn ions within a molecular cage coupled to Co through a spacer, is insensitive to interface roughness and MnPc therefore represents an ideal probing layer to study interlayer exchange coupling. Additionally, by performing XMCD measurements at different temperatures and magnetic fields, we experimentally estimated effective exchange fields of -80 T and -1 T for 1.5 ML and 7 ML of Cu, respectively. *Ab initio* calculations revealed that the magnetic interactions not only impact on the Mn ions. The other atomic sites within MnPc have an adsorption-induced spin polarization close to the Fermi energy. Furthermore, the calculations evidence a spin-dependent hybridization of the molecule-metal orbitals. The combination of the spin-polarization and the spin-dependent hybridization allows to anticipate promising spin-polarized transport properties that can largely exceed that of conventional ferromagnetic-molecule systems. As a perspective, we can in a first step experimentally monitor the adsorption-induced spin polarization close to the Fermi energy, for example by using spin-resolved ultraviolet photoemission spectroscopy. In a second step, we can fabricate complete transport devices and experimentally measure the spin-dependent transport. Moreover, the formation of the spinterface through a nonmagnetic spacer allows for a larger choice of molecules to investigate. Indeed, the choice of the molecules was limited to their deposition techniques as the exposure of the ferromagnetic layer to solvent or air could strongly affect its properties. In this work, we have shown that the spinterface properties can remain upon the ferromagnet protection by a thin layer of noble metal. Complementary studies should be performed to reinforce that point.

In the second part of this thesis, we investigated spin-crossover molecules on metallic surfaces. We chose the archetypal Fe-phen molecule for our investigations. The first important step was the successful clean deposition of the fragile Fe-phen molecules on surfaces. Using low temperature scanning tunneling microscopy, we then investigated the growth of Fe-phen on Cu(100) and Cu(111) surfaces. On both substrates, we observed a layer-by-layer growth that is of great importance for the perspective of SCO-based devices. Additionally, we determined the adsorption geometry of the molecules, which is similar on both substrates. The first-ML molecules have their NCS groups pointing towards the surface, while the second-ML molecules are upside down. From high-resolution STM topographies, we could observe two different conformations of the first-ML Fe-phen molecules, which we ascribed to the HS and LS states with the help of scanning tunneling spectroscopy. At first sight, the coexistence of both spin states at low temperatures is surprising as we would expect molecules only in the LS state. The spin-state coexistence and the integrity of the Fe-phen molecules were confirmed by XAS measurements. We unsuccessfully tried to switch single first-ML Fe-phen molecules on Cu(100) by applying voltage pulses and important tunneling currents. Only by passivating the surface with a CuN layer and thus by reducing the molecule-substrate coupling, we could switch the single Fe-phen molecules in a deterministic and reproducible way with application of voltage pulses of adequate polarity. Interestingly, the conductance of the molecule in the HS state is higher than that in the LS state. Furthermore, we developed a switching model involving an excited state of the molecule in qualitative agreement with the experimental observations.

Since spin-state switching was possible after reduction of the molecule-substrate coupling, we investigated the spin state of the second-ML Fe-phen molecules that are at least partially decoupled from the Cu(100) substrate by the first-ML molecules. The STM topographies and STS spectra carried out on the second-ML molecules suggest a dominant HS state. By varying the sample voltage, we observed topographic changes of the second-ML molecules, which suggest a spin transition from the HS to the LS state with increasing voltage. The topographic changes are fully reversible and do not indicate the presence of a metastable state. We proposed a dynamic switching model taking into account two competing switching mechanisms; the model can nicely reproduce the experimental data. We similarly observed topographic changes of the second-ML Fe-phen molecules on a Cu(111) surfaces.

We also carried out additional studies on the surprising spin-state coexistence of first-ML Fe-phen molecules at low temperature. We observed that the spin-state coexistence is also present for first-ML Fe-phen on Cu(111) and Au(111) surfaces. Moreover, varying the coverage of first-ML Fe-phen molecules on Cu(100) does not seem to affect the proportion of molecules in the HS state. Finally, we propose that the spin-state coexistence originates from the molecule-substrate coupling, and more particularly from the adsorption site of the molecule on the surface.

As perspectives of this work on Fe-phen molecule at low temperature, it would be great to study the influence of light irradiation and temperature on the spin state of the molecules. For instance, would the spin-state coexistence that we observe for

first-ML molecules evolve with temperature and/or light irradiation? Alternatively, as we measured different conductance for HS- and LS-state molecules, we can imagine to fabricate junctions composed of two metallic electrodes sandwiching a Fe-phen layer. Such junctions could be used as sensors provided that the spin state of the molecules depends on temperature and/or light irradiation. In relation with the work done in the first part of the thesis, we can also study the possible magnetic coupling of Fe-phen molecules to a ferromagnetic substrate. Toshio Miyamachi and myself have already carried out experimental investigations in that direction, together with theoretical investigations by Saber Gueddida and Mebarek Alouani. The actual results seem promising. At term, we can think about GMR devices where the spacer layer is composed of SCO molecules. The conductance of such junctions would depend on the magnetic alignment of the electrodes and on the spin-state of the molecule constituting the barrier. In that sens, such junctions would lead to four-state devices.

Appendices

Supplementary information for the study of MnPc on Co

In this appendix, we present thickness-dependent XAS spectra at the Mn $L_{3,2}$ edges that suggest a strong hybridization of first-ML MnPc on the Co substrate. Additionally, the evolution of the XAS spectra with increasing MnPc thickness is compatible with a charge transfer from the Co substrate to the Mn ion, predicted by the *ab initio* calculations. In the second part, we describe the methods relative to the *ab initio* DFT-based calculations and complementary calculations results. The calculations on the first-ML MnPc on a Co(100) substrate reveal that the MnPc molecule can bring additional uniaxial anisotropy to the system, most probably due to the adsorption-induced anisotropic distortion of the MnPc molecule. Finally we show that the Mn sites of second- and third-ML MnPc stacked into columns on top of Co exhibit AF ordering, in support to our exchange bias measurements.

A.1. MnPc-thickness dependence of the XAS spectra at the Mn $L_{3,2}$ edges

In this section we discuss about the evolution of the XAS spectra at the Mn $L_{3,2}$ edges with increasing MnPc thickness (see Fig. A.1). For 0.7 ML MnPc, the dominant peak at the Mn L_3 edge is positioned at 648.1 eV. When the MnPc coverage is increased to 1.9 ML, the dominant peak shifts towards lower energies to 647.1 eV (see Fig. A.1). The shape of the Mn L_3 edge is also modified when the molecular coverage is increased. Indeed, for 0.7 ML MnPc coverage, the satellite peak is located at the left of the dominant peak, while the satellite peak moves to the right of the dominant peak for 1.9 ML MnPc coverage. The XAS spectra for 3.5 ML MnPc coverage is very similar to that for 1.9 ML. This shift in peak position reveal a change in the electronic structure of the Mn within MnPc, which arises from the strong (weak)
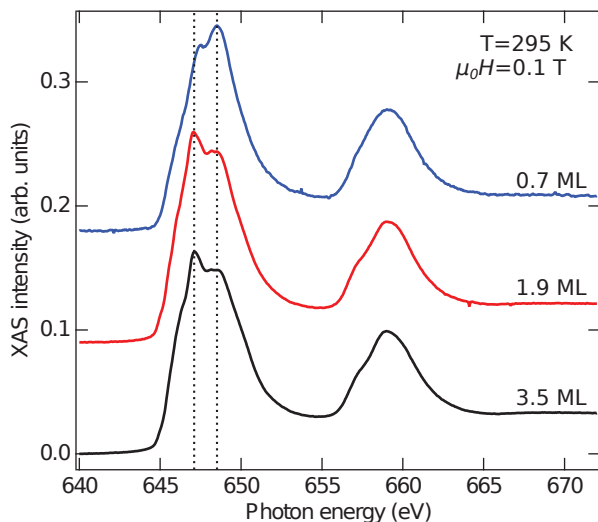
Figure A.1. – **XAS at the Mn $L_{3,2}$ edges as a function of MnPc thickness**. Averaged XAS spectra acquired at $295\,$K in $0.1\,$T with left and right photon helicities for $0.7\,$ML, $1.9\,$ML and $3.5\,$ML. The dashed lines are positioned at $647.1\,$eV and $648.5\,$eV and indicate the position of the thickness-dependent dominant peak at the L_3 edge. All the XAS spectra are normalized to their white-line integral.

electronic coupling of the first-ML (second- and subsequent-ML) molecules to the substrate. Furthermore, the shift of peak position in the XAS spectra is consistent with a change of the oxidation state of the first-ML Mn ions compared to that of the Mn ion of a free or uncoupled MnPc molecule. This is in agreement with the *ab initio* calculations that we present below.

A.2. *Ab initio* calculations of MnPc on Co

I would like to mention that Famita Ibrahim and Mebarek Alouani performed the *ab initio* study. Based on the output of their calculations, I generated the images.

A.2.1. Methods

The density-functional calculations were performed using the VASP package[393] and the generalized gradient approximation for exchange-correlation potential as parametrized by Perdew, Burke, and Ernzerhof.[394] They used the projector augmented wave pseudopotentials as provided by VASP.[395] They modeled the *Fcc* Co(100) surface by using a supercell of 3 atomic monolayers of 8×8 atoms separated by a vacuum region of

3 nm. They used the lattice parameter of Cu (0.36 nm) as experimentally, the Co was epitaxially grown on Cu. They used a kinetic energy cutoff of 450 eV for the plane-wave basis set and they sampled the first Brillouin zone at the Gamma point. They included van der Waals interactions within the so called GGA-D2 approach developed by Grimme[396] and later implemented in the VASP package,[5] and found an optimized structure of the first-ML MnPc adsorbed at 2.1 Å away from Co. They pertubatively included spin-orbit coupling in the augmentation region at each atomic site. Moreover, they have explored adding a second and third MnPc layer by taking into account several geometries of the relative Pc layers depending on three scenarios to position the top MnPc molecule's Mn site onto the bottom MnPc molecule: hollow, on top of N, and on top of Mn with the molecule rotated by 45°.

A.2.2. Magnetic properties of MnPc on Co

The adsorption and magnetic properties of first-ML MnPc molecules on a Co(100) substrate are discussed in details in Ref. 6 (see also Sec. 8.2). The Mn ion sits on a bridge site and the axes of the MnPc molecule are slightly rotated relative the the x and y axes defined by the underlying Co surface (see Fig. A.2a). First-ML MnPc molecules are strongly hybridized to the Co substrate, which leads to a severe distortion of first-ML MnPc molecules (see Fig. A.2b) compared to a non-distorted third-ML MnPc molecule (see Fig. A.2c). The electronic and the magnetic properties of the Mn ion within MnPc are influenced by the neighboring atoms that modify the ligand field. In Fig. A.2d, we thus focused on the nitrogen ions neighboring the Mn ion of the distorted first-ML MnPc molecule. As indicated by the numbers in Fig. A.2d, the relative height distribution of the nitrogen ions is strongly anisotropic. Indeed, for the four nitrogen ions closest to the Mn center, their relative heights are in average higher along the x direction than the y direction. Note that for the carbon ions, it is the opposite, *i.e.* the carbon heights are in average lower (higher) along the x (y) direction.

The strong hybridization of first-ML MnPc molecules to the Co(100) substrate leads to a gain of 3.5 electrons from the Co per MnPc molecule. We performed a Bader analysis on the Mn center of a first-ML MnPc, which reveals a charge of $1.03\,|e|$ for the Mn ion relative to a charge of $2\,|e|$ for the Mn center of a free molecule. As a result of the charge transfer and of the strong hybridization (including electronic screening), the manganese spin moment is reduced from $3.1\,\mu_{\mathrm{B}}$ to $2.54\,\mu_{\mathrm{B}}$ when an initially free MnPc molecules is adsorbed onto Co. We wanted to go further and see the implications of the topological anisotropy on the magnetic properties of the system. We calculated the in-plane magnetic anisotropy, by taking the difference in total energy between a magnetization of the system aligned along the x and y axes. We found a preferred x axis for the magnetization by $0.66\,\mathrm{meV/}$ supercell that we account for the in-plane magnetic anisotropy energy. We also found that the magnetic anisotropy energy per Mn site of first-ML molecules is $0.39\,\mathrm{meV}$. This corresponds the largest contribution to the in-plane anisotropy of the calculated supercell.
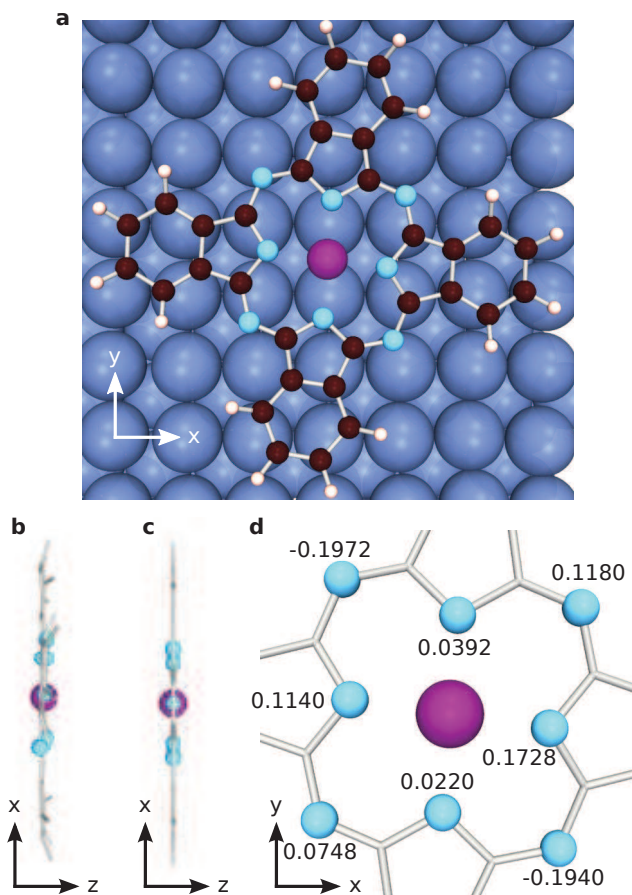
Figure A.2. – **Magnetic anisotropy of first-ML MnPc molecules on Co**. **a** Single first-ML MnPc molecule on the Co(100) substrate after atomic relaxation. The Mn ion sites on a bridge position. **b**, Side view of a first-ML MnPc molecule with noticeable distortions. Increasing z values correspond to larger distances to the Co surface. **c**, Side view of a non-distorted third-ML MnPc molecule (see Sec. A.2.3), **d**, Zoom on the Mn ion within the nitrogen cage of a first-ML MnPc molecule. The numbers indicated next to the nitrogen atoms correspond to the relative distance to the Mn center, expressed in Å.

A.2.3. AF ordering within MnPc columns on Co

Experimentally we observed an AF coupling between first- and second-ML Mn ions within MnPc molecules. To support these experimental observations, we performed *ab initio* DTF-based calculations on systems composed of two and three MnPc molecules stacked into columns. We first discuss about the calculations on systems comprising
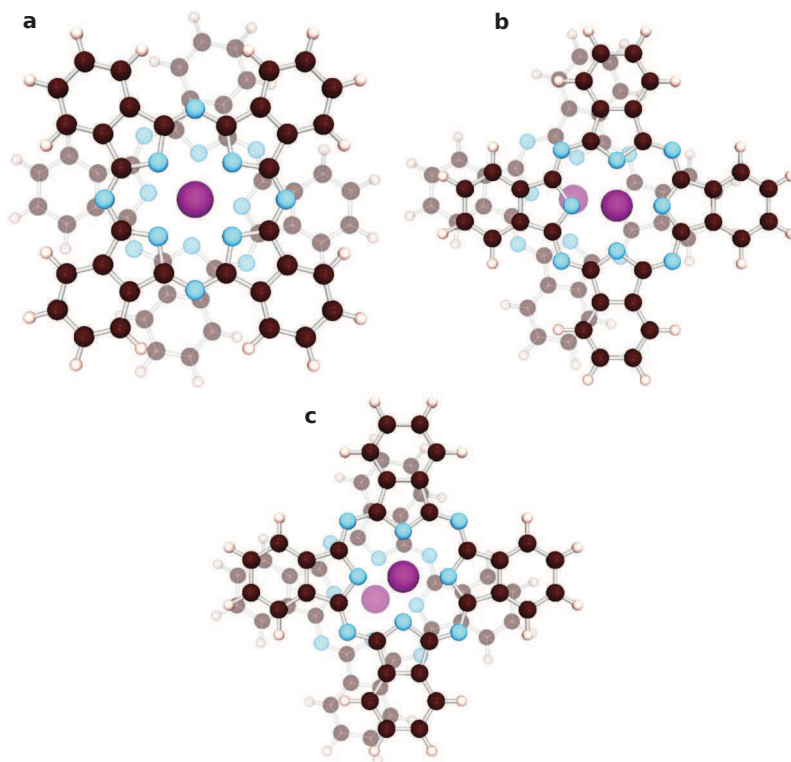
Figure A.3. – **The different adsorption geometries calculated for the second-ML MnPc**. **a**, The second-ML MnPc is on top of the semi-transparent first-ML MnPc, rotated by 45°. **b**, The second-ML MnPc is laterally shifted relative to the semi-transparent first-ML MnPc, such that the second-ML Mn ion sits on top of a first-ML nitrogen ion. **c**, The second-ML MnPc is laterally shifted relative to the first-ML MnPc, and the second-ML Mn ion sits on a hollow site.

two MnPc molecules. As the adsorption site of the second-ML MnPc molecules could not be experimentally determined, we considered three different configurations (see Fig. A.3). Config. **a** is characterized by a second-ML MnPc on top of the first-ML and rotated by 45° relative to the first-ML MnPc (see Fig. A.3a). This configuration is interesting as it is the one experimental resolved by Chen *et al.*[208] on first- and second-ML CoPc molecules on a Pb substrate. In the config. **b**, the Mn ion of the second-ML MnPc is sitting on top of a first-ML nitrogen ion (see Fig. A.3b). We considered this configuration as it corresponds to the one adopted by third-ML CoPc molecules on top of second-ML CoPc molecules on a Pb substrate, and experimentally observed by Chen *et al.*[208] In the config. **c**, the second-ML Mn ion sits in a hollow site of a first-ML MnPc molecule (see Fig. A.3c).

For the three adsorption geometries that we described, we calculated the total

	Config. a	Config. b	Config. c
E_{FM} (eV)	-2081.873	-2081.879	-2081.858
E_{AF} (eV)	-2081.906	-2081.884	-2081.865
$E_{FM} - E_{AF}$ (meV)	33	5	7
$E_{FM} - E_{AF}$ (K)	384	59	79
$m_s^{Mn_1}$ (μ_B)	2.51	2.54	2.53
$m_s^{Mn_2}$ (μ_B)	-3.04	-3.045	-3.05
$d_{Mn_1-Mn_2}$ (Å)	3.87	4.36	4.22
Δz (Å)	3.87	3.87	3.87

Table A.1. – *Ab initio* calculated total energy of ferromagnetic and antiferromagnetic configurations (E_{FM} and E_{AF}), the spin magnetic moment of the Mn ion i ($m_s^{Mn_i}$; $i = 1, 2$), the distance between the first-ML and second-ML Mn ions ($d_{Mn_1-Mn_2}$) and the distance between the two molecular planes (Δz; each molecular plane intersects a Mn ion). Config. a, b and c corresponds to the adsorption geometries reported in Figs. A.3a, A.3b and A.3c.

energy of the system by imposing either a FM or a AF alignment of the second-ML Mn moment relative to that of the first-ML Mn. The total energies and other calculated quantities are reported in Tab. A.1. We can observe that the AF coupling is preferred for the three different configurations. Config. **a** has the lowest calculated total energy and thus represent the favorable geometry, followed by config. **b** and **c**. Note that the difference in the total energy between the different configurations is relatively small, and prevents us to unambiguously ascertain the preferred experimental geometry. From the calculations on the three different systems, we can obverse that the calculated spin magnetic moments carried by the Mn ions are very similar, and we can only note differences in the amplitude of the AF coupling.

How does the magnetic coupling evolve when a third-ML MnPc is added to the system? We tentatively try to answer this question but we should note that the DTF calculations become challenging for three of more MnPc molecules stacked as a column on Co. Indeed, the system becomes very large (over 250 sites) with a large number of possible adsorption geometries of the third-ML MnPc on top of the second-ML MnPc. Note that some of the adsorption geometries would require to enlarge the supercell's size making the calculations even more challenging. Yet, as we found for second-ML MnPc molecules on top of first-ML molecules and as similarly found for columns of CoPc molecules,[202] we suppose that most of the adsorption geometries lead to an AF coupling between the Mn sites of the molecular planes. To support the speculation of a preferred AF correlations, we performed calculations on a system composed of three MnPc molecules on top of Co. The adsorption geometry we considered starts from

config. **a** on top of Co and a third-ML MnPc molecule that is adsorbed in a hollow site (see Fig. 9.6). As expected, we find a preferred AF coupling between second- and third-ML Mn ions, but the coupling strength is only 0.132 meV. However, we know that the coupling strength highly depends on the adsorption geometry (see Tab. A.1) and that our exchange bias measurements suggest an AF alignment of the third-ML Mn ion within MnPc up to at least 100 K.

$\mathcal{B}$

Preparation of CuN/Cu(100) surfaces

We used CuN/Cu(100) surfaces to electronically decouple Fe-phen molecules from the Cu(100) surface. In this appendix, we describe the preparation method and briefly characterize the surface.

CuN films were grown by sputtering nitrogen ions (kinetic energy of $500\,eV$) on a clean Cu(100) surface, followed by annealing to $330\,°C$. Depending on the nitrogen partial pressure during the sputtering process, we obtained two kinds of CuN/Cu(100) surfaces that we denote CuN-poor and CuN-rich (denomination borrowed from Ref. 126).

B.1. CuN-poor surfaces

In Fig. B.1, we show the topography of a CuN/Cu(100) surface obtained by nitrogen sputtering for $25\,min$ in a partial pressure of $1 \times 10^{-5}\,mbar$. We can see CuN square islands that have an area about $5\,nm \times 5\,nm$ and are observed as depressions. The edges of the CuN squares are along the [100] directions of the Cu(100) crystal.[397] The nitrogen layer forms a $c(2 \times 2)$ lattice with a mean lattice constant of $372\,pm$.[398] Since Cu has a lattice parameter of $361\,pm$, the nitrogen superstructure is incommensurate with the underlying Cu(100) surface and leads to surface strains.[398] In addition, using tunneling spectroscopy, Ruggerio et al.[399] have shown that the CuN work function is increased by $0.9\,eV$ compared to bare Cu(100). This confirm that CuN can actually reduce the coupling between adsorbates and the Cu(100) surface.[399]

When depositing Fe-phen molecules following the sublimation procedure described in Sec. 6.1.3 on CuN-poor surfaces (Fig. B.1) held at room temperature, the molecules are mainly located on bare Cu(100) areas. In Fig. B.2, we show a
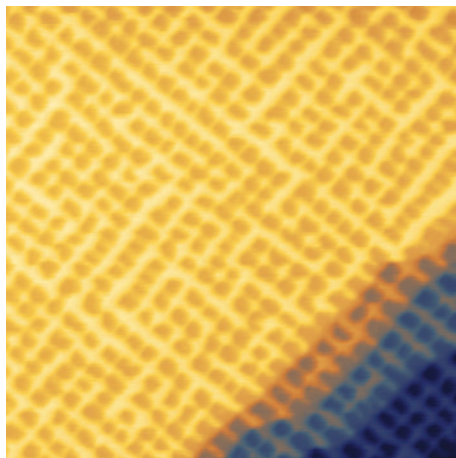
Figure B.1. – **Topography of a CuN-poor surface**. Square islands of CuN appear as depression on the Cu(100) surface (see text). Image size is 120 nm × 120 nm (V=1.0 V,I=120 pA).
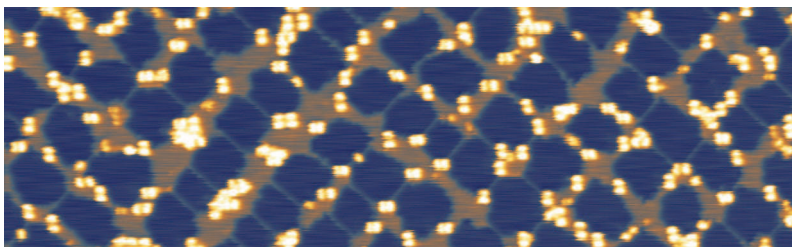
Figure B.2. – **Fe-phen molecules on a CuN-poor surface**. Fe-phen molecules are mainly located on the Cu(100) areas. Image size is 80 nm × 31 nm (V=1.0 V,I=100 pA).

large-scale topography on such a surface, and we can see that no Fe-phen molecule is adsorbed onto the CuN square islands.

B.2. CuN-rich surfaces

In order to actually have Fe-phen molecules on CuN islands, we increased the CuN coverage. To do so, the nitrogen partial pressure during sputtering was increased from 1×10^{-5} mbar to 1×10^{-4} mbar, and the nitrogen-sputtering duration kept to 25 min. In Fig. B.3a, we present a large-scale topography of the resulting surface. The surface is completely covered with nitrogen and is characterized by long trenches.[126, 400, 401] These trench structures are believed to arise from surface tension of the CuN layer on Cu(100).[126, 400, 401] In Fig. B.3b, we show a atomically-resolved topography of the
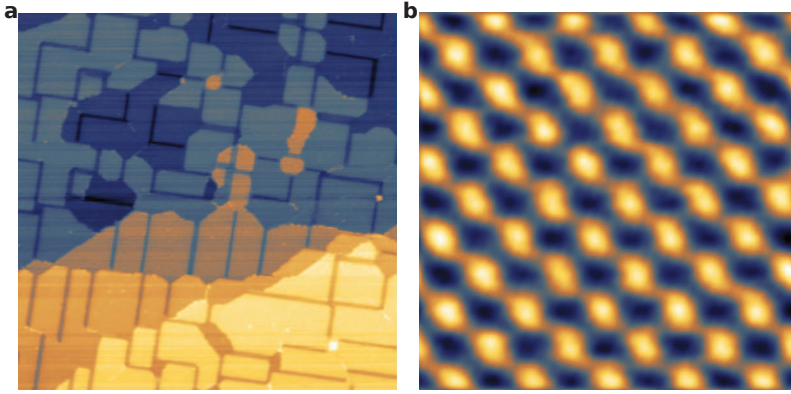
Figure B.3. – **Topography of a CuN-rich surface**. **a**, Large-scale topography of a complete CuN layer on Cu(100) (CuN-rich surface). **b**, Atomically resolved STM topography of the CuN-rich layer. Image sizes are **a**, 140 nm × 140 nm and **b**, 2.6 nm × 2.6 nm (V=0.2 V,I=30 pA). Topography **b** has been filtered using a 2D continuous wavelet transform.

surface. The periodicity of the square lattice is about (3.6 ± 0.2) Å, that is, within the experimental errors, the same than for CuN-poor surfaces.

In Fig. B.4, we show a topography of Fe-phen molecules deposited on a CuN-rich surface. We observe that a proportion of molecules is adsorbed on plain CuN while other Fe-phen molecules are located in the CuN trenches. All the work on Fe-phen on CuN/Cu(100) discussed in Chap. 14 was performed with Fe-phen molecules on plain CuN surfaces. We determined an adsorption geometry of the Fe-phen molecules with the phen groups facing upwards. However, the Fe-phen molecules located at the step edges of the trenches seem to have a different adsorption geometry that we did not further investigate.
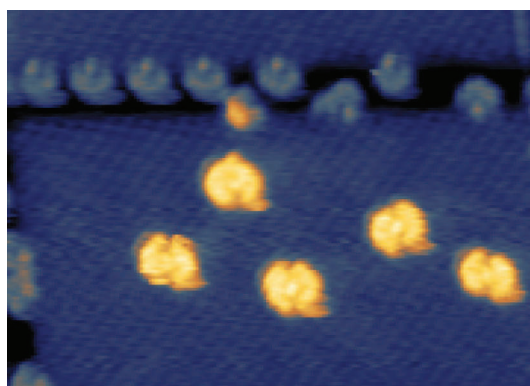
Figure B.4. – **Fe-phen molecules on a CuN-rich surface**. The Fe-phen molecules are either adsorbed on plain CuN surfaces or on trenches' edges. Image size is $14.3\,\mathrm{nm} \times 11.8\,\mathrm{nm}$ ($V{=}0.5\,\mathrm{V}$,$I{=}50\,\mathrm{pA}$).

C

Additional data of the topographic changes of second-ML Fe-phen on Cu(100)

In Sec. 14.3.1, we discussed the topographic changes induced by the sample voltage. We also tentatively ascribed these topographic changes to a dynamic switching between the two spin states; from the HS state at low voltages to a steady-state combination of HS and LS states at higher voltages. This assumption is supported by an analytic model, based on a few hypothesis (see Sec. 14.3.2), that is consistent with the experimental data obtained on the second-ML Fe-phen on Cu(100).

In this appendix, we show complete a data set of topographies of second-ML Fe-phen molecules acquired with different sample voltages. The second-ML Fe-phen molecules are relatively difficult to image compared to the first-ML Fe-phen molecules, which leads to STM images with a lower quality. In turn, it becomes difficult to identify the individual molecules, and even more difficult to read the distance between the lobes for a given second-ML Fe-phen molecule. Thus, the discussion of the topography sets will only be qualitative.

In Fig. C.1, we show topographies of the same location ($9\,\text{nm} \times 6\,\text{nm}$) acquired with different sample voltages. The initial STM image (top left) is taken with a sample voltage of $0.70\,\text{V}$ and two pairs of molecules are encircled. One of this pair of molecules is located within the "dense" and organized molecular area while the second pair is located at the periphery of a second-ML molecular cluster. When decreasing the sample voltage to $0.60\,\text{V}$ and $0.50\,\text{V}$ (Figs. C.1a-c), the apparent morphology of the molecules seems, to the first order, unchanged. However, for a sample voltage of $0.45\,\text{V}$ (Fig. C.1d) the situation becomes interesting. Although, the pair of molecules within the second-ML molecular cluster appears unchanged, the pair of molecules located at the periphery has a different appearance. The two molecules indicated at the periphery have their respective interlobe distances increased compared to the

interlobe distance observed in the topography acquired with a sample voltage of 0.70 V (Fig. C.1a).

With these new elements, we now discuss again about the possible origin of the topographic changes (see Sec. 14.3.1 and 14.3.2). If the interlobe distance variation is due to the probing of different orbitals, one would expect that it affects the second-ML uniformly. This is in contradiction with what we observe in the topography acquired with a sample voltage of 0.45 V. Yet referring to the dynamic switching model (see Sec. 14.3.2), we supposed the existence of an energy barrier between the HS and the LS states. This energy-barrier height and the Gibbs free energy difference between the two spin states (G_0) depends on the absorption sites of the second-ML molecules and on the second-ML neighboring molecules (cooperative effect[285]). Within the dynamic switching model, the different barrier height and G_0 results in a shift of the voltage threshold V_{Th}, and thus a shift of the voltage at which the transition becomes apparent. This, once more, consolidates a dynamic-switching origin of the interlobe variation.

When gradually decreasing the sample voltage from 0.45 V to 0.25 V (Figs. C.1d-h), the interlobe distance of the second-ML Fe-phen molecules gradually increases. This interlobe-distance increase is fully reversible: the interlobe distance of the second-ML molecules can again be strongly decreased as shown in the subsequent topography acquired with a sample voltage of 0.60 V (Fig. C.1i), that is quite similar to the topography acquired with the same voltage before the topographic changes (Fig. C.1b). The distance between the lobes of the second-ML Fe-phen molecules increases again upon decreasing the sample voltage to 0.25 V in the subsequent topography (Fig. C.1j). In the topographies of Figs. C.1k and C.1l, acquired respectively with voltages of 0.20 V and 0.15 V, indicate a further increase of the second-ML-molecule interlobe distance. The sample voltage is then gradually increased to 0.60 V to monitor the gradual shrinking of the lobes of the second-ML Fe-phen molecules (Figs. C.1m-q).

Figure C.1. – **Voltage-dependence of the topography of second-ML Fe-phen on Cu(100)**. Different topographies of the same area are consecutively acquired with different sample voltages that are indicated on the images. Two pairs of second-ML Fe-phen molecules are encircled in some of the topographies. The sequence order goes from left to right; top to bottom. Image sizes are $9\,\text{nm} \times 6\,\text{nm}$ ($I{=}15\,\text{pA}$ for the seven first images, and then $I{=}1.4\,\text{nA}$).

$\mathcal{D}$

Additional data of the topographic changes of second-ML Fe-phen on Cu(111)

In Appendix C we presented and discussed a data set of topographies of second-ML Fe-phen molecules on Cu(100) acquired with different sample voltage. In this appendix, we will present other data sets of topographies of second-ML Fe-phen molecules on Cu(111). We recall, that the adsorption geometry of the second-ML Fe-phen on Cu(111) is similar to the one of second-ML Fe-phen on Cu(100) (see Sec. 13.3), *i.e.*, the phenanthrolines lobes are facing towards the first-ML molecules white the NCS groups are facing upwards. Here also, we will only discuss qualitatively the STM topographies.

In Figs. D.1a-c, we present STM topographies of the same location (5.5 nm × 5.5 nm) acquired with negative sample voltage of −0.86 V, −0.60 V and −0.40 V, respectively. We can observe the interlobe distance of the second-ML Fe-phen molecules is "large", and does not evolve with the sample-voltage amplitude. For STM image acquired with low positive sample voltage of 0.30 V the interlobe distance of the second-ML Fe-phen molecules is still large, similar to what is obtained for negative sample voltage. When gradually increasing the sample voltage from 0.30 V to 1.00 V, the interlobe distance of the second-ML molecules gradually decreases (see Figs. D.1d-k).

A second set of voltage-dependent topographies is shown in Fig. D.2. The investigated area is now larger (18 nm × 18 nm) and presents bulk-like and dendritic-like structures. The topographies are evolving when sample voltage is gradually decreased from 1.25 V to 0.30 V (see Figs. D.2a-f). The interlobe distance of second-ML Fe-phen molecules, located both on the "bulk" or in the chain-like areas, is clearly larger in the 0.30 V (Fig. D.2f) topography than that of the 1.25 V (Fig. D.2a) or even 0.60 V (Fig. D.2d) topographies. The topographic changes are fully reversible as depicted by the topographies of Figs. D.2g-k. Fig. D.2l shows the topography acquired with a sample voltage of −0.20 V, which suggest "large" interlobe distance of the second-ML

molecules in the resolved areas. In general, the tunneling conditions with negative sample voltage are rather unstable, and often lead to the attachment of a second-ML molecule onto the STM tip.
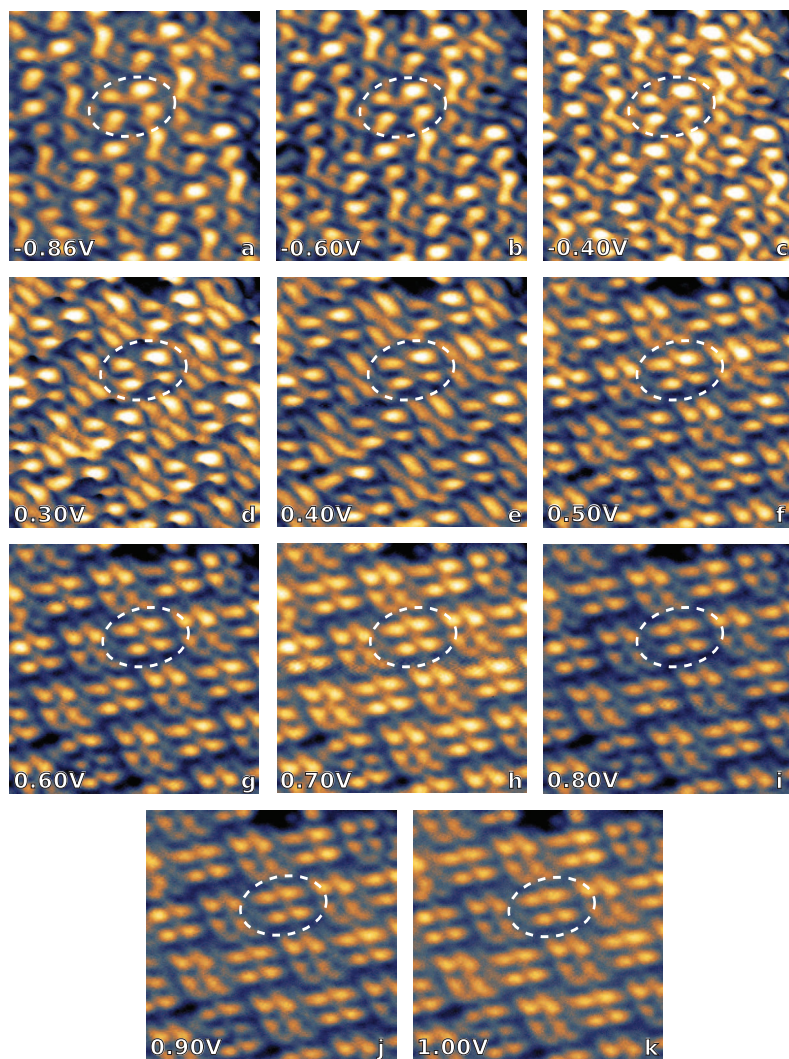
Figure D.1. – **Voltage-dependence of the topography of second-ML Fe-phen on Cu(111) - Serie 2**. Different topographies of the same area are consecutively acquired with different sample voltages that are indicated on the images. A pair of second-ML Fe-phen molecules are encircled in each topography, for clarity. The sequence order goes from left to right; top to bottom. Image sizes are $5.5\,\mathrm{nm} \times 5.5\,\mathrm{nm}$ ($I=210\,\mathrm{pA}$).
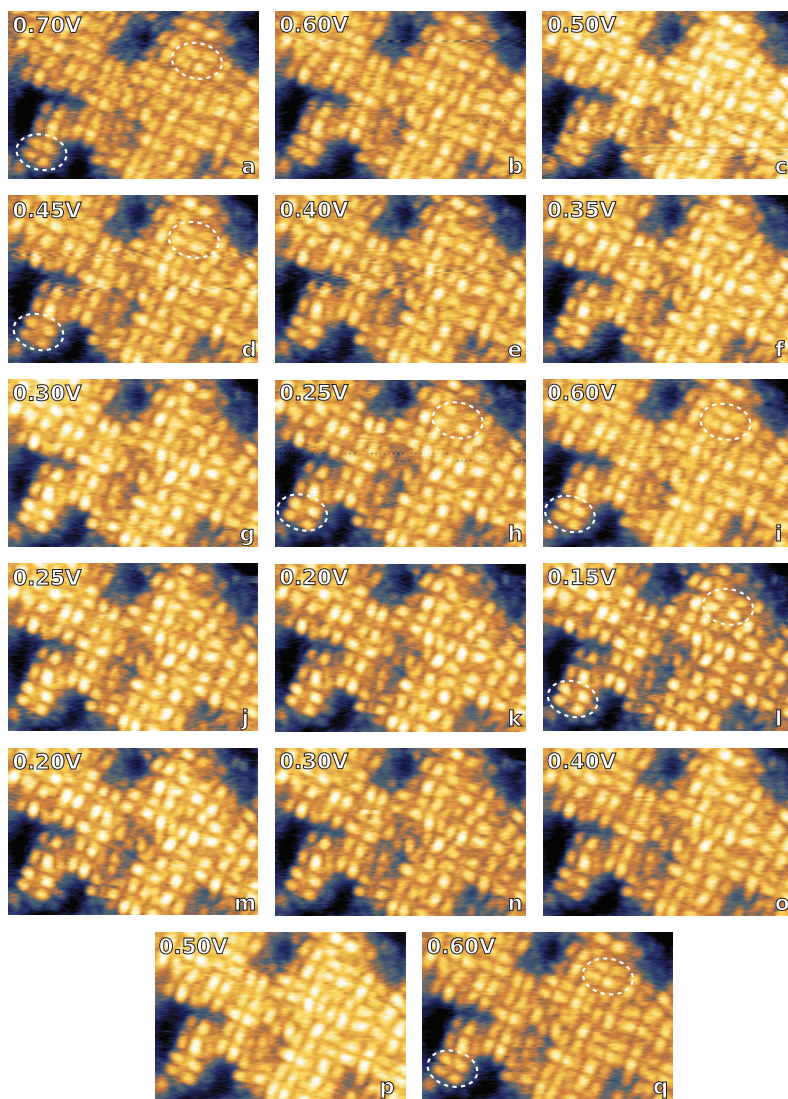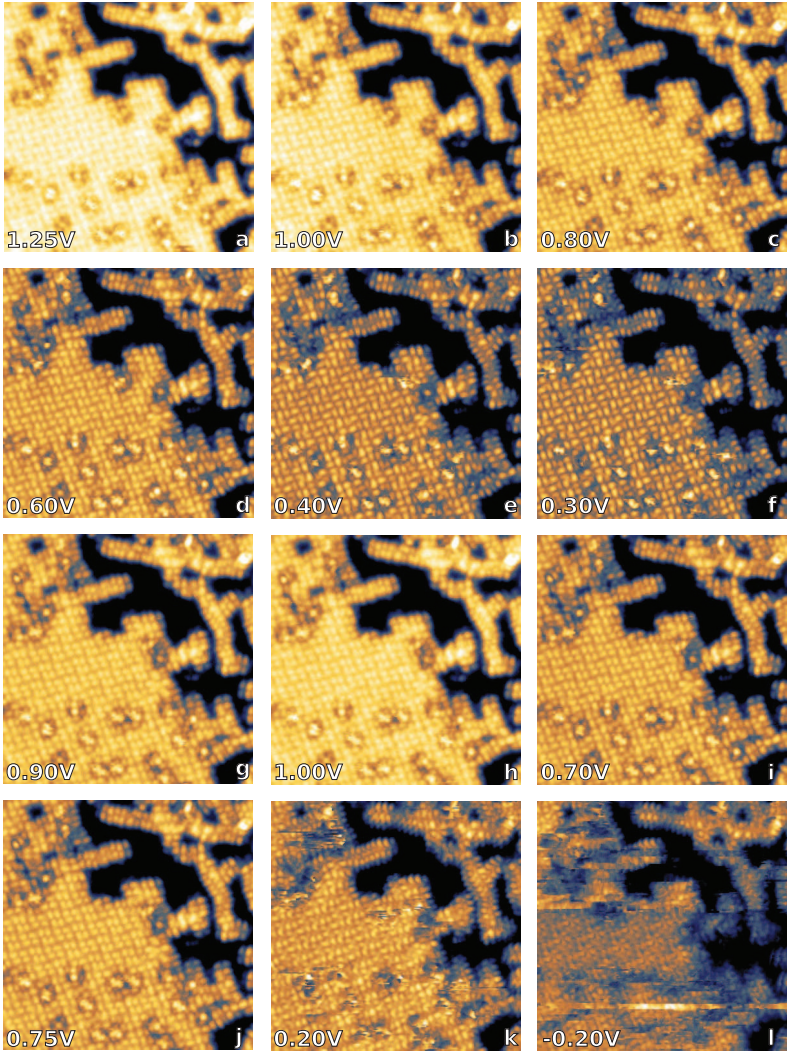
Figure D.2. – **Voltage-dependence of the topography of second-ML Fe-phen on Cu(111) - Serie 2**. Different topographies of the same location are consecutively acquired with different sample voltages that are indicated on the images. The sequence order goes from left to right; top to bottom. Image sizes are $18\,nm \times 18\,nm$ ($I{=}110\,pA$).

Constants

α_f	Fine structure constant $1/137.04$
$\hbar$	Reduced Planck's constant $1.05 \times 10^{-34}\,\mathrm{J\,s}$
μ_0	Permeability of free space $4\pi \times 10^{-7}\,\mathrm{V\,s\,A^{-1}\,m^{-1}}$
μ_B	Bohr magneton $9.27 \times 10^{-24}\,\mathrm{J\,T^{-1}}$
e	Elementary charge $1.60 \times 10^{-19}\,\mathrm{C}$
h	Planck's constant $6.63 \times 10^{-34}\,\mathrm{J\,s}$
k_B	Boltzman constant $1.38 \times 10^{-23}\,\mathrm{J\,K^{-1}}$
m_e	Mass of an electron $9.11 \times 10^{-31}\,\mathrm{kg}$
R	Molar gas constant $8.31\,\mathrm{J\,K^{-1}\,mol^{-1}}$

Experimental and theoretical background

$10Dq$	Energy splitting between t_{2g} and e_g orbitals
ΔA_j	Integral of the XMCD intensity over the L_j edge
Δ_o	Energy splitting between t_{2g} and e_g orbitals
Γ	Half-width at half maximum of the Kondo resonance
κ	Inverse decay length of the electron's wave function within the tunneling barrier
Λ	Oscillation period of the interlayer exchange coupling
$\mathscr{A}$	Prefactor of the transition matrix element $(4\pi^2 \alpha_f \hbar \omega)$
μ_x	Linear X-ray absorption coefficient
ϕ	Work function
Φ_0	Photon flux
Π	Electron-pairing energy

$\Psi(\vec{r})$	Wave function of a particle
$\rho(E)$	density of states
ρ_a	Atomic number density
$\rho_f(E)$	Density of final states
σ^{abs}	X-ray absorption cross section
θ	Angle between the surface normal and the photon-incidence vector
$\vec{\epsilon}$	unit photon polarization vector
$\vec{A}$	Vector potential of an electromagnetic field
$\vec{p}$	Electron momentum operator
A_j	Integral of the white line over the L_j edge
D	Thickness of the metallic layer
d	Thickness of the potential barrier
E	Energy
E_F	Fermi energy
E_K	Position of the Kondo resonance relative to the Fermi energy
H	External magnetic field
H_c	Coercive field
H_{EB}	Exchange-bias field
H_{int}	Light-matter interaction Hamiltonian
I^{ph}	X-ray photon intensity
j	Total angular momentum quantum number
k	Wave number of the electron's wave function outside the tunneling barrier
l	Orbital quantum number
m_j	Secondary total angular momentum quantum number
m_l	Magnetic quantum number
m_s	Secondary spin quantum number
$M_{\mu,\nu}$	Matrix tunneling element from the μ state to the ν state
m_{orb}	Orbital magnetic moment
m_{spin}	Spin magnetic moment
n	Principal quantum number
P_α^q	Electric dipole operator where q defines de photon polarization and α the incidence direction
q	Interference parameter for a Kondo resonance
$r_{v(s)}$	Reflection coefficient of an electron in a metallic layer at the layer-vacuum (layer-substrate) interface
s	Spin quantum number
T	Temperature
T_B	Blocking temperature
T_C	Curie temperature
T_K	Kondo temperature
T_N	Néel temperature

$U(\vec{r})$	Potential in which a particle evolve (energy)
U	Coulomb repulsion energy
U_0	Height of the potential barrier
V	Bias voltage

Mathematical symbols used in the spinterface part

$\Gamma_{l(s)}$	Long (short) period of interlayer exchange coupling oscillations
$\phi_{l(s)}$	Phase of long-period (short-period) interlayer exchange coupling oscillations
$A_{l(s)}$	Amplitude of long-period (short-period) interlayer exchange coupling oscillations
B_J	Proportion of paramagnetic moments with total angular moment J that are aligned against a magnetic referential (Brillouin function)
d_{Cu}	Cu thickness (usually expressed in MLs)
E_F	Fermi energy
g	Landé factor
H	Magnetic field
H_{eff}	Total effective magnetic field
H_{ex}	Effective exchange field
J	Total angular momentum quantum number
J_{IEC}	Interlayer exchange coupling
m_{Mn}	Magnetic moment of the Mn ion within MnPc
MR	Magnetoresistance
$N_{\uparrow(\downarrow)}$	DOS at the Fermi level in the spin up (down) channel
$N_{M(n)}$	DOS at the Fermi level in the majority (minority) spin channel
P^*	Effective spin polarization
P_i	Spin polarization of the DOS of electrode i usually taken at the Fermi energy
$R_{P(AP)}$	Resistance of junction with a parallel (antiparallel) magnetic configuration of the electrodes
S	Total spin quantum number
T	Temperature
TMR	Tunneling magnetoresistance
$v_{M(m)}$	Fermi velocity for majority- (minority-) spin electrons
Z	Atomic number

Mathematical symbols used in the spin-crossover part

α	Proportion of time spent in the HS state
$\alpha_{LS(HS)}$	Polarizability tensor of second-ML Fe-phen in the LS (HS) state
χ	Magnetic susceptibility
χ_m	Molar magnetic susceptibility
$\Delta_{1(2)}$	Barrier height for transition from LS to HS (HS to LS) states

Γ	Cooperativity term
ν_0	Attempt frequency in the scope of the transition-state theory
ρ_m	Molar density
σ	Overall cross section for transition from the excited to the ground state by a single-electron process
$\vec{\mu}_{LS(HS)}$	Static dipole moment of second-ML Fe-phen in the LS (HS) state
$\vec{E}$	Electric field
B	Magnetic field
d	distance between the lobes
$d_{tip-sample}$	Distance between the STM tip and the sample
E	Energy
$E_{HS(LS)}^{Stark}$	Additional potential energy for the SCO molecule in the HS (LS) state in the presence of an electric field
G	Gibbs free energy
G_0	Difference in Gibbs free energy between the LS and the HS states in the absence of external electric field
H	Enthalpy
I	Current
J	Total angular momentum quantum number
$k_{IS \to FS}$	Transition rate from initial state (IS) to final state (FS)
M	Magnetization
p	Pressure
p_{HS}	Proportion of molecules in the HS state
r	Spin-state-switching rate
S	Entropy
T	Temperature
$T_{1/2}$	Transition temperature
T_{LIESST}	Critical temperature for the LIESST effect
U	Internal energy of a system (thermodynamic)
V	Sample voltage
V_{Th}	Sample-voltage threshold (see Sec. 14.3.2 for definition)
$w_{IS \to FS}$	Switching rate from initial state (IS) to final state (FS) given by the transition-state theory

Acronyms

AF	antiferromagnetic
AFM	atomic force microscopy
AES	Auger electron spectroscopy
CIP	current in plane
CPP	current perpendicular to plane
CITS	current-imaging tunneling spectroscopy
DEIMOS	dichroism experimental installation for magneto-optical spectroscopy
DFT	density functional theory
DOS	density of states
EB	exchange bias
Fe-phen	$Fe(phen)_2(NCS)_2$
FM	ferromagnetic
fwhm	full with at half maximum
GMR	giant magnetoresistance
HOMO	highest-occupied molecular orbital
HOPG	highly-oriented pyrolytic graphite
HS	high spin
IEC	interlayer exchange coupling
IETS	inelastic electron tunneling spectroscopy
IPCMS	institut de physique et chimie des matériaux de Strasbourg
LDOS	local density of states
LEED	low energy electron diffraction

LFT	ligand field theory
LIESST	light-induced excited spin-state trapping
LUMO	lowest-unoccupied molecular orbital
LH	linear horizontal
LS	low spin
LT	low temperature
LV	linear vertical
MBE	molecular beam epitaxy
ML	monolayer
MnPc	manganese phthalocyanine
MOKE	magneto-optical Kerr effect
MR	magnetoresistance
MLCT	metal-ligand charge transfer
NEXAFS	near edge X-ray absorption fine structure
OSCs	organic semiconductors
Pc	phthalocyanine
phen	phenanthroline
QWS	quantum well state
RT	room temperature
SCO	spin crossover
SOLEIL	source optimisée de lumière d'énergie intermédiaire du Lure
SPM	scanning probe microscope
STS	scanning tunneling spectroscopy
STM	scanning tunneling microscopy
SOXIESST	soft X-ray induced excited spin-state trapping
TMR	tunneling magnetoresistance
UHV	ultra-high vacuum
XAS	X-ray absorption spectroscopy
XMCD	X-ray magnetic circular dichroism
XNLD	X-ray natural linear dichroism

Bibliography

[1] V. Alek Dediu, Luis E. Hueso, Ilaria Bergenti, and Carlo Taliani. Spin routes in organic semiconductors. *Nature Materials*, 8(9):707–716, 2009.

[2] Marc Warner, Salahud Din, Igor S. Tupitsyn, Gavin W. Morley, A. Marshall Stoneham, Jules A. Gardener, Zhenlin Wu, Andrew J. Fisher, Sandrine Heutz, Christopher W. M. Kay, and Gabriel Aeppli. Potential for spin-based information processing in a thin-film molecular semiconductor. *Nature*, 503(7477):504–508, 2013.

[3] Stefano Sanvito. Molecular spintronics. *Chemical Society Reviews*, 40(6):3336–3355, 2011.

[4] Clément Barraud, Pierre Seneor, Richard Mattana, Stéphane Fusil, Karim Bouzehouane, Cyrile Deranlot, Patrizio Graziosi, Luis Hueso, Ilaria Bergenti, Valentin Dediu, Frédéric Petroff, and Albert Fert. Unravelling the role of the interface for spin injection into organic semiconductors. *Nature Physics*, 6(8):615–620, 2010.

[5] S. Javaid, M. Bowen, S. Boukari, L. Joly, J.-B. Beaufrand, Xi Chen, Y. J. Dappe, F. Scheurer, J.-P. Kappler, J. Arabski, W. Wulfhekel, M. Alouani, and E. Beaurepaire. Impact on Interface Spin Polarization of Molecular Bonding to Metallic Surfaces. *Physical Review Letters*, 105(7):077201, 2010.

[6] F. Djeghloul, F. Ibrahim, M. Cantoni, M. Bowen, L. Joly, S. Boukari, P. Ohresser, F. Bertran, P. Le Fèvre, P. Thakur, F. Scheurer, T. Miyamachi, R. Mattana, P. Seneor, A. Jaafar, C. Rinaldi, S. Javaid, J. Arabski, J.-P. Kappler, W. Wulfhekel, N. B. Brookes, R. Bertacco, A. Taleb-Ibrahimi, M. Alouani, E. Beaurepaire, and W. Weber. Direct observation of a highly spin-polarized organic spinterface at room temperature. *Scientific Reports*, 3, 2013.

[7] S. Javaid, S. Lebègue, B. Detlefs, F. Ibrahim, F. Djeghloul, M. Bowen, S. Boukari, T. Miyamachi, J. Arabski, D. Spor, J. Zegenhagen, W. Wulfhekel, W. Weber,

E. Beaurepaire, and M. Alouani. Chemisorption of manganese phthalocyanine on Cu(001) surface promoted by van der Waals interactions. *Physical Review B*, 87(15):155418, 2013.

[8] James E. House. *Inorganic Chemistry*. Elsevier, 2008.

[9] Gary L. Miessler and Donald A. Tarr. *Inorganic chemistry*. Prentice Hall, 3rd edition, 2003.

[10] Andreas Hauser. Ligand Field Theoretical Considerations. In P. Gütlich and H. A. Goodwin, editors, *Spin Crossover in Transition Metal Compounds I*, number 233 in Topics in Current Chemistry, pages 49–58. Springer Berlin Heidelberg, 2004.

[11] W. H. Meiklejohn and C. P. Bean. New Magnetic Anisotropy. *Physical Review*, 102(5):1413–1414, 1956.

[12] W. H. Meiklejohn and C. P. Bean. New Magnetic Anisotropy. *Physical Review*, 105(3):904–913, 1957.

[13] J Nogués and Ivan K Schuller. Exchange bias. *Journal of Magnetism and Magnetic Materials*, 192(2):203–232, 1999.

[14] R. L. Stamps. Mechanisms for exchange bias. *Journal of Physics D: Applied Physics*, 33(23):R247, 2000.

[15] J. Nogués, J. Sort, V. Langlais, V. Skumryev, S. Suriñach, J. S. Muñoz, and M. D. Baró. Exchange bias in nanostructures. *Physics Reports*, 422(3):65–117, 2005.

[16] Florin Radu. *Fundamental Aspects of Exchange Bias Effect in AF/F Bilayers and Multilayers*. PhD thesis, Ruhr-Universität Buchum, 2005.

[17] C. Leighton, J. Nogués, Harry Suhl, and Ivan K. Schuller. Competing interfacial exchange and Zeeman energies in exchange biased bilayers. *Physical Review B*, 60(18):12837–12840, 1999.

[18] J. Nogués, D. Lederman, T. J. Moran, and Ivan K. Schuller. Positive Exchange Bias in FeF2-Fe Bilayers. *Physical Review Letters*, 76(24):4624–4627, 1996.

[19] T. Gredig, I. N. Krivorotov, P. Eames, and E. D. Dahlberg. Unidirectional coercivity enhancement in exchange-biased Co/CoO. *Applied Physics Letters*, 81(7):1270–1272, 2002.

[20] F. Radu, M. Etzkorn, R. Siebrecht, T. Schmitte, K. Westerholt, and H. Zabel. Interfacial domain formation during magnetization reversal in exchange-biased CoO/co bilayers. *Physical Review B*, 67(13):134409, 2003.

[21] E. C. Stoner and E. P. Wohlfarth. A Mechanism of Magnetic Hysteresis in Heterogeneous Alloys. *Philosophical Transactions of the Royal Society of London. Series A, Mathematical and Physical Sciences*, 240(826):599–642, 1948.

[22] Andreas Biternas. *Study of the training effect in exchange bias using the domain state model*. PhD thesis, University of York, 2009.

[23] Miguel Kiwi. Exchange bias theory. *Journal of Magnetism and Magnetic Materials*, 234(3):584–595, 2001.

[24] W. H. Meiklejohn. Exchange Anisotropy—a Review. *Journal of Applied Physics*, 33(3):1328–1335, 1962.

[25] R. Jungblut, R. Coehoorn, M. T. Johnson, J. aan de Stegge, and A. Reinders. Orientational dependence of the exchange biasing in molecular-beam-epitaxy-grown $Ni_{80}Fe_{20}/Fe_{50}Mn_{50}$ bilayers (invited). *Journal of Applied Physics*, 75(10):6659–6664, 1994.

[26] M. B. Salamon, Shantanu Sinha, J. J. Rhyne, J. E. Cunningham, Ross W. Erwin, Julie Borchers, and C. P. Flynn. Long-range incommensurate magnetic order in a Dy-Y multilayer. *Physical Review Letters*, 56(3):259–262, 1986.

[27] C. F. Majkrzak, J. W. Cable, J. Kwo, M. Hong, D. B. McWhan, Y. Yafet, J. V. Waszczak, and C. Vettier. Observation of a Magnetic Antiphase Domain Structure with Long-Range Order in a Synthetic Gd-Y Superlattice. *Physical Review Letters*, 56(25):2700–2703, 1986.

[28] P. Grünberg, R. Schreiber, Y. Pang, M. B. Brodsky, and H. Sowers. Layered Magnetic Structures: Evidence for Antiferromagnetic Coupling of Fe Layers across Cr Interlayers. *Physical Review Letters*, 57(19):2442–2445, 1986.

[29] S. S. P. Parkin, N. More, and K. P. Roche. Oscillations in exchange coupling and magnetoresistance in metallic superlattice structures: Co/Ru, Co/Cr, and Fe/Cr. *Physical Review Letters*, 64(19):2304–2307, 1990.

[30] S. S. P. Parkin. Systematic variation of the strength and oscillation period of indirect magnetic exchange coupling through the 3d, 4d, and 5d transition metals. *Physical Review Letters*, 67(25):3598–3601, 1991.

[31] Patrick Bruno. Quantum Size Effects and Related Phenomenon in Magnetic Ultrathin Films and Multilayers. In Éric Beaurepaire, Bernard Carrière, and Jean-Paul Kappler, editors, *Magnetism and synchrotron radiation: Mittelwihr, 1996 : lectures notes*. les Éd. de physique, 1997.

[32] S. S. P. Parkin and D. Mauri. Spin engineering: Direct determination of the Ruderman-Kittel-Kasuya-Yosida far-field range function in ruthenium. *Physical Review B*, 44(13):7131–7134, 1991.

[33] P. Bruno. Theory of interlayer magnetic coupling. *Physical Review B*, 52(1):411–439, 1995.

[34] Z. Q. Qiu and N. V. Smith. Quantum well states and oscillatory magnetic interlayer coupling. *Journal of Physics: Condensed Matter*, 14(8):R169, 2002.

[35] P. Bruno. Interlayer exchange coupling: a unified physical picture. *Journal of Magnetism and Magnetic Materials*, 121(1–3):248–252, 1993.

[36] P. Bruno and C. Chappert. Oscillatory coupling between ferromagnetic layers separated by a nonmagnetic metal spacer. *Physical Review Letters*, 67(12):1602–1605, 1991.

[37] Weber Wolfgang. Introduction to Magnetism. In Éric Beaurepaire, Hervé Bulou, Fabrice Scheurer, and Jean-Paul Kappler, editors, *Magnetism and Synchrotron*

Radiation. Sringer-Verlag, 2010.

[38] W. Meissner and B. Voigt. Messungen mit Hilfe von flüssigem Helium XI Widerstand der reinen Metalle in tiefen Temperaturen. *Annalen der Physik*, 399(8):892–936, 1930.

[39] W. J. de Haas, J. de Boer, and G. J. van dën Berg. The electrical resistance of gold, copper and lead at low temperatures. *Physica*, 1(7–12):1115–1124, 1934.

[40] Jun Kondo. Resistance Minimum in Dilute Magnetic Alloys. *Progress of Theoretical Physics*, 32(1):37–49, 1964.

[41] A. C. Hewson. *he Kondo problem to heavy fermions.* Cambridge university press, 1993.

[42] Steffen Kahle. *Magnetic Properties of Individual Molecules Studied by Scanning Tunneling Microscopy.* PhD thesis, Universität Konstanz, 2013.

[43] Kenneth G. Wilson. The renormalization group: Critical phenomena and the Kondo problem. *Reviews of Modern Physics*, 47(4):773–840, 1975.

[44] D. Goldhaber-Gordon, H. Shtrikman, D. Mahalu, D. Abusch-Magder, U. Meirav, and M. A. Kastner. Kondo effect in a single-electron transistor. *Nature*, 391(6663):156–159, 1998.

[45] Sara M. Cronenwett, Tjerk H. Oosterkamp, and Leo P. Kouwenhoven. A Tunable Kondo Effect in Quantum Dots. *Science*, 281(5376):540–544, 1998. PMID: 9677192.

[46] L. Kouwenhoven and L. Glazman. Revival of the Kondo effect. *arXiv preprint cond-mat/0104100*, 2001.

[47] Jiutao Li, Wolf-Dieter Schneider, Richard Berndt, and Bernard Delley. Kondo Scattering Observed at a Single Magnetic Impurity. *Physical Review Letters*, 80(13):2893–2896, 1998.

[48] V. Madhavan, W. Chen, T. Jamneala, M. F. Crommie, and N. S. Wingreen. Tunneling into a Single Magnetic Atom: Spectroscopic Evidence of the Kondo Resonance. *Science*, 280(5363):567–569, 1998. PMID: 9554843.

[49] H. C. Manoharan, C. P. Lutz, and D. M. Eigler. Quantum mirages formed by coherent projection of electronic structure. *Nature*, 403(6769):512–515, 2000.

[50] K. Nagaoka, T. Jamneala, M. Grobis, and M. F. Crommie. Temperature dependence of a single Kondo impurity. *Physical review letters*, 88(7):77205, 2002.

[51] P. Wahl, L. Diekhöner, M. A. Schneider, L. Vitali, G. Wittich, and K. Kern. Kondo temperature of magnetic impurities at surfaces. *Physical review letters*, 93(17):176603, 2004.

[52] A. F. Otte, M. Ternes, K. Von Bergmann, S. Loth, H. Brune, C. P. Lutz, C. F. Hirjibehedin, and A. J. Heinrich. The role of magnetic anisotropy in the Kondo effect. *Nature physics*, 4(11):847–850, 2008.

[53] Aidi Zhao, Qunxiang Li, Lan Chen, Hongjun Xiang, Weihua Wang, Shuan Pan, Bing Wang, Xudong Xiao, Jinlong Yang, J. G. Hou, and Qingshi Zhu. Controlling

the Kondo Effect of an Adsorbed Magnetic Ion Through Its Chemical Bonding. *Science*, 309(5740):1542–1544, 2005. PMID: 16141069.

[54] Violeta Iancu, Aparna Deshpande, and Saw-Wai Hla. Manipulating Kondo Temperature via Single Molecule Switching. *Nano Letters*, 6(4):820–823, 2006.

[55] Aidi Zhao, Zhenpeng Hu, Bing Wang, Xudong Xiao, Jinlong Yang, and J. G. Hou. Kondo effect in single cobalt phthalocyanine molecules adsorbed on Au(111) monoatomic steps. *The Journal of Chemical Physics*, 128(23):234705, 2008.

[56] U. G. E. Perera, H. J. Kulik, V. Iancu, L. G. G. V. Dias da Silva, S. E. Ulloa, N. Marzari, and S.-W. Hla. Spatially Extended Kondo State in Magnetic Molecules Induced by Interfacial Charge Transfer. *Physical Review Letters*, 105(10):106601, 2010.

[57] K. J. Franke, G. Schulze, and J. I. Pascual. Competition of Superconducting Phenomena and Kondo Screening at the Nanoscale. *Science*, 332(6032):940–944, 2011. PMID: 21596987.

[58] N. Tsukahara, S. Shiraki, S. Itou, N. Ohta, N. Takagi, and M. Kawai. Evolution of Kondo Resonance from a Single Impurity Molecule to the Two-Dimensional Lattice. *Physical review letters*, 106(18):187201, 2011.

[59] I. Fernández-Torrente, K. J. Franke, and J. I. Pascual. Vibrational Kondo Effect in Pure Organic Charge-Transfer Assemblies. *Physical Review Letters*, 101(21):217203, 2008.

[60] R. Temirov, A. Lassise, F. B. Anders, and F. S. Tautz. Kondo effect by controlled cleavage of a single-molecule contact. *Nanotechnology*, 19(6):065401, 2008.

[61] Yong-hui Zhang, Steffen Kahle, Tobias Herden, Christophe Stroh, Marcel Mayor, Uta Schlickum, Markus Ternes, Peter Wahl, and Klaus Kern. Temperature and magnetic field dependence of a Kondo system in the weak coupling regime. *Nature Communications*, 4, 2013.

[62] M. Ternes, A. J. Heinrich, and W. D. Schneider. Spectroscopic manifestations of the Kondo effect on single adatoms. *Journal of Physics: Condensed Matter*, 21(5):053001, 2008.

[63] Markus Ternes. *Scanning tunneling spectroscopy at the single atom scale*. PhD thesis, ÉCOLE POLYTECHNIQUE FÉDÉRALE DE LAUSANNE, 2006.

[64] A. M. Chang and J. C. Chen. The Kondo effect in coupled-quantum dots. *Reports on Progress in Physics*, 72(9):096501, 2009.

[65] Barbara A. Jones. The kondo effect. In Helmut Kronmüller and Stuart Parkin, editors, *Handbook of Magnetism and Advanced Magnetic Materials*. John Wiley & Sons, 2007.

[66] P. W. Anderson. Localized Magnetic States in Metals. *Physical Review*, 124(1):41–53, 1961.

[67] J. R. Schrieffer and P. A. Wolff. Relation between the Anderson and Kondo Hamiltonians. *Physical Review*, 149(2):491–492, 1966.

[68] L. Limot and R. Berndt. Kondo effect and surface-state electrons. *Applied Surface Science*, 237(1–4):572–576, 2004.

[69] U. Fano. Effects of Configuration Interaction on Intensities and Phase Shifts. *Physical Review*, 124(6):1866–1878, 1961.

[70] M. Plihal and J. W. Gadzuk. Nonequilibrium theory of scanning tunneling spectroscopy via adsorbate resonances: Nonmagnetic and Kondo impurities. *Physical Review B*, 63(8):085404, 2001.

[71] T. Jamneala, V. Madhavan, W. Chen, and M. F. Crommie. Scanning tunneling spectroscopy of transition-metal impurities at the surface of gold. *Physical Review B*, 61(15):9990–9993, 2000.

[72] Ying-Shuang Fu, Shuai-Hua Ji, Xi Chen, Xu-Cun Ma, Rui Wu, Chen-Chen Wang, Wen-Hui Duan, Xiao-Hui Qiu, Bo Sun, Ping Zhang, Jin-Feng Jia, and Qi-Kun Xue. Manipulating the Kondo Resonance through Quantum Size Effects. *Physical Review Letters*, 99(25):256601, 2007.

[73] Henning Prüser, Martin Wenderoth, Piet E. Dargel, Alexander Weismann, Robert Peters, Thomas Pruschke, and Rainer G. Ulbrich. Long-range Kondo signature of a single magnetic impurity. *Nature Physics*, 7(3):203–206, 2011.

[74] H. Prüser, M. Wenderoth, A. Weismann, and R. G. Ulbrich. Mapping Itinerant Electrons around Kondo Impurities. *Physical Review Letters*, 108(16):166604, 2012.

[75] D. J. Choi, M. V. Rastei, P. Simon, and L. Limot. Conductance-Driven Change of the Kondo Effect in a Single Cobalt Atom. *Physical Review Letters*, 108(26):266803, 2012.

[76] H. O. Frota and L. N. Oliveira. Photoemission spectroscopy for the spin-degenerate Anderson model. *Physical Review B*, 33(11):7871–7874, 1986.

[77] H. O. Frota. Shape of the Kondo resonance. *Physical Review B*, 45(3):1096–1099, 1992.

[78] T. A. Costi. Kondo Effect in a Magnetic Field and the Magnetoresistivity of Kondo Alloys. *Physical Review Letters*, 85(7):1504–1507, 2000.

[79] A. J. Heinrich, J. A. Gupta, C. P. Lutz, and D. M. Eigler. Single-Atom Spin-Flip Spectroscopy. *Science*, 306(5695):466–469, 2004.

[80] A. F. Otte, M. Ternes, S. Loth, C. P. Lutz, C. F. Hirjibehedin, and A. J. Heinrich. Spin excitations of a Kondo-screened atom coupled to a second magnetic atom. *Physical review letters*, 103(10):107203, 2009.

[81] P. Wahl, P. Simon, L. Diekhöner, V. S. Stepanyuk, P. Bruno, M. A. Schneider, and K. Kern. Exchange interaction between single magnetic adatoms. *Physical review letters*, 98(5):56601, 2007.

[82] Y. S. Fu, Q. K. Xue, and R. Wiesendanger. Spin-Resolved Splitting of Kondo Resonances in the Presence of RKKY-Type Coupling. *Physical Review Letters*, 108(8):87203, 2012.

[83] Christian Felix Hermanns. *X-ray absorption studies of metalloporphyrin molecules*

on surfaces: Electronic interactions, magnetic coupling, and chemical switches. PhD thesis, Freie Universität Berlin, 2013.

[84] Joachim Stöhr and Hans Christoph Siegmann. *Magnetism From Fundamentals to Nanoscale Dynamics.* Springer-Verlag Berlin Heidelberg, 2006.

[85] J. Stöhr. *NEXAFS Spectroscopy.* Springer. Springer Series in Surface Sciences, 1996.

[86] Reiko Nakajima, J. Stöhr, and Y. U. Idzerda. Electron-yield saturation effects in L-edge x-ray magnetic circular dichroism spectra of Fe, Co, and Ni. *Physical Review B*, 59(9):6421–6429, 1999.

[87] J. Lüning, F. Nolting, A. Scholl, H. Ohldag, J. W. Seo, J. Fompeyrine, J.-P. Locquet, and J. Stöhr. Determination of the antiferromagnetic spin axis in epitaxial LaFeO$_3$ films by x-ray magnetic linear dichroism spectroscopy. *Physical Review B*, 67(21):214433, 2003.

[88] W. L. O'Brien and B. P. Tonner. Orbital and spin sum rules in x-ray magnetic circular dichroism. *Physical Review B*, 50(17):12672–12681, 1994.

[89] T. J. Regan, H. Ohldag, C. Stamm, F. Nolting, J. Lüning, J. Stöhr, and R. L. White. Chemical effects at metal/oxide interfaces studied by x-ray-absorption spectroscopy. *Physical Review B*, 64(21):214422, 2001.

[90] G. van der Laan, B. T. Thole, G. A. Sawatzky, and M. Verdaguer. Multiplet structure in the L2,3 x-ray-absorption spectra: A fingerprint for high- and low-spin Ni2+ compounds. *Physical Review B*, 37(11):6587–6589, 1988.

[91] P. Sainctavit and M.-A. Arrio. Ligand Field Multiplet Theory Applied to the Caculation of X-ray Absorption Spectra. In Éric Beaurepaire, Bernard Carrière, and Jean-Paul Kappler, editors, *Magnetism and synchrotron radiation: Mittelwihr, 1996 : lectures notes.* les Éd. de physique, 1997.

[92] Frank de Groot. Multiplet effects in X-ray spectroscopy. *Coordination Chemistry Reviews*, 249(1–2):31–63, 2005.

[93] Eli Stavitski and Frank M. F. de Groot. The CTM4XAS program for EELS and XAS spectral shape analysis of transition metal L edges. *Micron*, 41(7):687–694, 2010.

[94] A. Lodi Rizzini, C. Krull, T. Balashov, J. J. Kavich, A. Mugarza, P. S. Miedema, P. K. Thakur, V. Sessi, S. Klyatskaya, M. Ruben, S. Stepanow, and P. Gambardella. Coupling Single Molecule Magnets to Ferromagnetic Substrates. *Physical Review Letters*, 107(17):177205, 2011.

[95] J. L. Erskine and E. A. Stern. Calculation of the M$_{23}$ magneto-optical absorption spectrum of ferromagnetic nickel. *Physical Review B*, 12(11):5016–5024, 1975.

[96] G. Schütz, W. Wagner, W. Wilhelm, P. Kienle, R. Zeller, R. Frahm, and G. Materlik. Absorption of circularly polarized x rays in iron. *Physical Review Letters*, 58(7):737–740, 1987.

[97] Paolo Carra, B. T. Thole, Massimo Altarelli, and Xindong Wang. X-ray circular

dichroism and local magnetic fields. *Physical Review Letters*, 70(5):694–697, 1993.

[98] C. T. Chen, Y. U. Idzerda, H. J. Lin, N. V. Smith, G. Meigs, E. Chaban, G. H. Ho, E. Pellegrin, and F. Sette. Experimental confirmation of the X-ray magnetic circular dichroism sum rules for iron and cobalt. *Physical review letters*, 75(1):152–155, 1995.

[99] J. Ph. Schillé, J. P. Kappler, Ph. Sainctavit, Ch. Cartier dit Moulin, C. Brouder, and G. Krill. Experimental and calculated magnetic dichroism in the Ho 3d x-ray-absorption spectra of intermetallic \mathrmHoCo$_2$. *Physical Review B*, 48(13):9491–9496, 1993.

[100] J. Stöhr. X-ray magnetic circular dichroism spectroscopy of transition metal thin films. *Journal of Electron Spectroscopy and Related Phenomena*, 75:253–272, 1995.

[101] Russell Young, John Ward, and Fredric Scire. The Topografiner: An Instrument for Measuring Surface Microtopography. *Review of Scientific Instruments*, 43(7):999–1011, 1972.

[102] G. Binnig, H. Rohrer, Ch Gerber, and E. Weibel. Tunneling through a controllable vacuum gap. *Applied Physics Letters*, 40(2):178–180, 1982.

[103] G. Binnig, H. Rohrer, Ch. Gerber, and E. Weibel. Surface Studies by Scanning Tunneling Microscopy. *Physical Review Letters*, 49(1):57–61, 1982.

[104] Claude Cohen-Tannoudji, Bernard Diu, and Franck Laloe. *Quantum Mechanics Vol. 1*. Hermann, 1977.

[105] Michael Schackert. *Scanning Tunneling Spectroscopy on Electron-Boson Interactions in Superconductors*. PhD thesis, Fakultät für Physik des Karlsruher Instituts für Technologie, 2014.

[106] J. Bardeen. Tunnelling from a Many-Particle Point of View. *Physical Review Letters*, 6(2):57–59, 1961.

[107] C. Julian Chen. *Introduction to Scanning Tunneling Microscopy*. Oxford University Press, 1993.

[108] J. Tersoff and D. R. Hamann. Theory and Application for the Scanning Tunneling Microscope. *Physical Review Letters*, 50(25):1998–2001, 1983.

[109] J. Tersoff and D. R. Hamann. Theory of the scanning tunneling microscope. *Physical Review B*, 31(2):805, 1985.

[110] Vladimir A. Ukraintsev. Data evaluation technique for electron-tunneling spectroscopy. *Physical Review B*, 53(16):11176–11185, 1996.

[111] T. E. Feuchtwang and P. H. Cutler. Tunneling and scanning tunnel microscopy: A critical review. *Physica Scripta*, 35(2):132, 2006.

[112] M. Ziegler, N. Néel, A. Sperl, J. Kröger, and R. Berndt. Local density of states from constant-current tunneling spectra. *Physical Review B*, 80(12):125402, 2009.

[113] Y. Yamagishi, S. Nakashima, K. Oiso, and T. K. Yamada. Recovery of nanomolecular electronic states from tunneling spectroscopy: LDOS of low-dimensional phthalocyanine molecular structures on Cu(111). *Nanotechnology*, 24(39):395704,

2013.

[114] B. C. Stipe, M. A. Rezaei, and W. Ho. Single-Molecule Vibrational Spectroscopy and Microscopy. *Science*, 280(5370):1732–1735, 1998.

[115] P. Gambardella, S. Rusponi, M. Veronese, S. S. Dhesi, C. Grazioli, A. Dallmeyer, I. Cabria, R. Zeller, P. H. Dederichs, K. Kern, C. Carbone, and H. Brune. Giant Magnetic Anisotropy of Single Cobalt Atoms and Nanoparticles. *Science*, 300(5622):1130–1133, 2003. PMID: 12750516.

[116] T. Balashov, T. Schuh, A. F. Takács, A. Ernst, S. Ostanin, J. Henk, I. Mertig, P. Bruno, T. Miyamachi, S. Suga, and W. Wulfhekel. Magnetic Anisotropy and Magnetization Dynamics of Individual Atoms and Clusters of Fe and Co on Pt(111). *Physical Review Letters*, 102(25):257203, 2009.

[117] Tobias Schuh, Toshio Miyamachi, Stefan Gerstl, Matthias Geilhufe, Martin Hoffmann, Sergey Ostanin, Wolfram Hergert, Arthur Ernst, and Wulf Wulfhekel. Magnetic Excitations of Rare Earth Atoms and Clusters on Metallic Surfaces. *Nano Letters*, 12(9):4805–4809, 2012.

[118] Toshio Miyamachi, Tobias Schuh, Tobias Märkl, Christopher Bresch, Timofey Balashov, Alexander Stöhr, Christian Karlewski, Stephan André, Michael Marthaler, Martin Hoffmann, Matthias Geilhufe, Sergey Ostanin, Wolfram Hergert, Ingrid Mertig, Gerd Schön, Arthur Ernst, and Wulf Wulfhekel. Stabilizing the magnetic moment of single holmium atoms by symmetry. *Nature*, 503(7475):242–246, 2013.

[119] C. L. Gao, A. Ernst, G. Fischer, W. Hergert, P. Bruno, W. Wulfhekel, and J. Kirschner. Spin Wave Dispersion on the Nanometer Scale. *Physical Review Letters*, 101(16):167201, 2008.

[120] T. Balashov, A. F. Takács, M. Däne, A. Ernst, P. Bruno, and W. Wulfhekel. Inelastic electron-magnon interaction and spin transfer torque. *Physical Review B*, 78(17):174404, 2008.

[121] S. Monturet and N. Lorente. Inelastic effects in electron transport studied with wave packet propagation. *Physical Review B*, 78(3):035445, 2008.

[122] Stefan Schmaus. *Spintronics with individual metal-organic molecules*. PhD thesis, Fakultät für Physik des Karlsruher Instituts für Technologie, 2010.

[123] Harald Ibach. *Physics of Surfaces and Interfaces*. Springer, 2006.

[124] J. Kirschner, H. Engelhard, and D. Hartung. An evaporation source for ion beam assisted deposition in ultrahigh vacuum. *Review of Scientific Instruments*, 73(11):3853–3860, 2002.

[125] L. Zhang, T. Miyamachi, T. Tomanić, R. Dehm, and W. Wulfhekel. A compact sub-Kelvin ultrahigh vacuum scanning tunneling microscope with high energy resolution and high stability. *Review of Scientific Instruments*, 82(10):103702–103702–8, 2011.

[126] Lei Zhang. *Sub-Kelvin scanning tunneling microscopy on magnetic molecules*. PhD thesis, Fakultät für Physik des Karlsruher Instituts für Technologie, 2012.

[127] Timofey Balashov. *Inelastic scanning tunneling spectroscopy : magnetic excitations on the nanoscale*. PhD thesis, Fakultät für Physik der Universität Karlsruhe (TH), 2009.

[128] Lukas Gerhard. *Magnetoelectric coupling at metal surfaces*. PhD thesis, Fakultät für Physik des Karlsruher Instituts für Technologie, 2012.

[129] R. Garcia and R. Perez. Dynamic atomic force microscopy methods. *Surface science reports*, 47(6):197–301, 2002.

[130] Franz J. Giessibl. High-speed force sensor for force microscopy and profilometry utilizing a quartz tuning fork. *Applied Physics Letters*, 73(26):3956–3958, 1998.

[131] Franz J. Giessibl. Advances in atomic force microscopy. *Reviews of Modern Physics*, 75(3):949–983, 2003.

[132] M. Nonnenmacher, M. P. Oboyle, and H. K. Wickramasinghe. Kelvin probe force microscopy. *Applied Physics Letters*, 58(25):2921–2923, 1991.

[133] W. Melitz, J. Shen, A. C. Kummel, and S. Lee. Kelvin probe force microscopy and its application. *Surface Science Reports*, 66(1):1–27, 2011.

[134] P. Ohresser, E. Otero, F. Choueikani, K. Chen, S. Stanescu, F. Deschamps, T. Moreno, F. Polack, B. Lagarde, J.-P. Daguerre, F. Marteau, F. Scheurer, L. Joly, J.-P. Kappler, B. Muller, O. Bunau, and Ph Sainctavit. DEIMOS: A beamline dedicated to dichroism measurements in the 350–2500 eV energy range. *Review of Scientific Instruments*, 85(1):013106, 2014.

[135] L. Joly, E. Otero, F. Choueikani, F. Marteau, L. Chapuis, and P. Ohresser. Fast continuous energy scan with dynamic coupling of the monochromator and undulator at the DEIMOS beamline. *Journal of Synchrotron Radiation*, 21(3):502–506, 2014.

[136] Stefan Blügel, Daniel Bürgler, Markus Morgenstern, Claus Schneider, and Rainer Waser. *Spintronics - from GMR to quantum information*. Forschungszentrum, Zentralbibliothek, Jülich, 2009.

[137] Igor Zutić, Jaroslav Fabian, and S. Das Sarma. Spintronics: Fundamentals and applications. *Reviews of Modern Physics*, 76(2):323, 2004.

[138] Sarah M. Thompson. The discovery, development and future of GMR: The Nobel Prize 2007. *Journal of Physics D: Applied Physics*, 41(9):093001, 2008.

[139] Saqib Javaid. *Magnetism and Electronic Structure at Hybrid Manganese-Phthalocyanine/Metal Interfaces*. PhD thesis, Strasbourg, 2011.

[140] Jean-Baptiste Beaufrand. *Couches minces de Phthalocyanine, de l'électronique organique vers l'électronic moléculaire*. PhD thesis, University of Strasbourg, 2011.

[141] Nabil Najari. *Basculement électrique dans des jonctions tunnel magnétiques à base de MgO*. PhD thesis, University of Strasbourg, 2011.

[142] Robert L. Stamps, Stephan Breitkreutz, Johan Åkerman, Andrii V. Chumak, YoshiChika Otani, Gerrit E. W. Bauer, Jan-Ulrich Thiele, Martin Bowen, Sara A. Majetich, Mathias Kläui, Ioan Lucian Prejbeanu, Bernard Dieny, Nora M. Dempsey, and Burkard Hillebrands. The 2014 Magnetism Roadmap. *Journal of*

Physics D: Applied Physics, 47(33):333001, 2014.

[143] M. N. Baibich, J. M. Broto, A. Fert, F. Nguyen Van Dau, F. Petroff, P. Etienne, G. Creuzet, A. Friederich, and J. Chazelas. Giant Magnetoresistance of (001)Fe/(001)Cr Magnetic Superlattices. *Physical Review Letters*, 61(21):2472–2475, 1988.

[144] G. Binasch, P. Grünberg, F. Saurenbach, and W. Zinn. Enhanced magnetoresistance in layered magnetic structures with antiferromagnetic interlayer exchange. *Physical Review B*, 39(7):4828–4830, 1989.

[145] N. F. Mott. The Electrical Conductivity of Transition Metals. *Proceedings of the Royal Society of London. Series A - Mathematical and Physical Sciences*, 153(880):699–717, 1936.

[146] N. F. Mott. The Resistance and Thermoelectric Properties of the Transition Metals. *Proceedings of the Royal Society of London. Series A - Mathematical and Physical Sciences*, 156(888):368–382, 1936.

[147] T. Valet and A. Fert. Theory of the perpendicular magnetoresistance in magnetic multilayers. *Physical Review B*, 48(10):7099–7113, 1993.

[148] W. J. M. Naber, S. Faez, and W. G. van der Wiel. Organic spintronics. *Journal of Physics D: Applied Physics*, 40(12):R205, 2007.

[149] A. Fert and H. Jaffrès. Conditions for efficient spin injection from a ferromagnetic metal into a semiconductor. *Physical Review B*, 64(18):184420, 2001.

[150] A Fert, J. M George, H. Jaffres, and R. Mattana. Semiconductors Between Spin-Polarized Sources and Drains. *IEEE Transactions on Electron Devices*, 54(5):921–932, 2007.

[151] M. Julliere. Tunneling between ferromagnetic films. *Physics Letters A*, 54(3):225–226, 1975.

[152] J. S. Moodera, Lisa R. Kinder, Terrilyn M. Wong, and R. Meservey. Large Magnetoresistance at Room Temperature in Ferromagnetic Thin Film Tunnel Junctions. *Physical Review Letters*, 74(16):3273–3276, 1995.

[153] T. Yaoi, S. Ishio, and T. Miyazaki. Dependence of magnetoresistance on temperature and applied voltage in a Ni-Fe/Al-Al$_2$O$_3$/Co tunneling junction. *Journal of Magnetism and Magnetic Materials*, 126(1–3):430–432, 1993.

[154] Stuart S. P. Parkin, Christian Kaiser, Alex Panchula, Philip M. Rice, Brian Hughes, Mahesh Samant, and See-Hun Yang. Giant tunnelling magnetoresistance at room temperature with MgO (100) tunnel barriers. *Nature Materials*, 3(12):862–867, 2004.

[155] Shinji Yuasa, Taro Nagahama, Akio Fukushima, Yoshishige Suzuki, and Koji Ando. Giant room-temperature magnetoresistance in single-crystal Fe/MgO/Fe magnetic tunnel junctions. *Nature Materials*, 3(12):868–871, 2004.

[156] W. H. Butler, X.-G. Zhang, T. C. Schulthess, and J. M. MacLaren. Spin-dependent tunneling conductance of Fe/MgO/Fe sandwiches. *Physical Review B*,

63(5):054416, 2001.

[157] X. G. Zhang and W. H. Butler. Band structure, evanescent states, and transport in spin tunnel junctions. *Journal of Physics: Condensed Matter*, 15(41):R1603, 2003.

[158] Manuel Bibes, Javier E. Villegas, and Agnès Barthélémy. Ultrathin oxide films and interfaces for electronics and spintronics. *Advances in Physics*, 60(1):5–84, 2011.

[159] S. Ikeda, J. Hayakawa, Y. Ashizawa, Y. M. Lee, K. Miura, H. Hasegawa, M. Tsunoda, F. Matsukura, and H. Ohno. Tunnel magnetoresistance of 604% at 300K by suppression of Ta diffusion in CoFeB/MgO/CoFeB pseudo-spin-valves annealed at high temperature. *Applied Physics Letters*, 93(8):082508, 2008.

[160] I. I. Mazin. How to Define and Calculate the Degree of Spin Polarization in Ferromagnets. *Physical Review Letters*, 83(7):1427–1430, 1999.

[161] J. M. D. Coey and S. Sanvito. Magnetic semiconductors and half-metals. *Journal of Physics D: Applied Physics*, 37(7):988, 2004.

[162] Jose Maria De Teresa, Agnès Barthélémy, Albert Fert, Jean Pierre Contour, François Montaigne, and Pierre Seneor. Role of Metal-Oxide Interface in Determining the Spin Polarization of Magnetic Tunnel Junctions. *Science*, 286(5439):507–509, 1999. PMID: 10521341.

[163] M. Bowen, M. Bibes, A. Barthélémy, J.-P. Contour, A. Anane, Y. Lemaı?tre, and A. Fert. Nearly total spin polarization in La2/3Sr1/3MnO3 from tunneling experiments. *Applied Physics Letters*, 82(2):233–235, 2003.

[164] R. H. Friend, R. W. Gymer, A. B. Holmes, J. H. Burroughes, R. N. Marks, C. Taliani, D. D. C. Bradley, D. A. Dos Santos, J. L. Brédas, M. Lögdlund, and W. R. Salaneck. Electroluminescence in conjugated polymers. *Nature*, 397(6715):121–128, 1999.

[165] Stefano Sanvito. Organic electronics: Spintronics goes plastic. *Nature Materials*, 6(11):803–804, 2007.

[166] Masashi Shiraishi and Tadaaki Ikoma. Molecular spintronics. *Physica E: Low-dimensional Systems and Nanostructures*, 43(7):1295–1317, 2011.

[167] Hongbo Gu, Xi Zhang, Huige Wei, Yudong Huang, Suying Wei, and Zhanhu Guo. An overview of the magnetoresistance phenomenon in molecular systems. *Chemical Society Reviews*, 42(13):5907–5943, 2013.

[168] C. B. Harris, R. L. Schlupp, and H. Schuch. Optically Detected Electron Spin Locking and Rotary Echo Trains in Molecular Excited States. *Physical Review Letters*, 30(21):1019–1022, 1973.

[169] V. I. Krinichnyi, S. D. Chemerisov, and Ya. S. Lebedev. EPR and charge-transport studies of polyaniline. *Physical Review B*, 55(24):16233–16244, 1997.

[170] Jung-Woo Yoo, Chia-Yi Chen, H. W. Jang, C. W. Bark, V. N. Prigodin, C. B. Eom, and A. J. Epstein. Spin injection/detection using an organic-based magnetic semiconductor. *Nature Materials*, 9(8):638–642, 2010.

[171] V. Dediu, M. Murgia, F. C. Matacotta, C. Taliani, and S. Barbanera. Room temperature spin polarized injection in organic semiconductor. *Solid State Communications*, 122(3–4):181–184, 2002.

[172] Z. H. Xiong, Di Wu, Z. Valy Vardeny, and Jing Shi. Giant magnetoresistance in organic spin-valves. *Nature*, 427(6977):821–824, 2004.

[173] C. W. Tang and S. A. VanSlyke. Organic electroluminescent diodes. *Applied Physics Letters*, 51(12):913–915, 1987.

[174] F. J. Wang, C. G. Yang, Z. Valy Vardeny, and X. G. Li. Spin response in organic spin valves based on $La_{2/3}Sr_{1/3}MnO_3$ electrodes. *Physical Review B*, 75(24):245324, 2007.

[175] A. Riminucci, I. Bergenti, L. E. Hueso, M. Murgia, C. Taliani, Y. Zhan, F. Casoli, M. P. de Jong, and V. Dediu. Negative Spin Valve effects in manganite/organic based devices. *arXiv:cond-mat/0701603*, 2007. arXiv: cond-mat/0701603.

[176] V. Dediu, L. E. Hueso, I. Bergenti, A. Riminucci, F. Borgatti, P. Graziosi, C. Newby, F. Casoli, M. P. De Jong, C. Taliani, and Y. Zhan. Room-temperature spintronic effects in Alq_3-based hybrid devices. *Physical Review B*, 78(11):115203, 2008.

[177] Sayani Majumdar, Himadri S. Majumdar, R. Laiho, and R. Österbacka. Comparing small molecules and polymer for future organic spin-valves. *Journal of Alloys and Compounds*, 423(1–2):169–171, 2006.

[178] W. Xu, G. J. Szulczewski, P. LeClair, I. Navarrete, R. Schad, G. Miao, H. Guo, and A. Gupta. Tunneling magnetoresistance observed in $La_{0.67}Sr_{0.33}MnO_3$/organic molecule/Co junctions. *Applied Physics Letters*, 90(7):072506, 2007.

[179] T. S. Santos, J. S. Lee, P. Migdal, I. C. Lekshmi, B. Satpati, and J. S. Moodera. Room-Temperature Tunnel Magnetoresistance and Spin-Polarized Tunneling through an Organic Semiconductor Barrier. *Physical Review Letters*, 98(1):016601, 2007.

[180] M. A. Baldo and S. R. Forrest. Interface-limited injection in amorphous organic semiconductors. *Physical Review B*, 64(8):085201, 2001.

[181] Paul S. Bagus, Volker Staemmler, and Christof Wöll. Exchangelike Effects for Closed-Shell Adsorbates: Interface Dipole and Work Function. *Physical Review Letters*, 89(9):096104, 2002.

[182] V. De Renzi, R. Rousseau, D. Marchetto, R. Biagi, S. Scandolo, and U. del Pennino. Metal Work-Function Changes Induced by Organic Adsorbates: A Combined Experimental and Theoretical Study. *Physical Review Letters*, 95(4):046804, 2005.

[183] Y. Q. Zhan, I. Bergenti, L. E. Hueso, V. Dediu, M. P. de Jong, and Z. S. Li. Alignment of energy levels at the $Alq_3/La_{0.7}Sr_{0.3}MnO_3$ interface for organic spintronic devices. *Physical Review B*, 76(4):045406, 2007.

[184] Hylke B. Akkerman, Ronald C. G. Naber, Bert Jongbloed, Paul A. van Hal, Paul W. M. Blom, Dago M. de Leeuw, and Bert de Boer. Electron tunneling through

alkanedithiol self-assembled monolayers in large-area molecular junctions. *Proceedings of the National Academy of Sciences*, 104(27):11161–11166, 2007. PMID: 17592120.

[185] Y. Q. Zhan, M. P. de Jong, F. H. Li, V. Dediu, M. Fahlman, and W. R. Salaneck. Energy level alignment and chemical interaction at Alq_3/Co interfaces for organic spintronic devices. *Physical Review B*, 78(4):045208, 2008.

[186] Y. Q. Zhan, X. J. Liu, E. Carlegrim, F. H. Li, I. Bergenti, P. Graziosi, V. Dediu, and M. Fahlman. The role of aluminum oxide buffer layer in organic spin-valves performance. *Applied Physics Letters*, 94(5):053301, 2009.

[187] Stefano Sanvito. Molecular spintronics: The rise of spinterface science. *Nature Physics*, 6(8):562–564, 2010.

[188] A. Braun and J. Tcherniac. Über die Produkte der Einwirkung von Acetanhydrid auf Phthalamid. *Berichte der deutschen chemischen Gesellschaft*, 40(2):2709–2714, 1907.

[189] Henri de Diesbach and Edmond von der Weid. Quelques sels complexes des o-dinitriles avec le cuivre et la pyridine. *Helvetica Chimica Acta*, 10(1):886–888, 1927.

[190] G. Guillaud, J. Simon, and J.P. Germain. Metallophthalocyanines: Gas sensors, resistors and field effect transistors. *Coordination Chemistry Reviews*, 178–180, Part 2:1433–1484, 1998.

[191] Zhenan Bao, Andrew J. Lovinger, and Ananth Dodabalapur. Highly ordered vacuum-deposited thin films of metallophthalocyanines and their applications in field-effect transistors. *Advanced Materials*, 9(1):42–44, 1997.

[192] Zhenan Bao, Andrew J. Lovinger, and Ananth Dodabalapur. Organic field-effect transistors with high mobility based on copper phthalocyanine. *Applied Physics Letters*, 69(20):3066–3068, 1996.

[193] D. Hohnholz, S. Steinbrecher, and M. Hanack. Applications of phthalocyanines in organic light emitting devices. *Journal of Molecular Structure*, 521(1–3):231–237, 2000.

[194] Michael G. Walter, Alexander B. Rudine, and Carl C. Wamser. Porphyrins and phthalocyanines in solar photovoltaic cells. *Journal of Porphyrins and Phthalocyanines*, 14(09):759–792, 2010.

[195] S. Yim, S. Heutz, and T. S. Jones. Model for the $\alpha{\to}\beta1$ phase transition in phthalocyanine thin films. *Journal of Applied Physics*, 91(6):3632–3636, 2002.

[196] R. D. Gould. Structure and electrical conduction properties of phthalocyanine thin films. *Coordination Chemistry Reviews*, 156:237–274, 1996.

[197] M. Ashida, N. Uyeda, and E. Suito. Thermal transformation of vacuum-condensed thin films of copper-phthalocyanine. *Journal of Crystal Growth*, 8(1):45–56, 1971.

[198] Jungyoon E, Sunmi Kim, Eunju Lim, Kiejin Lee, Deokjoon Cha, and Barry Friedman. Effects of substrate temperature on copper(II) phthalocyanine thin films.

Applied Surface Science, 205(1–4):274–279, 2003.

[199] R. D. Gould. Dependence of the mobility and trap concentration in evaporated copper phthalocyanine thin films on background pressure and evaporation rate. *Journal of Physics D: Applied Physics*, 19(9):1785, 1986.

[200] S. Heutz, C. Mitra, W. Wu, A. J. Fisher, A. Kerridge, M. Stoneham, A. H. Harker, J. Gardener, H.-H. Tseng, T. S. Jones, C. Renner, and G. Aeppli. Molecular Thin Films: A New Type of Magnetic Switch. *Advanced Materials*, 19(21):3618–3622, 2007.

[201] Thomas Gredig, Corneliu N. Colesniuc, Scott A. Crooker, and Ivan K. Schuller. Substrate-controlled ferromagnetism in iron phthalocyanine films due to one-dimensional iron chains. *Physical Review B*, 86(1):014409, 2012.

[202] Michele Serri, Wei Wu, Luke R. Fleet, Nicholas M. Harrison, Cyrus F. Hirjibehedin, Christopher W. M. Kay, Andrew J. Fisher, Gabriel Aeppli, and Sandrine Heutz. High-temperature antiferromagnetism in molecular semiconductor thin films and nanostructures. *Nature Communications*, 5, 2014.

[203] Meng-Sheng Liao and Steve Scheiner. Electronic structure and bonding in metal phthalocyanines, Metal=Fe, Co, Ni, Cu, Zn, Mg. *The Journal of Chemical Physics*, 114(22):9780–9791, 2001.

[204] Arrigo Calzolari, Andrea Ferretti, and Marco Buongiorno Nardelli. Ab initio correlation effects on the electronic and transport properties of metal(II)-phthalocyanine-based devices. *Nanotechnology*, 18(42):424013, 2007.

[205] Hiroyuki Yamada, Toshihiro Shimada, and Atsushi Koma. Preparation and magnetic properties of manganese(II) phthalocyanine thin films. *The Journal of Chemical Physics*, 108(24):10256–10261, 1998.

[206] M. Evangelisti, J. Bartolomé, L. J. de Jongh, and G. Filoti. Magnetic properties of α-iron(II) phthalocyanine. *Physical Review B*, 66(14):144410, 2002.

[207] C. G. Barraclough, R. L. Martin, S. Mitra, and R. C. Sherwood. Paramagnetic Anisotropy, Electronic Structure, and Ferromagnetism in Spin S = 32 Manganese(II) Phthalocyanine. *The Journal of Chemical Physics*, 53(5):1638–1642, 2003.

[208] Xi Chen, Ying-Shuang Fu, Shuai-Hua Ji, Tong Zhang, Peng Cheng, Xu-Cun Ma, Xiao-Long Zou, Wen-Hui Duan, Jin-Feng Jia, and Qi-Kun Xue. Probing Superexchange Interaction in Molecular Magnets by Spin-Flip Spectroscopy and Microscopy. *Physical Review Letters*, 101(19):197208, 2008.

[209] T. Kataoka, Y. Sakamoto, Y. Yamazaki, V.R. Singh, A. Fujimori, Y. Takeda, T. Ohkochi, S.-I. Fujimori, T. Okane, Y. Saitoh, H. Yamagami, and A. Tanaka. Electronic configuration of Mn ions in the π-d molecular ferromagnet β-Mn phthalocyanine studied by soft X-ray magnetic circular dichroism. *Solid State Communications*, 152(9):806–809, 2012.

[210] Wei Wu, N. M. Harrison, and A. J. Fisher. Electronic structure and exchange interactions in cobalt-phthalocyanine chains. *Physical Review B*, 88(2):024426, 2013.

[211] Alessandro Scarfato, Shih-Hsin Chang, Stefan Kuck, Jens Brede, Germar Hoffmann, and Roland Wiesendanger. Scanning tunneling microscope study of iron(II) phthalocyanine growth on metals and insulating surfaces. *Surface Science*, 602(3):677–683, 2008.

[212] M. Casarin, M. Di Marino, D. Forrer, M. Sambi, F. Sedona, E. Tondello, A. Vittadini, V. Barone, and M. Pavone. Coverage-Dependent Architectures of Iron Phthalocyanine on Ag(110): a Comprehensive STM/DFT Study. *The Journal of Physical Chemistry C*, 114(5):2144–2153, 2010.

[213] H. Peisert, T. Schwieger, J. M. Auerhammer, M. Knupfer, M. S. Golden, J. Fink, P. R. Bressler, and M. Mast. Order on disorder: Copper phthalocyanine thin films on technical substrates. *Journal of Applied Physics*, 90(1):466–469, 2001.

[214] Emilia Annese, Jun Fujii, Ivana Vobornik, Giancarlo Panaccione, and Giorgio Rossi. Control of the magnetism of cobalt phthalocyanine by a ferromagnetic substrate. *Physical Review B*, 84(17):174443, 2011.

[215] E. Annese, F. Casolari, J. Fujii, and G. Rossi. Interface magnetic coupling of Fe-phthalocyanine layers on a ferromagnetic surface. *Physical Review B*, 87(5):054420, 2013.

[216] Mattia Scardamaglia, Claudia Struzzi, Silvano Lizzit, Matteo Dalmiglio, Paolo Lacovig, Alessandro Baraldi, Carlo Mariani, and Maria Grazia Betti. Energetics and Hierarchical Interactions of Metal–phthalocyanines Adsorbed on Graphene/Ir(111). *Langmuir*, 29(33):10440–10447, 2013.

[217] A. Scheybal, T. Ramsvik, R. Bertschinger, M. Putero, F. Nolting, and T. A. Jung. Induced magnetic ordering in a molecular monolayer. *Chemical Physics Letters*, 411(1–3):214–220, 2005.

[218] H. Wende, M. Bernien, J. Luo, C. Sorg, N. Ponpandian, J. Kurde, J. Miguel, M. Piantek, X. Xu, Ph Eckhold, W. Kuch, K. Baberschke, P. M. Panchmatia, B. Sanyal, P. M. Oppeneer, and O. Eriksson. Substrate-induced magnetic ordering and switching of iron porphyrin molecules. *Nature Materials*, 6(7):516–520, 2007.

[219] Heiko Wende. Revelation of the crucial interactions in spin-hybrid systems by means of X-ray absorption spectroscopy. *Journal of Electron Spectroscopy and Related Phenomena*, 189:171–177, 2013.

[220] C. Iacovita, M. V. Rastei, B. W. Heinrich, T. Brumme, J. Kortus, L. Limot, and J. P. Bucher. Visualizing the Spin of Individual Cobalt-Phthalocyanine Molecules. *Physical Review Letters*, 101(11):116602, 2008.

[221] J. Brede and R. Wiesendanger. Spin-resolved characterization of single cobalt phthalocyanine molecules on a ferromagnetic support. *Physical Review B*, 86(18):184423, 2012.

[222] Jörg Schwöbel, Yingshuang Fu, Jens Brede, Andrew Dilullo, Germar Hoffmann, Svetlana Klyatskaya, Mario Ruben, and Roland Wiesendanger. Real-space observation of spin-split molecular orbitals of adsorbed single-molecule magnets. *Nature Communications*, 3:953, 2012.

[223] Alberto Lodi Rizzini, Cornelius Krull, Aitor Mugarza, Timofey Balashov, Corneliu Nistor, Raoul Piquerel, Svetlana Klyatskaya, Mario Ruben, Polina M. Sheverdyaeva, Paolo Moras, Carlo Carbone, Christian Stamm, Piter S. Miedema, Pardeep K. Thakur, Violetta Sessi, Marcio Soares, Flora Yakhou-Harris, Julio C. Cezar, Sebastian Stepanow, and Pietro Gambardella. Coupling of single, double, and triple-decker metal-phthalocyanine complexes to ferromagnetic and antiferromagnetic substrates. *Surface Science*.

[224] Stefan Schmaus, Alexei Bagrets, Yasmine Nahas, Toyo K. Yamada, Annika Bork, Martin Bowen, Eric Beaurepaire, Ferdinand Evers, and Wulf Wulfhekel. Giant magnetoresistance through a single molecule. *Nature Nanotechnology*, 6(3):185–189, 2011.

[225] Alexei Bagrets, Stefan Schmaus, Ali Jaafar, Detlef Kramczynski, Toyo Kazu Yamada, Mébarek Alouani, Wulf Wulfhekel, and Ferdinand Evers. Single Molecule Magnetoresistance with Combined Antiferromagnetic and Ferromagnetic Electrodes. *Nano Letters*, 12(10):5131–5136, 2012.

[226] Fatima Djeghloul. *Study of organic semiconductor/ferromagnet interfaces by spin-polarized electron scattering and photoemission*. PhD thesis, University of Strasbourg, 2013.

[227] Fatima Ibrahim. *Theoretical study of electronic structure and magnetism in materials for spintronics*. PhD thesis, Strasbourg, 2014.

[228] Philippe Sainctavit and Marie-Anne Arrio. Ligand Field Multiplet Theory Applied to the Calculation of X-Ray Absorption Spectra. In Éric Beaurepaire, Bernard Carrière, and Jean-Paul Kappler, editors, *Magnetism and synchrotron radiation: Mittelwihr, 1996 : lectures notes*. Les Éd. de physique, Les Ulis, 1997.

[229] F. Djeghloul, G. Garreau, M. Gruber, L. Joly, S. Boukari, J. Arabski, H. Bulou, F. Scheurer, P. Bertran, F. Le Fèvre, A. Taleb-Ibrahimi, W Wulfhekel, E. Beaurepaire, S. Hajjar-Garreau, P. Wetzel, M. Bowen, and W. Weber. Efficient, high-density, carbon-based spinterfaces. 2014. submitted.

[230] A. K. Schmid, D. Atlan, H. Itoh, B. Heinrich, T. Ichinokawa, and J. Kirschner. Fast interdiffusion in thin films: Scanning-tunneling-microscopy determination of surface diffusion through microscopic pinholes. *Physical Review B*, 48(4):2855–2858, 1993.

[231] T. G. Gopakumar, T. Brumme, J. Kröger, C. Toher, G. Cuniberti, and R. Berndt. Coverage-Driven Electronic Decoupling of Fe-Phthalocyanine from a Ag(111) Substrate. *The Journal of Physical Chemistry C*, 115(24):12173–12179, 2011.

[232] Yoshiki Teramura, Arata Tanaka, and Takeo Jo. Effect of Coulomb Interaction on the X-Ray Magnetic Circular Dichroism Spin Sum Rule in 3 Transition Elements. *Journal of the Physical Society of Japan*, 65(4):1053–1055, 1996.

[233] A. E. Berkowitz and Kentaro Takano. Exchange anisotropy — a review. *Journal of Magnetism and Magnetic Materials*, 200(1–3):552–570, 1999.

[234] W. Weber, A. Bischof, R. Allenspach, C. H. Back, J. Fassbender, U. May,

B. Schirmer, R. M. Jungblut, G. Güntherodt, and B. Hillebrands. Structural relaxation and magnetic anisotropy in Co/cu(001) films. *Physical Review B*, 54(6):4075–4079, 1996.

[235] K. O'Grady, L. E. Fernandez-Outon, and G. Vallejo-Fernandez. A new paradigm for exchange bias in polycrystalline thin films. *Journal of Magnetism and Magnetic Materials*, 322(8):883–899, 2010.

[236] Cinthia Piamonteze, Piter Miedema, and Frank M. F. de Groot. Accuracy of the spin sum rule in XMCD for the transition-metal L edges from manganese to copper. *Physical Review B*, 80(18):184410, 2009.

[237] R. K. Kawakami, E. Rotenberg, E. J. Escorcia-Aparicio, H. J. Choi, T. R. Cummins, J. G. Tobin, N. V. Smith, and Z. Q. Qiu. Observation of the quantum well interference in magnetic nanostructures by photoemission. *Physical review letters*, 80(8):1754–1757, 1998.

[238] W. Weber, R. Allenspach, and A. Bischof. Exchange Coupling Across Cu(100): A High-Precision Study. *EPL (Europhysics Letters)*, 31(8):491, 1995.

[239] R. K. Kawakami, E. Rotenberg, Hyuk J. Choi, Ernesto J. Escorcia-Aparicio, M. O. Bowen, J. H. Wolfe, E. Arenholz, Z. D. Zhang, N. V. Smith, and Z. Q. Qiu. Quantum-well states in copper thin films. *Nature*, 398(6723):132–134, 1999.

[240] Mark van Schilfgaarde and Walter A. Harrison. Oscillatory exchange coupling: RKKY or quantum-well mechanism? *Physical Review Letters*, 71(23):3870–3873, 1993.

[241] Ch Würsch, C. Stamm, S. Egger, D. Pescia, W. Baltensperger, and J. S. Helman. Quantum oscillations in a confined electron gas. *Nature*, 389(6654):937–939, 1997.

[242] C. H. Back, W. Weber, A. Bischof, D. Pescia, and R. Allenspach. Probing oscillatory exchange coupling with a paramagnet. *Physical Review B*, 52(18):13114–13117, 1995.

[243] W. E. Bailey, A. Ghosh, S. Auffret, E. Gautier, U. Ebels, F. Wilhelm, and A. Rogalev. Pd magnetism induced by indirect interlayer exchange coupling. *Physical Review B*, 86(14):144403, 2012.

[244] C. a. F. Vaz, J. a. C. Bland, and G. Lauhoff. Magnetism in ultrathin film structures. *Reports on Progress in Physics*, 71(5):056501, 2008.

[245] Arieh Aviram and Mark A. Ratner. Molecular rectifiers. *Chemical Physics Letters*, 29(2):277–283, 1974.

[246] Robert M. Metzger. Unimolecular electronics. *Journal of Materials Chemistry*, 18(37):4364–4396, 2008.

[247] Nicolas Weibel, Sergio Grunder, and Marcel Mayor. Functional molecules in electronic circuits. *Organic & Biomolecular Chemistry*, 5(15):2343–2353, 2007.

[248] Sense Jan van der Molen and Peter Liljeroth. Charge transport through molecular switches. *Journal of Physics: Condensed Matter*, 22(13):133001, 2010.

[249] Masahiro Irie. Diarylethenes for Memories and Switches. *Chemical Reviews*,

100(5):1685–1716, 2000.

[250] Byoung-Young Choi, Se-Jong Kahng, Seungchul Kim, Hajin Kim, Hyo Won Kim, Young Jae Song, Jisoon Ihm, and Young Kuk. Conformational Molecular Switch of the Azobenzene Molecule: A Scanning Tunneling Microscopy Study. *Physical Review Letters*, 96(15):156106, 2006.

[251] D. M. Eigler, C. P. Lutz, and W. E. Rudge. An atomic switch realized with the scanning tunnelling microscope. *Nature*, 352(6336):600–603, 1991.

[252] M. Womes, J. C. Jumas, J. Olivier-Fourcade, F. Aubertin, and U. Gonser. High spin ($^5T_2$)-low spin ($^1A_1$) equilibrium of iron (II) in $M_2FeSn_3S_8$ thiospinels (M = Cu, Ag). *Chemical Physics Letters*, 201(5–6):555–558, 1993.

[253] W. Robert Scheidt and Christopher A. Reed. Spin-state/stereochemical relationships in iron porphyrins: implications for the hemoproteins. *Chemical Reviews*, 81(6):543–555, 1981.

[254] M. F. Perutz, G. Fermi, B. Luisi, B. Shaanan, and R. C. Liddington. Stereochemistry of cooperative mechanisms in hemoglobin. *Accounts of Chemical Research*, 20(9):309–321, 1987.

[255] L. Cambi and L. Szegö. Über die magnetische Susceptibilität der komplexen Verbindungen. *Berichte der deutschen chemischen Gesellschaft (A and B Series)*, 64(10):2591–2598, 1931.

[256] P. Gütlich, A. Hauser, and H. Spiering. Thermal and optical switching of iron (II) complexes. *Angewandte Chemie International Edition in English*, 33(20):2024–2054, 1994.

[257] P. Gütlich, Y. Garcia, and H. A. Goodwin. Spin crossover phenomena in Fe (II) complexes. *Chem. Soc. Rev.*, 29(6):419–427, 2000.

[258] Philipp Gütlich and Harold A. Goodwin. *Spin Crossover in Transition Metal Compound I*. Springer, 2004.

[259] A. Bousseksou, G. Molnár, L. Salmon, and W. Nicolazzi. Molecular spin crossover phenomenon: recent achievements and prospects. *Chemical Society Reviews*, 40(6):3313–3335, 2011.

[260] Helena J. Shepherd, Gábor Molnár, William Nicolazzi, Lionel Salmon, and Azzedine Bousseksou. Spin Crossover at the Nanometre Scale. *European Journal of Inorganic Chemistry*, 2013:653–661, 2012.

[261] Eliseo Ruiz. Charge transport properties of spin crossover systems. *Physical Chemistry Chemical Physics*, 16(1):14–22, 2013.

[262] Malcolm A Halcrow. *Spin-crossover materials properties and applications*. J. Wiley and Sons, Inc., Chichester, 2013.

[263] W. A. Baker and H. M. Bobonich. Magnetic Properties of Some High-Spin Complexes of Iron(II). *Inorganic Chemistry*, 3(8):1184–1188, 1964.

[264] E. König and K. Madeja. Unusual magnetic behaviour of some iron (II)–bis-(1, 10-phenanthroline) complexes. *Chemical Communications (London)*, 3:61–62, 1966.

[265] E.W. Müller, H. Spiering, and P. Gütlich. Spin transition in [Fe(phen)$_2$(NCS)$_2$] and [Fe(bipy)$_2$(NCS)$_2$]: Hysteresis and effect of crystal quality. *Chemical Physics Letters*, 93(6):567–571, 1982.

[266] B. Gallois, J. A. Real, C. Hauw, and J. Zarembowitch. Structural changes associated with the spin transition in bis (isothiocyanato) bis (1, 10-phenanthroline) iron: a single-crystal x-ray investigation. *Inorganic Chemistry*, 29(6):1152–1158, 1990.

[267] David Collison, C. David Garner, Catherine M. McGrath, J. Frederick W. Mosselmans, Mark D. Roper, Jon M. W. Seddon, Ekk Sinn, and Nigel A. Young. Soft X-ray induced excited spin state trapping and soft X-ray photochemistry at the iron L$_{2,3}$ edge in [Fe(phen)$_2$(NCS)$_2$] and [Fe(phen)$_2$(NCSe)$_2$] (phen = 1,10-phenanthroline). *Journal of the Chemical Society, Dalton Transactions*, (22):4371–4376, 1997.

[268] M. Marchivie, P. Guionneau, J. A. K. Howard, G. Chastanet, J. F. Létard, A. E. Goeta, and D. Chasseau. Structural characterization of a photoinduced molecular switch. *Journal of the American Chemical Society*, 124(2):194–195, 2002.

[269] Edgar Koenig and K. Madeja. 5T2-1A1 Equilibriums in some iron(II)-bis(1,10-phenanthroline) complexes. *Inorganic Chemistry*, 6(1):48–55, 1967.

[270] K. Akabori, H. Matsuo, and Y. Yamamoto. Thermal properties of tris (1, 10-phenanthroline) complexes of iron (II) and nickel (II) salts. *Journal of Inorganic and Nuclear Chemistry*, 35(8):2679–2690, 1973.

[271] Prabuddha Ganguli, Philipp Gütlich, E. Wolfgang Müller, and Werner Irler. Further studies on the spin cross-over phenomenon in di-isothiocyanatobis(1,10-phenanthroline)iron(II). *Journal of the Chemical Society, Dalton Transactions*, (2):441–446, 1981.

[272] M. Reiher. Theoretical study of the Fe (phen)$_2$(NCS)$_2$ spin-crossover complex with reparametrized density functionals. *Inorganic chemistry*, 41(25):6928–6935, 2002.

[273] Koichi Momma and Fujio Izumi. VESTA3 for three-dimensional visualization of crystal, volumetric and morphology data. *Journal of Applied Crystallography*, 44(6):1272–1276, 2011.

[274] S. Shi, G. Schmerber, J. Arabski, J.-B. Beaufrand, D. J. Kim, S. Boukari, M. Bowen, N. T. Kemp, N. Viart, G. Rogez, E. Beaurepaire, H. Aubriet, J. Petersen, C. Becker, and D. Ruch. Study of molecular spin-crossover complex Fe(phen)$_2$(NCS)$_2$ thin films. *Applied Physics Letters*, 95(4):043303, 2009.

[275] Philipp Gütlich. Spin crossover in iron(II)-complexes. In *Metal Complexes*, number 44 in Structure and Bonding, pages 83–195. Springer Berlin Heidelberg, 1981.

[276] Michio Sorai. Heat Capacity Studies of Spin Crossover Systems. In *Spin Crossover in Transition Metal Compounds III*, number 235 in Topics in Current Chemistry, pages 153–170. Springer Berlin Heidelberg, 2004.

[277] M. Sorai and S. Seki. Phonon coupled cooperative low-spin ^{1}A$_1$ high-spin ^{5}T$_2$ transition in [Fe(phen)$_2$(NCS)$_2$] and [Fe(phen)$_2$(NCSe)$_2$] crystals. *Journal of Physics and Chemistry of Solids*, 35(4):555–570, 1974.

[278] Céline Etrillard. *Synthèse de nanoparticules à transition de spin et étude des propriétés, application en électronique moléculaire.* PhD thesis, Université Sciences et Technologies-Bordeaux I, 2011.

[279] Antoine Tissot. *Commutation thermo-et photo-induite de solides moléculaires a transition de spin: du monocristal aux nano-objets.* PhD thesis, Université Paris Sud-Paris XI, 2011.

[280] Vincent Davesne. *Organic spintronics : An investigation on spin-crossover complexes from isolated molecules to the device.* PhD thesis, Université de Strasbourg and Karlsruhe Institute of Technology, 2013.

[281] H. Spiering. Elastic Interaction in Spin-Crossover Compounds. In *Spin Crossover in Transition Metal Compounds III*, number 235 in Topics in Current Chemistry, pages 171–195. Springer Berlin Heidelberg, 2004.

[282] Andreas Hauser. Cooperative effects on the HS=>LS relaxation in the $[Fe(ptz)_6](BF_4)_2$ spin-crossover system. *Chemical Physics Letters*, 192(1):65–70, 1992.

[283] C. P. Slichter and H. G. Drickamer. Pressure-induced Electronic Changes in Compounds of Iron. *The Journal of Chemical Physics*, 56(5):2142–2160, 1972.

[284] H. Spiering, E. Meissner, H. Köppen, E. W. Müller, and P. Gütlich. The effect of the lattice expansion on high spin => low spin transitions. *Chemical Physics*, 68(1–2):65–71, 1982.

[285] Mikaël Kepenekian, Boris Le Guennic, and Vincent Robert. Primary Role of the Electrostatic Contributions in a Rational Growth of Hysteresis Loop in Spin-Crossover Fe(II) Complexes. *Journal of the American Chemical Society*, 131(32):11498–11502, 2009.

[286] Mikaël Kepenekian, Boris Le Guennic, and Vincent Robert. Magnetic bistability: From microscopic to macroscopic understandings of hysteretic behavior using ab initio calculations. *Physical Review B*, 79(9):094428, 2009.

[287] V. Meded, A. Bagrets, K. Fink, R. Chandrasekar, M. Ruben, F. Evers, A. Bernand-Mantel, J. S. Seldenthuis, A. Beukman, and H. S. J. Van der Zant. Electrical control over the Fe (II) spin crossover in a single molecule: Theory and experiment. *Physical Review B*, 83(24):245415, 2011.

[288] Manuel Gruber, Vincent Davesne, Martin Bowen, Samy Boukari, Eric Beaurepaire, Wulf Wulfhekel, and Toshio Miyamachi. Spin state of spin-crossover complexes: From single molecules to ultrathin films. *Physical Review B*, 89(19):195415, 2014.

[289] Jelena Jeftić, Roland Hinek, Silvia C. Capelli, and Andreas Hauser. Cooperativity in the Iron(II) Spin-Crossover Compound $[Fe(ptz)_6](PF_6)_2$ under the Influence of External Pressure (ptz = 1-n-Propyltetrazole). *Inorganic Chemistry*, 36(14):3080–3087, 1997.

[290] A. Bousseksou, G. Molnár, J. P. Tuchagues, N. Menéndez, É Codjovi, and F. Varret. Triggering the spin-crossover of Fe (phen)$_2$(NCS)$_2$ by a pressure pulse. Pressure and magnetic field induce 'mirror effects'. *Comptes Rendus Chimie*, 6(3):329–335,

2003.

^{291} Vadim Ksenofontov, Ana B. Gaspar, and Philipp Gütlich. Pressure Effect Studies on Spin Crossover and Valence Tautomeric Systems. In *Spin Crossover in Transition Metal Compounds III*, number 235 in Topics in Current Chemistry, pages 23–64. Springer Berlin Heidelberg, 2004.

^{292} José Antonio Real, Ana Belén Gaspar, and M. Carmen Muñoz. Thermal, pressure and light switchable spin-crossover materials. *Dalton Transactions*, (12):2062–2079, 2005.

^{293} V. Ksenofontov, G. Levchenko, H. Spiering, P. Gütlich, J.-F. Létard, Yacine Bouhedja, and O. Kahn. Spin crossover behavior under pressure of Fe(PM-L)$_2$(NCS)$_2$ compounds with substituted 2'-pyridylmethylene 4-anilino ligands. *Chemical Physics Letters*, 294(6):545–553, 1998.

^{294} T. Granier, B. Gallois, J. Gaultier, J. A. Real, and J. Zarembowitch. High-pressure single-crystal x-ray diffraction study of two spin-crossover iron (II) complexes: Fe(phen)$_2$(NCS)$_2$ and Fe(btz)$_2$(NCS)$_2$. *Inorganic Chemistry*, 32(23):5305–5312, 1993.

^{295} J. M. D. Coey. *Magnetism and Magnetic Materials*. Cambridge University Press, Cambridge, 2010.

^{296} Y. Qi, E. W. Müller, H. Spiering, and P. Gütlich. The effect of a magnetic field on the high-spin α low-spin transition in [Fe(phen)$_2$(NCS)$_2$]. *Chemical Physics Letters*, 101(4–5):503–505, 1983.

^{297} J. Lejay, A. G. M. Jansen, P. Wyder, W. Bronger, and W. Kläui. Spin equilibrium of Co^{3+} complexes influenced by a magnetic field. *Physical Review B*, 43(10):8196–8198, 1991.

^{298} A. Bousseksou, N. Negre, M. Goiran, L. Salmon, J.-P. Tuchagues, M.-L. Boillot, K. Boukheddaden, and F. Varret. Dynamic triggering of a spin-transition by a pulsed magnetic field. *The European Physical Journal B - Condensed Matter and Complex Systems*, 13(3):451–456, 2000.

^{299} A. Bousseksou, F. Varret, M. Goiran, K. Boukheddaden, and J. P. Tuchagues. The Spin Crossover Phenomenon Under High Magnetic Field. In *Spin Crossover in Transition Metal Compounds III*, number 235 in Topics in Current Chemistry, pages 65–84. Springer Berlin Heidelberg, 2004.

^{300} John J. McGravey and Ian Lawthers. Photochemically-induced perturbation of the 1A 5T equilibrium in Fe11 complexes by pulsed laser irradiation in the metal-to-ligand charge-transfer absorption band. *Journal of the Chemical Society, Chemical Communications*, (16):906–907, 1982.

^{301} S. Decurtins, P. Gütlich, C. P. Köhler, H. Spiering, and A. Hauser. Light-induced excited spin state trapping in a transition-metal complex: the hexa-1-propyltetrazole-iron (II) tetrafluoroborate spin-crossover system. *Chemical Physics Letters*, 105(1):1–4, 1984.

^{302} Andreas Hauser. Light-Induced Spin Crossover and the High-Spin=>Low-Spin

Relaxation. In *Spin Crossover in Transition Metal Compounds II*, number 234 in Topics in Current Chemistry, pages 155–198. Springer Berlin Heidelberg, 2004.

[303] A. Hauser. Reversibility of light-induced excited spin state trapping in the $Fe(ptz)_6(BF_4)_2$, and the $Zn_{1-x}Fe_x(ptz)_6(BF_4)_2$ spin-crossover systems. *Chemical Physics Letters*, 124(6):543–548, 1986.

[304] A. Cannizzo, C.J. Milne, C. Consani, W. Gawelda, Ch. Bressler, F. van Mourik, and M. Chergui. Light-induced spin crossover in Fe(II)-based complexes: The full photocycle unraveled by ultrafast optical and X-ray spectroscopies. *Coordination Chemistry Reviews*, 254(21–22):2677–2686, 2010.

[305] Majed Chergui. On the interplay between charge, spin and structural dynamics in transition metal complexes. *Dalton Transactions*, 41(42):13022–13029, 2012.

[306] Ch Bressler, C. Milne, V.-T. Pham, A. ElNahhas, R. M. van der Veen, W. Gawelda, S. Johnson, P. Beaud, D. Grolimund, M. Kaiser, C. N. Borca, G. Ingold, R. Abela, and M. Chergui. Femtosecond XANES Study of the Light-Induced Spin Crossover Dynamics in an Iron(II) Complex. *Science*, 323(5913):489–492, 2009. PMID: 19074309.

[307] Eric Collet, Nicolas Moisan, Chérif Baldé, Roman Bertoni, Elzbieta Trzop, Claire Laulhé, Maciej Lorenc, Marina Servol, Hervé Cailleau, Antoine Tissot, Marie-Laure Boillot, Timothy Graber, Robert Henning, Philip Coppens, and Marylise Buron-Le Cointe. Ultrafast spin-state photoswitching in a crystal and slower consecutive processes investigated by femtosecond optical spectroscopy and picosecond X-ray diffraction. *Physical Chemistry Chemical Physics*, 14(18):6192–6199, 2012.

[308] Nils Huse, Hana Cho, Kiryong Hong, Lindsey Jamula, Frank M. F. de Groot, Tae Kyu Kim, James K. McCusker, and Robert W. Schoenlein. Femtosecond Soft X-ray Spectroscopy of Solvated Transition-Metal Complexes: Deciphering the Interplay of Electronic and Structural Dynamics. *The Journal of Physical Chemistry Letters*, 2(8):880–884, 2011.

[309] Nils Huse, Munira Khalil, Tae Kyu Kim, Amanda L. Smeigh, Lindsey Jamula, James K. McCusker, and Robert W. Schoenlein. Probing reaction dynamics of transition-metal complexes in solution via time-resolved X-ray spectroscopy. *Journal of Physics: Conference Series*, 148(1):012043, 2009.

[310] Nils Huse, Tae Kyu Kim, Lindsey Jamula, James K. McCusker, Frank M. F. de Groot, and Robert W. Schoenlein. Photo-Induced Spin-State Conversion in Solvated Transition Metal Complexes Probed via Time-Resolved Soft X-ray Spectroscopy. *Journal of the American Chemical Society*, 132(19):6809–6816, 2010.

[311] Munira Khalil, Matthew A. Marcus, Amanda L. Smeigh, James K. McCusker, Henry H. W. Chong, and Robert W. Schoenlein. Picosecond X-ray Absorption Spectroscopy of a Photoinduced Iron(II) Spin Crossover Reaction in Solution. *The Journal of Physical Chemistry A*, 110(1):38–44, 2006.

[312] Carmen Sousa, Coen de Graaf, Andrii Rudavskyi, Ria Broer, Jörg Tatchen, Mihajlo Etinski, and Christel M. Marian. Ultrafast Deactivation Mechanism of the

Excited Singlet in the Light-Induced Spin Crossover of $[Fe(2,2'-bipyridine)_3]^{2+}$. *Chemistry – A European Journal*, 19(51):17541–17551, 2013.

[313] E. Buhks, G. Navon, M. Bixon, and J. Jortner. Spin conversion processes in solutions. *Journal of the American Chemical Society*, 102(9):2918–2923, 1980.

[314] P. Adler, H. Spiering, and P. Guetlich. Investigation of the $^1A_1 => {^5}T_2$ intersystem crossing dynamics of an iron(II) spin-crossover complex in the solid state by Moessbauer spectroscopy. *Inorganic Chemistry*, 26(23):3840–3845, 1987.

[315] Peter Adler, Andreas Hauser, Andreas Vef, Hartmut Spiering, and Philipp Gütlich. Dynamics of spin state conversion processes in the solid state. *Hyperfine Interactions*, 47-48(1-4):343–356, 1989.

[316] Andreas Hauser. Excited-state lifetimes of $[Fe(bipy)_3]^{2+}$ and $[Fe(phen)_3]^{2+}$. *Chemical Physics Letters*, 173(5–6):507–512, 1990.

[317] Sabine Schenker, Andreas Hauser, Wei Wang, and I. Y Chan. Matrix effects on the high-spin→low-spin relaxation in $[M_{1-x}Fe_x(bpy)_3](PF_6)_2$ (M=Cd, Mn and Zn, bpy=2,2'-bipyridine). *Chemical Physics Letters*, 297(3–4):281–286, 1998.

[318] Cristian Enachescu, Hector Constant-Machado, Epiphane Codjovi, Jorge Linares, Kamel Boukheddaden, and François Varret. Direct access to the photo-excitation and relaxation terms in photo-switchable solids: non-linear aspects. *Journal of Physics and Chemistry of Solids*, 62(8):1409–1422, 2001.

[319] Jean-François Létard, Guillaume Chastanet, Philippe Guionneau, and Cedric Desplanches. Optimizing the Stability of Trapped Metastable Spin States. In Lcolm a Halcrow, editor, *Spin-Crossover Materials*, pages 475–506. John Wiley & Sons Ltd, 2013.

[320] Jean-François Létard, Laurence Capes, Guillaume Chastanet, Nicolas Moliner, Sylvie Létard, José-Antonio Real, and Olivier Kahn. Critical temperature of the LIESST effect in iron(II) spin crossover compounds. *Chemical Physics Letters*, 313(1–2):115–120, 1999.

[321] Jean-François Létard, Philippe Guionneau, Olivier Nguyen, José Sánchez Costa, Silvia Marcén, Guillaume Chastanet, Mathieu Marchivie, and Laurence Goux-Capes. A Guideline to the Design of Molecular-Based Materials with Long-Lived Photomagnetic Lifetimes. *Chemistry – A European Journal*, 11(16):4582–4589, 2005.

[322] Naonobu Shimamoto, Shin-ichi Ohkoshi, Osamu Sato, and Kazuhito Hashimoto. Control of Charge-Transfer-Induced Spin Transition Temperature on Cobalt-iron Prussian Blue Analogues. *Inorganic Chemistry*, 41(4):678–684, 2002.

[323] E. Freysz, S. Montant, S. Létard, and J. F. Létard. Single laser pulse induces spin state transition within the hysteresis loop of an Iron compound. *Chemical Physics Letters*, 394(4–6):318–323, 2004.

[324] Sébastien Bonhommeau, Gábor Molnár, Ana Galet, Antoine Zwick, José-Antonio Real, John J. McGarvey, and Azzedine Bousseksou. Cover Picture: One Shot Laser Pulse Induced Reversible Spin Transition in the Spin-Crossover Complex

[Fe($C_4H_4N_2$)Pt(CN)$_4$] at Room Temperature. *Angewandte Chemie International Edition*, 44(26):3943–3943, 2005.

[325] K. Kato, M. Takata, Y. Moritomo, A. Nakamoto, and N. Kojima. On-off optical switching of the magnetic and structural properties in a spin-crossover complex. *Applied Physics Letters*, 90(20):201902, 2007.

[326] R. Herber and L. M. Casson. Light-induced excited-spin-state trapping: evidence from variable temperature Fourier transform measurements. *Inorganic chemistry*, 25(6):847–852, 1986.

[327] C. Cartier dit Moulin, P. Rudolf, A. M. Flank, and C. T. Chen. Spin transition evidenced by soft X-ray absorption spectroscopy. *The Journal of Physical Chemistry*, 96(15):6196–6198, 1992.

[328] Jey-Jau Lee, Hwo-shuenn Sheu, Chi-Rung Lee, Jin-Ming Chen, Jyh-Fu Lee, Chih-Chieh Wang, Chun-Hsun Huang, and Yu Wang. X-ray Absorption Spectroscopic Studies on Light-Induced Excited Spin State Trapping of an Fe(II) Complex. *Journal of the American Chemical Society*, 122(24):5742–5747, 2000.

[329] V. Briois, Ch. Cartier dit Moulin, Ph. Sainctavit, Ch. Brouder, and A.-M. Flank. Full Multiple Scattering and Crystal Field Multiplet Calculations Performed on the Spin Transition FeII(phen)$_2$(NCS)$_2$ Complex at the Iron K and L$_{2,3}$ X-ray Absorption Edges. *Journal of the American Chemical Society*, 117(3):1019–1026, 1995.

[330] M. Bernien. *X-Ray Absorption Spectroscopy of Fe Complexes on Surfaces: Electronic Interactions and Tailoring of the Magnetic Coupling.* PhD thesis, PhD thesis, Freie Universität Berlin, Germany, 2009.

[331] Toshio Miyamachi, Manuel Gruber, Vincent Davesne, Martin Bowen, Samy Boukari, Loïc Joly, Fabrice Scheurer, Guillaume Rogez, Toyo Kazu Yamada, Philippe Ohresser, Eric Beaurepaire, and Wulf Wulfhekel. Robust spin crossover and memristance across a single molecule. *Nature Communications*, 3:938, 2012.

[332] Matthias Bernien, Dennis Wiedemann, Christian F. Hermanns, Alex Krüger, Daniela Rolf, Wolfgang Kroener, Paul Müller, Andreas Grohmann, and Wolfgang Kuch. Spin Crossover in a Vacuum-Deposited Submonolayer of a Molecular Iron(II) Complex. *The Journal of Physical Chemistry Letters*, 3(23):3431–3434, 2012.

[333] V. Davesne, M. Gruber, T. Miyamachi, V. Da Costa, S. Boukari, F. Scheurer, L. Joly, P. Ohresser, E. Otero, F. Choueikani, A. B. Gaspar, J. A. Real, W. Wulfhekel, M. Bowen, and E. Beaurepaire. First glimpse of the soft x-ray induced excited spin-state trapping effect dynamics on spin cross-over molecules. *The Journal of Chemical Physics*, 139(7):074708–074708–6, 2013.

[334] Ben Warner, Jenny C. Oberg, Tobias G. Gill, Fadi El Hallak, Cyrus F. Hirjibehedin, Michele Serri, Sandrine Heutz, Marie-Anne Arrio, Philippe Sainctavit, Matteo Mannini, Giordano Poneti, Roberta Sessoli, and Patrick Rosa. Temperature- and Light-Induced Spin Crossover Observed by X-ray Spectroscopy on Isolated Fe(II) Complexes on Gold. *The Journal of Physical Chemistry Letters*,

4(9):1546–1552, 2013.

[335] György Vankó, Franz Renz, Gábor Molnár, Thomas Neisius, and Szilvia Kárpáti. Hard-X-ray-Induced Excited-Spin-State Trapping. *Angewandte Chemie International Edition*, 46(28):5306–5309, 2007.

[336] Nadjib Baadji, Manuel Piacenza, Tugba Tugsuz, Fabio Della Sala, Giuseppe Maruccio, and Stefano Sanvito. Electrostatic spin crossover effect in polar magnetic molecules. *Nature Materials*, 8(10):813–817, 2009.

[337] A. Droghetti and S. Sanvito. Electric Field Control of Valence Tautomeric Interconversion in Cobalt Dioxolene. *Physical Review Letters*, 107(4):047201, 2011.

[338] Colette Boskovic. Valence Tautomeric Transitions in Cobalt-dioxolene Complexes. In Lcolm a Halcrow, editor, *Spin-Crossover Materials*, pages 203–224. John Wiley & Sons Ltd, 2013.

[339] N. Baadji and S. Sanvito. Giant Resistance Change across the Phase Transition in Spin-Crossover Molecules. *Physical Review Letters*, 108(21):217201, 2012.

[340] Paulo Nuno Martinho, Cyril Rajnak, and Mario Ruben. Nanoparticles, Thin Films and Surface Patterns from Spin-Crossover Materials and Electrical Spin State Control. In Lcolm a Halcrow, editor, *Spin-Crossover Materials*, pages 375–404. John Wiley & Sons Ltd, 2013.

[341] F. Prins, M. Monrabal-Capilla, E. A. Osorio, E. Coronado, and H. S. J. van der Zant. Room-Temperature Electrical Addressing of a Bistable Spin-Crossover Molecular System. *Advanced Materials*, 23(13):1545–1549, 2011.

[342] Aurelian Rotaru, Il'ya A. Gural'skiy, Gábor Molnár, Lionel Salmon, Philippe Demont, and Azzedine Bousseksou. Spin state dependence of electrical conductivity of spin crossover materials. *Chemical Communications*, 48(35):4163–4165, 2012.

[343] Aurelian Rotaru, Julien Dugay, Reasmey P. Tan, Ilya A. Guralskiy, Lionel Salmon, Philippe Demont, Julian Carrey, Gábor Molnár, Marc Respaud, and Azzedine Bousseksou. Nano-electromanipulation of Spin Crossover Nanorods: Towards Switchable Nanoelectronic Devices. *Advanced Materials*, 25(12):1745–1749, 2013.

[344] Edgar A. Osorio, Kasper Moth-Poulsen, Herre S. J. van der Zant, Jens Paaske, Per Hedegård, Karsten Flensberg, Jesper Bendix, and Thomas Bjørnholm. Electrical Manipulation of Spin States in a Single Electrostatically Gated Transition-Metal Complex. *Nano Letters*, 10(1):105–110, 2010.

[345] M. S. Alam, M. Stocker, K. Gieb, P. Müller, M. Haryono, K. Student, and A. Grohmann. Spin-State Patterns in Surface-Grafted Beads of Iron (II) Complexes. *Angewandte Chemie International Edition*, 49(6):1159–1163, 2009.

[346] Andreas Grohmann, Marco Haryono, Katja Student, Paul Müller, and Michael Stocker. Mapping the Spin State in Spin-Crossover Complex Assemblies: Current-Imaging Tunnelling Spectroscopy (CITS). *European Journal of Inorganic Chemistry*, 2013(5-6):662–669, 2013.

[347] T. G. Gopakumar, F. Matino, H. Naggert, A. Bannwarth, F. Tuczek, and

R. Berndt. Electron-Induced Spin Crossover of Single Molecules in a Bilayer on Gold. *Angewandte Chemie International Edition*, 51(25):6262–6266, 2012.

[348] Xin Zhang, Tatiana Palamarciuc, Jean-François Létard, Patrick Rosa, Eduardo Vega Lozada, Fernand Torres, Luis G. Rosa, Bernard Doudin, and Peter A. Dowben. The spin state of a molecular adsorbate driven by the ferroelectric substrate polarization. *Chemical Communications*, 50(18):2255–2257, 2014.

[349] O. Kahn and C. J. Martinez. Spin-transition polymers: from molecular materials toward memory devices. *Science*, 279(5347):44–48, 1998.

[350] Jean-François Létard, Philippe Guionneau, and Laurence Goux-Capes. Towards Spin Crossover Applications. In *Spin Crossover in Transition Metal Compounds III*, number 235 in Topics in Current Chemistry, pages 221–249. Springer Berlin Heidelberg, 2004.

[351] Gábor Molnár, Lionel Salmon, William Nicolazzi, Ferial Terki, and Azzedine Bousseksou. Emerging properties and applications of spin crossover nanomaterials. *Journal of Materials Chemistry C*, 2013.

[352] R. Lloyd Carroll and Christopher B. Gorman. The Genesis of Molecular Electronics. *Angewandte Chemie International Edition*, 41(23):4378–4400, 2002.

[353] Azzedine Bousseksou, Christophe Vieu, Jean-François Letard, Philippe Demont, Jean-Pierre Tuchagues, Laurent Malaquin, Jérôme Menegotto, and Lionel Salmon. Molecular Memory and Method for Making Same, 2003.

[354] Tarik Mahfoud, Gábor Molnár, Saioa Cobo, Lionel Salmon, Christophe Thibault, Christophe Vieu, Philippe Demont, and Azzedine Bousseksou. Electrical properties and non-volatile memory effect of the $[Fe(HB(pz)_3)_2]$ spin crossover complex integrated in a microelectrode device. *Applied Physics Letters*, 99(5):053307, 2011.

[355] Jean-François Letard, Nathalie Daro, and Sandie Auffret. Spin Transition Material, 2009.

[356] Azzedine Bousseksou, Lionel Salmon, Gabor Molnar, Saioa Cobo, and Lionel Rechignat. Method for Defining a Sports or Playing Area by Means of a Thermochromatic Spin Transition Material, 2010.

[357] Yann Garcia, Petra J. van Koningsbruggen, Epiphane Codjovi, René Lapouyade, Olivier Kahn, and Louis Rabardel. Non-classical FeII spin-crossover behaviour leading toan unprecedented extremely large apparent thermal hysteresis of 270 K:application for displays. *Journal of Materials Chemistry*, 7(6):857–858, 1997.

[358] Helena J. Shepherd, Il'ya A. Gural'skiy, Carlos M. Quintero, Simon Tricard, Lionel Salmon, Gábor Molnár, and Azzedine Bousseksou. Molecular actuators driven by cooperative spin-state switching. *Nature Communications*, 4, 2013.

[359] A. Ruaudel-Teixier, A. Barraud, P. Coronel, and O. Kahn. Spin transition in a magnetic Langmuir-Blodgett film. *Thin Solid Films*, 160(1–2):107–115, 1988.

[360] Jean François Létard, Olivier Nguyen, Hélène Soyer, Christophe Mingotaud, Pierre Delhaès, and Olivier Kahn. First Evidence of the LIESST Effect in a Langmuir-

blodgett Film. *Inorganic Chemistry*, 38(13):3020–3021, 1999.

[361] Y. Bodenthin, G. Schwarz, Z. Tomkowicz, M. Lommel, Th. Geue, W. Haase, H. Möhwald, U. Pietsch, and D. G. Kurth. Spin-crossover phenomena in extended multi-component metallo-supramolecular assemblies. *Coordination Chemistry Reviews*, 253(19–20):2414–2422, 2009.

[362] Saioa Cobo, Gábor Molnár, José Antonio Real, and Azzedine Bousseksou. Multilayer Sequential Assembly of Thin Films That Display Room-Temperature Spin Crossover with Hysteresis. *Angewandte Chemie International Edition*, 45(35):5786–5789, 2006.

[363] M. Cavallini, I. Bergenti, S. Milita, G. Ruani, I. Salitros, Z. R. Qu, R. Chandrasekar, and M. Ruben. Micro-and Nanopatterning of Spin-Transition Compounds into Logical Structures. *Angewandte Chemie International Edition*, 47(45):8596–8600, 2008.

[364] Keita Kuroiwa, Tomoko Shibata, Sono Sasaki, Masaaki Ohba, Atsushi Takahara, Toyoki Kunitake, and Nobuo Kimizuka. Supramolecular control of spin-crossover phenomena in lipophilic Fe(II)-1,2,4-triazole complexes. *Journal of Polymer Science Part A: Polymer Chemistry*, 44(17):5192–5202, 2006.

[365] Masaki Matsuda and Hiroyuki Tajima. Thin Film of a Spin Crossover Complex $[Fe(dpp)_2(BF_4)_2$. *Chemistry Letters*, 36(6):700–701, 2007.

[366] Edna M. Hernández, Carlos M. Quintero, Olena Kraieva, Christophe Thibault, Christian Bergaud, Lionel Salmon, Gábor Molnár, and Azzedine Bousseksou. AFM Imaging of Molecular Spin-State Changes through Quantitative Thermomechanical Measurements. *Advanced Materials*, 26(18):2889–2893, 2014.

[367] Yuehui Wang and Weidong Zhou. A Review on Inorganic Nanostructure Self-Assembly. *Journal of Nanoscience and Nanotechnology*, 10(3):1563–1583, 2010.

[368] Edward C. Ellingsworth, Brittany Turner, and Greg Szulczewski. Thermal conversion of $[fe(phen)_3](SCN)_2$ thin films into the spin crossover complex $Fe(phen)_2(NCS)_2$. *RSC Advances*, 3(11):3745–3754, 2013.

[369] H. Naggert, A. Bannwarth, S. Chemnitz, T. von Hofe, E. Quandt, and F. Tuczek. First observation of light-induced spin change in vacuum deposited thin films of iron spin crossover complexes. *Dalton Transactions*, 40(24):6364–6366, 2011.

[370] T. Palamarciuc, J. C. Oberg, F. El Hallak, C. F. Hirjibehedin, M. Serri, S. Heutz, J. F. Létard, and P. Rosa. Spin crossover materials evaporated under clean high vacuum and ultra-high vacuum conditions: from thin films to single molecules. *Journal of Materials Chemistry*, 22(19):9690–9695, 2012.

[371] Thiruvancheril G. Gopakumar, Matthias Bernien, Holger Naggert, Francesca Matino, Christian F. Hermanns, Alexander Bannwarth, Svenja Mühlenberend, Alex Krüger, Dennis Krüger, Fabian Nickel, Waldemar Walter, Richard Berndt, Wolfgang Kuch, and Felix Tuczek. Spin-Crossover Complex on Au(111): Structural and Electronic Differences Between Mono- and Multilayers. *Chemistry – A European Journal*, 19(46):15702–15709, 2013.

[372] Xin Zhang, Tatiana Palamarciuc, Patrick Rosa, Jean-François Létard, Bernard Doudin, ZhengZheng Zhang, Jian Wang, and Peter A. Dowben. Electronic Structure of a Spin Crossover Molecular Adsorbate. *The Journal of Physical Chemistry C*, 116(44):23291–23296, 2012.

[373] Alex Pronschinske, Yifeng Chen, Geoffrey F. Lewis, David A. Shultz, Arrigo Calzolari, Marco Buongiorno Nardelli, and Daniel B. Dougherty. Modification of Molecular Spin Crossover in Ultrathin Films. *Nano Letters*, 13(4):1429–1434, 2013.

[374] Anton V. Sinitskiy, Andrei L. Tchougréeff, Andrei M. Tokmachev, and Richard Dronskowski. Modeling molecular crystals formed by spin-active metal complexes by atom–atom potentials. *Physical Chemistry Chemical Physics*, 11(46):10983–10993, 2009.

[375] S. Gueddida and M. Alouani. Spin crossover in a single $Fe(phen)_2(NCS)_2$ molecule adsorbed onto metallic substrates: An ab initio calculation. *Physical Review B*, 87(14):144413, 2013.

[376] X. H. Qiu, G. V. Nazin, and W. Ho. Mechanisms of Reversible Conformational Transitions in a Single Molecule. *Physical Review Letters*, 93(19):196806, 2004.

[377] S. W. Wu, N. Ogawa, G. V. Nazin, and W. Ho. Conductance Hysteresis and Switching in a Single-Molecule Junction. *The Journal of Physical Chemistry C*, 112(14):5241–5244, 2008.

[378] Thomas Leoni, Olivier Guillermet, Hermann Walch, Véronique Langlais, Andrew Scheuermann, Jacques Bonvoisin, and Sébastien Gauthier. Controlling the Charge State of a Single Redox Molecular Switch. *Physical Review Letters*, 106(21):216103, 2011.

[379] Cyrus F. Hirjibehedin, Christopher P. Lutz, and Andreas J. Heinrich. Spin Coupling in Engineered Atomic Structures. *Science*, 312(5776):1021–1024, 2006. PMID: 16574821.

[380] Tadahiro Komeda, Hironari Isshiki, Jie Liu, Yan-Feng Zhang, Nicolás Lorente, Keiichi Katoh, Brian K. Breedlove, and Masahiro Yamashita. Observation and electric current control of a local spin in a single-molecule magnet. *Nature Communications*, 2:217, 2011.

[381] Aitor Mugarza, Cornelius Krull, Roberto Robles, Sebastian Stepanow, Gustavo Ceballos, and Pietro Gambardella. Spin coupling and relaxation inside molecule–metal contacts. *Nature Communications*, 2:490, 2011.

[382] Dmitri B. Strukov, Gregory S. Snider, Duncan R. Stewart, and R. Stanley Williams. The missing memristor found. *Nature*, 453(7191):80–83, 2008.

[383] L.O. Chua. Memristor-The missing circuit element. *IEEE Transactions on Circuit Theory*, 18(5):507–519, 1971.

[384] M. Bowen, J. L. Maurice, A. Barthélémy, P. Prodhomme, E. Jacquet, J. P. Contour, D. Imhoff, and C. Colliex. Bias-crafted magnetic tunnel junctions with bistable spin-dependent states. *Applied physics letters*, 89(10):103517–103517, 2006.

[385] Thiruvancheril G. Gopakumar, Falk Müller, and Michael Hietschold. Scanning Tunneling Microscopy and Scanning Tunneling Spectroscopy Studies of Planar and Nonplanar Naphthalocyanine on Graphite (0001). Part 2: Tip-sample Distance-Dependent I-v Spectroscopy. *The Journal of Physical Chemistry B*, 110(12):6060–6065, 2006.

[386] Thiruvancheril G. Gopakumar, Jan Meiss, Davoud Pouladsaz, and Michael Hietschold. HOMO-LUMO Gap Shrinking Reveals Tip-Induced Polarization of Molecules in Ultrathin Layers: Tip-sample Distance-Dependent Scanning Tunneling Spectroscopy on d^8 (Ni, Pd, and Pt) Phthalocyanines. *The Journal of Physical Chemistry C*, 112(7):2529–2537, 2008.

[387] Martin Diefenbach and Kwang S. Kim. Towards Molecular Magnetic Switching with an Electric Bias. *Angewandte Chemie*, 119(40):7784–7787, 2007.

[388] Sujeet K. Shukla and Stefano Sanvito. Electron transport across electrically switchable magnetic molecules. *Physical Review B*, 80(18):184429, 2009.

[389] Joseph A. Stroscio and D. M. Eigler. Atomic and Molecular Manipulation with the Scanning Tunneling Microscope. *Science*, 254(5036):1319–1326, 1991.

[390] Alex Pronschinske, Robert C. Bruce, Geoff Lewis, Yifeng Chen, Arrigo Calzolari, Marco Buongiorno-Nardelli, David A. Shultz, Wei You, and Daniel B. Dougherty. Iron(II) spin crossover films on Au(111): scanning probe microscopy and photoelectron spectroscopy. *Chemical Communications*, 49(89):10446–10452, 2013.

[391] Gautier Félix, William Nicolazzi, Lionel Salmon, Gábor Molnár, Marine Perrier, Guillaume Maurin, Joulia Larionova, Jérôme Long, Yannick Guari, and Azzedine Bousseksou. Enhanced Cooperative Interactions at the Nanoscale in Spin-Crossover Materials with a First-Order Phase Transition. *Physical Review Letters*, 110(23):235701, 2013.

[392] Karthik V. Raman, Alexander M. Kamerbeek, Arup Mukherjee, Nicolae Atodiresei, Tamal K. Sen, Predrag Lazić, Vasile Caciuc, Reent Michel, Dietmar Stalke, Swadhin K. Mandal, Stefan Blügel, Markus Münzenberg, and Jagadeesh S. Moodera. Interface-engineered templates for molecular spin memory devices. *Nature*, 493(7433):509–513, 2013.

[393] G. Kresse and J. Furthmüller. Efficient iterative schemes for ab initio total-energy calculations using a plane-wave basis set. *Physical Review B*, 54(16):11169–11186, 1996.

[394] John P. Perdew, Kieron Burke, and Matthias Ernzerhof. Generalized Gradient Approximation Made Simple. *Physical Review Letters*, 77(18):3865–3868, 1996.

[395] G. Kresse and D. Joubert. From ultrasoft pseudopotentials to the projector augmented-wave method. *Physical Review B*, 59(3):1758–1775, 1999.

[396] Stefan Grimme. Semiempirical GGA-type density functional constructed with a long-range dispersion correction. *Journal of Computational Chemistry*, 27(15):1787–1799, 2006.

[397] F. M. Leibsle, C. F. J. Flipse, and A. W. Robinson. Structure of the Cu{100}-

c(2×2)n surface: A scanning-tunneling-microscopy study. *Physical Review B*, 47(23):15865–15868, 1993.

[398] T. Choi, C. D. Ruggiero, and J. A. Gupta. Incommensurability and atomic structure of c(2×2)n/cu(100): A scanning tunneling microscopy study. *Physical Review B*, 78(3):035430, 2008.

[399] C. D. Ruggiero, T. Choi, and J. A. Gupta. Tunneling spectroscopy of ultrathin insulating films: CuN on Cu(100). *Applied Physics Letters*, 91(25):253106, 2007.

[400] F. M. Leibsle, S. S. Dhesi, S. D. Barrett, and A. W. Robinson. STM observations of Cu(100)-c(2×2)n surfaces: evidence for attractive interactions and an incommensurate c(2 × 2) structure. *Surface Science*, 317(3):309–320, 1994.

[401] Charles D. Ruggiero. *Scanning Tunneling Microscopy Studies of Cu_2N Films*. PhD thesis, The Ohio State University, 2009.

Manuel GRUBER
Electronic and magnetic
properties of hybrid interfaces.
From single molecules to
ultra-thin films on metallic
substrates.

Résumé

Comprendre les propriétés des interfaces molécules/métaux est d'une importance capitale pour la spintronique organique. La première partie porte sur l'étude des propriétés magnétiques de molécules de phtalocyanine de manganèse. Nous avons montré que les premières couches moléculaires forment des colonnes avec un arrangement antiferromagnétique sur la surface de Co(100). Ces dernières mènent à de l'anisotropie d'échange. La seconde partie porte sur l'étude d'une molécule à transition de spin, la Fe(phen)$_2$(NCS)$_2$, sublimée sur différentes surfaces. Nous avons identifié les états de spin d'une molécule unique sur du Cu(100). De plus, nous avons commuté l'état de spin d'une molécule unique pourvu qu'elle soit suffisamment découplée du substrat.

Mots clés : Spintronique organique, transition de spin, phtalocyanine, Fe(phen)$_2$(NCS)$_2$, couplage d'échange, spinterface, effet Kondo, spectroscopie d'absorption des rayons X, dichroïsme circulaire magnétique de rayons X, microscopie à effet tunnel.

Summary

Understanding the properties of molecules at the interface with metals is a fundamental issue for organic spintronics. The first part is devoted to the study of magnetic properties of planar manganese-phthalocyanine molecules and Co films. We evidenced that the first molecular layers form vertical columns with antiferromagnetic ordering on the Co(100) surface. In turn, these molecular columns lead to exchange bias. The second part is focused on the study of a spin-crossover complex, Fe(phen)$_2$(NCS)$_2$ sublimed on different metallic surfaces. We identified the two spin states of a single molecules on Cu(100). By applying voltages pulses, we switched the spin state of a single molecule provided that it is sufficiently decoupled from the substrate.

Keywords: Organic spintronic, spin crossover, phthalocyanine, Fe(phen)$_2$(NCS)$_2$, exchange bias, interlayer exchange coupling, spinterface, Kondo effect, X-ray absorption spectroscopy, X-ray magnetic circular dichroism, scanning tunneling microscopy.